Cosmic ray modulation processes in the heliosphere

Etienne Eben Vos

Cosmic ray modulation processes in the heliosphere

Etienne Eben Vos
20068034

Dissertation submitted in partial fulfilment of the requirements for the degree *Master of Science in Physics* at the Potchefstroom Campus of the North-West University

Supervisor: Prof. M. S. Potgieter
Assistant Supervisor: Dr. M. Hitge

December 2011
Potchefstroom
South Africa

To my brother,
Jacques Ebva Vos.

Abstract

The solar minimum of 2009 has been identified as an exceptional event with regard to cosmic ray (CR) modulation, since conditions in the heliosphere have reached unprecedented quiet levels. This unique minimum has been observed by the Earth-orbiting satellite, PAMELA, launched in June, 2006, from which vast sets of accurate proton and electron preliminary observations have been made available. These simultaneous measurements from PAMELA provide the ideal opportunity to conduct an in-depth study of CR modulation, in particular charge-sign dependent modulation. In utilizing this opportunity, a three-dimensional, steady-state modulation model was used to reproduce a selection of consecutive PAMELA proton and electron spectra from 2006 to 2009. This was done by assuming full drifts and simplified diffusion coefficients, where the rigidity dependence and absolute value of the mean free paths for protons and electrons were sequentially adjusted below ~ 3 GV and ~ 300 MV, respectively. Care has been taken in calculating yearly-averaged current-sheet tilt angle and magnetic field values that correspond to the PAMELA spectra. Following this study where the numerical model was used to investigate the individual effects resulting from changes in the tilt angle, diffusion coefficients, and global drifts, it was found that *all* these modulation processes played significant roles in contributing to the total increase in CR intensities from 2006 to 2009, as was observed by PAMELA. Furthermore, the effect that drifts has on oppositely charged particles was also evident from the difference between the peak-shaped time profiles of protons and the flatter time profiles of electrons, as is expected for an $A < 0$ polarity cycle. Since protons, which drift into the heliosphere along the heliospheric current-sheet, haven't yet reached maximum intensity levels by 2008, their intensities increased notably more than electrons toward the end of 2009. The time and energy dependence of the electron to proton ratios were also studied in order to further illustrate and quantify the effect of drifts during this remarkable solar minimum period.

Keywords: Cosmic rays, modulation, heliosphere, solar minimum, particle diffusion, particle drifts, galactic protons, galactic electrons.

Opsomming

Die periode van minimum sonaktiwiteit van 2009 is geïdentifiseer as 'n uitsonderlike gebeurtenis wat die modulasie van kosmiese strale (KS) betref, omdat toestande in die heliosfeer ongekende stil vlakke bereik het. Hierdie unieke minimum is goed waargeneem deur die PAMELA satelliet wat in Junie, 2006 gelanseer is. Groot stelle akkurate proton en elektron voorlopige waarnemings is bekendgestel. Dié gelyktydige metings van PAMELA bied die ideale geleentheid om 'n deeglike studie van die modulasie van KS uit te voer, in die besonder ladings-afhanklike modulasie. Hierdie geleentheid is benut deur 'n drie-dimensionele, stasionêre toestand modulasiemodel te gebruik om 'n seleksie van opeenvolgende PAMELA proton en elektron spektra, vanaf 2006 tot 2009, te herproduseer. Dit is gedoen deur volle dryf te aanvaar met vereenvoudigde diffusiekoëffisiënte, waar die styfheidsafhanklikheid en absolute waarde van die gemiddelde vryeweglengte vir protone en elektrone sekwensieel aangepas is onder $\sim 3\,\mathrm{GV}$ en $\sim 300\,\mathrm{MV}$, onderskeidelik. Noukeuringe jaarlikse gemiddelde waardes vir die kantelhoek van die heliosferiese neutrale vlak en die magneetveld is bereken om ooreen te stem met die PAMELA spektra. Na aanleiding van hierdie studie waar die numeriese model gebruik is om die individuele effekte te ondersoek wat ten voorskyn kom weens veranderinge in die kantelhoek, diffusie-koëffisiënte, en globale dryf, is bevind dat *al* hiérdie modulasieprosesse belangrike rolle gespeel het in die bydra tot die totale toename in KS intensiteite soos deur PAMELA waargeneem. Boonop het die effek wat dryf op teenoorgesteld-gelaaide deeltjies het ook duidelik gevolg vanuit die verskil tussen die piek-vormige tydprofiele van protone en die platter tydprofiele van elektrone, soos verwag word vir 'n $A < 0$ polariteit siklus. Aangesien protone, wat die heliosfeer binnedryf langs die neutrale vlak, nog nie maksimum intensiteitsvlakke bereik het teen 2008 nie, het hul intensiteite meer as die van elektrone teen die einde van 2009 toegeneem. Die tyd en energie afhanklikhede van die elektron-tot-proton verhoudings is ook bestudeer ten einde die effek van dryf gedurende hierdie merkwaardige sonminimum verder te illustreer en te kwantifiseer.

Sleutelwoorde: Kosmiese strale, modulasie, heliosfeer, sonminimum, deeltjie diffusie, deeltjie dryf, galaktiese protone, galaktiese elektrone.

Nomenclature

1D	One-Dimensional
2D	Two-Dimensional
3D	Three-Dimensional
ACR	Anomalous Cosmic Ray
ADI	Alternating Direction Implicit
BS	Bow Shock
CIR	Corotating Interaction Region
CME	Coronal Mass Ejection
CR	Cosmic Ray
DC	Diffusion Coefficient
FLS	Fast Latitude Scan
GCR	Galactic Cosmic Ray
HCS	Heliospheric Current-Sheet
HMF	Heliospheric Magnetic Field
HP	Heliopause
ISM	Interstellar Medium
LIS	Local Interstellar Spectrum
LISM	Local Interstellar Medium
MFP	Mean Free Path
MHD	Magnetohydrodynamic
NLGC	Non-Linear Guiding Center
NM	Neutron Monitor
PAMELA	Payload for Antimatter Matter Exploration and Light-nuclei Astrophysics
QLT	Quasi-Linear Theory
SEP	Solar Energetic Particle
SN	Supernova
SNR	Supernova Remnant
SSN	Sunspot Number
SW	Solar Wind
TPE	Transport Equation
TS	Termination Shock

Contents

Chapter 1

Introduction

Galactic cosmic rays (GCRs) are fully charged energetic particles (and antiparticles) that originate from various sources in the Galaxy and beyond. As these particles travel through interstellar space they arrive at the heliosphere – a region of space surrounding our solar system, which is formed by the outward expanding solar wind (SW). Within the heliosphere the energy-dependent intensities of cosmic rays (CRs) are decreased through their interaction with the SW and the heliospheric magnetic field (HMF), a process referred to as heliospheric modulation. The study of CR modulation is primarily concerned with the description of the transport of these particles in heliospheric space. *Parker* (1965) derived a transport equation (TPE) which describes the transport and modulation of CRs in the heliosphere, and that contains all the physical modulation processes. In order to compute the intensity of CRs throughout the heliosphere, this TPE is solved numerically as a three-dimensional (3D) modulation model.

For this study, the computed CR intensities at Earth are of particular importance, since these solutions will be compared to preliminary observations from an Earth-orbiting satellite, PAMELA (a Payload for Antimatter Matter Exploration and Light-nuclei Astrophysics). A selection of PAMELA proton and electron observations, from 2006 to 2009, will be accurately reproduced by carefully adjusting certain modulation parameters in this numerical model. Such results will yield valuable information about the development of the recent solar minimum, with regard to particle drifts and diffusion. Moreover, since simultaneous PAMELA measurements of protons and electrons are available, a comprehensive study of the charge-sign dependent modulation of CRs is also possible, from which the effect of HMF polarity-dependent particle drifts can directly be investigated.

The main objective for this study, therefore, is to reproduce the mentioned selection of PAMELA proton and electron spectra (from $100\,\mathrm{MeV}$ to $50\,\mathrm{GeV}$), in order to obtain tangible evidence of the influence and contribution of the various CR modulation processes during the recent solar minimum, as well as to investigate, specifically, the

charge-sign dependence in the modulation of these particles. These results are furthermore compared to that of other authors where necessary. The structure of this study is arranged in the following chapters:

Chapter 2 is devoted to introductory discussions of the physics related to CRs and the heliosphere in general. These discussions include topics such as the discovery, origin and major populations of CRs, the structure and features of the heliosphere, as well as the Sun and how it contributes to the observed ~ 11-year and ~ 22-year solar activity cycles. An overview of the SW and the termination shock (TS) is given, followed by a discussion of the Parker HMF model and various modifications thereof. The heliospheric current-sheet (HCS) is introduced in this chapter and discussed in light of the so-called current-sheet tilt angle, a parameter that influences the charge-sign dependent modulation of CRs. A brief overview of CR variations through the solar cycle is also given by means of neutron monitor (NM) counts. This chapter concludes with an overview of the ongoing PAMELA space mission.

The numerical transport model used for this study, as well as the underlying mathematical model, is discussed in detail in **Chapter 3**. Attention is given to the assumed drift and diffusion coefficients for protons and electrons, in particular their dependence on rigidity. These coefficients are compared to those used by other authors. A brief overview of the history of numerical modulation models is given, followed by an explanation of the numerical scheme. Features of the 3D modulation model used in this study are discussed.

In **Chapter 4** the numerical model is applied to proton modulation with the aim of reproducing PAMELA proton spectra in order to better understand the modulation experienced by protons during the recent solar minimum. The local interstellar spectrum (LIS) for protons is discussed and compared to various other LIS estimates. This is followed by an overview of the PAMELA monthly-averaged proton spectra from July, 2006 to December, 2009. Due to the apparent unusual modulation conditions that prevailed during the recent solar minimum, the corresponding sunspot number (SSN), NM counts, HCS tilt angle and the average HMF are investigated. The computed proton spectra are compared to PAMELA proton spectra of subsequent years, and the corresponding changes required to be made to modulation parameters, in particular the diffusion coefficients, are investigated. A study of the effect that various modulation processes have on CR modulation for this solar minimum is conducted with respect to energy and time.

Similar to Chapter 4, the numerical model is applied to simulate the transport and modulation of galactic electrons in **Chapter 5**. The electron LIS is discussed in detail and compared to local interstellar spectra (LIS's) proposed by other authors. This is followed by an overview of the monthly-averaged PAMELA electron observations

from July, 2006 to December, 2009, and a comparison between the solutions of subsequent computed electron spectra and PAMELA observations. A similar study, as was done for protons, of the contributing effects from various modulation processes is performed.

The results of Chapters 4 and 5 are combined in **Chapter 6**, where the computed electron to proton ratios are investigated and compared to PAMELA ratios. This chapter starts with a brief summary of previous observations and numerical modelling studies that concern the charge-sign dependent modulation of CRs. The proton and electron results from the previous two chapters are reviewed and compared to each other. In order to further illustrate the effect of charge-sign dependent modulation on CRs, a comparison is made between the time dependence of simultaneously observed proton and electron measurements from PAMELA. The time development of the electron to proton ratios, in particular at rigidities where the diffusion coefficients of these particles are similar, as presented in this chapter, provide a clear indication of how charge-sign dependent drift motions affect the modulation of oppositely charged particles.

Chapter 7 consists of a concise summary of the work presented in the preceding chapters, along with the conclusions that are made from the results. Future research aims are also suggested.

Aspects of this study were presented at the 2009 International Heliophysical Year (IHY) Africa workshop in Livingstone, Zambia, held in June, 2009.

Chapter 2

Cosmic Rays and the Heliosphere

2.1 Introduction

Our heliosphere, situated near the Orion spiral arm at the outer reaches of the Milky Way Galaxy, moves at a velocity of ~ 25 km.s^{-1} through the interstellar medium, being constantly bombarded by vast amounts of highly energetic atomic and subatomic particles, called cosmic rays. As these particles enter and travel through our heliosphere, they are affected by various modulation processes causing them to lose energy and decrease in intensity before reaching Earth.

This chapter is devoted to a discussion of the heliosphere and cosmic rays in general, where special attention will be given to the solar wind, the heliospheric magnetic field and other aspects related to CR modulation and solar activity. The PAMELA satellite and space mission will also be introduced and discussed.

2.2 Cosmic Rays

Cosmic rays, first observed by Viktor Hess (1883-1964) during the renowned balloon flights in 1911 and 1912, are charged particles with energies ranging from the order of MeV to as high as 10^{20} eV. Being mainly composed of $\sim 98\%$ atomic nuclei (most of which are protons) and $\sim 2\%$ electrons, positrons and anti-protons, along with small abundances of heavier nuclei, CRs are subjected to modulation conditions inside the heliosphere, which affect both their energy and intensity. Modulated CRs that reach the Earth serve as an indirect probe that provide us with valuable information about unexplored regions of the heliosphere (e.g. *Heber*, 2001).

Generally, CRs are classified in four major populations, the first of which is galactic cosmic rays. These CRs originate from far outside the solar system where they are accelerated by i.a. supernovae (SNe) explosions and active galactic nuclei (AGNs) to energies between a few hundred keV to as high as 3.2×10^{20} eV (e.g. *Koyama et al.*,

1995, and *Tanimori et al.*, 1998). Furthermore, *Ginzburg and Syrovatskii* (1969) suggested that GCRs probably originate not only from such explosions, but also from supernova remnants (SNRs) which may include neutron stars. Assuming that the energy of a SN explosion is in the order of $\sim 10^{51}$ erg, with an occurrence rate of 1 every 30 years, it is calculated that about 15% of the kinetic energy of the ejecta of a SN is needed to maintain the observed CR energy density $\omega_{CR} \approx 1.5\,\mathrm{eV/cm^3}$. CRs are also accelerated by the outward propagating SN shockwave through a mechanism called diffusive shock acceleration, which is a version of Fermi type acceleration. Direct evidence of particle acceleration in SNRs is evident in non-thermal radio, X-ray and gamma-ray radiation (e.g. *Ptuskin*, 2005). The energy spectrum of GCRs has the form of a power law that goes like $j \propto E^{-\gamma}$, with the spectral index $\gamma \approx 2.6$, E the kinetic energy in MeV.nuc^{-1}, and j the differential intensity, normally measured in units of particles.m^{-2}.s^{-1}.sr^{-1}.MeV^{-1}. At energies below ~ 30 GeV, GCRs measured at Earth no longer have a spectral index of $\gamma = 2.6$ due to solar modulation effects that become increasingly important.

Solar energetic particles (SEPs) are another class of CRs that originate from either the solar corona or regions close to the Sun and are related to solar flares (e.g. *Forbush*, 1946) and coronal mass ejections (CMEs), as well as interplanetary shocks (see *Cliver*, 2000 for a detailed review). These particles are intermittently observed at Earth, usually during solar maximum activity, having energies at the lower end of the spectrum up to several hundred MeV.

A third class of CRs is anomalous cosmic rays (ACRs). These particles enter the heliosphere as neutral interstellar atoms, unaffected by the heliospheric magnetic field, after which they become singly ionized relatively close to the Sun, either through charge-exchange or photo-ionization (*Pesses et al.*, 1981). These ions are then "picked up" by the HMF, now called pick-up ions, and transported to the solar wind termination shock where they are accelerated through a process of first order Fermi acceleration up to energies of ~ 100 MeV (see e.g. *Fichtner*, 2001, for a review; see also *Strauss*, 2010).

Jovian electrons, discovered in 1973 by Pioneer 10 during the Jupiter fly-by, forms the fourth class of CR particles that originate from Jupiter's magnetosphere, which is known to be a relatively strong source of electrons at energies ~ 30 MeV (e.g. *Simpson et al.*, 1974, and *Chenette et al.*, 1974). These electrons, dominating at the lower end of the electron spectrum, are primarily found within the first ~ 10 AU from the Sun. See *Ferreira* (2002) for a detailed study of the transport of Jovian electrons in the heliosphere. The latter three classes of CRs will not be considered in this study.

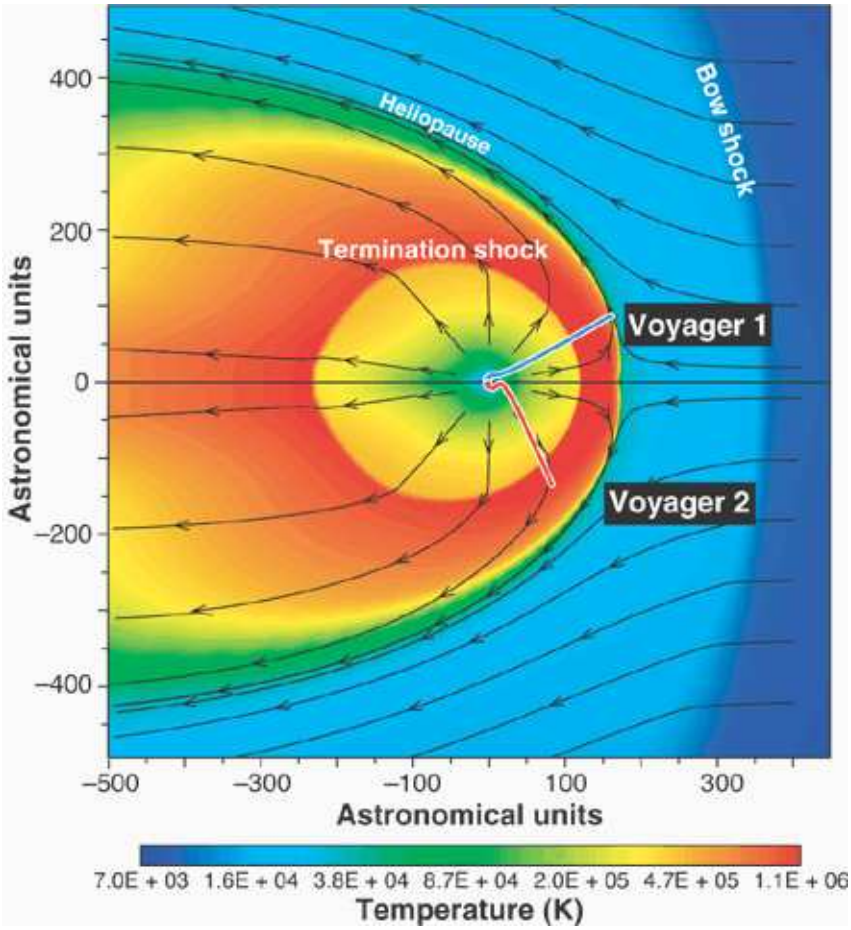

Figure 2.1: A magnetohydrodynamic simulation of the heliosphere indicating the temperatures. From this meridional cut, the positions of the TS, heliopause and the bow shock are clearly seen, along with the indicated Voyager 1 and 2 trajectories. At the TS, the SW plasma heats up to 10^6 K as the SW plasma speed transitions from supersonic to subsonic. Figure taken from *Zank* (1999).

2.3 Structure of the Heliosphere

It is well known that, due to a pressure difference, the solar corona is not confined to the Sun's surface, but continually expands into interplanetary space at supersonic speeds. As our solar system moves through space, this outward expanding solar wind, consisting of a continuous stream of ionized gas, eventually encounters and interacts with the interstellar medium (ISM) to form a spherical quasi-static "bubble" that serves as a defining boundary between the SW plasma and the ISM. This boundary is referred to as the heliopause (HP; see e.g. *Fichtner and Scherer*, 2000 for an overview). It is at this boundary that the SW plasma turns around and merges with the surrounding local interstellar medium (LISM). This region of space occupied by the outward flowing SW plasma is called the heliosphere, and it encloses the borders of our solar system and

beyond. The structure of the heliosphere is therefore primarily determined by the SW, as well as the interstellar "wind". Figure 2.1 shows a magnetohydrodynamic (MHD) simulation of the heliosphere in the meridional plane which indicates the plasma temperatures (taken from *Zank*, 1999). From this figure the various regions within and around the heliosphere are apparent, among which are the termination shock and the bow shock (BS). See e.g. *Suess* (1990) and *Zank* (1999) for comprehensive reviews of the global properties of the heliosphere.

As the SW expands outward, it remains virtually unaffected by the celestial bodies in the solar system. At a heliocentric distance of between 70 AU and 100 AU (e.g. *Whang and Burlaga*, 2000), where the SW ram pressure equals the external interstellar thermal pressure, the supersonic SW plasma rapidly decreases to subsonic speeds. At this point the SW plasma interacts violently with the interstellar gas, resulting in the formation of a heliospheric shock, called the termination shock (*Florinski et al.*, 2003; *Strauss et al.*, 2010a, 2010b). It is at the TS that the SW is slowed down by its interaction with the LISM. This region, between the TS and the HP, is called the heliosheath. As previously mentioned, it is believed that the TS is the primary source region of ACRs (e.g. *Strauss et al.*, 2010a, 2010b).

The TS is, however, considered to be a dynamic shock, and its position varies depending on the solar cycle. Evidence of this nature of the TS was found when Voyager 1 crossed the TS at a distance of ~ 94 AU from the Sun, followed by Voyager 2, which crossed at a distance of ~ 10 AU closer than that of Voyager 1 (see e.g. *Stone et al.*, 2005, and *Stone et al.*, 2008). It has also been speculated that the HP exhibits the same dynamic nature than that of the TS (e.g. *Webber and Intriligator*, 2011).

The BS is situated beyond the HP, at a distance of ~ 350 AU from the Sun, which supposedly includes a region known as the outer heliosheath. Concerning the propagation of CRs in the heliosphere, it has been shown by *Scherer et al.* (2011) that galactic protons already experience modulation in this outer region of the heliosphere.

2.4 The Sun and Solar Activity

Our Sun is the primary source of energy for all forms of life on Earth. Being a main-sequence yellow dwarf, with an effective temperature of 5.778×10^3 K, our Sun is classified as a star of spectral type G2V (*Stix*, 2004) and by mass consists of about 70% hydrogen, 28% helium, and 2% heavier nuclei. The Sun also possesses a magnetic field, similar to that of a typical magnetic dipole, where the Northern and Southern hemispheres have opposite polarities. As the SW expands, it also convects the solar magnetic field outward across the heliosphere to form what is known as the heliospheric magnetic field. It is well known that the HMF is the primary influencing factor

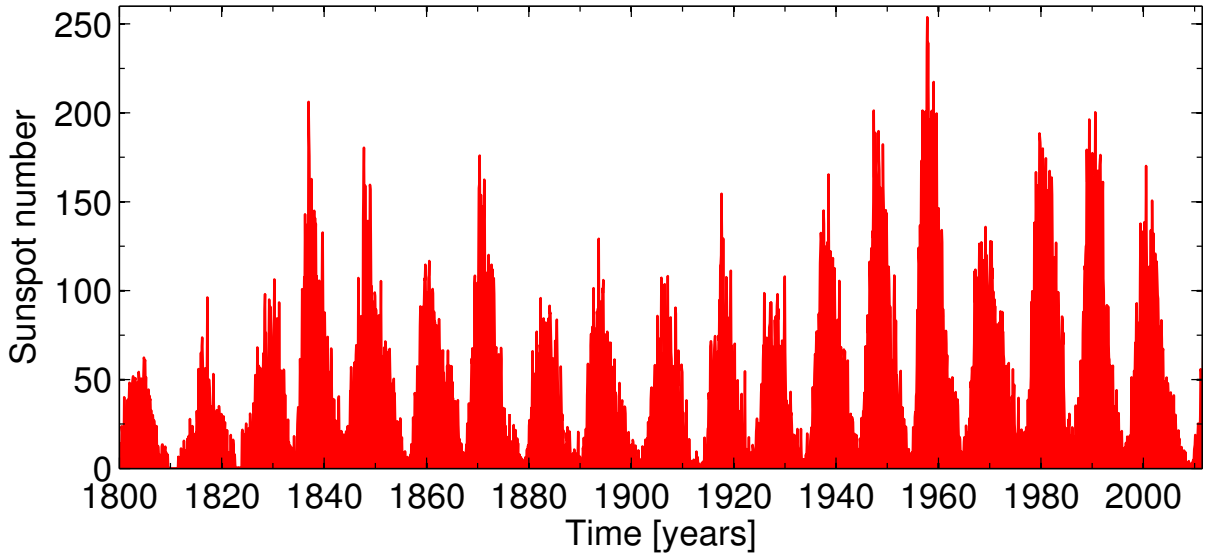

Figure 2.2: Monthly-averaged sunspot number from 1800 to 2011. From this graph the 11-year solar cycle is clearly seen in the sunspot number fluctuations. Data obtained from http://sidc.oma.be/.

of, and driving force behind, the solar activity cycle throughout the heliosphere.

Historical observations of the Sun and sunspots, dating back to as early as 350 BC, became the foundation of our understanding of how the Sun behaves in light of the solar cycle. Sunspots are dark regions that form on the photosphere of the Sun that have a lower temperature than their surrounding environment. It is well known that sunspots possess intense magnetic fields and usually appear in groups. Sunspot observations, therefore, directly reflect on the current state of the Sun, thereby providing us with valuable information about the solar cycle and solar activity. Figure 2.2 gives the monthly average sunspot number (i.e. the number of visible sunspots on the solar surface) as function of time, from 1800 to 2011. From this figure it is clear that there is a quasi-periodic variation in solar activity, with an apparent periodicity of ~ 11 years during which the sunspot number fluctuate between successive maxima and minima, referred to as solar maximum and minimum (e.g. *Smith and Marsden*, 2003). Sunspot numbers, therefore, effectively serve as a fundamental solar activity index (see e.g. *Simon*, 1980 for an overview).

Apart from the above-mentioned 11-year cycle in sunspot numbers, it was found that the solar polarity itself also has a periodic variation, now with a 22-year periodicity. After every 11-year cycle, the solar magnetic field undergoes a polarity reversal so that after every two successive 11-year cycles the Sun's polarity assumes its initial configuration, hence the 22-year cycle. When the solar magnetic field points outward in the Northern hemisphere and inward in the Southern hemisphere, the Sun is said to be

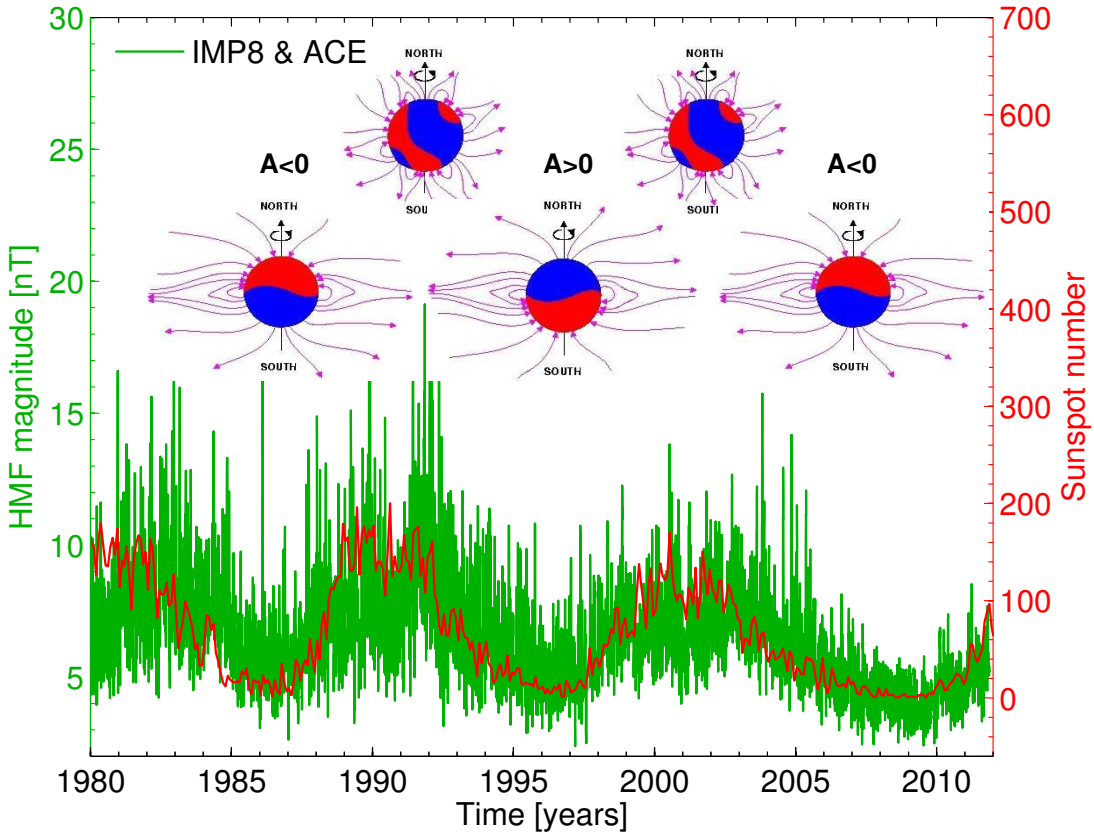

Figure 2.3: The correlation between the heliospheric magnetic field magnitude (green) and the sunspot number (red) are clearly seen in the 11-year cycle, during which both quantities fluctuate between solar maximum and solar minimum. The inserted illustrations represent the solar polarity epoch during an $A > 0$ and $A < 0$ cycle, as well as during the transitional phase between these cycles. Data obtained from http://nssdc.gsfc.nasa.gov/.

in an $A > 0$ cycle, whereas during an $A < 0$ cycle the solar magnetic field points inward in the Northern- and outward in the Southern hemispheres respectively. In addition to the polarity reversal, the magnetic field magnitude also shows a similar fluctuating pattern that correlates with the sunspot number counts. Figure 2.3 gives a plot of the HMF magnitude (as measured by IMP 8 and ACE) from 1980 to 2010 overlaid by the SSN counts. Schematic illustrations of the solar polarity epoch during an $A > 0$ cycle (middle) and an $A < 0$ cycle (left and right), are also shown, both of which occur at solar minimum. The top illustrations correspond to solar maximum conditions. It is clearly visible that the HMF is significantly weaker during solar minimum conditions (with an average magnitude of ~ 5 nT) compared to solar maximum conditions (with magnitudes between about 10 nT and 12 nT. See e.g. *Smith* (2008) for a detailed discussion of the HMF in light of the solar cycle.

Not surprisingly the solar wind is also correlated to solar activity, as well as the tilt angle of the so-called heliospheric current-sheet, which is a thin neutral sheet where

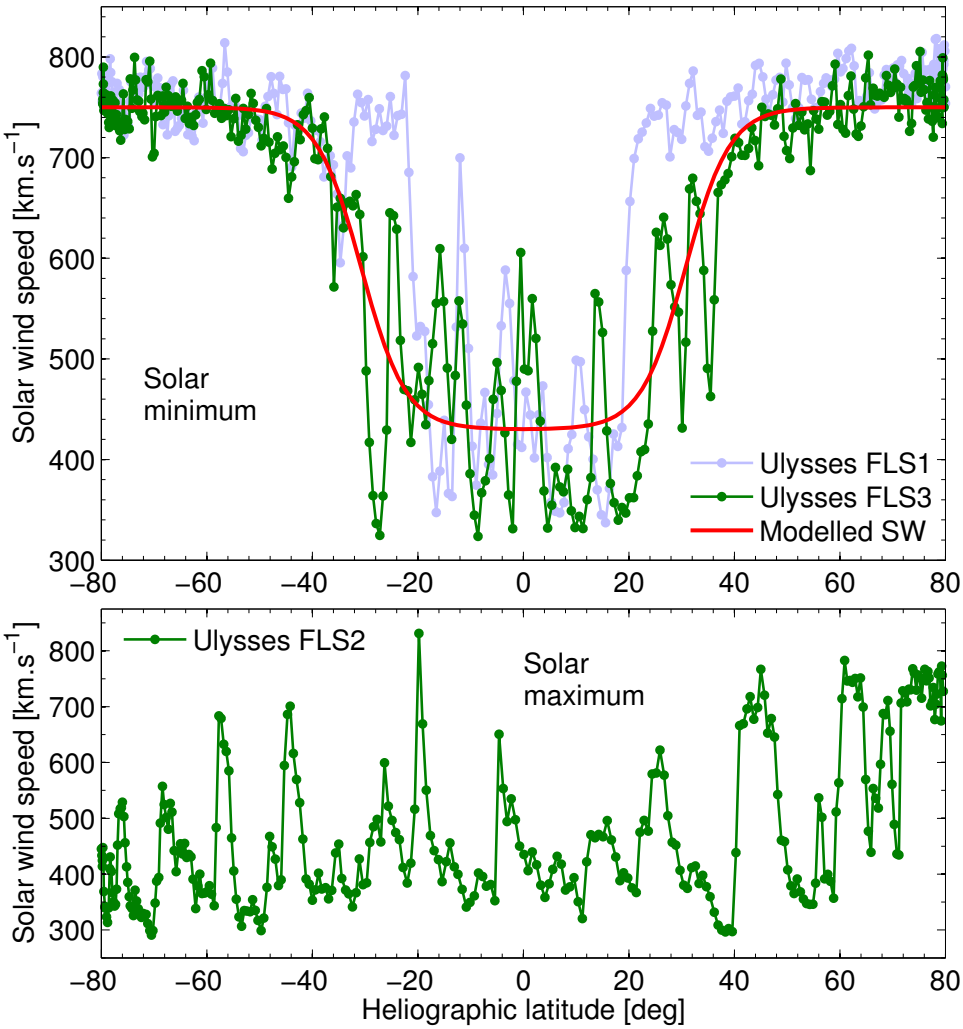

Figure 2.4: The latitudinal dependence of the SW speed at solar minimum (top panel) and solar maximum (bottom panel). Ulysses's first and third fast latitude scans show a clear SW latitudinal dependence (during solar minimum), whereas Ulysses's second fast latitude scan doesn't. The red curve represents the assumed SW profile that gives the best fit to the third fast latitude scan profile. Data obtained from http://cohoweb.gsfc.nasa.gov/.

the oppositely directed open magnetic field lines from the Sun meet. These topics, along with their relation to the solar cycle, will be discussed in detail in the following sections.

2.5 The Solar Wind and Termination Shock

Early cometary studies on the orientations of ionic comet tails led scientists to propose various theories in an attempt to explain their observations. Biermann published a series of papers between 1951 and 1957 wherein he first postulated the existence of a continuous emission of solar particles, which was, in those days, known as the "solar

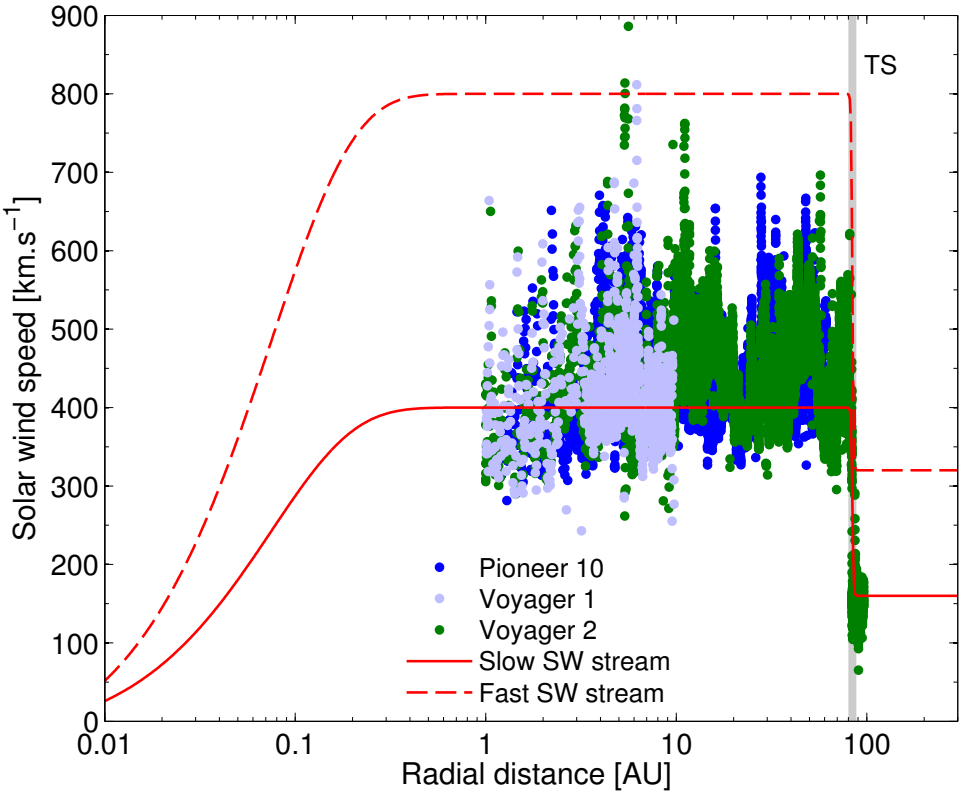

Figure 2.5: The radial dependence of the SW speed. Shown here are three sets of Pioneer and Voyager measurements as function of radial distance. The red curves represent the modelled SW radial speed profiles that correspond to the fast and slow SW components. This model includes a TS at 84 AU. Data obtained from http://cohoweb.gsfc.nasa.gov/.

corpuscular radiation" (*Biermann*, 1961; see also *Fichtner*, 2001, and references therein). Biermann based his postulate on the fact that the ion tails of comets passing close by the Sun always point radially away from the Sun, a phenomenon that couldn't be held responsible for solar radiation pressure. In 1958, Eugene Parker presented his theory of this corpuscular radiation, calling it the "solar wind", in which he describes it as a supersonic magnetized fluid (*Parker*, 1958). *Parker* (1963) showed that the only way in which the Sun could remain in equilibrium was if the solar corona was expanding at supersonic speeds.

The very existence of the SW is ascribed to a difference in pressure between the corona and the interstellar medium. This leads to the corona emitting a continuous stream of ionized gas. As a result of the fact that the SW is coupled with the corona, the SW structure largely depends on the coronal structure which, in turn, is shaped by the magnetic field structures present in the corona. The solar magnetic field, therefore, dominates the original SW outflow.

During solar minimum condition, the Sun's global magnetic field has its simplest

form, and there can be distinguished between two different types of coronal magnetic field structures: regions containing open magnetic field lines, and regions containing closed magnetic field lines. These structures eventually result in different SW and interplanetary magnetic field properties. In regions that contain closed field lines, the magnetic field is perpendicular to the radial SW outflow, which presumably inhibits the outflow. Such regions, called slow SW streams, are generally found at low heliographic latitudes, where the SW has typical velocities of $\sim 400\,\mathrm{km.s^{-1}}$ (*Schwenn*, 1983; *Marsch*, 1991). Conversely, fast SW streams, associated with open magnetic field structures, originate from large unipolar coronal holes located at higher heliographic latitudes near the solar poles (e.g. *Krieger et al.*, 1973). Typical velocities of the SW in these regions are about $800\,\mathrm{km.s^{-1}}$. Other readily observed transient phenomena that appear in the SW include, among other, corotating interaction regions (CIRs), which are regions of high compression that are formed when fast SW streams catch up with slower SW streams (see *Heber et al.*, 1999, for an overview of CIRs).

The existence of these different SW regions readily imply a latitudinal dependence in the SW speed, which has been confirmed by the Ulysses spacecraft (e.g. *Phillips et al.*, 1995). Figure 2.4 shows the daily average SW speed measured by Ulysses during its three fast latitudinal scans (FLSs) as a function of heliographic latitude. The first and final FLS (top panel), which took place during solar minimum, displays a clear latitudinal dependence in the speed profile. Here the slow SW streams are observed in the equatorial region between $\sim 20°$S and $\sim 20°$N, whereas the fast SW streams appear at latitudes $\gtrsim 20°$ in the Northern and Southern hemispheres. Superimposed on the Ulysses data in Figure 2.4, is the assumed latitudinal dependence used for modelling purposes (red curve). For solar maximum, however, there appears to be a mixture of fast and slow SW streams so that no well-defined speed profile is visible, as can be seen in the bottom panel of Figure 2.4 (e.g. *Richardson et al.*, 2001).

Concerning the radial SW speed dependence, *Sheeley et al.* (1997) found that the SW, across all latitudes, accelerates within 0.1 AU from the Sun, after which it becomes a steady flow at 0.3 AU. This is illustrated in Figure 2.5, which shows the SW speed measurements from Voyager 1 and 2, and Pioneer 10, as a function of radial distance. At ~ 84 AU the Voyager 2 measurements show a sudden decrease in speed, which corresponds to the TS crossing. As with Figure 2.4, this behaviour in the radial direction is emulated by the theoretical speed profile, which shows two modelled scenarios that correspond to the fast and slow SW components (red solid and dashed curves). Within the first 0.1 AU the SW accelerates, after which, beyond 0.3 AU, it expands at a constant supersonic speed. Since the supersonic flow cannot steadily decelerate to subsonic flow, the supersonic flow energy is dissipated discontinuously in a shock, i.e. the TS, at ~ 84 AU.

To construct a coherent model for the SW speed profile that is axially symmetric, it is assumed that the radial and latitudinal dependencies are independent of each other, so that the outward directed SW velocity, $\mathbf{V}_{sw}(r,\theta)$, can be written as

$$\mathbf{V}'_{sw}(r,\theta) = V'_{sw}(r,\theta)\,\mathbf{e}_r = V_0 V_r(r) V_\theta(\theta)\mathbf{e}_r, \tag{2.1}$$

with r the radial distance from the Sun (in AU), θ the polar angle (or co-latitude), $V_0 = 400$ km.s^{-1}, and $\mathbf{e}_r$ the unit vector in the radial direction. The characteristic SW latitude dependence $V_\theta(\theta)$ (for solar minimum conditions), represented by the red curve in Figure 2.4, is given by

$$V_\theta(\theta) = 1.475 \mp 0.4\tanh\left[6.8\left(\theta - \frac{\pi}{2} \pm \xi\right)\right], \tag{2.2}$$

where the top and bottom signs correspond to the Northern (for $0 \leq \theta \leq \frac{\pi}{2}$) and Southern (for $\frac{\pi}{2} < \theta \leq \pi$) hemispheres respectively. Here, $\xi = \alpha + 15\pi/180$, with α the angle between the Sun's rotational and magnetic axis, previously referred to as the HCS tilt angle. The effect of ξ is to establish the polar angle (i.e. co-latitude) at which V begins to transition from the slow to the fast SW speed.

According to this model, it can be seen from Figure 2.4 that the fast SW in the polar regions now has a maximum speed of 750 km.s^{-1}, whereas in the equatorial region the slow SW has a minimum speed of 430 km.s^{-1}. This combination of parameters (for Equation 2.2) has been chosen to give the best fit to the SW speed data from Ulysses's third FLS. As previously mentioned, no clear latitudinal dependence exists for solar maximum conditions, so that $V_\theta(\theta)$ is simply assumed to be unity in Equation 2.1. Apart from the altered parameters, a similar SW model approach SW was used by e.g. *Hattingh* (1998), *Langner* (2004) and *Strauss* (2010).

The radial dependence, $V_r(r)$, inside the TS is given by

$$V_r(r) = 1 - \exp\left[\frac{40}{3}\left(\frac{r_\odot - r}{r_0}\right)\right], \tag{2.3}$$

with $r_\odot = 0.005$ AU the Sun's radius, and $r_0 = 1$ AU. For a heliosphere without a TS, the radial SW speed profile would, according to the above equation, remain at a constant velocity throughout the heliosphere. Conversely, for a heliosphere that includes a TS, the radial speed profile would typically look like the modelled curves of Figure 2.5, which, in this case, is given by

$$V_{sw}(r,\theta) = V'_{sw}(r_{TS},\theta)\,\frac{s+1}{2s} - V'_{sw}(r_{TS},\theta)\,\frac{s-1}{2s}\tanh\left(\frac{r - r_{TS}}{L}\right), \tag{2.4}$$

with r_{TS} the radial position of the TS (in this case 84 AU), $L = 1.2$ AU the shock scale

length, and $s = 2.5$ the shock compression ratio in the downstream region (further away from the Sun, beyond the shock). The shock compression ratio is defined by $s = V_1/V_2$, with V_1 the flow speed in the upstream region (closer to the Sun, ahead of the shock) and V_2 the flow speed in the downstream region. See e.g. *Li et al.* (2008) for a discussion about the properties of the TS. See also e.g. *Marsch et al.* (2003) for a further review about the SW.

2.6 The Heliospheric Magnetic Field

According to MHD fluid theory, the existence of an interplanetary magnetic field simply follows from the concept of having a magnetic field frozen into a fluid. Within this frame of reference one can think of an outward flowing plasma that virtually drags the frozen-in field along with it, resulting in a magnetic structure that corresponds to the plasma flow. However, for the radially expanding SW, this only apply to regions where the plasma flow dominates the frozen-in magnetic field, which occur at radial distances beyond a heliocentric distance of $\sim 2.5 r_\odot$ (which describes a surface referred to as the solar source surface). At this distance the open magnetic field lines become approximately radial so that they are carried off into interplanetary space to become the HMF. Conversely, at distances closer to the Sun the magnetic field dominates the plasma outflow (see e.g. *Wang and Sheeley*, 1995, and *Smith*, 2008).

The HMF plays a critical role in heliospheric modulation in that it effectively determines the transport of CRs in the heliosphere. The overall behaviour of these charged particles, therefore, primarily depend on the HMF line configuration and its embedded turbulence.

2.6.1 The Parker Magnetic Field

It is apparent that, since the Sun rotates about an axis perpendicular to the equatorial plane, the HMF exhibits a spiral structure, which is known as the Parker spiral (*Parker*, 1963). In describing the HMF, Parker used an approach where he avoided electric fields and currents, a theory known as magnetohydrodynamics. The Parker model is basically a SW hydrodynamic model which ignores the magnetic field as long as the acceleration of the coronal plasma is unaffected. The magnetic field is simply added to serve as a "tracer" in the SW flow (e.g. *Smith*, 2008). See *Parker* (2001) for a review on early HMF developments.

The analytical model that describes the Parker spiral for radial distances $r \geq r_\odot$, as

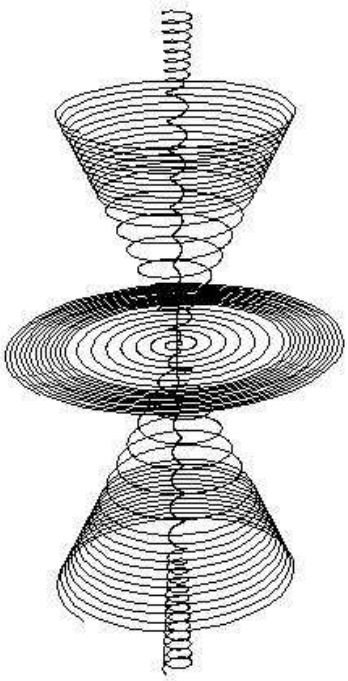

Figure 2.6: The Parker magnetic field has the basic form of Archimedian spirals as shown here. Figure taken from *Strauss* (2010).

derived by *Parker* (1958), is given by the expression

$$\mathbf{B} = B_n \left(\frac{r_0}{r}\right)^2 (\mathbf{e}_r - \tan\psi \mathbf{e}_\phi) \left[1 - 2H\left(\theta - \theta'\right)\right], \tag{2.5}$$

where $\mathbf{e}_r$ and $\mathbf{e}_\phi$ are unit vectors in the radial and azimuthal directions respectively, and B_n used to determine the HMF magnitude at $r_0 = 1$ AU (Earth), with

$$\tan\psi = \frac{\Omega\left(r - r_\odot\right)\sin\theta}{V_{sw}}, \tag{2.6}$$

with $\Omega = 2.67 \times 10^{-6}$ rad.s^{-1} the average angular rotation speed of the Sun, V_{sw} the SW speed, and ψ the Parker spiral angle, defined to be the angle between the radial direction and the direction of the average HMF at a given position. The Heaviside step function, H in Equation 2.5, determines the polarity of the magnetic field which causes the HMF to change direction across the HCS, and is given by

$$H\left(\theta - \theta'\right) = \begin{cases} 0 & \text{for } \theta < \theta' \\ 1 & \text{for } \theta > \theta', \end{cases} \tag{2.7}$$

with θ' the polar position of the HCS. The basic HMF structure resembles that of

Archimedean spirals traversing cones of constant heliographic latitude, as shown in Figure 2.6. In the equatorial plane, the spiral angle ψ at Earth is typically $45°$, after which it increases with distance to $90°$ at $r \gtrsim 10$ AU.

The magnetic field magnitude of Equation 2.5, $|\mathbf{B}|$, is given by

$$B = B_n \left(\frac{r_0}{r}\right)^2 \sqrt{1 + (\tan\psi)^2}, \tag{2.8}$$

from which it is evident that B decreases as r^{-2} at the poles. It is known however, that, since the solar surface near the poles are granular and turbulent regions that constantly change with time, the radial magnetic field lines in these regions are in a state of unstable equilibrium. This turbulence results in transverse magnetic field components in the polar regions which regularly lead to deviations from the smooth Parker field geometry (*Jokipii and Kóta*, 1989, and *Forsyth et al.*, 1996). The net effect of these deviations is a highly irregular and compressed field line. As a result, the average magnetic field magnitude in the polar regions is greater than that of regions away from the poles.

2.6.2 The Jokipii-Kóta Modification

Jokipii and Kóta (1989) consequently suggested a modification to the Parker spiral field, by introducing a parameter $\delta(\theta)$, which increases the field strength at large radial distances in the polar regions. With this modification, the Parker spiral field now becomes

$$\mathbf{B} = B_n \left(\frac{r_0}{r}\right)^2 \left[\mathbf{e}_r + \left(\frac{r\delta(\theta)}{r_\odot}\right)\mathbf{e}_\theta - \tan\psi \mathbf{e}_\phi\right] \left[1 - 2H\left(\theta - \theta'\right)\right], \tag{2.9}$$

where the magnitude thereof is given by

$$B = B_n \left(\frac{r_0}{r}\right)^2 \sqrt{1 + (\tan\psi)^2 + \left(\frac{r\delta(\theta)}{r_\odot}\right)^2}. \tag{2.10}$$

The effect of this modification is that B now decreases as r^{-1} in the polar and equatorial regions. The modification is given by

$$\delta(\theta) = \frac{\delta_m}{\sin\theta}, \tag{2.11}$$

with $\delta_m = 8.7 \times 10^{-5}$, so that $\delta(\theta) = 0.002$ near the poles and $\delta(\theta) \approx 0$ in the equatorial plane. This modification, therefore, brings about the required changes in the HMF in the polar regions without altering the field noticeably in the equatorial plane. A further consequence of the $1/\sin\theta$ dependence of $\delta(\theta)$ is that the magnetic field is kept divergence free, i.e. $\nabla \cdot \mathbf{B} = 0$ (*Langner*, 2004).

This modification is qualitatively supported by Ulysses's HMF measurements over the polar regions (see e.g. *Balogh et al.*, 1995). For further applications of this modification where $\delta(\theta) = 0.002$ throughout the whole heliosphere, see e.g. *Haasbroek and Potgieter* (1995), *Jokipii et al.* (1995), *Hattingh* (1998), *Potgieter and Ferreira* (1999), and *Potgieter* (2000). The Jokipii-Kóta modification to the HMF is used in this study. See also *Moraal* (1990) for a modification that incorporates the same compensating physical effects than the Jokipii-Kóta modification does.

2.6.3 The Smith-Bieber Modification

Led by magnetic field observations, *Smith and Bieber* (1991) introduced yet another modification where they proposed that the magnetic field is not fully radial below the Alfvén radius, i.e. below the radius at which the magnetic field and solar corona rotate in phase, presumably between $10r_{\odot}$ and $30r_{\odot}$. This modification, parametrized by the ratio of the tangential (azimuthal) magnetic field component to that of the radial component, is incorporated in Equation 2.6, which gives

$$\tan\psi = \frac{\Omega(r-b)\sin\theta}{V_{sw}(r,\theta)} - \frac{rV_{sw}(b,\theta)}{bV_{sw}(r,\theta)}\left(\frac{B_T(b)}{B_R(b)}\right), \tag{2.12}$$

where $b = 20r_{\odot}$, so that, according to an estimate by *Smith and Bieber*, $B_T(b)/B_R(b) \approx -0.02$. This modification changes the geometry of the HMF so that, as a result, it affects the polar field strength. See e.g. *Haasbroek* (1993), *Haasbroek et al.* (1995) and *Minnie* (2002) for the implementation of this modification in numerical models.

2.6.4 Fisk Type Fields

Apart from the above mentioned modifications, the Archimedean Parker spiral has become the standard and generally accepted model for the HMF. This model has been set up under the assumption that the Sun rotates rigidly about its axis. However, according to e.g. *Snodgrass* (1983), the Sun actually undergoes differential rotation, where the solar poles rotate $\sim 20\%$ slower than the solar equator (the former and latter of which have rotation periods of ~ 25 days and ~ 32 days respectively). In 1996, *Fisk* (1996) pointed out that a correction had to be made to the Parker spiral model to account for this, if it is assumed that the HMF footpoints are connected to the differentially rotating photosphere. According to the Fisk model, the HMF exhibits a behaviour which comes from two simultaneous rotational "modes", namely the rigid rotation of the HMF about the solar magnetic axis (at a rate Ω), and the differential rotation ω (dependent on latitude) about a virtual axis inclined at an angle β with respect to the solar rotational axis. See e.g. *Burger and Hattingh* (2001), *Burger* (2005) and *Engelbrecht* (2008)

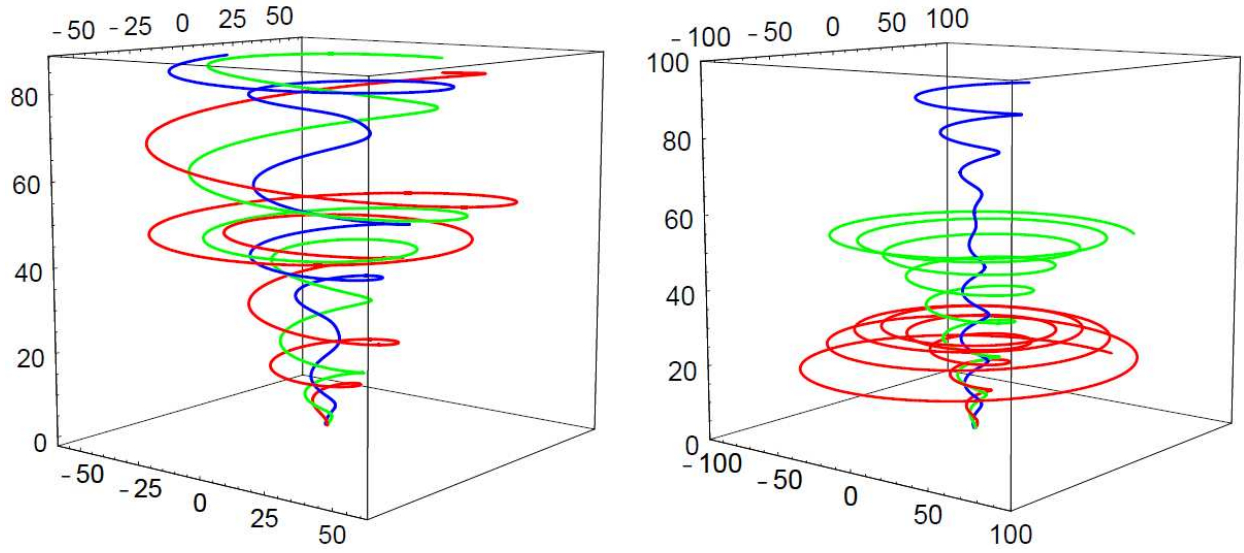

Figure 2.7: Heliospheric magnetic field lines for the type I (left) and type II (right) Fisk field. The field lines originate from 30° co-latitude, but at different longitudes. Radial distances are in AU, with the Sun at the center. Figures taken from *Burger and Hattingh* (2001).

for detailed discussions of the Fisk field.

When these footpoint trajectories of the HMF can be approximated by circles offset from the Sun's rotational axis by β, the components of the Fisk field are (*Zurbuchen et al.*, 1997)

$$\begin{aligned} B_r &= B_n \left(\tfrac{r_0}{r}\right)^2 \\ B_\theta &= B_r \tfrac{(r-r_{ss})}{V_{sw}} \sin\beta \sin\left(\phi + \tfrac{\Omega(r-r_{ss})}{V_{sw}}\right) \\ B_\phi &= B_r \tfrac{(r-r_{ss})}{V_{sw}} \left[\omega \sin\beta \cos\theta \cos\left(\phi + \tfrac{\Omega(r-r_{ss})}{V_{sw}}\right) + \sin\theta(\omega\cos\beta - \Omega)\right], \end{aligned} \tag{2.13}$$

with r_{ss} the solar surface radius. This set of equations describe what is known by *Burger and Hattingh* (2001) as the type I Fisk field, whereas for $\beta = 90°$ Equation 2.13 simplifies to the so-called type II Fisk field. Figure 2.7 schematically shows the HMF magnetic field lines of both types of Fisk fields. Even though the existence of a Fisk HMF might be supported by a tilt angle varying in time, causing regular meridional HMF components (*Kota*, 1997, and *Kota*, 1999), no observational evidence of its existence has been found by *Roberts et al.* (2007), which still leaves the Fisk HMF model as a controversial topic (e.g. *Sternal et al.*, 2011).

A modification of the Fisk HMF has also been proposed by *Burger and Hitge* (2004), known as the Fisk-Parker hybrid field. In this hybrid field the HMF is considered to be a pure Parker field in the equatorial and polar regions, but a pure Fisk field at mid-latitudes, so that in the intermediate regions the HMF is a combination of both Parker and Fisk fields. See also *Burger and Hattingh* (2001) and *Burger et al.* (2008) for

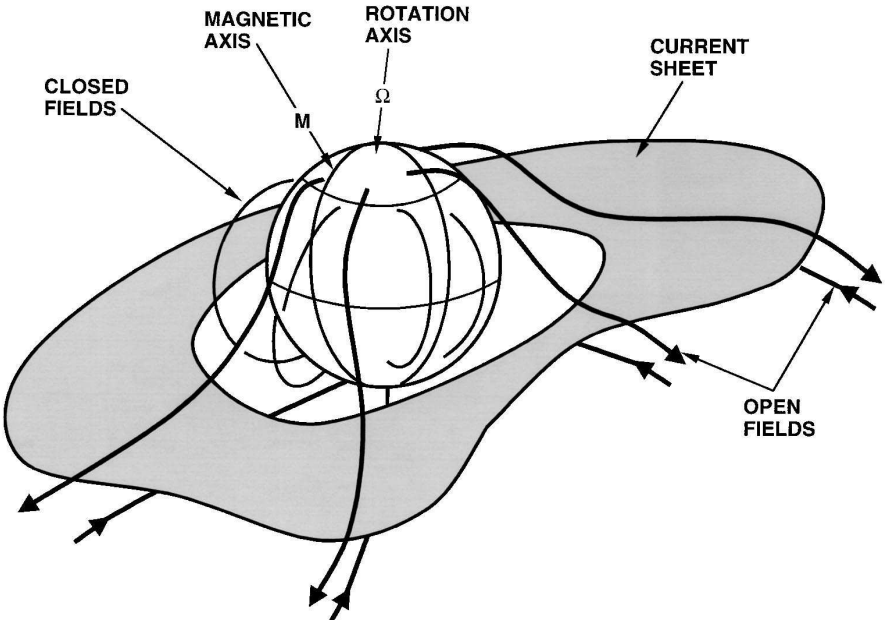

Figure 2.8: A schematic illustration of the heliospheric current-sheet. The open magnetic field lines from the poles (which are at opposite polarities) are separated by the shaded current-sheet. Figure taken from *Smith* (2001).

detailed discussions of the Fisk-Parker hybrid HMF. Since the Fisk field is inherently three dimensional and time dependent, the increased complexity of incorporating such a field in a numerical model is beyond the scope of study for this work.

2.7 The Heliospheric Current-Sheet

As previously mentioned, the magnetic field in the Northern and Southern hemispheres are at opposite polarities. These hemispheres are divided by a three-dimensional corotating current-sheet, which serves as the heliospheric magnetic equator where the open magnetic field lines from the poles meet, as illustrated in Figure 2.8. After every ~ 11-year solar cycle the HMF changes sign across this neutral sheet, so that the magnetic field direction in the two hemispheres alternate with each consecutive cycle. Since the magnetic dipole axis of the Sun is misaligned by an angle α (called the HCS tilt angle) with respect to the solar rotational axis (e.g. *Hoeksema*, 1992), the solar magnetic equator also does not coincide with the heliographic equator. As a result, the HCS is not confined to a plane near the equatorial regions, but instead has a wavy appearance. The amount of waviness is determined by the tilt angle, which in turn is correlated with solar activity. During low levels of solar activity the tilt angle becomes small, with typical values between 5° and 10°, so that the magnetic equator and the he-

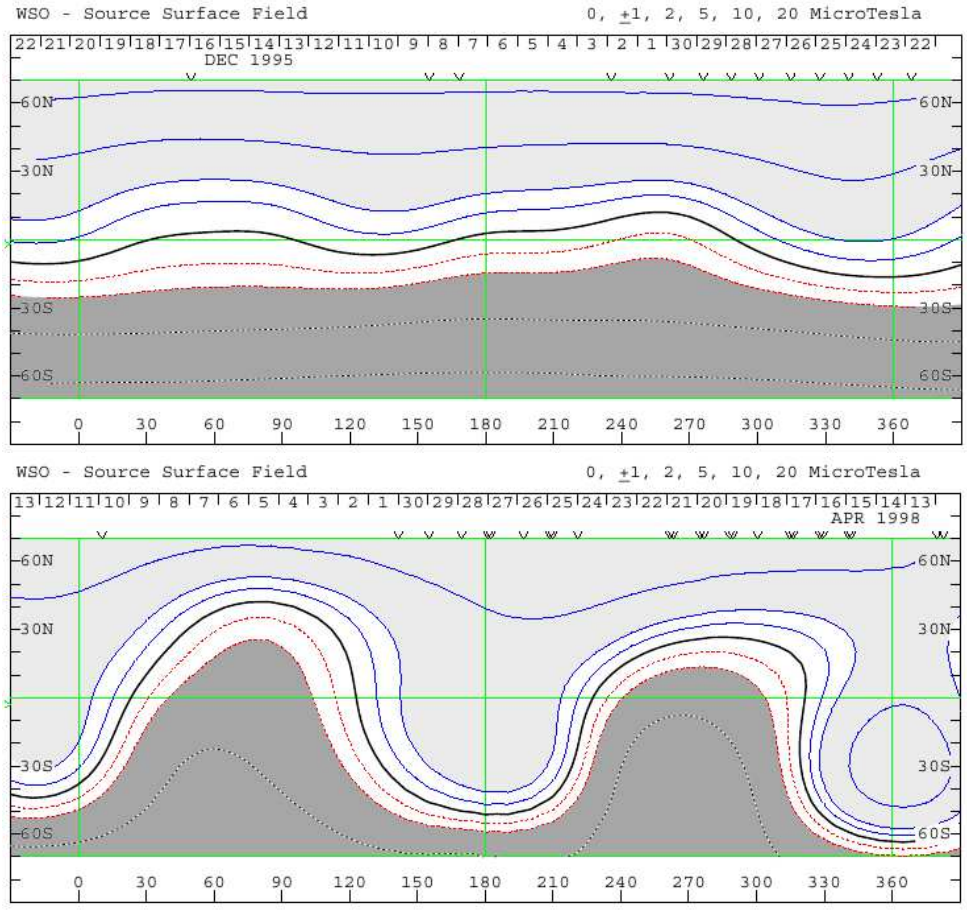

Figure 2.9: The computed source surface field maps ($0°$ to $360°$ in azimuthal angle) during low levels of solar activity (top panel), in December, 1995, and high levels of solar activity (bottom panel), in April, 1998. The solar polar magnetic field strength is indicated by the contour lines, where the bold black line corresponds to the heliospheric current-sheet. The different shades of grey correspond to different polarities. Figures obtained from the Wilcox Solar Observatory: http://wso.stanford.edu/.

liographic equator become closely aligned, resulting in relatively small current-sheet waviness. For solar maximum, however, the wavy structure's amplitude increases to tilt angle values as high as $75°$. See e.g. *Smith* (2001).

The effects of the HCS were first observed in magnetic field measurements from the early Pioneer missions (*Smith*, 1989). These measurements indicated that the HMF alternated polarity in adjacent regions or "sectors", which led to the so-called "sector-structure" explanation (*Wilcox and Ness*, 1965). It was only later realized by *Alfven* (1977) that these alternating polarity sectors were, in fact, separated by a current-sheet which the Pioneer spacecraft repeatedly crossed (see also e.g. *Levy*, 1976).

A clear indication of the existence of the HCS is evident from Figure 2.9, which give synoptic charts for the solar source surface (at $2.5r_{\odot}$) in terms of magnetic fields (obtained from Wilcox Solar Observatory: http://wso.stanford.edu). These charts show

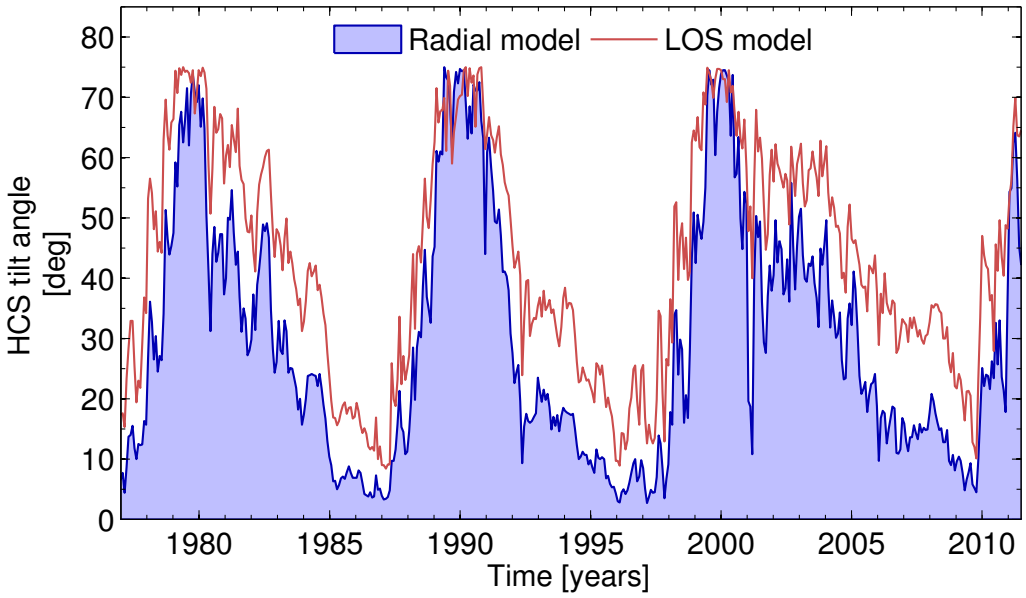

Figure 2.10: Shown in this figure is the computed tilt angle, α, as function of time from 1975 until present. The area plot correspond to tilt angle values calculated by the so-called radial model, whereas the red plot shows tilt angle values calculated from the line-of-sight model. Data obtained from the Wilcox Solar Observatory: http://wso.stanford.edu/, courtesy of J. T. Hoeksema

the magnetic field strength and polarity in the Northern and Southern hemispheres during low levels of solar activity (top panel), in December, 1995, and high levels of solar activity (bottom panel), in April, 1998, where the HCS, identified by the bold black contour, separates the regions of opposite polarity (indicated by the shades of grey). The wavy structure of the HCS is also readily observed in Figure 2.9, especially during high levels of solar activity, when the current-sheet extends to larger polar angles for large tilt angle values. This wavy structure, first suggested by *Thomas and Smith* (1981), plays a key role in CR modulation and particle drift motions, which will be discussed in the next section.

A theoretical expression of this wavy HCS for a constant radial SW was derived by *Jokipii and Thomas* (1981), and is given by

$$\theta' = \frac{\pi}{2} + \sin^{-1}\left\{\sin\alpha \sin\left[\phi + \frac{\Omega\,(r - r_{\odot})}{V_{sw}}\right]\right\}. \tag{2.14}$$

For sufficiently small values of α, the above equation reduces to

$$\theta' \approx \frac{\pi}{2} + \alpha \sin\left[\phi + \frac{\Omega\,(r - r_{\odot})}{V_{sw}}\right], \tag{2.15}$$

where θ' is the polar extent of the HCS.

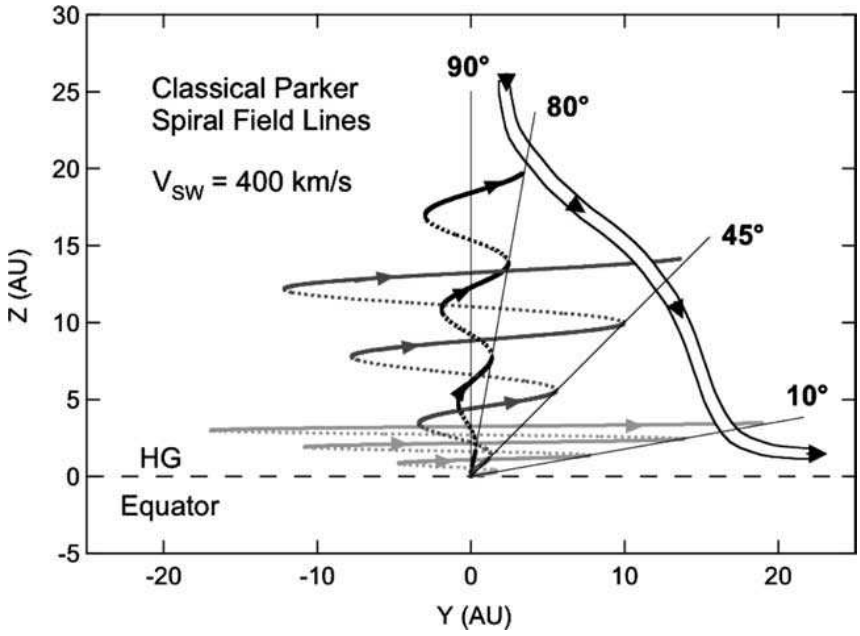

Figure 2.11: A schematic representation of Parker magnetic field lines at various latitudes. The broad outlined-line gives an indication of the possible drift motions for positively charged particles during an $A > 0$ magnetic polarity cycle. Figure taken from *McKibben* (2005).

Since the waviness of the HCS is correlated with solar activity, which is a function of time, the HCS's waviness also exhibits a time dependence that is reflected in the tilt angle. Figure 2.10 shows a graph of the HCS tilt angle as a function of time computed by two models, namely the classic "line-of-sight" model and a newer and possibly more accurate radial model (see http://wso.stanford.edu/for further discussion of these models). The HCS tilt angle, being correlated with solar activity, also shows a clear 11-year cycle that relates with SSN counts and the HMF strength, as would be expected. The HCS tilt angle, therefore, is generally considered as a good proxy for solar activity in CR modulation studies. See e.g. *Kota and Jokipii* (1983) for simulations of CR modulation using a 3D approximation for the HCS.

2.8 Cosmic Ray Variations through the Solar Cycle

It is known that the guiding-center of charged particles undergo gradient and curvature drift motions in the presence of a magnetic field. The HCS, therefore, as well as the global HMF, has significant influences on the transport of CRs in the heliosphere (e.g. *Jokipii et al.*, 1977). Since the HMF has opposite polarities in the regions separated by the HCS, particle drift motions are induced along the HCS. For an $A > 0$ cycle, when the HMF is directed outward in the Northern hemisphere and inward in the Southern hemisphere, positively charged particles undergo drift motions from the polar regions

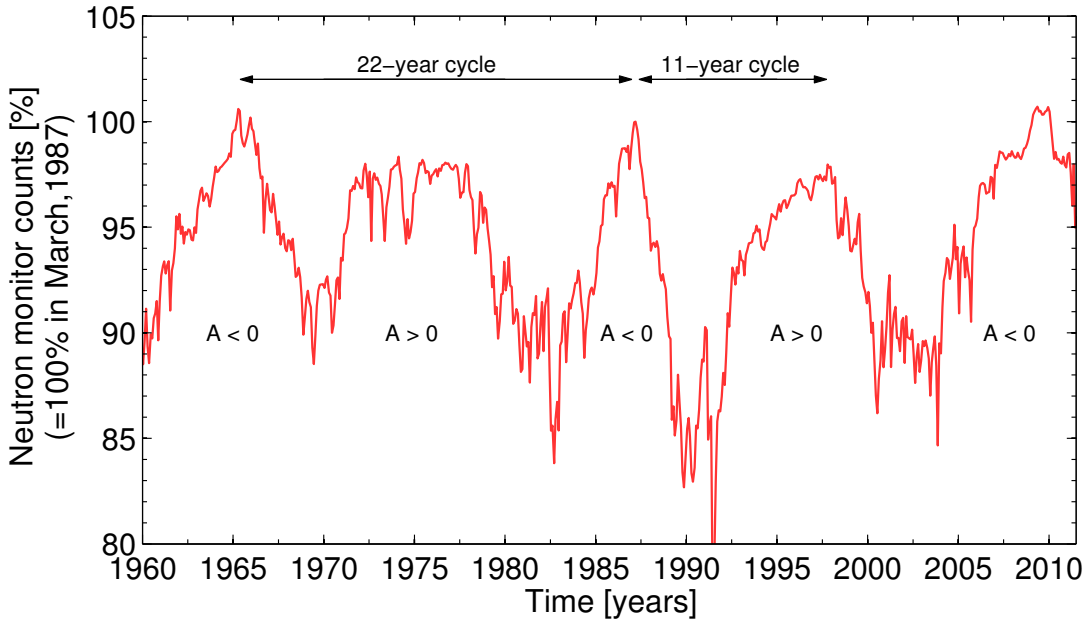

Figure 2.12: Neutron monitor counts as a function of time, as measured by the Hermanus neutron monitor. These counts are normalized with respect to March, 1987, which is at 100%. The $\sim$ 11-year and $\sim$ 22-year cycles are clearly noticeable. The cutoff rigidity for CRs at Hermanus, South Africa, is 4.6 GV. Data obtained from http://www.nwu.ac.za/content/neutron-monitor-data.

toward the equatorial region, and outward along the HCS, as illustrated in Figure 2.11. Negatively charged particles drift in opposite directions (and hence the term charge-sign dependent modulation). During an $A < 0$ cycle the drift directions are reversed. As a result, the amount of waviness of the HCS, as well as the drift direction, directly influence the ability of charged particles to reach certain regions in the heliosphere. These drift motions do, however, only contribute significantly to CR modulation during solar minimum conditions, when the HMF exhibits a well-ordered structure (e.g. *Ferreira and Potgieter*, 2004, and *Ndiitwani et al.*, 2005).

When CRs reach the Earth they collide with molecules in the atmosphere, producing air showers of secondary particles (e.g. *Krüger*, 2006). These secondary particles are then detected by ground-based neutron monitors, giving an indication of the CR flux at Earth. As an example of long-term observations of the modulation of GCRs, Figure 2.12 gives a graph of NM counts, measured by the Hermanus NM, as a function of time from 1960 until present. As could be expected, the 11-year solar activity cycle also gives rise to an 11-year CR modulation cycle, which is identified by times of increased CR flux in Figure 2.12 that occurred around 1965, 1976, 1987, 1997, and recently in 2009. However, a comparison of this figure with Figures 2.2, 2.3 and 2.10 reveals that the observed CR flux is anti-correlated with solar activity, meaning that higher CR

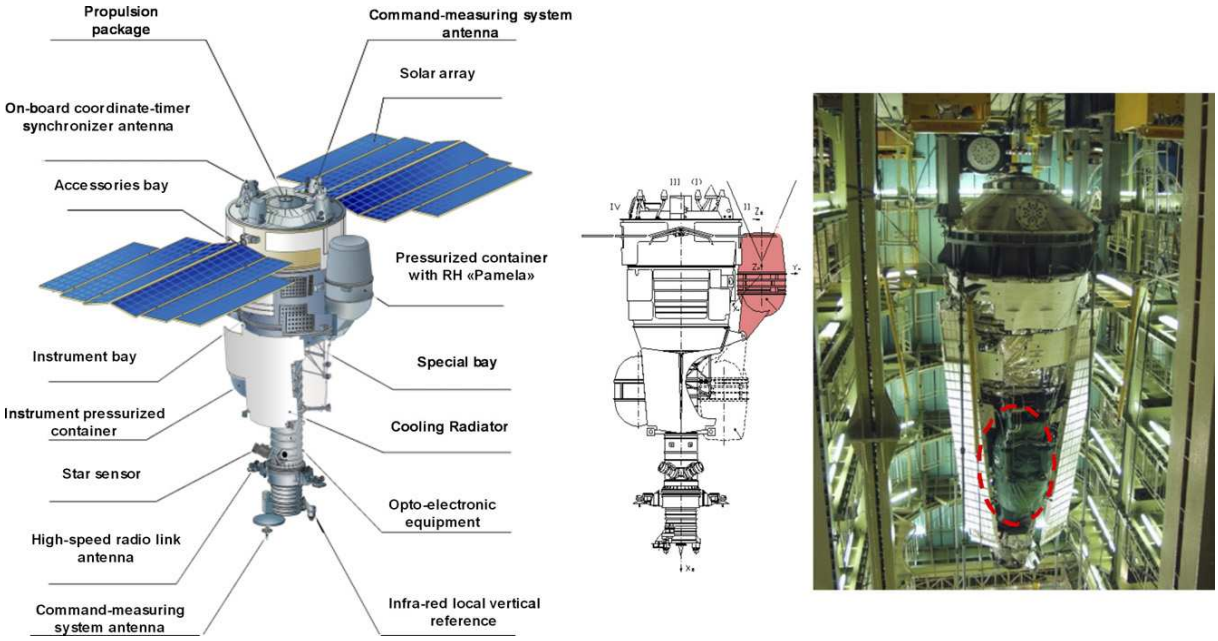

Figure 2.13: A schematic overview of the Resurs-DK1 satellite which carries the PAMELA detector (left). The detector, housed inside a pressurized container, is located on the right, as also indicated by the red shaded region in the center panel. The photograph on the right shows the satellite at the assembly facility in Samara, Russia. The dashed circle shows the location of the pressurized container in which the PAMELA detector resides. Images taken from *Casolino et al.* (2008).

fluxes are measured during solar minimum conditions.

Furthermore, the 22-year cycle, related to the HMF polarity reversal, can also be identified from Figure 2.12. During $A < 0$ polarity cycles, peaks are formed through heliospheric modulation, whereas for $A > 0$ polarity cycles the modulated flux has plateau shapes. These features can be ascribed to the drift motions experienced by charged CR particles. Another feature that is evident from NM counts are the intermittent decreases in intensity. These sudden decreases, referred to as Forbush decreases, are supposedly related to violent transient solar events (like coronal mass ejections) that lead to the formation of propagating diffusion barriers such as co-rotating interaction regions. See e.g. *Potgieter* (2008) for a review.

2.9 The PAMELA Space Mission

As of June 15^{th}, 2006, a new satellite-borne detector, named PAMELA (a Payload for Antimatter Matter Exploration and Light-nuclei Astrophysics), has been orbiting the Earth. The PAMELA detector is housed inside a pressurized contained attached to a Russian Resurs-DK1 Earth-observation satellite that was launched into space by a

Table 2.1: Design goals for PAMELA's performance (*Picozza et al.*, 2007).

Cosmic ray particle	**Energy range**
Protons	80 MeV – 700 GeV
Antiprotons	80 MeV – 190 GeV
Electrons	50 MeV – 400 GeV
Positrons	50 MeV – 270 GeV
Electrons + positrons	up to 2 TeV
Light nuclei (up to $z = 6$)	100 MeV.nuc^{-1} – 250 GeV.nuc^{-1}
Light nuclei (up to $z = 8$)	up to ~ 100 GeV.nuc^{-1}
Antinuclei	**Sensitivity 95%**
Antihelium	of the order of 10^{-8}
Antihelium/helium ratio	of the order of 10^{-7}

Soyuz-U rocket from the Baikonur cosmodrome in Kazakhstan. The satellite is orbiting the Earth in an elliptical semi-polar orbit at altitudes varying between 350 km and 600 km and with an inclination of $70°$ (*Picozza et al.*, 2007). A schematic overview of the Resurs-DK1 satellite, shown in Figure 2.13, gives an indication of where the PAMELA detector is located. Also shown on the right of this figure is a photograph taken of the satellite at the assembly facility, in the city of Samara, Russia.

The instrument is built around a 0.43 T permanent magnet spectrometer and is comprised by a number of sub-detectors capable of detecting CR particles and to provide accurate information about particle charge, mass, momentum and rigidity over a wide energy range (see e.g. *Casolino et al.*, 2008, and references therein). The design goals for PAMELA's performance are summarized in Table 2.1, which shows the various CR components and corresponding energy ranges over which PAMELA is capable of observing.

The PAMELA apparatus is composed of the following sub-detectors:

- A time-of-flight system, which measures the time-of-flight of incident particles (with a resolution of ~ 300 ps) and also provides a fast signal for triggering of the data acquisition. This system allows electrons to be separated from anti-protons (up to 1 Gev$/c$), and to reject Albedo particles.

- Anticoincidence systems, which is used to distinguish between CR particles and secondary particles produced from interactions between CRs and the mechanical structure of the apparatus.

- A magnetic spectrometer, which forms the central part of the PAMELA apparatus, and which is used to measure the rigidity and charge sign of CR particles.

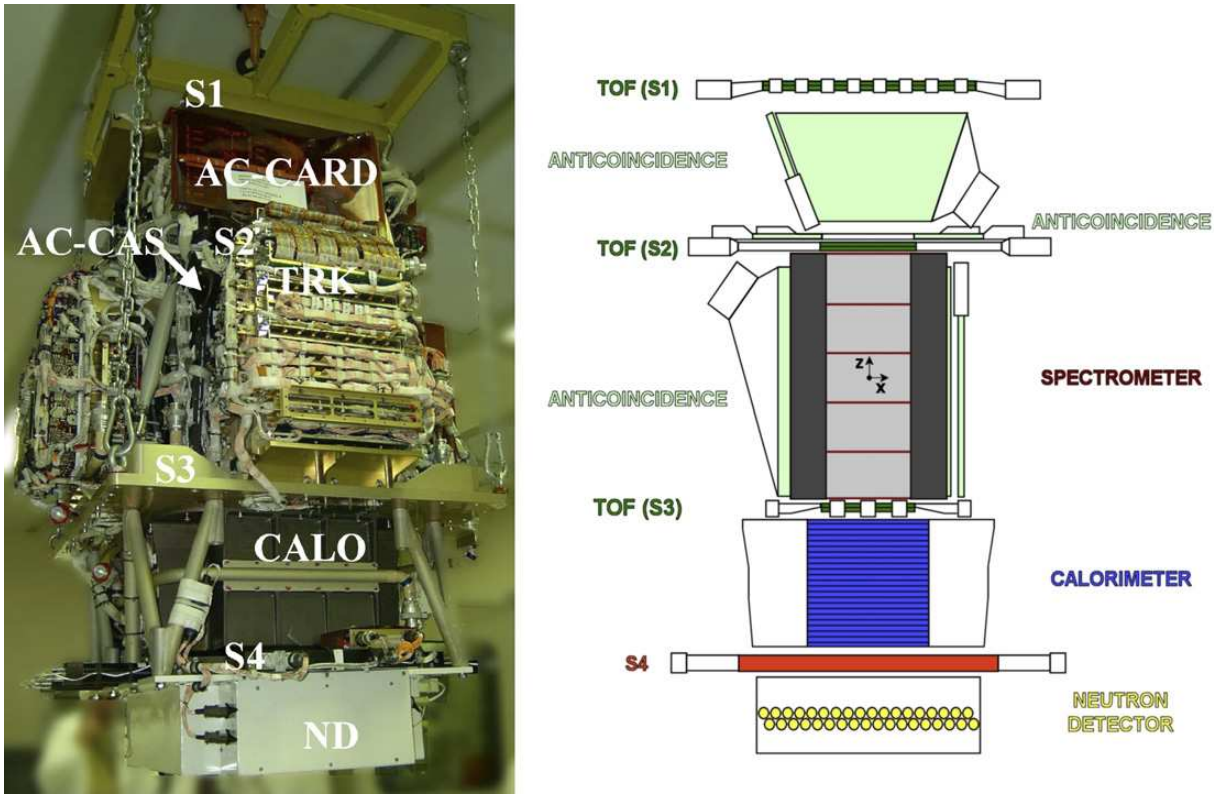

Figure 2.14: The photograph on the left shows the PAMELA detector during its final phase at the Tor Vergata clean room facilities in Rome. Shown on the right, approximately to scale with the photograph, is a schematic overview of where the various sub-detectors are located. Images taken from *Casolino et al.* (2008).

- An electromagnetic calorimeter, with a primary task of identifying positrons and antiprotons from a background of more abundant like-charge components that is dominated by protons and electrons
- A shower tail catcher scintillator, which improves PAMELA's electron-hadron separation performance.
- A neutron monitor, which aid in the electron-proton discrimination capabilities of the calorimeter.

The PAMELA detector has a total mass payload of 470 kg, and its combined power consumption is 355 W. Figure 2.14 shows a photograph of the detector during its final integration phase at the INFN Tor Vergata clean room facilities in Rome, alongside a schematic representation of the various detectors, approximately to scale with the photograph. See e.g. *Picozza et al.* (2007) and *Casolino et al.* (2008) for more details about the technical specifications of the detector subsystems as well as PAMELA's integration, launch and commissioning.

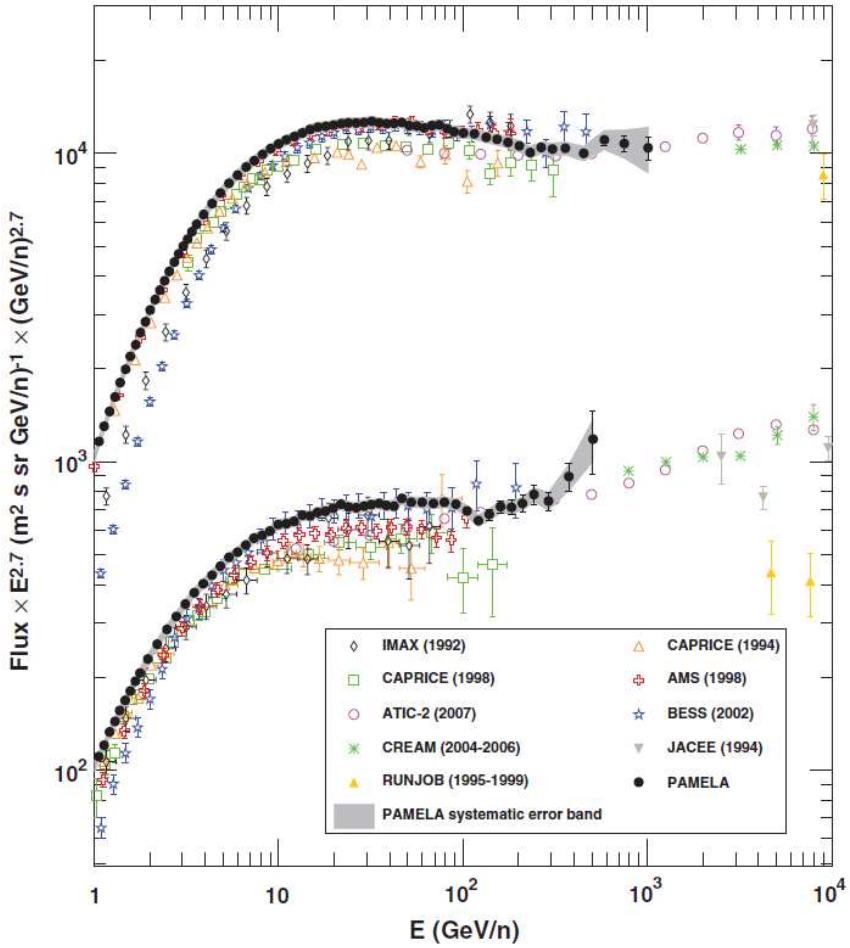

Figure 2.15: Absolute proton and helium fluxes measured by PAMELA in the rigidity range between 1 GeV.nuc^{-1} and 1.2 TeV.nuc^{-1}, compared to similar measurements made during previous balloon-borne and satellite-borne experiments. The error bars on the PAMELA data indicate statistical uncertainties (within one standard deviation), whereas the grey shaded region represents the estimated systematic uncertainty (*Adriani et al.*, 2011a).

Some of the PAMELA mission objectives are to investigate dark matter, the baryon asymmetry in the Universe, cosmic ray generation and propagation in the Galaxy and the solar system, as well as studies of solar modulation and the influence of the Earth's magnetosphere on CRs (see e.g. *Picozza et al.*, 2009, *Boezio et al.*, 2009, and *Adriani et al.*, 2009a). Another concomitant goal of PAMELA, which is of great importance for this work, is the study of solar physics and solar modulation during the 24^{th} solar minimum (see also e.g. *Adriani et al.*, 2009b, and *Casolino et al.*, 2009). The primary scientific goal for PAMELA, however, is to study the antimatter ($\bar{p}$, e^+) component of the cosmic radiation at 1 AU, and perhaps even anti-helium (*Picozza et al.*, 2007).

As PAMELA orbits the Earth it travels through various regions of interest within the Earth's magnetosphere, among which are the Van Allen radiation belts. This allows PAMELA to study the high energy trapped particle components in these belts through

precise measurements of the energy spectrum of these particles. The long and short term temporal fluctuations of these belts will also be studied (e.g. *Casolino et al.*, 2008). Furthermore, the detection of solar energetic particles (SEPs) also forms a key field of interest to be studied during the duration of the PAMELA mission. Such an event has been observed by PAMELA during December, 2006, which evidently was also the first time that a single instrument took direct measurements of an SEP event in the energy range between ~ 80 MeV and 3 GeV (*Adriani et al.*, 2011b). In addition to this, it might also be possible for PAMELA to investigate the high energy Jovian electron component with such accuracy. PAMELA's ability to measure the combined electron and positron spectrum up to 2 TeV will also allow for the opportunity to conduct in-depth research toward the contribution of local sources to the cosmic radiation spectrum (e.g. *Atoyan et al.*, 1995).

More recently, *Adriani et al.* (2011a) published measurements of absolute CR proton and helium spectra across a rigidity interval of 1 GeV and 1.2 TeV between 2006 and 2008, which is shown in Figure 2.15. It is evident that the PAMELA measurements are consistent with those of other experiments, taking into account the statistical and systematic uncertainties. From these measurements *Adriani et al.* (2011a) could draw two prominent conclusions, the first of which is evident in the different spectral shapes. For the rigidity range under consideration, it was found that, by fitting a single power law to the data, protons have a spectral index of $\gamma_p = 2.820 \pm 0.008$, while for helium the spectral index is $\gamma_{He} = 2.732 \pm 0.008$, where the errors account for statistical and systematic uncertainties. A second conclusion that is noticeable from Figure 2.15, is that the PAMELA data shows clear deviations from a single power law model at high energies.

Together with results such as these, long-term studies of antiparticle spectra over an extensive energy range will undoubtedly broaden horizons of numerous questions concerning cosmic ray physics, among which research fields include particle production, galactic particle propagation, heliospheric charge-sign dependent modulation (e.g. *Di Felice*, 2010, and *De Simone*, 2011) and dark matter detection (*Boezio et al.*, 2009, and references therein; see also e.g. *Casolino et al.*, 2008).

2.10 Summary

In this chapter some of the key heliospheric features were discussed with regard to CR modulation. In Section 2.3 it was shown that both the SW and the HMF play a vital roles in determining the structure of the heliosphere, both of which have their origins at the Sun. These components are also primarily responsible for CR modulation in the heliosphere.

The solar wind, as discussed in Section 2.5 has two distinct components, namely the fast and slow SW streams, which are formed presumably as a result of the structure of the solar magnetic dipole field. The SW is accelerated within 0.3 AU to supersonic speeds (~ 400 km.s^{-1} in the slow SW streams near the equatorial regions, and ~ 800 km.s^{-1} in the fast SW streams at the polar regions) after which it slows down to subsonic speeds at ~ 90 AU, forming the termination shock in the process.

In Section 2.6 the structure of the HMF has been examined in light of four prominent field models. The pure Parker field is considered to be too simplistic, which consequently led to various modified versions of this model, namely the Jokipii-Kòta modification and the Smith-Bieber modification, among others. The Fisk HMF model has been constructed as an attempt to account for effects caused by the differentially rotating nature of the Sun.

Section 2.7 gave a discussion of the heliospheric current-sheet, a three-dimensional co-rotating structure that is formed as a result of the magnetic dipole structure of the Sun. The open magnetic field lines emanating from the polar regions of the Sun (that are at opposite polarities) meet at this thin neutral current-sheet. Even though the HCS is located near the equatorial regions, it has a wavy appearance which comes as a result of the fact that the solar rotational and magnetic axes are misaligned by the so-called HCS tilt angle. This tilt angle, in addition to SSNs, serves as an important indicator of solar activity.

The HMF is the primary heliospheric constituent responsible for charge-sign dependent modulation. Together with the HCS, the HMF also leads to various intriguing CR modulation processes, such as particle drift motions for example. The drift motions experienced by CR particles, caused by the magnetic field curvature and gradients as well as the HCS, depend on particle charge-signs, so that these motions also alternate with the magnetic polarity cycle of the Sun, leading to the 11-year and 22-year cycles discussed in Sections 2.4 and 2.8.

In Section 2.9 a discussion was given about the PAMELA detector, which is orbiting the Earth on board a Russian satellite. With the performance of this detector, it is able to take accurate measurements of various CR particle species, including antiparticles, across a wide energy range which will enable for in-depth studies of charge-sign dependent modulation of CRs in the heliosphere. The data from this experiment also forms a central part of validating the results obtained in this work from simulations of heliospheric modulation of CRs.

Chapter 3

Numerical Model for Cosmic Ray Transport and Modulation

3.1 Introduction

When galactic cosmic rays enter the heliosphere they are subjected to various modulation processes within a given boundary. These physical processes are responsible for altering the differential intensity and distribution of CRs as function of energy, position in the heliosphere and time. The four major modulation processes include: outward convection by the solar wind, adiabatic cooling, diffusive random motions along and across the heliospheric magnetic field, and particle guiding center drift motions as a result of the presence of gradients and curvatures in the magnetic field, and the heliospheric current-sheet, across which the magnetic field direction changes abruptly. The basic modulation processes were first combined by *Parker* (1965) into a comprehensive transport equation.

The purpose of this work is to simulate the transport of CRs within the heliosphere by including all of the above mentioned modulation processes into a full three-dimensional numerical model. It is therefore necessary to discuss the relevant theory behind each of these processes in order to gain a better understanding of the numerical modulation model. This chapter is devoted to such discussions. An overview of the Parker TPE will be given, as well as the theory of the underlying transport and modulation processes, with emphasis on particle drifts, diffusion coefficients (DCs), and the diffusion tensor. The numerical model will also be discussed in detail.

3.2 The Transport Equation

Within a coordinate system that rotates with the Sun, the time-dependent TPE, as derived by *Parker* (1965), which describes the transport and modulation of CRs in the

heliosphere, is given by

$$\underbrace{\frac{\partial f}{\partial t}}_{\text{a}} = -(\underbrace{\mathbf{V}_{sw}}_{\text{b}} + \underbrace{\langle \mathbf{v}_d \rangle}_{c}) \cdot \nabla f + \underbrace{\nabla \cdot (\mathbf{K}_s \cdot \nabla f)}_{d} + \underbrace{\frac{1}{3} (\nabla \cdot \mathbf{V}_{sw}) \frac{\partial f}{\partial \ln p}}_{e} + \underbrace{Q}_{f} \tag{3.1}$$

for the omnidirectional distribution function $f(\mathbf{r}, p, t)$ of CRs, where f itself is a function of position $\mathbf{r}$, particle momentum p, and time t. The physical transport and modulation mechanisms contained in Equation 3.1 are: (a) time-dependent changes in the CR distribution function, (b) outward convection caused by the radially expanding SW velocity within the corotating frame $\mathbf{V}_{sw}$, (c) CR gradient and curvature drift motions in the global HMF in terms of the averaged pitch angle guiding center drift velocity $\langle \mathbf{v}_d \rangle$, (d) spatial diffusion caused by the irregular HMF through the symmetric diffusion tensor $\mathbf{K}_s$, (e) adiabatic energy changes (deceleration or acceleration) determined by the SW divergence ($\nabla \cdot \mathbf{V}_{sw}$), (f) possible additional sources of CRs within the heliosphere (for example, Jovian electrons), as they appear from left to right in Equation 3.1 (see e.g. *Potgieter*, 1998, 2011, and *Fisk*, 1999 for overviews of all the heliospheric transport processes).

Even though the numerical model used for this study includes a termination shock, the effects of Fermi II acceleration that particles undergo at the termination shock are excluded for the purpose of this study. For a TPE which contains an additional term for the inclusion of Fermi II acceleration (stochastic acceleration), derived from a more general Fokker-Planck equation, see e.g. *Schlickeiser* (2002) and *Strauss* (2010). See *Gleeson and Axford* (1967) for a rederivation of the TPE, as well as *Gleeson and Axford* (1968) and *Jokipii and Parker* (1970) for details on further refinement of the TPE.

For this study the TPE is solved in a coordinate system that rotates with the Sun, which allows the use of a time-stationary expression for the HMF. This, in turn, enables one to obtain a time-independent solution for the TPE in Equation 3.1. That is,

$$\mathbf{V}_{sw} = \mathbf{V}^*_{sw} - \mathbf{\Omega} \times \mathbf{r} = V_{sw}\mathbf{e}_r - \Omega r \sin\theta \mathbf{e}_\phi, \tag{3.2}$$

where $\mathbf{V}^*_{sw}$ is the stationary SW velocity and $\mathbf{\Omega}$ is the rotational velocity of the Sun. In this case, the partial derivative of f with respect to time simply reduces to zero in Equation 3.1. Since the primary focus of this work is on particles of galactic origin, the source term in the TPE is also disregarded.

Even though the TPE is written in terms of momentum, it is generally solved in numerical modulation studies in terms of rigidity, which is defined as

$$P = \frac{pc}{q} = \frac{mvc}{Ze}, \tag{3.3}$$

where

$$\mathbf{p} = m\mathbf{v} = \frac{m_0\mathbf{v}}{\sqrt{1 - v^2/c^2}} \tag{3.4}$$

is the particle's momentum, $q = Ze$ its charge, v the speed (with $v = |\mathbf{v}|$), m the relativistic mass, m_0 the rest-mass, and c the speed of light in a vacuum. For a relativistic particle, then, the total energy in terms of momentum is given by

$$E_p^2 = (T_p + E_{0,p})^2 = p^2c^2 + m_0^2c^4, \tag{3.5}$$

with T_p the total kinetic energy and $E_{0,p}$ the rest-mass energy of the particle ($E_0 = 0.938$ GeV for protons and $E_0 = 5.11\times10^{-4}$ GeV for electrons). Also, in terms of rigidity, the total energy of such a particle is given by

$$E_p^2 = (T_p + E_{0,p})^2 = P^2(Ze)^2 + E_{0,p}^2. \tag{3.6}$$

If E is the total energy per nucleon, T the kinetic energy per nucleon, and A the number of nucleons in the particle (i.e. the mass number), then the total energy per particle can be written as

$$A^2E^2 = (AT + AE_0)^2 = P^2(Ze)^2 + A^2E_0^2. \tag{3.7}$$

The kinetic energy per nucleon in terms of particle rigidity is

$$T = \sqrt{P^2\left(\frac{Ze}{A}\right)^2 + E_0^2} - E_0, \tag{3.8}$$

so that, conversely, the rigidity can be written in terms of kinetic energy per nucleon as

$$P = \left(\frac{A}{Ze}\right)\sqrt{(T + E_0)^2 - E_0^2} = \left(\frac{A}{Ze}\right)\sqrt{T\,(T + 2E_0)}. \tag{3.9}$$

These equations allow for the definition of another useful quantity, namely the ratio of particle speed to the speed of light, β, given by

$$\beta = \frac{v}{c} = \frac{pc}{mc^2} = \frac{PZe}{AE} = \frac{PZe}{\sqrt{P^2(Ze)^2 + A^2E_0^2}} = \frac{P}{\sqrt{P^2 + \left(\frac{A}{Ze}\right)^2 E_0^2}} \tag{3.10}$$

in terms of rigidity, or by

$$\beta = \frac{v}{c} = \frac{pc}{mc^2} = \frac{\sqrt{E_p^2 - E_{0,p}^2}}{E_p} = \frac{\sqrt{E^2 - E_0^2}}{E} = \frac{\sqrt{T(T + 2E_0)}}{T + E_0} \tag{3.11}$$

in terms of kinetic energy. The relation between rigidity, kinetic energy and β is there-

fore summarized by

$$P = \frac{A}{Z}\sqrt{T\left(T + 2E_0\right)} = \left(\frac{A}{Z}\right)\beta\left(T + E_0\right). \tag{3.12}$$

Furthermore, the particle density within a region d^3r, for particles with momenta between $\mathbf{p}$ and $\mathbf{p} + d\mathbf{p}$, is related to the full CR distribution function (which includes a pitch angle distribution) by

$$n = \int F(\mathbf{r}, \mathbf{p}, t) d^3p = \int_p p^2 \left[\int_\Omega F(\mathbf{r}, \mathbf{p}, t) d\Omega\right] dp, \tag{3.13}$$

where $d^3p = p^2 dp d\Omega$. The differential particle density, U_p, is related to n by

$$n = \int U_p(\mathbf{r}, p, t) dp, \tag{3.14}$$

which leads to

$$U_p(\mathbf{r}, p, t) = \int_\Omega p^2 F(\mathbf{r}, \mathbf{p}, t) d\Omega. \tag{3.15}$$

The omni-directional (i.e. pitch angle) average of $F(\mathbf{r}, \mathbf{p}, t)$ is calculated as

$$f(\mathbf{r}, p, t) = \frac{\int_\Omega F(\mathbf{r}, \mathbf{p}, t) d\Omega}{\int_\Omega d\Omega} = \frac{1}{4\pi}\int_\Omega F(\mathbf{r}, \mathbf{p}, t) d\Omega, \tag{3.16}$$

which leads to

$$U_p(\mathbf{r}, p, t) = 4\pi p^2 f(\mathbf{r}, p, t). \tag{3.17}$$

The differential intensity, in units of particles/unit area/unit time/unit momentum/unit solid angle, is defined as

$$j_p = \frac{v U_p(\mathbf{r}, p, t)}{\int_\Omega d\Omega} = \frac{v U_p(\mathbf{r}, p, t)}{4\pi} = v p^2 f(\mathbf{r}, p, t). \tag{3.18}$$

The particle speed can be eliminated from the above equation through substitution, where

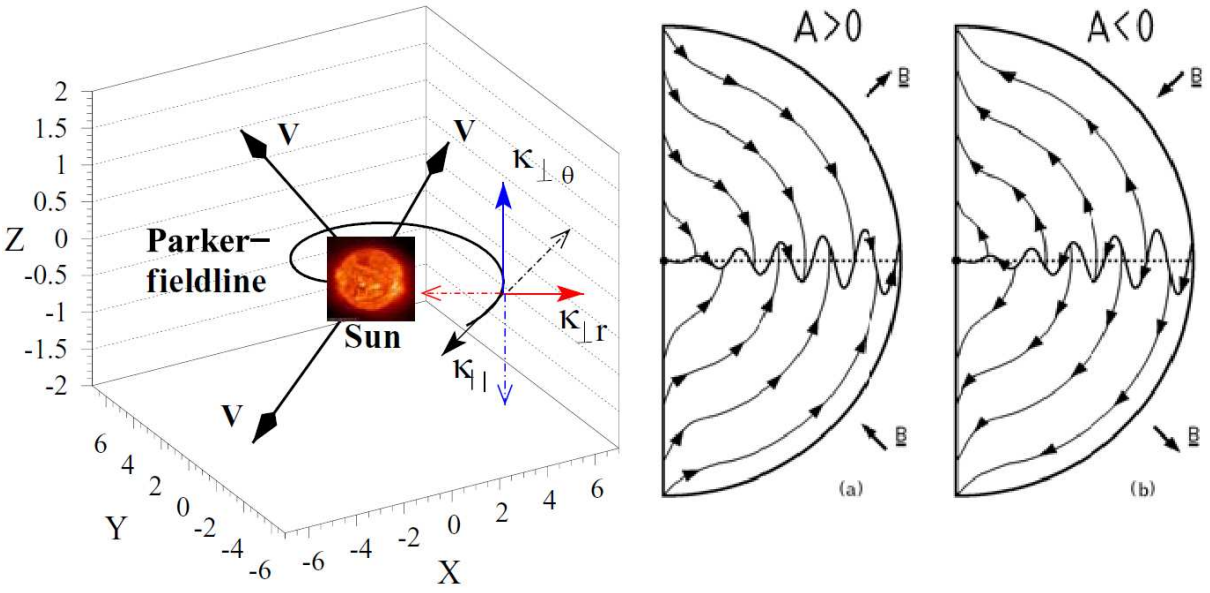

Figure 3.1: The directions of the parallel and perpendicular diffusion coefficient components of symmetrical tensor are illustrated in the left panel, with respect to a magnetic field line in the equatorial plane. The radially expanding solar wind is indicated by the arrows emanating from the Sun. The global drift patterns (including current-sheet drifts) for positively charged particles are illustrated in the right panel, for both magnetic polarity cycles. Figure taken from *Heber and Potgieter* (2006); see also references therein.

$$\frac{\partial p}{\partial E} = \frac{1}{v}, \tag{3.19}$$

and with the relation $jdE = j_p dp$, so that

$$j(\mathbf{r}, p, t) = \frac{v}{4\pi} U_p \frac{dp}{dE} = \frac{1}{4\pi} U_p = p^2 f(\mathbf{r}, p, t), \tag{3.20}$$

where $j(\mathbf{r}, p, t)$ is the differential intensity in units of particles/area/time/energy/solid angle. See also *Potgieter* (1984) and *Strauss* (2010).

3.2.1 The Diffusion Tensor

For a magnetic field without a θ-component, an HMF-aligned coordinate system has one axis parallel to the mean HMF in the $r\phi$-plane ($\mathbf{e}_{\parallel}$), another perpendicular to the first in the $\mathbf{e}_\theta$ direction ($\mathbf{e}_1$), and a third axis in the $r\theta$-plane perpendicular to the first two ($\mathbf{e}_2$), forming a right-handed coordinate system. Within such a system, an asymmetrical diffusion tensor, consisting of a symmetrical diffusion tensor ($\mathbf{K}_s$, as is present in Equation 3.1) and an asymmetrical drift tensor ($\mathbf{K}_A$), can be set up. This tensor contains the necessary diffusion and drift coefficients that determine the extent to which

charged particles are transported and modulated, and is given by

$$\begin{aligned}\mathbf{K} &= \mathbf{K}_s + \mathbf{K}_A \\ &= \begin{bmatrix}\kappa_{\parallel} & 0 & 0\\ 0 & \kappa_{\perp\theta} & 0\\ 0 & 0 & \kappa_{\perp r}\end{bmatrix} + \begin{bmatrix}0 & 0 & 0\\ 0 & 0 & \kappa_A\\ 0 & -\kappa_A & 0\end{bmatrix} \\ &= \begin{bmatrix}\kappa_{\parallel} & 0 & 0\\ 0 & \kappa_{\perp\theta} & \kappa_A\\ 0 & -\kappa_A & \kappa_{\perp r}\end{bmatrix}.\end{aligned} \tag{3.21}$$

The diffusion coefficients in the symmetrical tensor describe particle diffusion parallel to the mean HMF ($\kappa_{\parallel}$), as well as in the polar ($\kappa_{\perp\theta}$) and radial ($\kappa_{\perp r}$) directions perpendicular to it, whereas the coefficients in the asymmetrical tensor describe gradient, curvature and current-sheet drifts experienced by particles. Figure 3.1 gives a schematic illustration of the directions in which these diffusion (left panel) and drift (right panel) coefficients operate with respect to the HMF magnetic field.

By combining these tensors in such a way, it is possible to rewrite the TPE in a more compact form, as

$$-\mathbf{V}_{sw}\cdot\nabla f + \nabla\cdot(\mathbf{K}\cdot\nabla f) + \frac{1}{3}(\nabla\cdot\mathbf{V}_{sw})\frac{\partial f}{\partial \ln p} = 0, \tag{3.22}$$

where the average guiding center drift velocity $\langle \mathbf{v}_A \rangle$ is now included in the asymmetrical tensor $\mathbf{K}$. Take note that both the source term Q and the time-dependent changes $\frac{\partial f}{\partial t}$ in Equation 3.1 have now been reduced to zero.

3.2.2 The Transport Equation in Spherical Coordinates

Since the geometry of the heliosphere is of a spherical nature, it is convenient to rewrite Equation 3.22 in terms of spherical coordinates. The HMF-aligned coordinate system is related to the spherical coordinate system by

$$\begin{aligned}\mathbf{e}_{\parallel} &= \cos\psi\mathbf{e}_r - \sin\psi\mathbf{e}_{\phi} \\ \mathbf{e}_1 &= \mathbf{e}_{\theta} \\ \mathbf{e}_2 &= \mathbf{e}_{\parallel}\times\mathbf{e}_1 = \sin\psi\mathbf{e}_r + \cos\psi\mathbf{e}_{\phi},\end{aligned} \tag{3.23}$$

where ψ is the spiral angle, defined as the angle between the parallel component of the magnetic field (in the $\mathbf{e}_{\parallel}$ direction) and the radial direction $\mathbf{e}_r$. This coordinate system will be referred to as the magnetic coordinate system. The asymmetrical diffusion tensor $\mathbf{K}$ can therefore also be written in terms of spherical coordinates by specifying

the appropriate transformation matrix $\mathbf{T}$, for which it is required that $\det(\mathbf{T}) = 1$. This matrix is given by

$$\mathbf{T} = \begin{bmatrix} \cos\psi & 0 & \sin\psi \\ 0 & 1 & 0 \\ -\sin\psi & 0 & \cos\psi \end{bmatrix}, \tag{3.24}$$

so that the diffusion tensor in Equation 3.21 in spherical coordinates is

$$\begin{aligned} \begin{bmatrix} \kappa_{rr} & \kappa_{r\theta} & \kappa_{r\phi} \\ \kappa_{\theta r} & \kappa_{\theta\theta} & \kappa_{\theta\phi} \\ \kappa_{\phi r} & \kappa_{\phi\theta} & \kappa_{\phi\phi} \end{bmatrix} &= \mathbf{T}\mathbf{K}\mathbf{T}^T \\ &= \begin{bmatrix} \cos\psi & 0 & \sin\psi \\ 0 & 1 & 0 \\ -\sin\psi & 0 & \cos\psi \end{bmatrix} \begin{bmatrix} \kappa_{\parallel} & 0 & 0 \\ 0 & \kappa_{\perp\theta} & \kappa_A \\ 0 & -\kappa_A & \kappa_{\perp r} \end{bmatrix} \begin{bmatrix} \cos\psi & 0 & -\sin\psi \\ 0 & 1 & 0 \\ \sin\psi & 0 & \cos\psi \end{bmatrix} \\ &= \begin{bmatrix} \kappa_{\parallel}\cos^2\psi + \kappa_{\perp r}\sin^2\psi & -\kappa_A\sin\psi & \left(\kappa_{\perp r} - \kappa_{\parallel}\right)\cos\psi\sin\psi \\ \kappa_A\sin\psi & \kappa_{\perp\theta} & \kappa_A\cos\psi \\ \left(\kappa_{\perp r} - \kappa_{\parallel}\right)\cos\psi\sin\psi & -\kappa_A\cos\psi & \kappa_{\parallel}\sin^2\psi + \kappa_{\perp r}\cos^2\psi \end{bmatrix} \end{aligned} \tag{3.25}$$

The TPE in Equation 3.1 can now be written in terms of spherical coordinates as

$$\begin{aligned} &\left[\frac{1}{r^2}\frac{\partial}{\partial r}\left(r^2 K_{rr}\right) + \frac{1}{r\sin\theta}\frac{\partial}{\partial\theta}\left(K_{\theta r}\sin\theta\right) + \frac{1}{r\sin\theta}\frac{\partial K_{\phi r}}{\partial\phi} - V_{sw}\right]\frac{\partial f}{\partial r} \\ +\ &\left[\frac{1}{r^2}\frac{\partial}{\partial r}\left(rK_{r\theta}\right) + \frac{1}{r^2\sin\theta}\frac{\partial}{\partial\theta}\left(K_{\theta\theta}\sin\theta\right) + \frac{1}{r^2\sin\theta}\frac{\partial K_{\phi\theta}}{\partial\phi}\right]\frac{\partial f}{\partial\theta} \\ +\ &\left[\frac{1}{r^2\sin\theta}\frac{\partial}{\partial r}\left(rK_{r\phi}\right) + \frac{1}{r^2\sin\theta}\frac{\partial K_{\theta\phi}}{\partial\theta} + \frac{1}{r^2\sin^2\theta}\frac{\partial K_{\phi\phi}}{\partial\phi} - \Omega\right]\frac{\partial f}{\partial\phi} \\ +\ &K_{rr}\frac{\partial^2 f}{\partial r^2} + \frac{K_{\theta\theta}}{r^2}\frac{\partial^2 f}{\partial\theta^2} + \frac{K_{\phi\phi}}{r^2\sin^2\theta}\frac{\partial^2 f}{\partial\phi^2} \\ +\ &\frac{2K_{r\phi}}{r\sin\theta}\frac{\partial^2 f}{\partial r\partial\phi} + \frac{1}{3r^2}\frac{\partial}{\partial r}\left(r^2 V_{sw}\right)\frac{\partial f}{\partial\ln p} = 0, \end{aligned} \tag{3.26}$$

where it is assumed that the solar wind is axis-symmetrical and directed radially outward, i.e. $\mathbf{V}_{sw} = V_{sw}\mathbf{e}_r$. This version of the TPE is rearranged in order to isolate the various terms that contribute to diffusion, drift, convection, and adiabatic energy losses,

so that Equation 3.26 now becomes

$$
\begin{aligned}
&\overbrace{\left[\frac{1}{r^2}\frac{\partial}{\partial r}\left(r^2 K_{rr}\right)+\frac{1}{r\sin\theta}\frac{\partial K_{\phi r}}{\partial \phi}\right]\frac{\partial f}{\partial r}+\left[\frac{1}{r^2\sin\theta}\frac{\partial}{\partial\theta}\left(K_{\theta\theta}\sin\theta\right)\right]\frac{\partial f}{\partial\theta}}^{\text{diffusion}} \\
&+\overbrace{\left[\frac{1}{r^2\sin\theta}\frac{\partial}{\partial r}(rK_{r\phi})+\frac{1}{r^2\sin^2\theta}\frac{\partial K_{\phi\phi}}{\partial\phi}-\Omega\right]\frac{\partial f}{\partial\phi}}^{\text{diffusion}} \\
&+\overbrace{K_{rr}\frac{\partial^2 f}{\partial r^2}+\frac{K_{\theta\theta}}{r^2}\frac{\partial^2 f}{\partial\theta^2}+\frac{K_{\phi\phi}}{r^2\sin^2\theta}\frac{\partial^2 f}{\partial\phi^2}+\frac{2K_{r\phi}}{r\sin\theta}\frac{\partial^2 f}{\partial r\partial\phi}}^{\text{diffusion}} \\
&+\overbrace{\left[-\langle\mathbf{v}_A\rangle_r\right]\frac{\partial f}{\partial r}+\left[-\frac{1}{r}\langle\mathbf{v}_A\rangle_\theta\right]\frac{\partial f}{\partial\theta}+\left[-\frac{1}{r\sin\theta}\langle\mathbf{v}_A\rangle_\phi\right]\frac{\partial f}{\partial\phi}}^{\text{drift}} \\
&-\overbrace{V_{sw}\frac{\partial f}{\partial r}}^{\text{convection}} \\
&+\overbrace{\frac{1}{3r^2}\frac{\partial}{\partial r}\left(r^2 V_{sw}\right)\frac{\partial f}{\partial\ln p}}^{\text{adiabatic energy losses}}=0,
\end{aligned}
\tag{3.27}
$$

where the first first three lines contain the terms that describe the inward diffusion of CR particles, the fourth line contains the particle drift motions, and the fifth and sixth lines give the convection and adiabatic energy losses respectively (see also e.g. *Hattingh*, 1998).

3.3 Particle Diffusion

As a result of fluctuations in the HMF, CRs undergo diffusive propagation in the heliosphere through a process called pitch angle scattering, which can be described by weak turbulence quasi-linear theory (QLT), first introduced by *Jokipii* (1966). Such turbulence, generally interpreted either as waves (e.g. *Schlickeiser*, 1988) or dynamical turbulence (e.g. *Bieber and Matthaeus*, 1991), are described by the diffusion coefficients in the asymmetrical tensor $\mathbf{K}$, each of which are related to a mean free path (MFP) λ by

$$\kappa = \frac{v}{3}\lambda, \tag{3.28}$$

whereby each diffusion coefficient (in units of area/time) are transformed to a more tangible variable (in units of length). For the case when κ is the drift coefficient, λ will be referred to as the drift scale. A detailed study of these coefficients as well as turbulence theory is beyond the scope of this study. See e.g. *Hattingh* (1998), *Minnie*

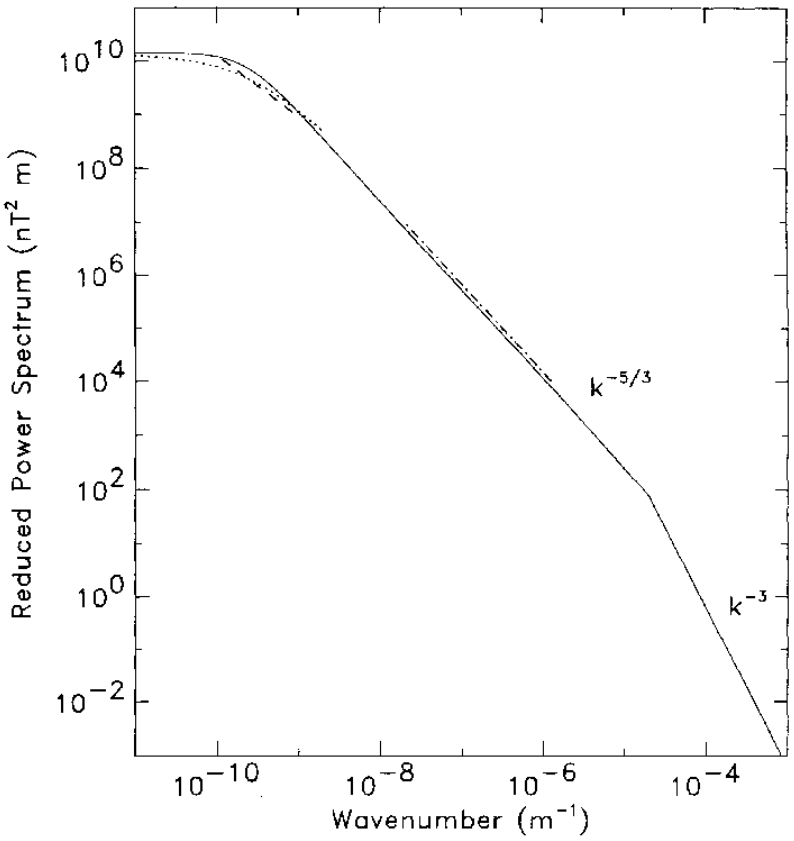

Figure 3.2: A typical slab turbulence power spectrum model (solid line) for the heliosphere at Earth compared to observations (dashed and dotted lines). Figure taken from *Bieber et al.* (1994).

(2006) and *Engelbrecht* (2008) for in-depth studies about the elements of the diffusion tensor.

3.3.1 Parallel Diffusion

An expression for the parallel diffusion coefficient, in terms of the Fokker-Planck coefficient $\Phi(\mu)$, can be derived from the Fokker-Planck equation using the method of *Earl* (1974). From this it follows that

$$\kappa_{\parallel} = \frac{v^2}{8} \int_{-1}^{1} \frac{\left(1-\mu^2\right)^2}{\Phi(\mu)} d\mu, \tag{3.29}$$

where $\Phi(\mu)$, which is essentially the rate of particle scattering, depends on the turbulence model considered. In order to calculate $\Phi(\mu)$, a power spectrum of the magnetic field fluctuations is required, an example of which is shown in Figure 3.2. Such a power spectrum can be divided into three distinct ranges: the energy range, where the power

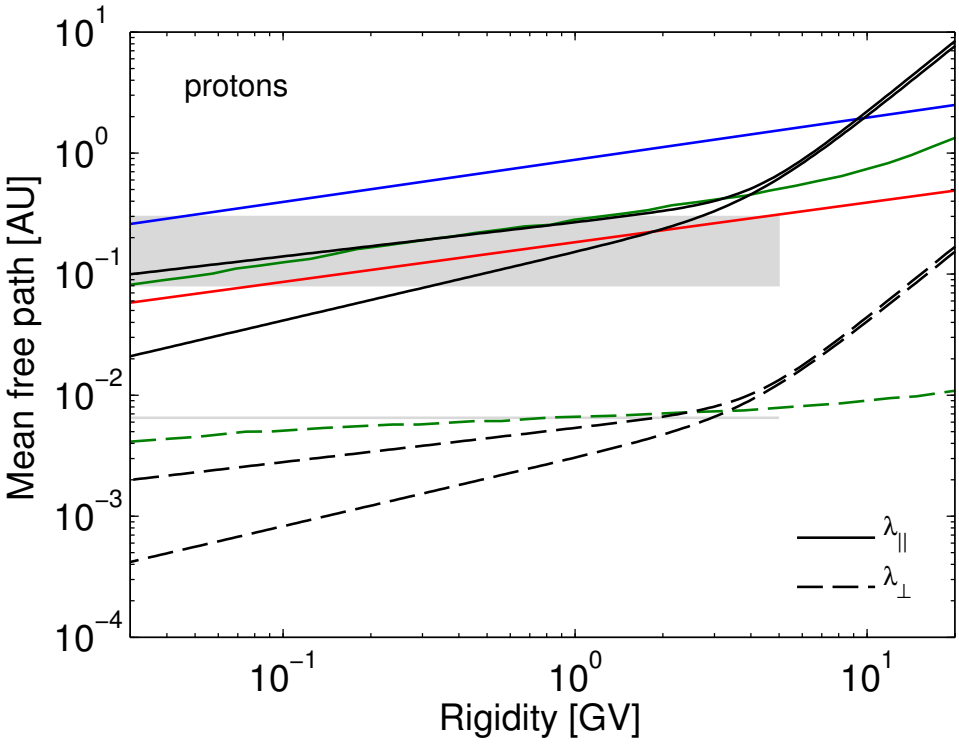

Figure 3.3: The parallel (solid black) and perpendicular (dashed black) MFPs for galactic protons at Earth, as used in this study, as function of rigidity in the equatorial plane. Here the difference between the two sets of MFPs (top and bottom black curves) correspond to a time-dependent change as a result of different average tilt angle and HMF values. The grey-shaded region and line represents the Palmer consensus values (*Palmer*, 1982) for these parameters. The blue line shows the parallel MFP used by *Langner* (2004), while the red line represents the parallel MFP predicted by *Teufel and Schlickeiser* (2003). The solid and dashed green lines give the parallel and perpendicular MFPs from *Bieber et al.* (2004) respectively.

spectrum variation is independent of the wavenumber k, the inertial range, where the variation is proportional to $k^{-5/3}$, and the dissipation range, where the variation is proportional to k^{-3}. See *Teufel and Schlickeiser* (2003) for a derivation of piecewise continuous expressions for the parallel MFPs from QLT for a full turbulence spectrum for two models of dynamical turbulence, namely the damping model and the random sweeping model (*Bieber et al.*, 1994).

The MFPs derived from such a turbulence approach posed problems with regard to the numerical stability of the 3D modulation model used in this study. Consequently, a more simplified approach for the diffusion coefficients' rigidity dependence is used in this study which gives a reasonable approximation to the results obtained from turbulence theory (see also *Langner*, 2004, *Ferreira et al.*, 2001b and *Strauss*, 2010, for similar approaches). Furthermore, it is also assumed that the spatial dependence of the parallel diffusion coefficient is inversely proportional to the magnetic field magnitude. An

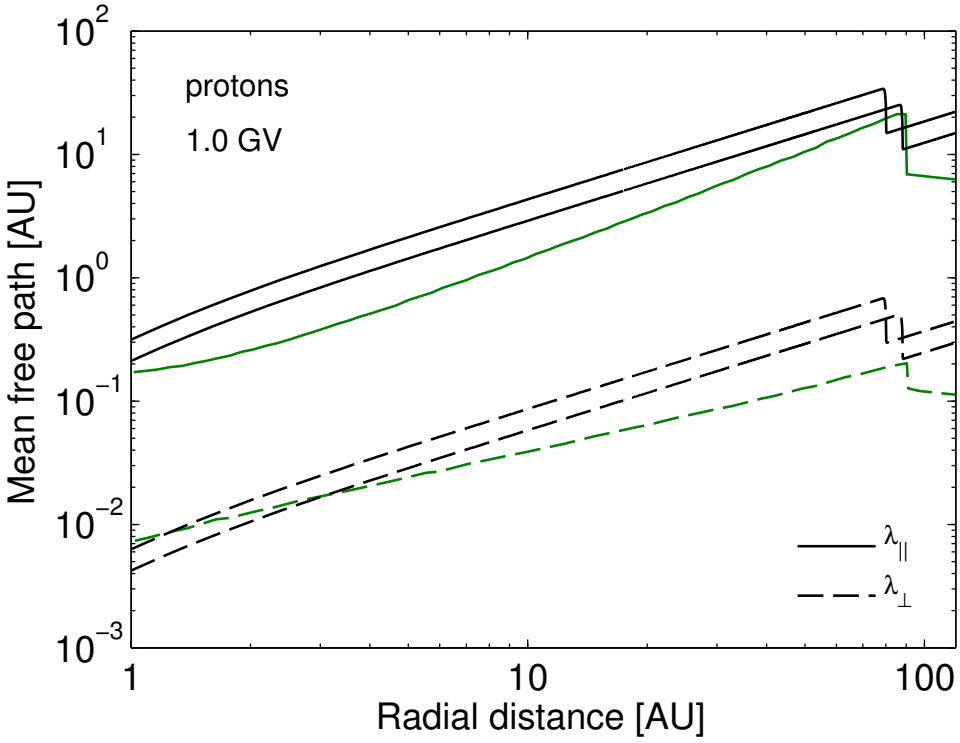

Figure 3.4: The parallel (solid black) and perpendicular (dashed black) MFPs for 1 GV protons, as used in this study, as function of radial distance in the equatorial plane. See Figure 3.3 for an explanation of the difference between these sets of MFPs (top and bottom black curves). Here the termination shock is situated at different radial distances. The green line shows the radial dependence of the parallel MFP used by *Strauss* (2010) for the same rigidity.

expression for the parallel diffusion of protons and electrons is given by

$$\kappa_{\parallel} = \kappa_{\parallel,0}\beta\frac{B_0}{B}\left[\frac{\left(\frac{P}{P_0}\right)^c + \left(\frac{P_k}{P_0}\right)^c}{1+\left(\frac{P_k}{P_0}\right)^c}\right]^{\frac{b-a}{c}}\left(\frac{P}{P_0}\right)^a, \tag{3.30}$$

where $\kappa_{\parallel,0}$ is a constant in units of 10^{20} cm^2.s^{-1}, with $P_0 = 1$ GV and $B_0 = 1$ nT added to obtain the correct units. Here a and b are dimensionless constants that respectively determine the slope of the rigidity dependence below and above a rigidity P_k, and c another dimensionless constant (whose value varies between 3 and 4) that determine the smoothness of the transition between the two slopes P^a and P^b at P_k. The rigidity dependence for $\kappa_{\parallel}$ is therefore essentially a double power-law. Figure 3.3 shows a graph of $\lambda_{\parallel}$ for protons at Earth, as used in this study (solid black curves), compared to that used and predicted by various other authors. The blue line represents the parallel MFP used by *Langner* (2004; based on the expressions from *Burger et al.*, 2000), and the red line gives the parallel MFP calculated by *Teufel and Schlickeiser* (2003), which was

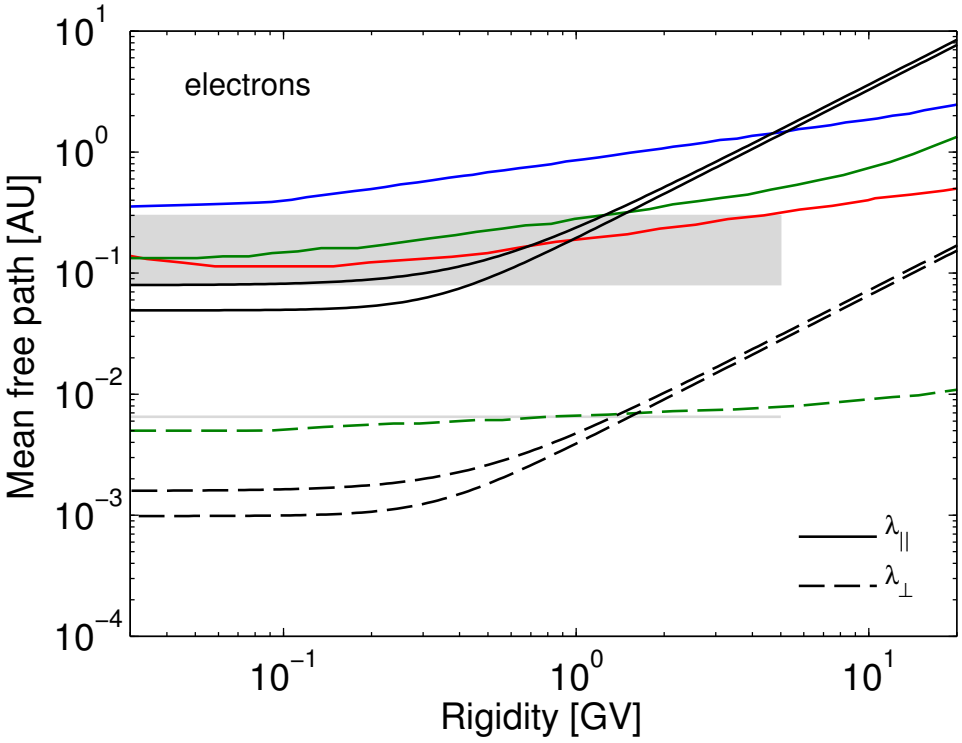

Figure 3.5: Similar to Figure 3.3, but for galactic electrons at Earth.

also used by *Strauss* (2010). The solid green line gives the parallel MFP from *Bieber et al.* (2004), which corresponds to the damping model of dynamical slab turbulence from *Bieber et al.* (1994). See also *Potgieter* (1996, 2000).

For rigidities above ~ 5 GV, $\lambda_{\parallel}$ assumes a $P^{1.95}$ dependence, which, apart from the lower rigidity at which this dependence appears, agrees with the P^2 dependence predicted by *Teufel and Schlickeiser* (2003) (not visible in the rigidity range of Figure 3.3). This transitional steeper dependence begins to appear at ~ 10 GV in the *Bieber et al.* (2004) parallel MFP. In spite of this strong rigidity dependence of $\lambda_{\parallel}$ at these rigidities, the absolute value remains comparable to that used by *Langner* (2004). Below ~ 5 GV, $\lambda_{\parallel}$ for protons has a rigidity dependence that varies between $P^{0.564}$ and $P^{0.282}$ (to be discussed further in Chapter 4), which agrees well with the observational Palmer consensus values (*Palmer*, 1982), as well as with the $\sim P^{0.3}$ dependence predicted by *Teufel and Schlickeiser* (2003).

Figure 3.4 gives the radial dependence of $\lambda_{\parallel}$ for 1 GV protons (solid black lines). The difference between these MFPs, similar to the different rigidity dependencies in Figure 3.3, can be ascribed to time-dependent changes (to be discussed further in Chapter 4). As a result of the B^{-1} dependence of $\kappa_{\parallel}$, the radial dependence of $\lambda_{\parallel}$ is proportional to r, which follows directly from Equation 2.8. Compared to the radial

dependence of *Strauss* (2010), indicated by the solid green line, which is based on QLT and the random sweeping model from *Teufel and Schlickeiser* (2003), the $\lambda_{\parallel} \propto r$ proportionality used in this study is reasonably similar with regard to the slope and absolute value.

Furthermore, the functional form of the electron parallel diffusion is similarly described by Equation 3.30, except for a different rigidity dependence (i.e. different parameter values for a, b, c, and P_k). As with Figure 3.3, Figure 3.5 now gives the rigidity dependence of $\lambda_{\parallel}$ for galactic electrons at Earth, as used in this study (solid black curves), where the blue, green, and red curves once again represent the MFPs used and predicted by other authors, as explained in the prior paragraphs. For rigidities above $\sim$ 1 GV, the electron parallel MFP assumes a $P^{1.23}$ dependence, whereas for lower rigidities $\lambda_{\parallel}$ becomes independent of rigidity. Below $\sim$ 0.2 GV, $\lambda_{\parallel}$ assumes a value of between 0.05 AU and 0.08 AU. For the rigidity range under consideration, the absolute value remains comparable to both the Palmer consensus values, as well as the MFPs from other authors. Since $\lambda_{\parallel}$ for electrons also has a B^{-1} dependence, the radial dependence thereof is similar to that of protons given in Figure 3.4.

Since CR protons experience large adiabatic energy changes below $\sim$ 300 MeV ($\sim$ 800 MV), proton modulation seems unaffected by changes in $\lambda_{\parallel}$ at these energies (e.g. *Potgieter*, 1984, 2000). For electrons, however, changes in $\lambda_{\parallel}$ directly influence the modulation at energies below 100 MV.

3.3.2 Perpendicular Diffusion

The scattering of CR particles perpendicular to the magnetic field can be caused either as a result of the particles' gyrocentres that are displaced transverse to the mean HMF through scattering, or due to the random walk of the magnetic field lines themselves. These processes are collectively taken into account in numerical models via the perpendicular diffusion coefficient, $\kappa_{\perp}$. As previously mentioned, $\kappa_{\perp}$ can be subdivided into two possibly independent coefficients describing the perpendicular diffusion in the radial ($\kappa_{\perp,r}$) and polar ($\kappa_{\perp,\theta}$) directions. It has also been established that $\kappa_{\perp}$ plays a significant role in the modulation of CRs (see e.g. *Potgieter*, 1996, 2000 and *Ferreira et al.*, 2000). See also e.g. *Jokipii* (2001) for further theoretical work regarding $\kappa_{\perp}$.

In the presence of parallel diffusion, however, a pure field line random walk scenario gives an insufficient description of perpendicular diffusion, because particles sometimes retrace their paths after they backscatter - a process that hasn't been taken into account until the proposed non-linear guiding center (NLGC) theory of particle diffusion by *Matthaeus et al.* (2003). According to this theory, the process of perpendicular diffusion is a combination of field line random walk, backscattering from parallel

diffusion, and the transfer of particles across field lines due to the perpendicular complexity of the magnetic field. See *Bieber et al.* (2004) for a discussion of the general properties of the NLGC theory and comparison with observations.

For this work, as has in general become standard practice, $\kappa_\perp$ is scaled as $\kappa_\parallel$. This assumption has been confirmed by a.o. *Giacalone and Jokipii* (1999), who found that the ratio $\kappa_\perp/\kappa_\parallel$ has a value between 0.02 and 0.04. Furthermore, observations from the Ulysses spacecraft revealed that the latitude dependence of CR protons is significantly less than predicted by classical drift models (e.g. *Potgieter and Haasbroek*, 1993), which evidently led *Kóta and Jokipii* (1995) to propose the concept of an anisotropic $\kappa_\perp$, where $\kappa_{\perp,\theta} > \kappa_{\perp,r}$ in the off-equatorial regions (e.g. *Potgieter*, 1996 and *Burger et al.*, 2000). The effect of such anisotropic perpendicular diffusion on CR modulation has been studied in detail by e.g. *Ferreira et al.* (2000) (see also e.g. *Fichtner et al.*, 2000). The anisotropy in $\lambda_\perp$ has also been accounted for in this work, as done by *Langner* (2000), so that

$$\kappa_{\perp,r} = \kappa^0_{\perp,r}\kappa_\parallel \tag{3.31}$$

and

$$\kappa_{\perp,\theta} = f(\theta)\kappa^0_{\perp,\theta}\kappa_\parallel, \tag{3.32}$$

where $\kappa^0_{\perp,r} = \kappa^0_{\perp,\theta} = 0.02$ are dimensionless constants, and

$$f(\theta) = A^+ + A^- \tanh\left[\frac{1}{\Delta\theta}\left(\widetilde{\theta} - \frac{\pi}{2} + \theta_F\right)\right]. \tag{3.33}$$

Here $A^\pm = \frac{d\pm1}{2}$, $\Delta\theta = 1/8$, with

$$\widetilde{\theta} = \begin{cases} \theta & \text{for } \theta \geq \frac{\pi}{2} \\ \pi - \theta & \text{for } \theta < \frac{\pi}{2}, \end{cases} \tag{3.34}$$

and

$$\theta_F = \begin{cases} \frac{-35^\circ\pi}{180^\circ} & \text{for } \theta \geq \frac{\pi}{2} \\ \frac{35^\circ\pi}{180^\circ} & \text{for } \theta < \frac{\pi}{2}, \end{cases} \tag{3.35}$$

where d is a dimensionless constant that determines the enhancement factor of $\kappa_{\perp,\theta}$ from its value in the equatorial plane toward the poles, with respect to $\kappa_\parallel$. Figure 3.3 gives the rigidity dependence of $\kappa_\perp$ for protons at Earth in the equatorial plane (dashed black lines), where it has been assumed that both $\kappa_{\perp,r}$ and $\kappa_{\perp,\theta}$ has the same rigidity dependence, and is scaled by $\kappa_\parallel$. Compared to the perpendicular MFP predicted by the NLGC theory from *Bieber et al.* (2004), the rigidity dependence of $\lambda_\perp$ used in this work is remarkably similar for rigidities below 4 GV, and is also in agreement with the Palmer consensus values. The radial dependence of $\lambda_\parallel$ for protons and electrons in the

equatorial plane, given in Figure 3.4 by the dashed black lines, is also comparable to the MFP of *Burger et al.* (2000), also used by *Strauss* (2010). For electrons, in Figure 3.5, $\lambda_\perp$ for this work gives a steeper rigidity dependence above 0.3 GV compared to MFP predicted by NLGC theory.

3.4 Particle Drifts

The significance of particle drifts, not included, however, in the original derivation of the TPE, wasn't realized until *Jokipii et al.* (1977) pointed out that the contribution thereof might influence CR modulation (see also e.g. *Potgieter and Moraal*, 1985). The global background HMF induces drift motions in CRs associated with gradients in the magnetic field magnitude, the curvature of the field, and any sudden changes in the field direction (such as is found at the HCS, e.g. *Burger and Potgieter*, 1989), in addition to a charge asymmetry as a result of the sensitivity of drifts to the HMF polarity. See Figure 3.1 for a schematic illustration of the drift directions experienced by positively charged particles during both magnetic polarity cycles.

The average pitch angle guiding center drift velocity is, in the general case, given by

$$\langle \mathbf{v}_A \rangle = \frac{pv}{3q} \frac{(\omega\tau_A)^2}{1+(\omega\tau_A)^2} \nabla \times \frac{\mathbf{B}}{B^2}, \tag{3.36}$$

where provision is made for the suppression of drifts through scattering (e.g. *Minnie et al.*, 2007), with ω the gyro-frequency of particles, and τ_A is a time scale defined by scattering. Equation 3.36 can be rewritten as

$$\begin{aligned} \langle \mathbf{v}_A \rangle &= \nabla \times \frac{pc}{q}\frac{v}{c}\frac{1}{3B}\frac{(\omega\tau_A)^2}{1+(\omega\tau_A)^2}\frac{\mathbf{B}}{B} \\ &= \nabla \times \frac{P\beta}{3B}\frac{(\omega\tau_A)^2}{1+(\omega\tau_A)^2}\frac{\mathbf{B}}{B} \\ &= \nabla \times r_L \frac{v}{3}\frac{(\omega\tau_A)^2}{1+(\omega\tau_A)^2}\mathbf{e}_B, \end{aligned} \tag{3.37}$$

where

$$\mathbf{e}_B = [1 - 2H(\theta - \theta')]\,\mathbf{e}'_B, \tag{3.38}$$

is a unit vector directed along $\mathbf{B}$, for

$$\mathbf{e}'_B = \frac{\mathbf{B}}{B} = \frac{\mathbf{e}_r + \left(\frac{r\delta(\theta)}{r_\odot}\right)\mathbf{e}_\theta - \tan\psi \mathbf{e}_\phi}{\sqrt{1+\left(\frac{r\delta(\theta)}{r_\odot}\right)^2 + \tan^2\psi}}, \tag{3.39}$$

where the variables are defined as in Chapter 2. In Equation 3.37 the maximal Larmor radius (i.e. the 90° pitch angle) is defined as

$$r_L = \frac{mv}{qB} = \frac{P}{Bc}. \tag{3.40}$$

A scenario in which it is assumed that a particle undergoes a large number of gyrations before being scattered, leads to an approximation of $\omega\tau_A \gg 1$, which reduces Equation 3.37 to the well known weak-scattering limit for the guiding center drift velocity of an ensemble of charged particles (e.g. *Rossi and Olbert*, 1970, and *Burger et al.*, 1985), given by

$$\langle \mathbf{v}_A \rangle^{ws} = \frac{pv}{3q} \nabla \times \frac{\mathbf{B}}{B^2}. \tag{3.41}$$

Using a vector product identity, Equation 3.41 can be rewritten as

$$\begin{aligned} \langle \mathbf{v}_A \rangle^{ws} &= \nabla \times \frac{pv}{3qB} \frac{\mathbf{B}}{B} \\ &= \nabla \times \frac{v}{3} r_L \mathbf{e}_B \\ &= \nabla \times \kappa_A \mathbf{e}_B, \end{aligned} \tag{3.42}$$

with the weak-scattering drift coefficient given by

$$\kappa_A^{ws} = \frac{pv}{3qB} = \frac{v}{3} r_L. \tag{3.43}$$

The drift coefficient is related to the so-called drift scale through

$$\lambda_A = \kappa_A \frac{3}{v}, \tag{3.44}$$

so that for the weak-scattering scenario, the drift scale becomes $\lambda_A^{ws} = r_L$. Even though the exact form of the suppression factor on κ_A^{ws} as a result of particle scattering is not yet known, it continues to be studied (e.g. *Minnie et al.*, 2007; *Visser*, 2009). See also *Strauss* (2010).

By substituting Equation 2.9 into Equation 3.42, $\langle \mathbf{v}_A \rangle$ can alternatively be written as

$$\begin{aligned} \mathbf{v}_A &= \nabla \times \kappa_A \mathbf{e_B} \\ &= [\nabla \times (\kappa_A \mathbf{e}'_B)] \left[1 - 2H(\theta - \theta')\right] + 2\delta(\theta - \theta') \kappa_A \mathbf{e}'_B \times \nabla(\theta - \theta'), \end{aligned} \tag{3.45}$$

for both the weak-scattering and modified drift scenarios, with δ the Dirac-Delta func-

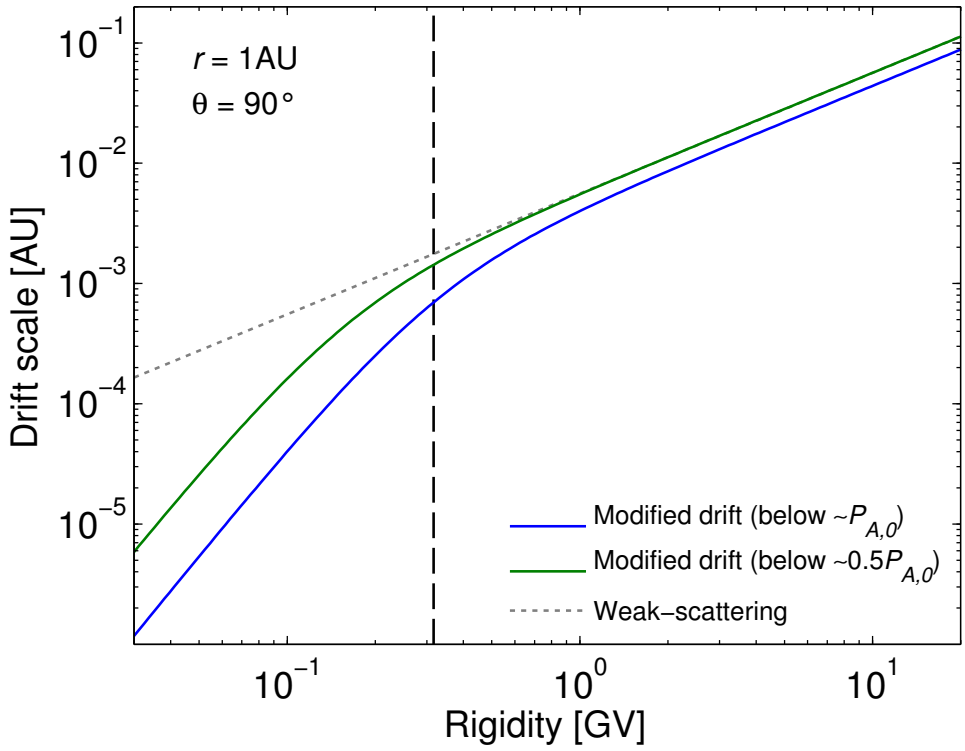

Figure 3.6: The particle drift scale in the equatorial plane at Earth, as function of rigidity. The blue and green lines represent λ_A for different average HMF values, as well as for where drifts are modified significantly below $\sim P_{A,0}$ and $\sim 0.5P_{A,0}$ respectively (where the value for $P_{A,0}$ is indicated by the vertical dashed line). Also shown by the grey dotted line is the weak-scattering drift limit for one of the scenarios.

tion given by

$$\delta(\theta - \theta') = \begin{cases} \infty & \text{if } \theta = \theta' \\ 0 & \text{if } \theta \neq \theta'. \end{cases} \tag{3.46}$$

The first term in Equation 3.45 describes particle drifts due to gradients and curvatures in the HMF, whereas the second term describes drift motions along the HCS.

In this study it has been assumed that $(\omega\tau_A) \propto P$, which gives

$$\kappa_A = \kappa_{A,0}\frac{v}{3}r_L\frac{\left(\frac{P}{P_{A,0}}\right)^2}{1+\left(\frac{P}{P_{A,0}}\right)^2}, \tag{3.47}$$

with $P_{A,0}$ (in GV) added to retain the correct units, and $\kappa_{A,0} \in [0.0, 1.0]$ a dimensionless parameter that determines the amount of drift (see e.g. *Burger et al.*, 2000, and *Burger et al.*, 2008, for similar approaches).

Even though *Potgieter et al.* (1989) has shown that full drifts at all energies are highly unlikely, such a scenario, as a result of the unusual minimum of solar cycle 24, has

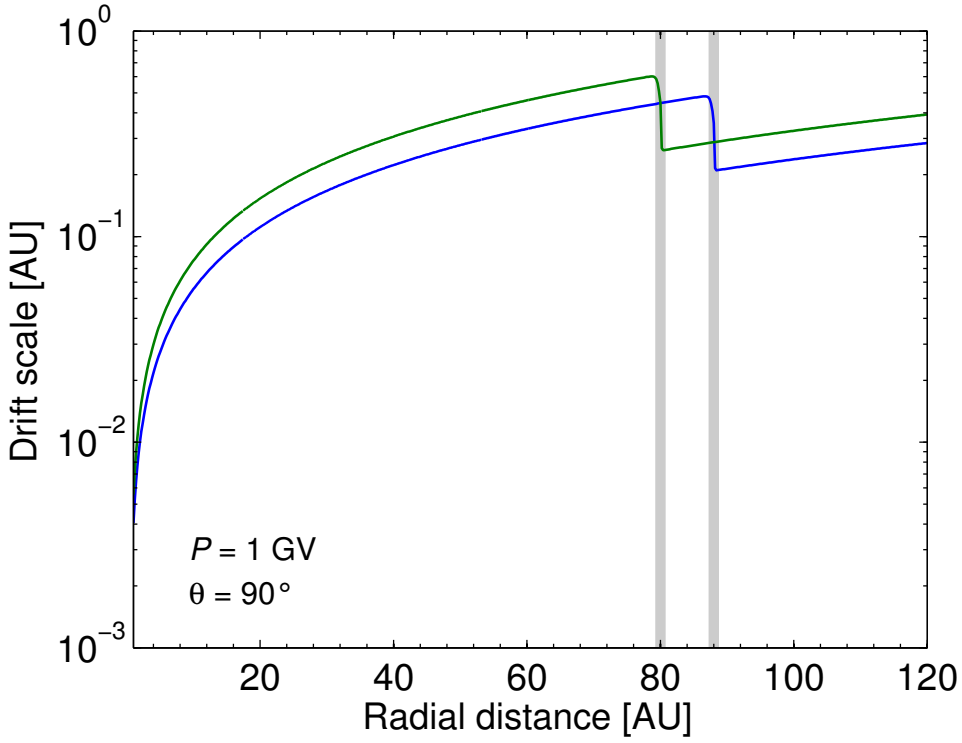

Figure 3.7: The particle drift scale in the equatorial plane, as function of radial distance. At this rigidity it follows that $\lambda_A \approx r_L$. The blue and green lines correspond to the two modified drift scenarios in Figure 3.6 at 1 GV for which the TS (indicated by the grey shaded regions) is also situated at different positions.

been investigated in this study. It has therefore been assumed that $\kappa_{A,0} = 1.0$ to obtain maximum possible drift effects, with $P_{A,0} = 1/\sqrt{10}$, as used by *Langner* (2004) and *Strauss* (2010). During solar maximum, however, *Ferreira and Potgieter* (2004) has shown that $\kappa_{A,0}$ should be less than 10% in order to reproduce observations. See also *Ndiitwani et al.* (2005).

Figure 3.6 shows the drift scale, λ_A, as a function of rigidity for where drifts has been modified significantly below $\sim 0.5P_{A,0}$ and below $\sim P_{A,0}$. The vertical displacement in the drift scale can be ascribed to an increase in the magnetic field magnitude (to be discussed in the following chapters). The weak-scattering limit for λ_A (see Equation 3.43) is also shown by the dashed line in Figure 3.6 for one of the scenarios. The radial dependence of λ_A at 1 GV, for the above mentioned scenarios, is given in Figure 3.4, where the TS is also assumed to be located at different positions (80 AU and 88 AU). At this rigidity λ_A is representative of the Larmor gyro-radius. From the above Equations it follows that the spatial dependence of λ_A is essentially governed by B, and therefore also by $\mathbf{V}_{sw}$, as discussed in Chapter 2.

Considering drift in the TPE, the radial, polar, and azimuthal components of the

average guiding center drift velocity in Equation 3.27, due to the presence of HMF gradients and curvatures, as well as the HCS, are given by

$$\begin{aligned} \langle \mathbf{v}_A \rangle_r &= -\frac{A}{r \sin\theta} \frac{\partial}{\partial \theta} \left(\sin\theta K_{\theta r} \right), \\ \langle \mathbf{v}_A \rangle_\theta &= -\frac{A}{r} \left[\frac{1}{\sin\theta} \frac{\partial}{\partial \phi} (K_{\phi\theta}) + \frac{\partial}{\partial r} (r K_{r\theta}) \right], \\ \langle \mathbf{v}_A \rangle_\phi &= -\frac{A}{r} \frac{\partial}{\partial \theta} (K_{\theta\phi}), \end{aligned} \tag{3.48}$$

where $A = \text{sign}(Bq)$ determines the drift directions of charged particles.

3.5 The Numerical Model

3.5.1 A Brief Overview of Numerical Modulation Models

Some 40 years ago *Fisk* (1971), assuming a spherically symmetric heliosphere, developed the first one-dimensional (1D) steady-state numerical solution of the TPE, with radial distance as the only spatial variable. The polar angle was later added to this model to form an axisymmetric two-dimensional (2D) model (*Fisk*, 1973), after which improvements were made by *Moraal and Gleeson* (1975). Gradient and curvature drifts for a flat HCS were included in separately developed steady-state 2D models by *Moraal et al.* (1979) and *Jokipii and Kopriva* (1979), followed by the first 2D model wherein the waviness of the HCS were emulated *Potgieter* (1984; see also e.g. *Potgieter and Moraal*, 1985, and *Burger*, 1987). An improved 2D wavy current-sheet model was developed hereafter by *Hattingh* (1993) and *Langner* (2004).

In 1983, the first three-dimensional (3D) steady-state model, which included particle drifts as well as a wavy HCS, was developed by *Kota and Jokipii* (1983) and later by *Hattingh* (1998). It was also shown by *Hattingh* (1998) and *Ferreira* (1998) that the 2D and 3D steady-state models delivered remarkably similar results, thereby validating the use of both these models. Steady-state 3D models, which included the Jovian magnetosphere as a source of low-energy electrons, were independently developed by *Fichtner et al.* (2000) and *Ferreira et al.* (2001a).

Perko and Fisk (1983) developed the first spherically symmetric time-dependent model which was later extended to two and three dimensions (*le Roux*, 1990; *Fichtner et al.*, 2001). The effects of a heliospheric TS, i.e. diffusive shock acceleration, was first incorporated into an axisymmetric model by *Jokipii* (1986), whereafter *Potgieter* (1989) developed a 2D shock acceleration model. In the following years *Steenkamp* (1995) independently developed a 2D shock acceleration model with a discontinuous solar wind TS transition, whereas *le Roux et al.* (1996) developed a similar model, but

with a continuous transition.

Langner (2004) used a 2D time-dependent TS model based on various other 2D steady-state and time-dependent shock acceleration models. This model, significantly modified, was also used by *Strauss* (2010); see also *Strauss et al.* (2010a, 2010b). For this study, however, since particle drifts are inherently 3D phenomena, an improved 3D steady-state model of *Hattingh* (1998) is used which includes a wavy current-sheet and a heliosheath, but without shock acceleration at the TS. See *Ferreira* (2002) and *Langner* (2004) for a detailed overview of the history of numerical modulation models.

3.5.2 Numerical Scheme

In order to solve the TPE within a spherical coordinate system that rotates with the Sun, Equation 3.26 can be written in a condensed form, in terms of rigidity, as

$$\begin{aligned} & a_0(r,\theta,\phi,P)\frac{\partial f}{\partial r} + b_0(r,\theta,\phi,P)\frac{\partial f}{\partial \theta} + c_0(r,\theta,\phi,P)\frac{\partial f}{\partial \phi} + d_0(r,\theta,\phi,P)\frac{\partial^2 f}{\partial r \partial \phi} \\ + \;& e_0(r,\theta,\phi,P)\frac{\partial^2 f}{\partial r^2} + l_0(r,\theta,\phi,P)\frac{\partial^2 f}{\partial \theta^2} + m_0(r,\theta,\phi,P)\frac{\partial^2 f}{\partial \phi^2} \\ + \;& s_0(r,\theta,\phi,P)\frac{\partial f}{\partial \ln P} = 0, \end{aligned} \tag{3.49}$$

with

$$\begin{aligned} a_0(r,\theta,\phi,P) &= \frac{1}{r^2}\frac{\partial}{\partial r}\left(r^2 K_{rr}\right) + \frac{1}{r\sin\theta}\frac{\partial}{\partial \theta}\left(K_{\theta r}\sin\theta\right) + \frac{1}{r\sin\theta}\frac{\partial K_{\phi r}}{\partial \phi} - V_{sw} \\ b_0(r,\theta,\phi,P) &= \frac{1}{r^2}\frac{\partial}{\partial r}\left(r K_{r\theta}\right) + \frac{1}{r^2\sin\theta}\frac{\partial}{\partial \theta}\left(K_{\theta\theta}\sin\theta\right) + \frac{1}{r^2\sin\theta}\frac{\partial K_{\phi\theta}}{\partial \phi} \\ c_0(r,\theta,\phi,P) &= \frac{1}{r^2\sin\theta}\frac{\partial}{\partial r}\left(r K_{r\phi}\right) + \frac{1}{r^2\sin\theta}\frac{\partial K_{\theta\phi}}{\partial \theta} + \frac{1}{r^2\sin^2\theta}\frac{\partial K_{\phi\phi}}{\partial \phi} - \Omega \\ d_0(r,\theta,\phi,P) &= \frac{2K_{r\phi}}{r\sin\theta} \\ e_0(r,\theta,\phi,P) &= K_{rr} \\ l_0(r,\theta,\phi,P) &= \frac{K_{\theta\theta}}{r^2} \\ m_0(r,\theta,\phi,P) &= \frac{K_{\phi\phi}}{r^2\sin^2\theta} \\ s_0(r,\theta,\phi,P) &= \frac{1}{3r^2}\frac{\partial}{\partial r}\left(r^2 V_{sw}\right). \end{aligned} \tag{3.50}$$

Evidently, Equation 3.49 is a parabolic differential equation which can be solved with a modified Crank-Nicholson finite difference method, called the Alternating Direction Implicit (ADI) method. The ADI method was initially developed by *Peaceman and Rachford* (1955) and *Douglas* (1955) to solve parabolic differential equations in terms of two

spatial coordinates and time, after which *Douglas* (1962) extended this method to include three spatial coordinates and time. For the numerical model used in this work, the ADI method is applied for three spatial coordinates and rigidity. See *Potgieter* (1984) for a full discussion.

The LIS ($f_g(P)$) is taken as an input spectrum at the outer boundary of the heliosphere, located at $r_b = 120$ AU, for all values of θ and ϕ. The inner boundary is taken at $r_1 > r_\odot$. Furthermore, at the poles (for $\theta = 0$ and $\theta = \pi$) it is assumed that $\partial f/\partial\theta = 0$, assuming symmetry with respect to the polar line. A solution is then obtained by first calculating an initial solution at one third of a rigidity step forward by solving the differential equation implicitly in the direction of the first spatial coordinate, i.e. the radial distance r. A second solution is then calculated at another third of a rigidity step forward, using the first solution, by solving the differential equation implicitly in the direction of the second spatial coordinate, the polar angle θ. For a solution at the final third of the rigidity step, this process is repeated for the last spatial coordinate, the azimuthal angle ϕ, using the previous two solutions. As a result, a system of linear equations is obtained which can be solved using the Thomas algorithm (e.g. *Lapidus and Pinder*). For locally developed models, *Williams* (1990) was the first to implement this numerical scheme in order to solve the TPE in three spatial coordinates, with rigidity as the fourth coordinate, for a flat HCS, after which *Hattingh* (1998) applied it for a wavy HCS model.

A 3D grid is constructed across which the TPE is solved. The radial grid points $r_i = (i-1)\Delta r + r_1$, for $i = 1, 2, \ldots, N_r$, run from $r = r_1$ at the inner boundary to $r = r_b$ at the outer boundary, with the radial increments $\Delta r = (r_b - r_1)/(N_r - 1)$. The polar grid points are $\theta_j = (j-1)\Delta\theta$, for $j = 1, 2, \ldots, N_\theta$, and run from $\theta = 0^\circ$ at the north pole to $\theta = 180^\circ$ at the south pole, with the polar increments $\Delta\theta = \pi/(N_\theta - 1)$. The azimuthal grid points $\phi_k = (k-1)\Delta\phi$, for $k = 1, 2, \ldots, N_\phi$, run from $\phi = 0^\circ$ to $\phi = 360^\circ$ for a full solar rotation, where the azimuthal increments are $\Delta\phi = 2\pi/(N_\phi - 1)$. Furthermore, the rigidity decreases logarithmically from an initial maximum value P_{max} to a minimum value P_{min}, so that $P_{n+1} = P_n/\exp(\Delta \ln P)$, for $n = 1, 2, \ldots$, with $\Delta \ln P > 0$ the rigidity increment. The solution, however, becomes unstable when the rigidity steps are large relative to the squares of the spatial increments, so that the value for $\Delta \ln P$ is chosen in such a way so as to improve the stability of the solution.

In terms of the grid points, the distribution function is

$$f(r_i, \theta_j, \phi_k, P_n) = f(i\Delta r, j\Delta\theta, k\Delta\phi, n\Delta \ln P) = f_{i,j,k,n}, \tag{3.51}$$

so that, from Taylor series expansions, the central finite difference approximations for

the first, second and mixed derivatives of f are given by

$$\begin{aligned}
\frac{\partial f(x)}{\partial x} &= \frac{f(x+\Delta x) - f(x-\Delta x)}{2\Delta x} \\
\frac{\partial^2 f(x)}{\partial x^2} &= \frac{f(x+\Delta x) - 2f(x) + f(x-\Delta x)}{(\Delta x)^2} \\
\frac{\partial^2 f(x)}{\partial x \partial y} &= \frac{f(x+\Delta x, y+\Delta y) - f(x+\Delta x, y-\Delta y) - f(x-\Delta x, y+\Delta y)}{4\Delta x \Delta y} \\
&\quad + \frac{f(x-\Delta x, y-\Delta y)}{4\Delta x \Delta y}.
\end{aligned} \tag{3.52}$$

The error on the first two equations is $(\Delta x)^2$, and on the third it is $\Delta x \Delta y$. In terms of the grid points, these equations are written as

$$\begin{aligned}
\frac{\partial f}{\partial x} &= \frac{f_{i+1} - f_{i-1}}{2\Delta x} \\
\frac{\partial^2 f}{\partial x^2} &= \frac{f_{i+1} - 2f_i + f_{i-1}}{(\Delta x)^2} \\
\frac{\partial^2 f}{\partial x \partial y} &= \frac{f_{i+1,j+1} - f_{i+1,j-1} - f_{i-1,j+1} + f_{i-1,j-1}}{4\Delta x \Delta y}.
\end{aligned} \tag{3.53}$$

The solutions for f at the different rigidity steps are indicated by

$$\begin{aligned}
f_{i,j,k,n} &= f_{i,j,k} \\
f_{i,j,k,n+\frac{1}{3}} &= f^*_{i,j,k} \\
f_{i,j,k,n+\frac{2}{3}} &= g_{i,j,k} \\
f_{i,j,k,n+1} &= h_{i,j,k}.
\end{aligned} \tag{3.54}$$

The first solution, $f^*_{i,j,k}$, is calculated by solving Equation 3.49 implicitly in the radial direction at one third of a rigidity step backward. This is achieved by evaluating half of the central difference equations 3.52 in r at the present rigidity step and half of them at a third of a rigidity step backward. For the second solution, $g_{i,j,k}$, this process is repeated by once again solving Equation 3.49 implicitly, in terms of $f^*_{i,j,k}$, in the θ-direction. Similarly, the third solution, $h_{i,j,k}$, in terms of $f^*_{i,j,k}$ and $g_{i,j,k}$, is obtained at one full rigidity step backward by solving Equation 3.49 implicitly in the ϕ-direction. This process is repeated for all rigidity values in order to obtain a solution for the final distribution function f, which is related to the differential intensity (j) by $j = P^2 f$. See *Hattingh* (1998) for a full discussion on solving the 3D transport equation numerically.

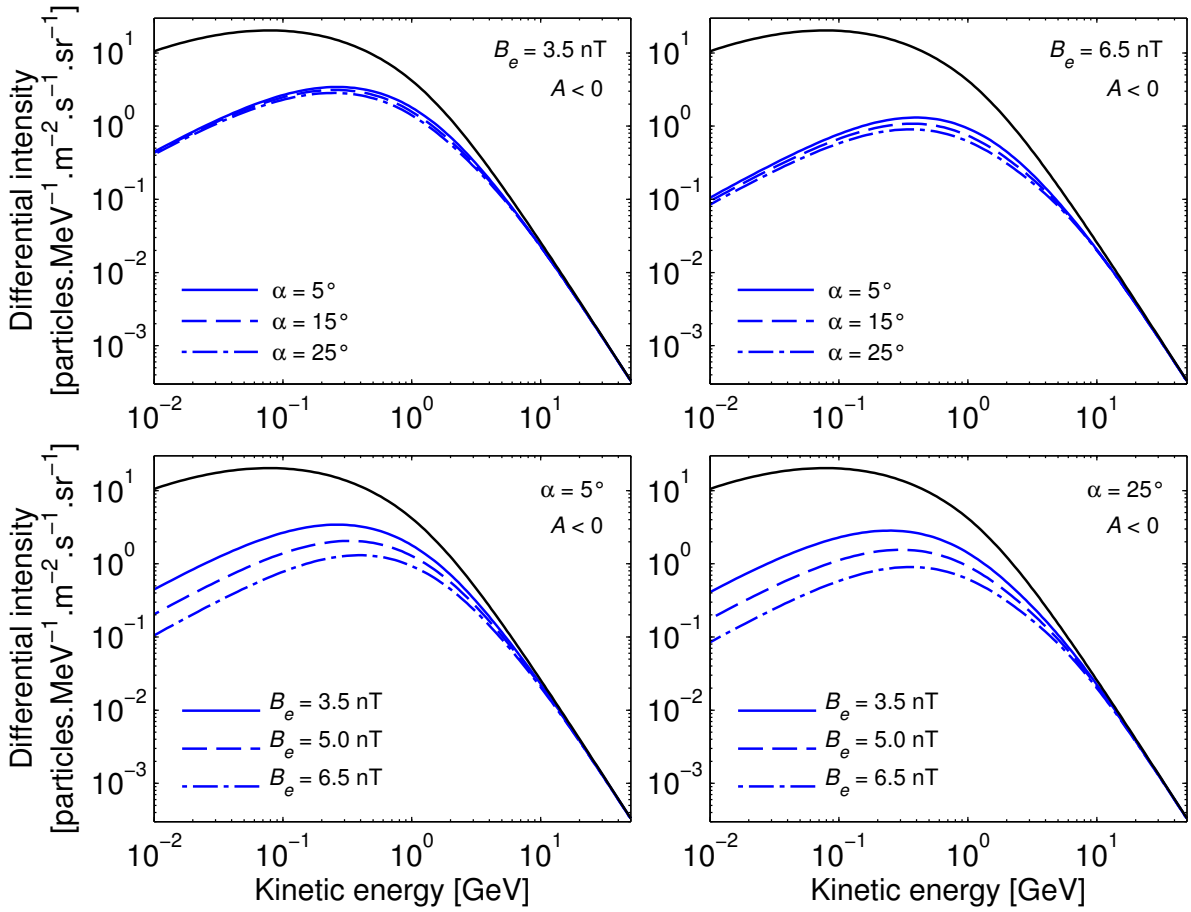

Figure 3.8: Shown here are the energy spectra for protons during an $A < 0$ cycle for different current-sheet tilt angle values (top panels) when the average HMF at Earth is 3.5 nT (left) and 6.5 nT (right). The bottom panels show similar graphs for $\alpha = 5°$ (left) and $\alpha = 25°$ (right).

3.6 Features of the 3D Numerical Model

In order to apply the 3D numerical model to CR modulation, it is necessary to investigate some of the defining features it exhibits. Since the primary focus of this study also involves changes in heliospheric conditions, of which the average HCS tilt angle and the HMF both play central roles, it is necessary to perform such an investigation by means of a parameter study. This is done by varying the current-sheet tilt angle and the HMF values across predefined ranges applicable to the scope of study which is determined by the time frame of interest. Even though, as a result of $\kappa_{\parallel} \propto B^{-1}$ and $\kappa_A \propto B^{-1}$, both the parallel and perpendicular MFPs as well as the gradient, curvature and HCS drift scales are also indirectly altered upon changing the HMF magnitude, this joint behaviour ultimately determines the resulting energy spectrum.

From the end of 2006 to the end of 2009, the current-sheet tilt angle varied from a maximum value of $\alpha \sim 25°$ (moderate solar minimum conditions) to a minimum value

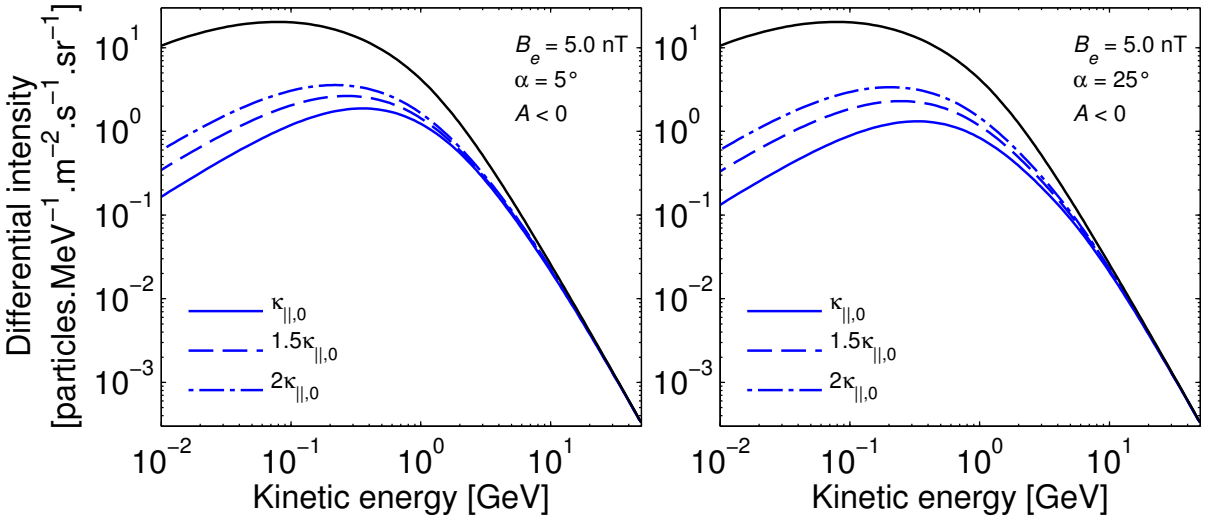

Figure 3.9: Proton energy spectra for different values of $\kappa_{\|,0}$ for HCS tilt angle values of $5°$ (left) and $25°$ (right). The average HMF at Earth is kept constant at 5.0 nT.

of $\alpha \sim 5°$ (solar minimum conditions), together with a variation in the average HMF at Earth (B_e) between ~ 6.5 nT and ~ 3.5 nT. Figure 3.8 shows the resulting effects on proton energy spectra produced by changes in α and B_e for an $A < 0$ polarity cycle. In the top panels, α was varied for values of $5°$, $15°$, and $25°$ for $B_e = 3.5$ nT (left) and $B_e = 6.5$ nT (right). From these panels the effect of larger current-sheet tilt angles, i.e. an increasingly wavy current-sheet, are clearly illustrated. Since protons drift inward along the HCS and outward through the polar regions during an $A < 0$ cycle, larger tilt angles cause protons to travel a longer path, during which time more protons are scattered. Protons therefore experience more modulation (lower intensities) for larger tilt angles. For $B_e = 3.5$ nT the intensities at energies in the region of the peak in intensity (~ 300 MeV) decrease by a mere factor of ~ 1.25 when α changes from $5°$ to $25°$, whereas for $B_e = 6.5$ nT the intensities at ~ 400 MeV decrease by a factor of ~ 1.7. The reason for this less pronounced intensity decrease for a smaller HMF is due to the fact that smaller HMF values result in larger MFPs and drift scales (due to the B^{-1} dependencies), which causes less modulation.

The bottom panels of Figure 3.8 give a similar comparison for where B_e has been varied between 3.5 nT, 5.0 nT, and 6.5 nT for $\alpha = 5°$ (left) and $\alpha = 25°$ (right). Here it is seen that when B_e is changed from 3.5 nT to 6.5 nT, the modulation increases by a factor of ~ 2.5 and ~ 3.3 for $5°$ and $25°$ tilt angles respectively.

For the numerical model used in this study, the effects from changes in particle diffusion are more prominent than that of particle drifts. Consequently, the effect of changing $\kappa_{\|}$ directly by means of $\kappa_{\|,0}$ for protons during an $A < 0$ cycle is also investi-

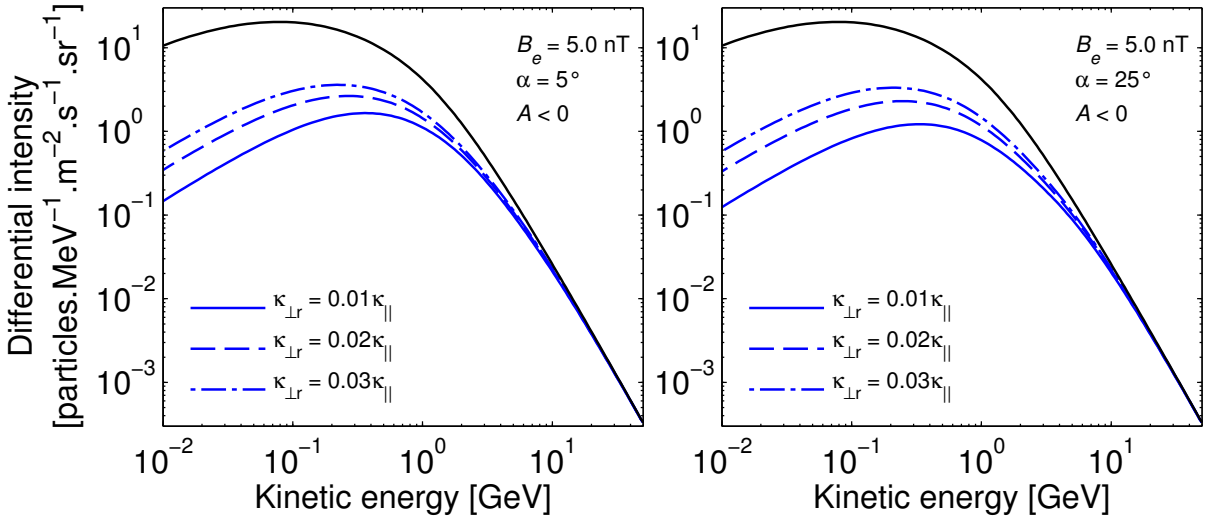

Figure 3.10: Similar to Figure 3.9, but for $\kappa_{\perp,r}$ scaled by 1%, 2%, and 3% of $\kappa_{\parallel}$.

gated, and is shown in Figure 3.9. Here $\kappa_{\parallel}$ (with dependencies as discussed in previous sections) has been varied from an arbitrary $\kappa_{\parallel,0}$ to $1.5\kappa_{\parallel,0}$ and $2\kappa_{\parallel,0}$, for $\alpha = 5°$ (left) and $\alpha = 25°$ (right), using an average HMF value of $B_e = 5.0$ nT at Earth. It should be noted, however that $\kappa_{\perp}$ is still scaled by 2% of $\kappa_{\parallel}$. In these scenarios, since B_e is held fixed, the amount of drifts experienced by particles, apart from what is contributed by the different tilt angles, are unchanged. By changing only $\kappa_{\parallel,0}$, the results shown in Figure 3.9 illustrate the effect that larger MFPs have on current-sheet drifts. For large MFPs, particles travel longer distances before being scattered, resulting in less modulation. Moreover, magnetic field gradients, which directly determine the amount of particle drifts, are also diminished by larger MFPs. These effects are seen by comparing the differences in the solid lines to that of the dashed-dotted lines, the latter of which ($2\kappa_{\parallel,0}$) correspond to particle MFPs that are twice as long as that of the former ($\kappa_{\parallel,0}$). This comparison shows that for the $\kappa_{\parallel,0}$ scenarios, CR modulation increased by a factor of ~ 1.4 when the current-sheet tilt angle changed from $5°$ to $25°$, whereas for the $2\kappa_{\parallel,0}$ scenarios there is nearly no change in intensity when α is increased. A similar behaviour is also found when changing only $\kappa_{\perp r}$, as is shown in Figure 3.10.

3.7 Summary

In this chapter the Parker TPE was discussed, as well as the various transport phenomena that contribute to the modulation of CRs. The TPE, which is solved using a finite difference method, forms the central equation that determines the transport and modulation of CRs within the heliosphere. Contained within the TPE is the diffusion

tensor which contains all the necessary coefficients that describe how particles undergo diffusion and gradient, curvature and current-sheet drifts. The theoretical and mathematical aspects concerning these diffusion and drift coefficients were also discussed. In Section 3.5 an overview was given about various numerical models used in CR modulation studies followed by a discussion on the numerical scheme used in the model to obtain a solution for the TPE. This chapter concluded with a discussion of some of the important features of the 3D modulation model used in this study.

The following three chapters are devoted to discussions about the results obtained from this 3D modulation model in light of recent proton and electron spectra from the PAMELA satellite.

Chapter 4

Proton Modulation

4.1 Introduction

The minimum of 2009 has been widely recognized as being atypical to a great extent compared to other solar minima. With access to high precision preliminary PAMELA proton spectra from 2006 to 2009, this unusual solar minimum event can be studied in detail with regard to particle intensities. One of the primary objectives of this work is to accurately reproduce the heliospheric conditions responsible for this solar minimum by using the numerical model described in Chapter 3. Furthermore, by using CR proton spectra measured by PAMELA as validation for the computed intensities, the aim is to reproduce the proton energy spectra during this time by simulating the transport of these particles from the HP to the Earth. Such results will contribute to an in-depth investigation of the recent solar minimum, from which reliable conclusions can be made.

4.2 The Local Interstellar Proton Spectrum

Being one of the most abundant particle species in the Galaxy, protons, together with helium, serve as the primary measure of the CR energy density in the ISM. Consequently, a proper knowledge of the exact shape of the proton energy spectra in the LISM is of particular importance for the study of heliospheric modulation, since it also serves as the primary input spectrum.

Over the years many attempts have been made in order to obtain accurate estimates for, among other, the proton LIS. However, despite the importance of such a spectrum, neither the absolute flux nor the spectral shape could have been successfully determined to adequate precision (*Menn et al.*, 2000). The amount by which these quantities vary is evident from a collection of published proton spectra shown in *Gaisser and Schaefer* (1992). Nonetheless, more recent studies have contributed significantly

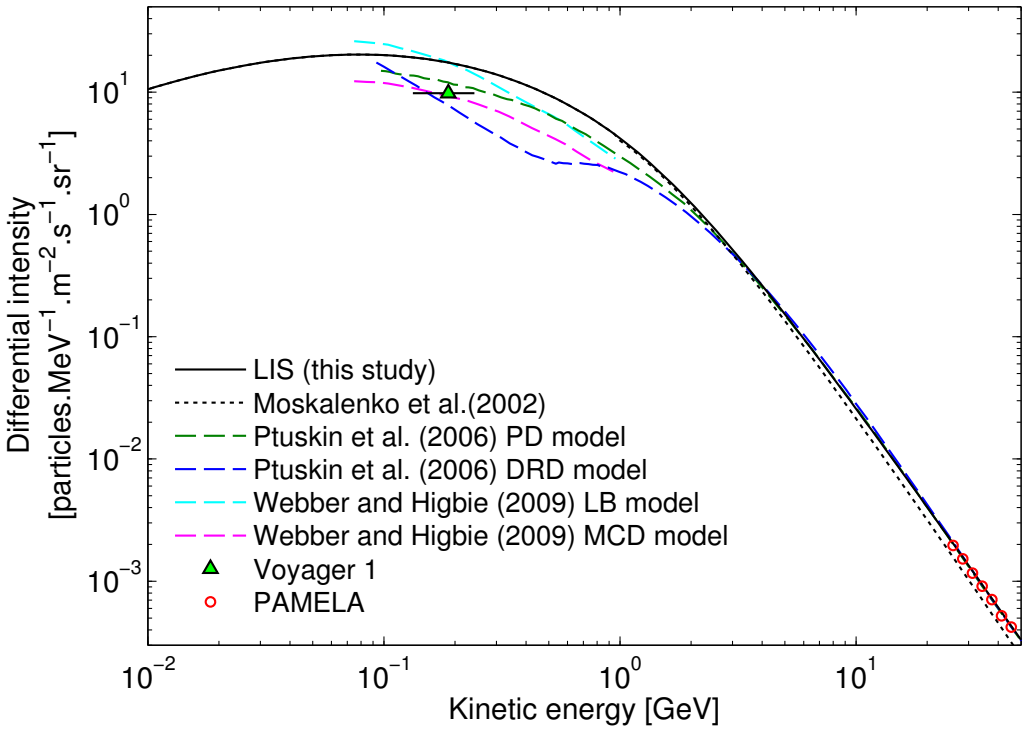

Figure 4.1: A comparison between the original (dotted black) and modified (solid black) proton LIS from *Moskalenko et al.* (2002), the latter of which is used in this work, and various other LIS models. Also shown at high energies are the PAMELA proton intensities from November, 2006 (*PAMELA-group, private communication*), along with the average intensity of recent low energy Voyager 1 measurements taken at $\sim$ 118 AU around June, 2011 (data obtained from http://voyager.gsfc.nasa.gov/).

toward CR measurements of increased accuracy that, as is the case with the PAMELA experiment (*Picozza et al.*, 2007), also include higher energies at which heliospheric modulation is negligible. With measurements at these energies it is possible to confine the proton LIS above $\sim$ 30 GeV within a region indicative of its true value. For energies below $\sim$ 30 GeV the adiabatic energy losses that protons experience become increasingly important, along with other modulation processes. As a result of this, and due to the fact that, at present, no *in situ* local interstellar measurements are available, the low-energy proton LIS remains uncertain to some extent.

However, according to *Webber and Intriligator* (2011) this might not be the prevailing conditions for much longer. Assuming that the HP has a constant equilibrium distance of between 1.4 and 1.6 times the heliospheric TS distance, Voyager 1 is expected to cross the HP and enter interstellar space in 2012 $\pm$ 1 year , at which time it might be able to obtain direct measurements of the LIS. If this is not the case, it is unlikely that Voyager 1 will reach the LISM before 2016 (*Scherer et al.*, 2011). Moreover, since Voyager 1 is probably, at present, located close to the HP, the CR proton intensities that it measures effectively serves as a lower boundary for the LIS. By taking into account

the PAMELA observations at high energies, as well as recent Voyager 1 observations at lower energies, a reasonable accurate estimate for the proton LIS can be inferred.

In order to compare the results of this work to that of *Langner* (2000, 2004), the proton LIS from *Moskalenko et al.* (2002) is adopted as the primary input spectrum. However, at energies between 30 GeV and 50 GeV, this LIS yields a spectral index of -2.82 ± 0.01, whereas the PAMELA proton observations indicate a slightly weaker index of -2.74 ± 0.02 at the same energies (data obtained from the *PAMELA-group – private communication*). It is in this energy range that heliospheric modulation has little to no effect on CRs, thereby allowing the opportunity for assured normalization of the LIS to CR measurements. The LIS from *Moskalenko et al.* (2002), therefore, had to be modified to account for the difference in spectral index and for proper normalization to the PAMELA observations. The modified proton LIS is given by

$$j_{LIS,p^+} = \begin{cases} 0.8 \exp\left(4.64 - 0.08\left(\ln E\right)^2 - 2.91E^{0.5}\right) & \text{for } E < 1.4 \text{ GeV} \\ 0.775 \exp\left(3.22 - 2.78\left(\ln E\right) - 1.5E^{-1}\right) & \text{for } E \geq 1.4 \text{ GeV,} \end{cases} \tag{4.1}$$

where E is the kinetic energy in GeV, $j_{LIS} = P^2 f$ the differential intensity, specified in units of particles.m^{-2}.s^{-1}.sr^{-1}.MeV^{-1}, with P the rigidity in GV and f the CR distribution function.

Figure 4.1 shows both the original and corrected LIS from *Moskalenko et al.* (2002), the latter of which coincides with the PAMELA observations above ~ 30 GeV. Furthermore, as is also required, the LIS at ~ 200 MeV is reasonably above the current proton intensities measured by Voyager 1 at an approximate distance of 118 AU. Also shown in Figure 4.1 are other proposed LIS models from *Ptuskin et al.* (2006) and *Webber and Higbie* (2009). Even though *Ptuskin et al.* (2006) successfully fitted observations from AMS I, BESS, and CAPRICE using both the so-called Plain Diffusion (PD) and Diffusive Reacceleration with Damping (DRD) models, it is more likely that the true proton LIS might be somewhat higher than the PD model in the 200 MeV region. The Monte Carlo Diffusion (MCD) model of *Webber and Higbie* (2009) also gives a spectrum slightly lower than the marginal Voyager 1 intensity, whereas their Leaky Box (LB) model produces a conveniently higher spectrum which allows sufficient room for further possible increase in intensity as Voyager 1 approaches the LISM.

Overall, as is apparent from Figure 4.1, the modified *Moskalenko et al.* (2002) LIS is expected to be a fairly good approximation, since it closely resembles the shape of other reasonable LIS models and its absolute value also adheres to the conditions imposed on intensities by CR measurements.

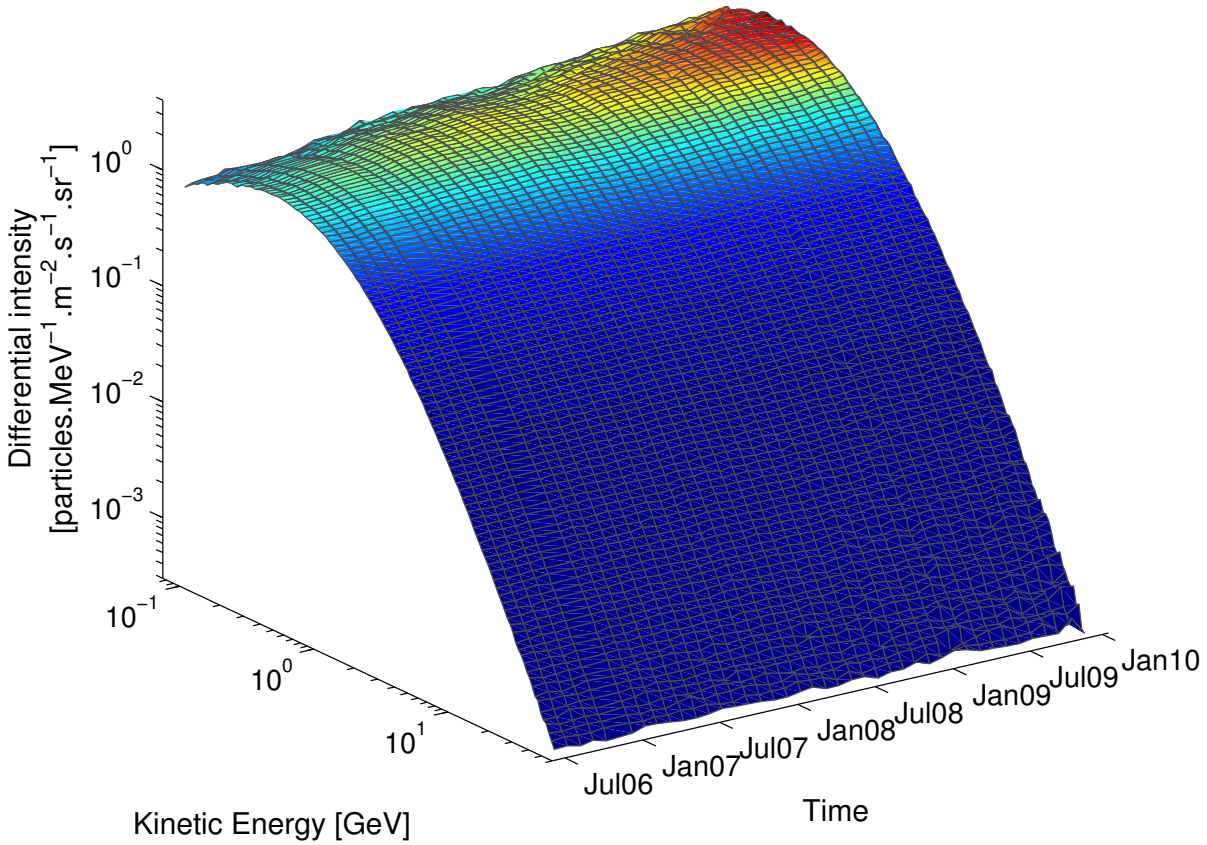

Figure 4.2: An overview of how the proton intensities developed from July, 2006 to December, 2009, according to PAMELA measurements. This surface is constructed by interpolating between monthly energy spectra averages. Data obtained from the *PAMELA-group* (*private communication*).

4.3 The PAMELA Proton Spectra

The PAMELA satellite entered into orbit just as solar cycle 23 approached its final phase, from around 2006, during which time heliospheric conditions relaxed for the onset of solar minimum. CR intensities measured by PAMELA during this time enable us to study the recent solar minimum to a greater degree of accuracy than what was possible before. By comparing PAMELA observations to HCS tilt angle and HMF measurements, it is possible to obtain a better understanding of the heliospheric conditions that led to the recent solar minimum.

Figure 4.2 gives an overview of the PAMELA CR proton measurements, interpolated from monthly averages, which illustrates how the intensities developed from July, 2006 toward the end of 2009. The most apparent feature in the intensity progress during this time is evident in the varying color-coded region of the surface, where the transition of light-blue to dark-red corresponds to the progress of intensities from ~ 1.5

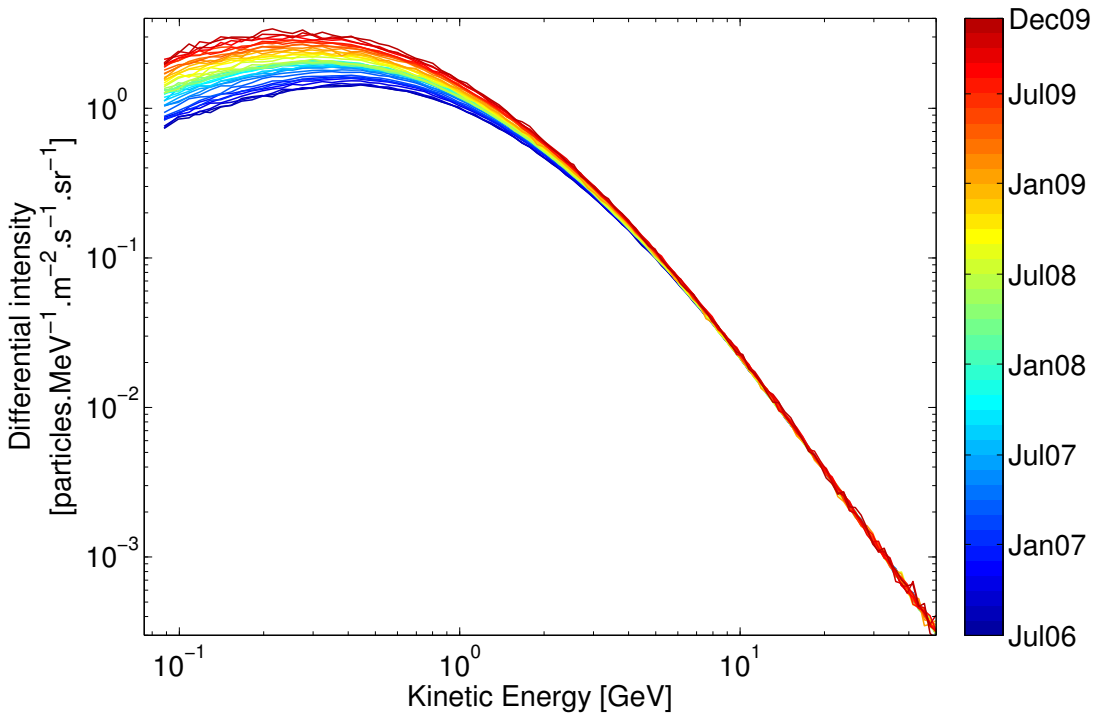

Figure 4.3: The colored curves indicate how the proton spectra developed as particle intensities approached the period of minimum CR modulation, from July, 2006 (blue), to December, 2009 (red). The region between the blue and red curves indicates the spread in proton intensities during this time. Data obtained from the *PAMELA-group* (*private communication*).

to ~ 3.5 particles.m^{-2}.s^{-1}.sr^{-1}.MeV^{-1}. Figure 4.3 shows a similar plot of the proton energy spectra, from which a closer inspection thereof reveals that intensities in the energy range between about 80 MeV and 2 GeV have the greatest increase. Even though heliospheric modulation has an affect on all charged particles with energies below ~ 30 GeV, it is clear from Figure 4.3 that particles below ~ 2 GeV experience the greatest influence. With a maximum intensity of 1.4 particles.m^{-2}.s^{-1}.sr^{-1}.MeV^{-1} in July, 2006, situated around 440 MeV, the energy spectra peak shifted to about 210 MeV by the end of 2009. Also, with an accompanying increase in the intensities by a factor of almost 2.5, the proton intensity reached a maximum of 3.4 particles.m^{-2}.s^{-1}.sr^{-1}.MeV^{-1} in the region of the peak by the end of 2009.

The largest increase, however, occurred at the lower end of the energy spectrum, where intensities increased by more than a factor of 3. This can be seen in Figure 4.4, which gives the ratios of consecutive monthly-averaged spectra relative to July, 2006. In this energy region (around 100 MeV), proton intensities increased by $\sim 50\%$ over twelve months, from December, 2006 to December, 2007, with a slightly larger increase of $\sim 60\%$ from December, 2007 to December, 2008. For 2009, however, during which solar minimum conditions continued to prevail throughout the heliosphere, intensities

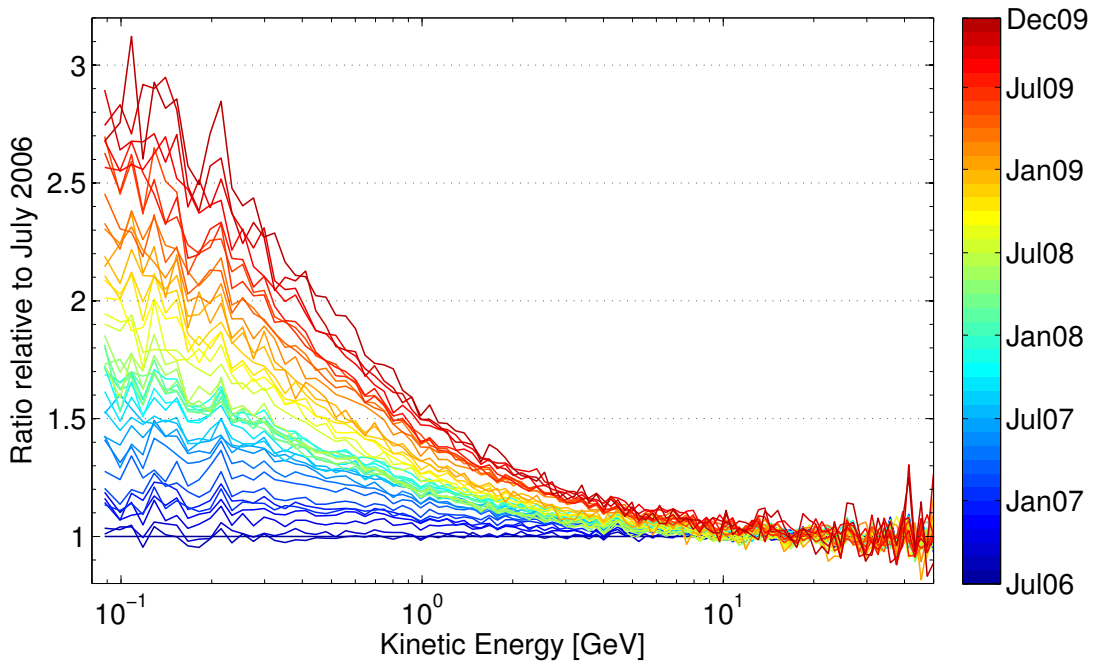

Figure 4.4: Ratios of consecutive PAMELA monthly-averaged proton spectra with respect to July, 2006. The colorbar indicates the time that corresponds to the proton ratios. Data obtained from the *PAMELA-group* (*private communication*).

increased by almost 90%. From the data available for this study, it is evident that protons across the greater part of the energy spectrum reached maximum intensities at the end of 2009, thereby marking the climax of the solar cycle 23/24 minimum.

4.4 The Minimum of Solar Cycle 23

The solar minimum of cycle 23 has been identified by others (*McDonald et al.*, 2010; *Russell et al.*, 2010; *Heber et al.*, 2009; *Mewaldt et al.*, 2010) to be quite significant in many ways. According to *McDonald et al.* (2010), this solar minimum has been unlike any other over the past century in the sense that it has shown an extended period of very low solar activity from 2006 to December, 2009. For this reason it is necessary to take a closer look at the heliospheric conditions that led to such a solar minimum.

With the Sun being the primary varying impetus over timescales of decades, it is apparent that the level of solar activity determines the state of the heliosphere, which in turn influences the modulation experienced by CR particles. Over the past 60 years' minima the lowest average SSN has been of the order of 10, reflecting the fact that in spite of a supposedly quiet Sun, some level of activity still persisted. However, except for a few transient periods of moderate activity, the SSN during the recent solar minimum has remained at a very low level from around 2007 to the end of 2008, displaying

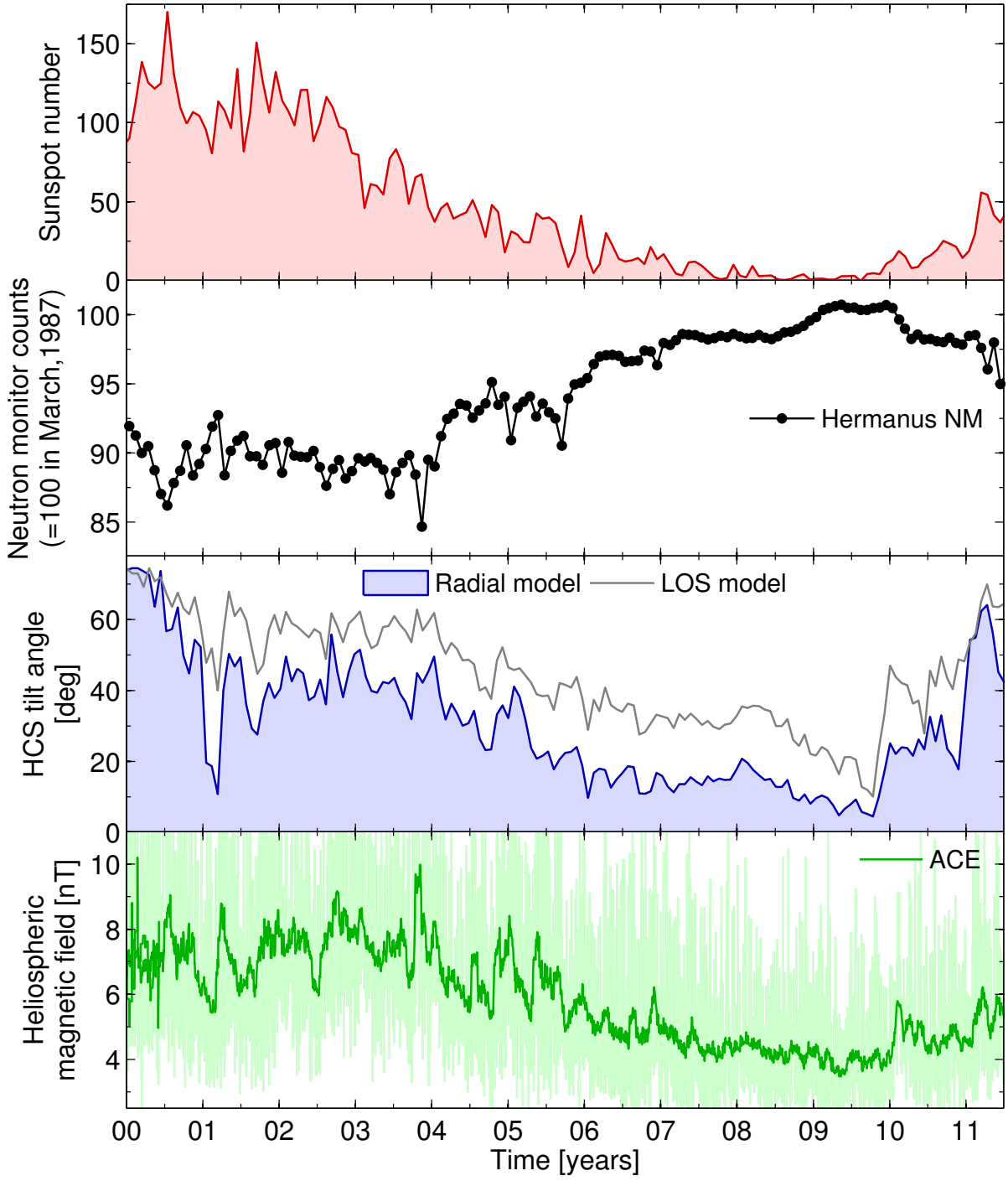

Figure 4.5: The above collection of panels clearly illustrate how the heliospheric conditions of cycle 23 declined from solar maximum, in ~ 2000, to solar minimum, in ~ 2009. Shown in the top panel is the sunspot number, which serves as a proxy for the measure of the level of solar activity (data from http://sidc.oma.be/). The second panel gives the Hermanus neutron monitor count rate, which has a cutoff rigidity at ~ 4.9 GV (data from http://www.nwu.ac.za/content/neutron-monitor-data). The radial- and line-of-sight (LOS) models for the HCS tilt angle, measured by the Wilcox Solar Observatory, are shown in the third panel as an alternative proxy for solar activity (data from http://wso.stanford.edu/). The fourth panel gives the monthly (green) and daily (light green) HMF averages at Earth as measured by ACE (data from http://nssdc.gsfc.nasa.gov/).

the highest total number of spotless days since the minimum of cycle 14/15 (*McDonald et al.*, 2010). Figure 4.5 gives an outline of the heliospheric conditions from 2000 to 2011, with the SSNs presented in the first panel, along with CR neutron monitor data, HCS tilt angle measurements, and averaged HMF values from the second to fourth panels respectively.

Looking back in history at the HCS tilt angle, it is found that the HCS has reached a minimum annual tilt of $\sim 3^{\circ}$ (according to the radial model) since observations began at the Wilcox Solar Observatory. Conversely, current-sheet tilt values for the recent minimum have remained higher than usual, with values between $\sim 15^{\circ}$ and $\sim 5^{\circ}$, between 2007 and 2009, which is evident in the third panel of Figure 4.5. In addition to this, a noticeable increase appeared in the beginning of 2008, during which the current-sheet tilt reached values greater than 20° over a period of around 3 months. By using this unique opportunity, *McDonald et al.* (2010) reported a response time of ~ 4 solar rotations between changes in the tilt angle and the onset of CR decreases. The line-of-sight (LOS) model essentially shows a similar qualitative pattern to that of the radial model, but with a higher average displacement of $\sim 15^{\circ}$.

Possibly the most significant phenomenon of the previous solar minimum, can be seen in the development of the HMF, shown in the bottom panel of Figure 4.5. By using, among other, measurements of the solar wind in the ecliptic plane and over the poles, *Svalgaard and Cliver* (2007) have identified a "floor" in the solar magnetic field which acts as a baseline to which the magnetic field falls during solar minimum conditions. During such periods, they found that the HMF has a base value of ~ 4.6 nT at 1 AU in the equatorial plane, while the radial component of the HMF in the polar regions are ~ 3.0 nT at a distance of 1 AU. Over the previous four solar minima the HMF has weakened to similar values of ~ 5.0 nT (*McDonald et al.*, 2010; see also Figure 2.3 in Chapter 2).

During the recent solar minimum, the HMF has dropped to values as low as 3.5 nT in May, 2009, 30% less than the 5.0 nT of the previous four minima (see also e.g. *Smith and Balogh*, 2008). In addition to this, *Wang et al.* (2009) have also reported that the polar magnetic fields of the Sun were about 40% weaker during this time, compared to the previous three sunspot minima. Even though both the HCS tilt angle and the HMF decreased sufficiently as solar cycle 23 reached its minimum, the increase in CR intensities, as seen in the second panel of Figure 4.5, were not as steep as expected (*Heber et al.*, 2009).

Furthermore, by using Ulysses observations, *McComas et al.* (2008) have reported that the solar wind pressure has decreased by $\sim 20\%$ compared to solar cycle 22, as well as that solar wind density measurements have reached the lowest values ever measured, which indicates that the heliosphere has reached exceptional quiet modula-

tion conditions.

Such unusual modulation conditions result in particle intensities that are unlike those seen in the past five solar minima. These conditions provide a rare opportunity to more accurately investigate the influences of a weaker HMF, changes in the HCS tilt angle, and changes in the structure of the heliosphere. *McDonald et al.* (2010) also pointed out the possibility that this solar minimum could provide valuable insight into the conditions that resulted in the previous so-called "Grand Minima", such as the Dalton minimum (1810), the Maunder minimum (1645-1715), the Spöerer minimum (1420-1540) and even the Oort minimum (1050 AD).

4.5 Modelling the PAMELA Proton Spectra

4.5.1 A Sample Selection of PAMELA Spectra

Equipped with a thorough knowledge of heliospheric conditions during the recent solar minimum, accurate CR measurements from PAMELA at Earth, and an attentively bench-marked 3D model, the aim is now to reproduce intermittent proton energy spectra from 2006 to 2009. This is done by taking a sample selection of monthly-averaged spectra from PAMELA measurements, each of which is separated by approximately one year, from the end of 2006 to the end of 2009. For each consecutive monthly spectra, average representative values are calculated for the SW speed profile, the HCS tilt angle, and the HMF over the preceding months, which reflect the actual prevailing conditions throughout the heliosphere. These sets of average values are then used to adjust the numerical model for each sampled spectrum, so as to simulate the modulation of CR particles under conditions that closely resemble that of the actual heliosphere. By utilizing such an approach, one is able to obtain a better understanding of how the recent solar minimum progressed and gain deeper insight into the various modulation processes that affected the outcome of this minimum.

The four monthly-averaged proton spectra which will be focused on in this study are: November of 2006, December of 2007, December of 2008, and December of 2009, the latter of which displays the highest measurements from the available data and thereby marking the pinnacle of proton intensities for this minimum. The reason as to why the November spectrum is used for 2006 instead of December, is due to the solar particle events that occurred during mid-December which resulted in transient spectral intensities in the 80 MeV to 3 GeV energy range (*Adriani et al.*, 2011b). These four sampled monthly spectra will from hereon simply be referred to as the 2006, 2007, 2008 and 2009 spectra.

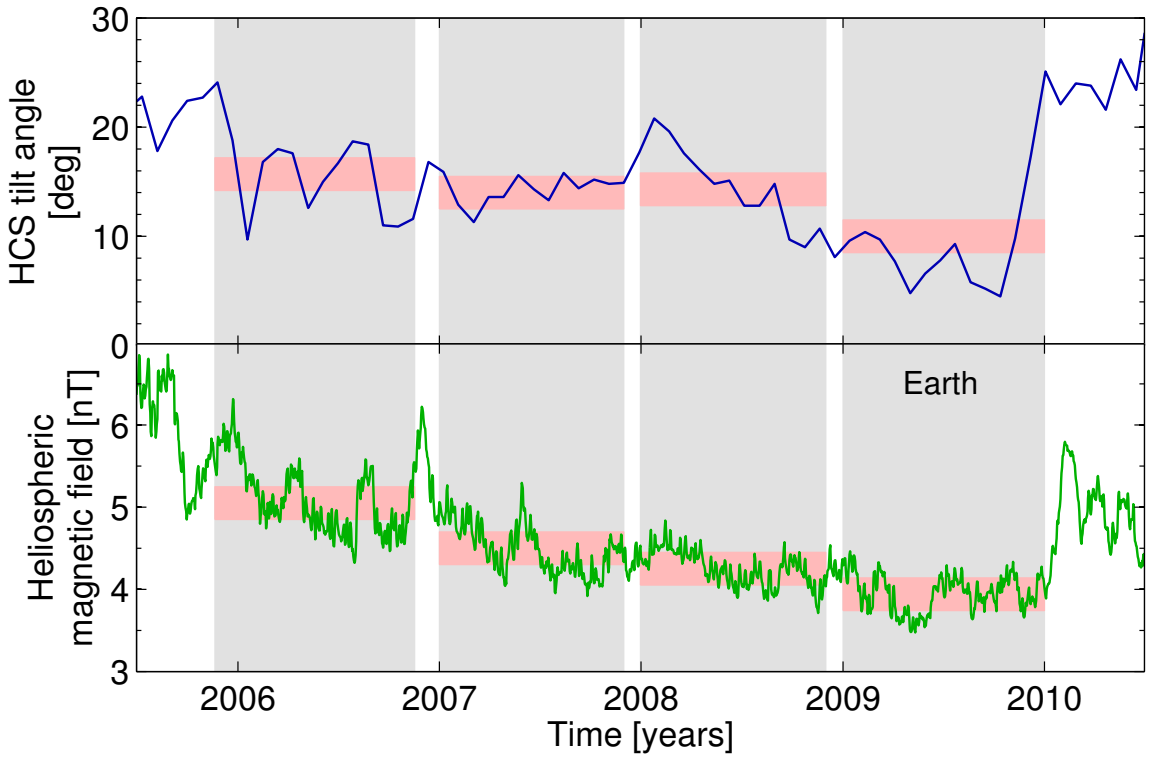

Figure 4.6: Yearly average values are calculated for the HCS tilt angle and HMF as an attempt to estimate modulation conditions in the heliosphere throughout the prior year. The light-grey regions of interest correspond to the timeframes over which averages are calculated, while the red highlighted bands give an indication of the calculated averages (along with some margin of error). The first panel shows the radial model for the HCS tilt angle, with the monthly-averaged HMF values at Earth measured by ACE in the bottom panel.

In order to reproduce modulation conditions that coincide with the sampled monthly spectra, the first objective is to calculate average values for the SW speed, the HCS tilt angle, and the HMF for each spectrum that give representative approximations to the actual preceding heliospheric conditions. However, even though most of these variables show significant variation over the timescales considered here, the fact that the SW speed essentially remains steady throughout solar minimum conditions allows for the use of a single average SW speed profile for all four sampled spectra (see Figures 2.4 and 2.5 in Chapter 2).

As the HCS tilt angle and the solar magnetic field changed, the expanding SW transports these changes, embedded within the SW, outward through the heliosphere. During typical solar minimum conditions it takes about a year (or more) before these changes reach the outermost regions of the heliosphere. Consequently, to obtain values for these quantities that accurately represent the preceding modulation conditions, averages are calculated over timescales of approximately one year.

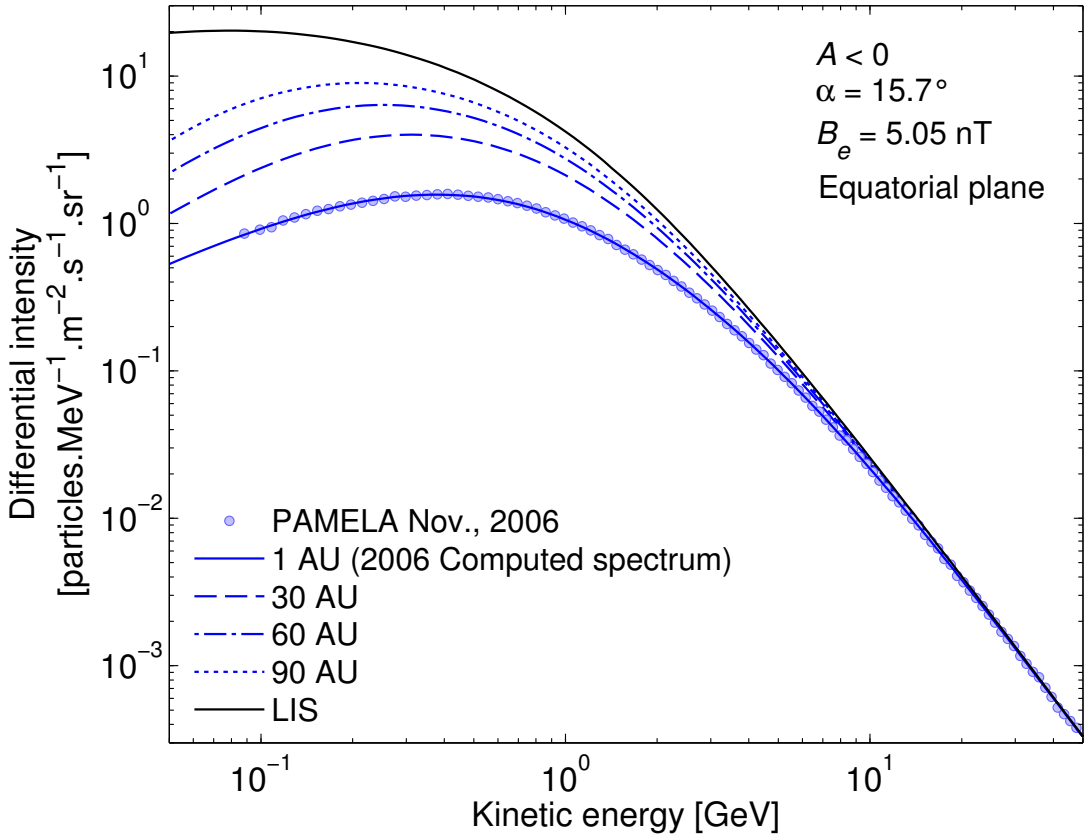

Figure 4.7: The November, 2006 PAMELA proton intensities with the computed spectra overlaid. The dotted, dashed-dotted, and dashed lines correspond to the modulated intensities in the equatorial plane at 90 AU, 60 AU, and 30 AU respectively, together with the LIS (solid black) at 120 AU. The modelled spectra are for an $A < 0$ cycle, where $\alpha = 15.7°$ and $B_e = 5.05$ nT.

Figure 4.6 illustrates how these averages are calculated and how they approximate the actual observed values. The calculated average tilt angle values for the HCS, from 2006 to 2009, are $15.7°$, $14.0°$, $14.3°$, and $10.0°$ respectively, with corresponding average magnetic field values at Earth (B_e) of 5.05 nT, 4.50 nT, 4.25 nT, and 3.94 nT, respectively.

Furthermore, because of the dynamic nature of the heliosphere, as mentioned in Section 4.4, the position of the TS is expected to vary with time. This effect has also been accounted for in this study, where it is assumed that the TS is situated at heliocentric distances of 88 AU, 86 AU, 84 AU, and 80 AU during 2006, 2007, 2008, and 2009, respectively (*Webber and Intriligator*, 2011). After incorporating all of the above parameters in the numerical model, the diffusion coefficients were carefully adjusted while still sufficiently adhering to conditions imposed on particle MFPs by the theory and from recent research, in order to obtain desired results which best fit the PAMELA observations. These results are discussed in the following sections.

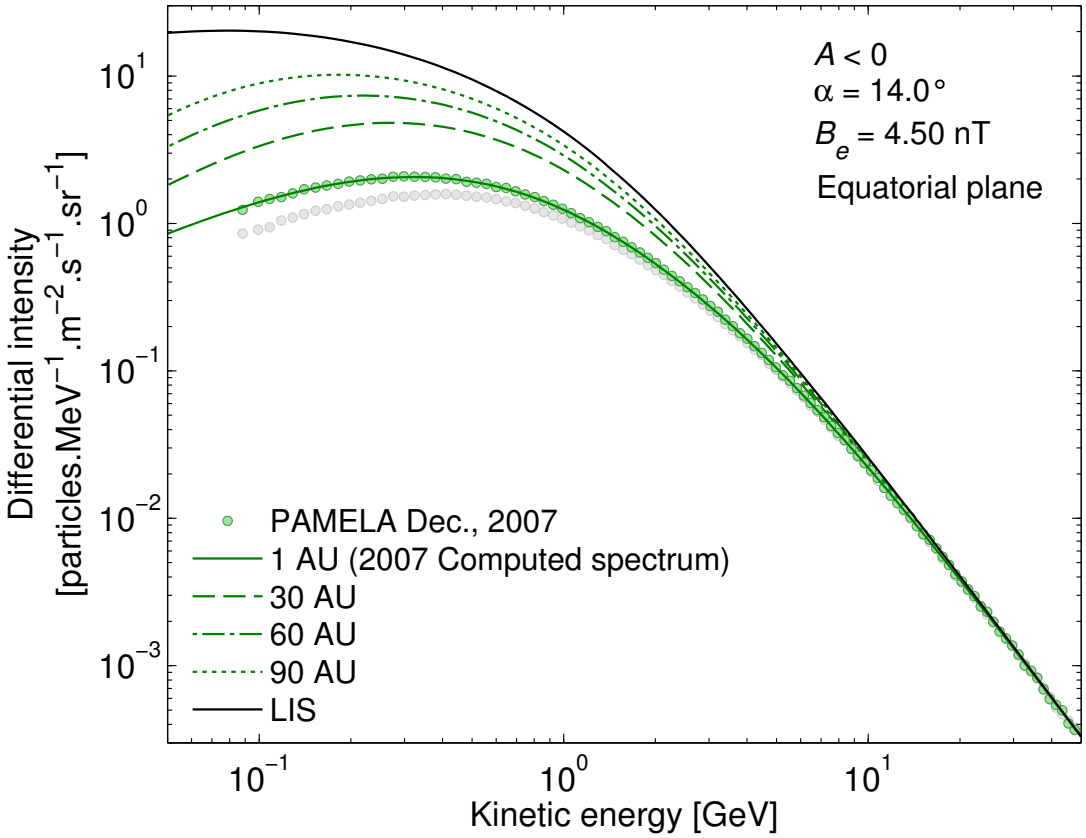

Figure 4.8: Similar to Figure 4.7, but for the December, 2007 PAMELA proton spectrum with the corresponding computed spectra overlaid, with $\alpha = 14.0°$ and $B_e = 4.50$ nT. For comparison, the light-grey data points correspond to the 2006 PAMELA spectrum as shown in Figure 4.7.

4.5.2 The Numerically Reproduced PAMELA Spectra

Figure 4.7 shows the PAMELA proton differential intensity for November, 2006 overlaid by the computed modulated spectrum in the equatorial plane at Earth, for an $A < 0$ polarity cycle. Also shown in this figure are the computed intensities at distances of 30 AU, 60 AU, and 90 AU from the Sun. All these spectra are calculated at their respective distances in the equatorial plane (i.e. $\theta = 90°$). For the 2006 spectrum, the HCS had an average tilt of about $15.7°$, and the HMF at Earth had an average value of 5.05 nT during the prior year (the latter of which is used to normalize the simulated HMF at Earth).

As mentioned before, it is established that heliospheric modulation only becomes noticeable below ~ 30 GeV, at which point the observed intensities drop below the interstellar intensities. The numerical model accurately imitates this behaviour, which can be seen at the higher end of the spectrum in Figure 4.7, where the modulated spectrum at 1 AU deviates from the -2.74 spectral index. The computed spectrum at

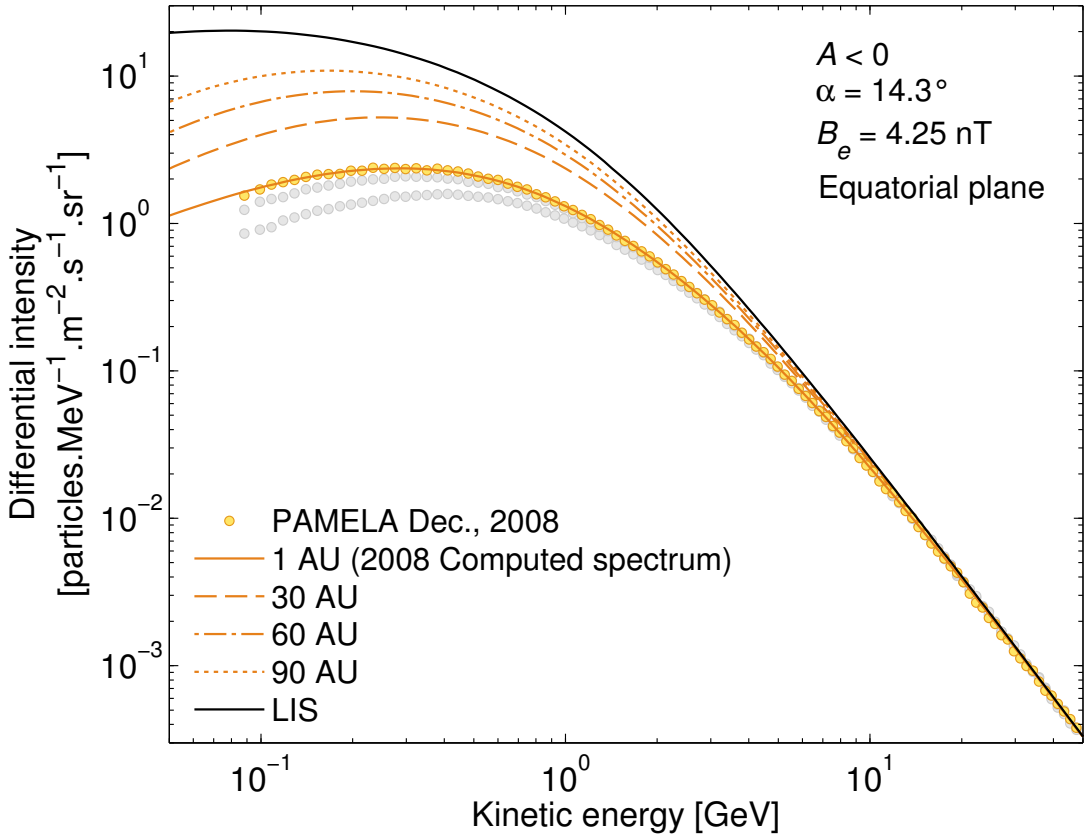

Figure 4.9: Similar to Figure 4.7 and Figure 4.8, but for the December, 2008 PAMELA spectrum, where the light-grey data points correspond to the 2006 and 2007 PAMELA spectra, as shown in the previous figures. Here $\alpha = 14.3°$ and $B_e = 4.25$ nT.

Earth gives a clear and exact fit to the PAMELA observations at all energies, reaching a peak intensity of 1.57 particles.m^{-2}.s^{-1}.sr^{-1}.MeV^{-1} at 400 MeV before starting to bend into the characteristic adiabatic slope.

During 2007 the average current-sheet tilt decreased by a mere $\sim 1.7°$ from 2006, which, in contrast, was accompanied by a relatively large decrease of 0.5 nT in the HMF at Earth. Figure 4.8 shows the proton intensities measured by PAMELA in December, 2007. Similar to Figure 4.7, the computed spectrum at 1 AU is overlaid, giving once again an exact fit to the observations across all energies. For comparison, the light-grey data points represent the 2007 spectrum of Figure 4.8, from which it can be seen that the proton intensities of the 2007 spectrum only starts to deviate noticeably from that of the 2006 spectrum below ~ 5 GeV. At the peak, now situated at ~ 310 MeV, the intensity increased by $\sim 30\%$ from 2006, to 2.07 particles.m^{-2}.s^{-1}.sr^{-1}.MeV^{-1} in 2007, whereas at 100 MeV the intensity increased by $\sim 55\%$. At distances of 30 AU, 60 AU, and 90 AU the 2007 intensities at 100 MeV increased by about $\sim 45\%$, $\sim 35\%$, and $\sim 30\%$ from 2006, respectively, according to the computed solutions.

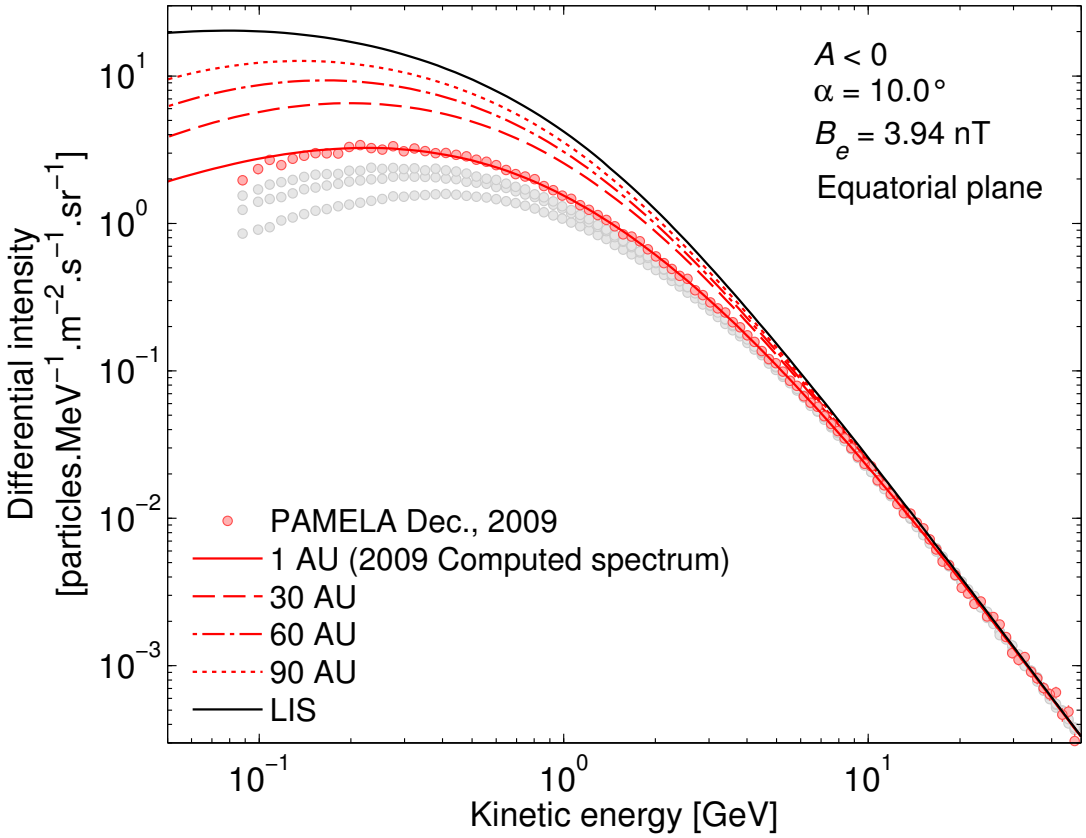

Figure 4.10: Similar to Figure 4.7 and Figure 4.8, but for the December, 2009, PAMELA spectrum, where the light-grey data points now correspond to the 2006, 2007, and 2008 PAMELA spectra. For these computations, $\alpha = 10.0°$ and $B_e = 3.94$ nT.

As a result of the transient increase in the HCS tilt angle at the beginning of 2008 (see Figure 4.6), the average current-sheet tilt for 2008 is $14.3°$, which is slightly larger than for 2007. The average HMF at Earth during 2008 has decreased by 0.25 nT to 4.25 nT, which is 50% less than with what it decreased during 2007. This comparatively smaller decrease in the HMF, together with the larger current-sheet tilt angle explains why the December spectrum of 2008 is located so close to the 2007 spectrum, as seen in Figure 4.9. By assuming, to a good approximation, that the average current-sheet tilt for 2008 has remained constant with respect to 2007, it can be inferred that the apparent change in proton intensities during 2008 could mainly be due to the change in the average HMF (including modulation processes dependent on the HMF).

Consistent with Figures 4.7 and 4.8, the computed spectrum at 1 AU gives a clear fit to the PAMELA proton observations from December, 2008. Closer inspection of this figure reveals that the peak, now situated at $\sim$ 300 MeV, has shifted by only 10 MeV from 2007, with a corresponding $\sim$ 15% increase in intensity at Earth. As is expected from the model, similar comparatively smaller intensity increases of $\sim$ 30%,

$\sim 25\%$, $\sim 15\%$, and $\sim 10\%$ respectively occured at 1 AU, 30 AU, 60 AU, and 90 AU for 100 MeV protons between 2007 and 2008. Furthermore, unlike the transition between 2006 and 2007, the intensities of 2008 remained at the same level than those of 2007 for energies as low as 1.5 GeV.

Solar cycle 23 reached its absolute minimum around the middle of 2009, followed by an abrupt increase in the tilt angle from October onward, marking the onset of new solar activity for cycle 24. With this increase taken into account, the average current-sheet tilt has a value of 10°, which is slightly higher than what it might have been if the tilt angle remained at lower values throughout 2009. The HMF has remained significantly low throughout 2009, thereby also yielding a corresponding low average value of 3.94 nT.

The December PAMELA proton spectrum of 2009, overlaid by the computed spectrum, is given in Figure 4.10. It is evident from this figure that the data for the 2009 spectrum shows significantly more variation in absolute value compared to the previous three spectra. These variations, ascribed to systematic errors, are more prominent at energies above 10 GeV and below 400 MeV. In spite of this, the numerically computed spectrum still gives a fairly accurate fit to the PAMELA observations with the exception of energies below 200 MeV, where PAMELA observations shows a tendency to decrease at a much steeper slope. As a result, the measured intensities at the lower end of the spectrum are lower than what is predicted by the model.

Nevertheless, for energies where the measurements and numerical solutions are consistent, the largest increase in intensity, between 2008 and 2009, occurred near the peak at 200 MeV, where the intensity has risen by about 40%. No definitive consensus can be given with regard to proton intensities below ~ 200 MeV, because of the uncertainty in absolute intensity at lower energies.

Figure 4.11 illustrates, by means of the above calculated spectra, the total decrease in modulation from 2006 to 2009, similar to what is observed from PAMELA measurements in Figure 4.3. Also shown by the green lines are the LIS (solid) and $A < 0$ modulated spectrum (dashed) in the equatorial plane at Earth from *Langner et al.* (2003) and *Langner* (2004). This modulated spectrum has been computed from a 2D shock acceleration and drift modulation model (see also *Potgieter and Ferreira*, 2002), where the heliopause boundary is situated at 120 AU and with $\alpha = 10^{\circ}$.

As discussed by *Langner et al.* (2003), their modulated spectrum agrees well with solar minimum observations of protons from the previous $A < 0$ cycle in 1987 (given by the symbols; *McDonald et al.*, 1998), except at 1 GeV, where the computed spectrum lies above the observations. Compared to the 2006 computed spectrum, the *Langner et al.* (2003) spectrum produces higher intensities (by a factor of ~ 2) in the region of 1 GeV, but lower intensities below ~ 100 MeV. It follows that the 1987 proton mea-

surements coincide with PAMELA measurements from 2006 to ∼2007, although it is evident from the 2009 PAMELA spectrum that the recent solar minimum resulted in significantly higher intensities compared to the minimum of cycle 21. Overall, the 2006 computed spectrum in Figure 4.11 (solid blue) gives a reasonably better fit to the 1987 observations than the *Langner et al.* (2003) spectrum, while simultaneously also giving an exact fit to the PAMELA observations as illustated earlier. Moreover, the LIS used by *Langner et al.* (2003) and *Langner* (2004), based on the *Moskalenko et al.* (2002) LIS, is similar to the modified LIS used in this study with regard to shape below ~ 3 GeV, but differs in absolute value across all energies.

Also shown in Figure 4.11 are the proton LIS (solid light blue) used by *Burger et al.* (2000), as well as the corresponding modulated $A < 0$ energy spectrum (dashed light blue). This spectrum was computed with a steady-state 2D modulation model where the heliospheric boundary is situated at 100 AU and for which the effect of a wavy current-sheet, at a tilt angle of $\alpha = 15°$, is simulated by an averaged drift field. Even though this LIS differs from the modified *Moskalenko et al.* (2002) LIS used in this study, the *Burger et al.* (2000) modulated spectrum at Earth, apart from slightly higher intensities around 300 MeV, is remarkably similar to the computed 2006 spectrum.

4.5.3 Development of the Proton Rigidity Dependence

As the heliosphere approached solar minimum conditions it can be inferred that the HMF became more structured (see e.g. *McComas et al.*, 2008), which thereby effectively reduced the amount of turbulence in the heliosphere. Since proton intensities across the greater part of the spectrum increased with time, where the greatest relative increases occurred at lower energies (as seen in Figure 4.4), it can be established that proton MFPs also increased from 2006 to 2009 where, correspondingly, the greatest increase is expected to occur below 1 GeV (i.e. ≈ 1.7 GV). The numerical solutions from Figures 4.7 to 4.10 were obtained by implementing this approach using simplified expressions for the parallel and perpendicula MFPs as discussed in Chapter 3, while also taking into account constrains imposed by the Palmer consensus values (*Palmer*, 1982). By carefully adjusting the slope of the rigidity dependence for $\kappa_{\parallel}$ and $\kappa_{\perp}$ below ~ 2 GV, the amount of diffusion, and modulation, required for each consecutive PAMELA spectrum is obtained. It is furthermore assumed that $\kappa_{\perp}$ has the same functional dependence than $\kappa_{\parallel}$, the former of which is scaled at 2% of the latter (see e.g. *Palmer*, 1982 and *Bieber et al.*, 2004).

Figure 4.12 indicates how the rigidity dependence of $\lambda_{\parallel}$ and $\lambda_{\perp}$ (related to $\kappa_{\parallel}$ and $\kappa_{\parallel}$ by Equation 3.28) for protons at Earth was required to change from 2006 to 2009 in order to reproduce the PAMELA measurements shown in Figures 4.7 to 4.10. Through-

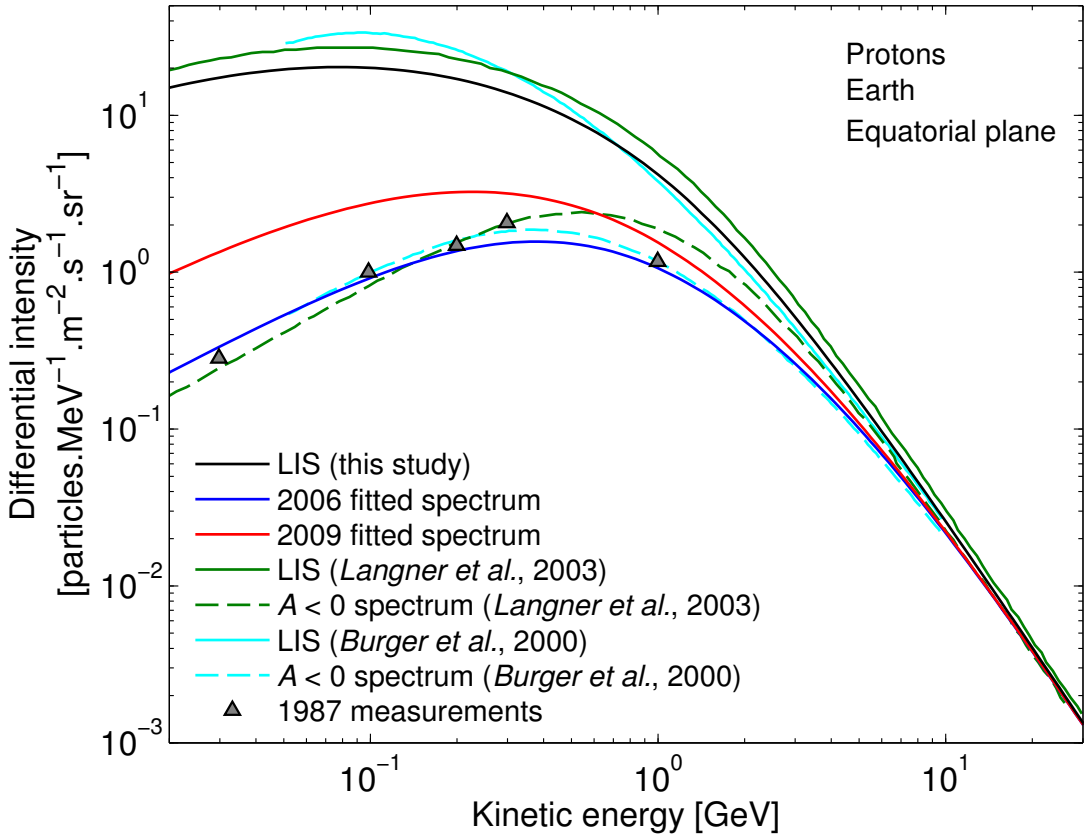

Figure 4.11: A comparison of the 2006 (solid blue) and 2009 (solid red) computed energy spectra to spectra from various other authors. The green and light blue lines give the LIS (solid) and the $A < 0$ modulated spectra (dashed) from *Langner et al.* (2003) and *Burger et al.* (2000) respectively (see also *Langner*, 2004). Also shown by the symbols are proton measurements from the previous $A < 0$ solar minimum (cycle 21) in 1987 (obtained from a collection of Voyager, IMP, and Pioneer observations from *McDonald et al.*, 1998).

out this time the rigidity slope for $\lambda_{\parallel}$ and $\lambda_{\perp}$ were kept fixed above 5 GV, whereas for rigidities below 5 GV the slope was decreased for each consecutive year, resulting in larger MFPs at these energies. It is also considered that particle MFPs are less affected by diffusion (and therefore also changes in the HMF) at high rigidities, resulting in little to no change in their absolute values. This assumption can be justified by Figure 4.4, from which it is evident that, apart from small fluctuations due to systematic errors, CR intensities show no significant change at high energies. However, the absolute value of the MFPs for 2009 is slightly increased in order to account for larger systematic fluctuations at high rigidities in the 2009 PAMELA observations.

In 2006, from Figure 4.12, the parallel and perpendicular MFPs initially assumed a $P^{0.56}$ dependence below 2 GV. For 2007, 2008, and 2009, this dependence decreased to $P^{0.48}$, $P^{0.39}$, and $P^{0.28}$ respectively, across the same rigidities. In the bottom-right panel, the region between the red and the bottom light-grey curves effectively indi-

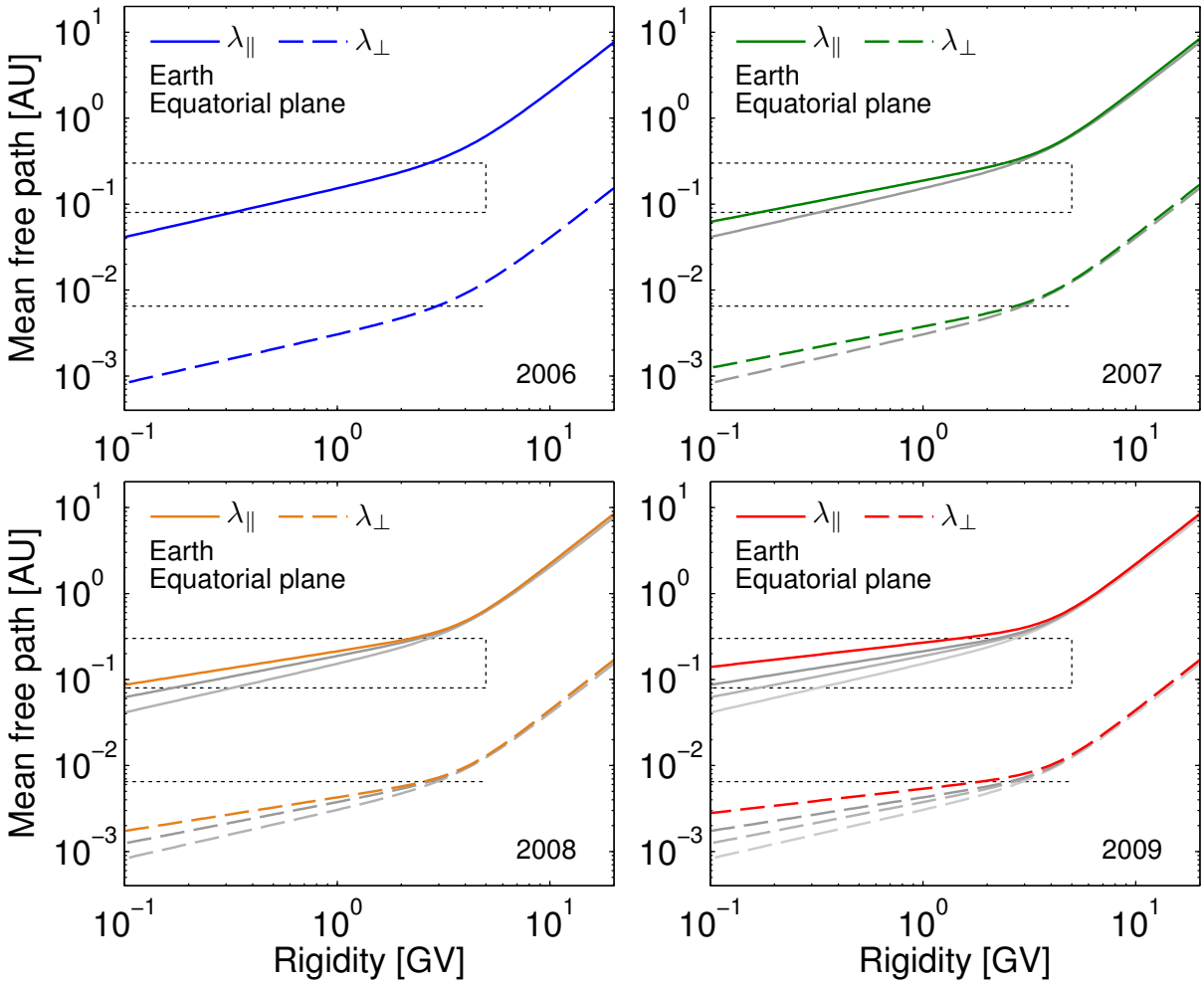

Figure 4.12: Rigidity dependencies for the parallel and perpendicular MFPs of protons at 1 AU in the equatorial plane. These panels illustrate how the rigidity dependence for the MFPs was required to change from 2006 to 2009 in order to obtain the computed spectra of Figures 4.7 to 4.10. The grey lines correspond to the MFPs of the prior years. The perpendicular MFP is scaled by 2% of the parallel MFP. See Section 3.3 for further discussion about particle MFPs.

cates the total change in rigidity dependence of $\lambda_\parallel$ and $\lambda_\perp$ required for the recent solar minimum. For all scenarios the MFPs sufficiently adhere to the Palmer consensus values (*Palmer*, 1982) indicated by the rectangular regions. As discussed in Section 3.3, these MFPs also remain within close proximity of those used by various other authors (*Burger et al.*, 2000; *Teufel and Schlickeiser*, 2003; *Langner*, 2004; *Strauss*, 2010). It can be seen that, from 2006 to 2009, the parallel and perpendicular MFPs of 0.4 GV protons (≈ 0.1 GeV) at Earth increased by a factor of more than 2, from 0.09 AU to 0.20 AU. Table 4.1 gives a summary of the various parameters used (see Equations 3.30 to 3.35 and Equation 3.47) to produce the yearly computed spectra in Figures 4.7 to 4.10.

Table 4.1: Summary of best-fit parameters used to produce the 2006 to 2009 computed proton spectra (see Equations 3.30 to 3.35 and Equation 3.47).

Parameter	**2006**	**2007**	**2008**	**2009**
α [deg]	15.7	14.0	14.3	10.0
B_e [nT]	5.05	4.50	4.25	3.94
$\kappa_{\parallel,0}$ [10^{20} cm^2.s^{-1}]	1157	1270	1357	1585
$\kappa^0_{\perp,r}$, $\kappa^0_{\perp,\theta}$	0.02	0.02	0.02	0.02
$\kappa_{A,0}$	1.0	1.0	1.0	1.0
a	0.56	0.48	0.39	0.28
b	1.95	1.95	1.95	1.95
c	3.0	3.0	3.0	3.0
d	3.0	3.0	3.0	3.0
$P_{A,0}$	$\frac{1}{\sqrt{10}}$	$\frac{1}{\sqrt{10}}$	$\frac{1}{\sqrt{10}}$	$\frac{1}{2\sqrt{10}}$
P_k [GV]	4.0	4.0	4.0	4.2

4.5.4 Contribution from Various Modulation Processes

Being the only major modulation process dependent on charge-sign, particle drifts have a fairly discernable and important effect on CR modulation in the heliosphere (*Jokipii et al.*, 1977 and *Jokipii and Levy*, 1977; *Potgieter and Moraal*, 1985). Ever since simultaneous measurements of GCR electrons and helium became available in the 1980's, the topic of charge-sign dependent modulation has been studied in great detail, especially with regard to long-term CR modulation (see e.g. *Potgieter et al.*, 1993; *le Roux and Potgieter*, 1995; *Ferreira et al.*, 2003).

It is well known that particle drifts are quite effective during solar minimum periods, varying between 80% and 100% for at least three years around every minimum (see e.g. *Ferreira and Potgieter*, 2004 and *Potgieter*, 2010). Furthermore, *Langner* (2004) has also shown that, by using 55% drifts, the numerical results produced by a 2D shock acceleration model gave reasonable fits to a vast range of measurements from, among other, BESS, IMAX, CAPRICE and IMP. Following the same approach, *Strauss* (2010) also incorporated 55% drifts in modulation studies of anomalous cosmic rays. This altogether provides substantial evidence for the importance of drift effects, escpecially during solar minimum conditions. Even though drift effects might be partially obscured by diffusion processes, the contribution from particle drifts, considered to possibly be at a maximum for this solar minimum (i.e. $\kappa_{A,0} = 1.0$), should be fairly easy to identify.

In order to uncover qualitatively, as well as quantitatively, the contribution delivered toward CR modulation by various processes during the recent minimum, each

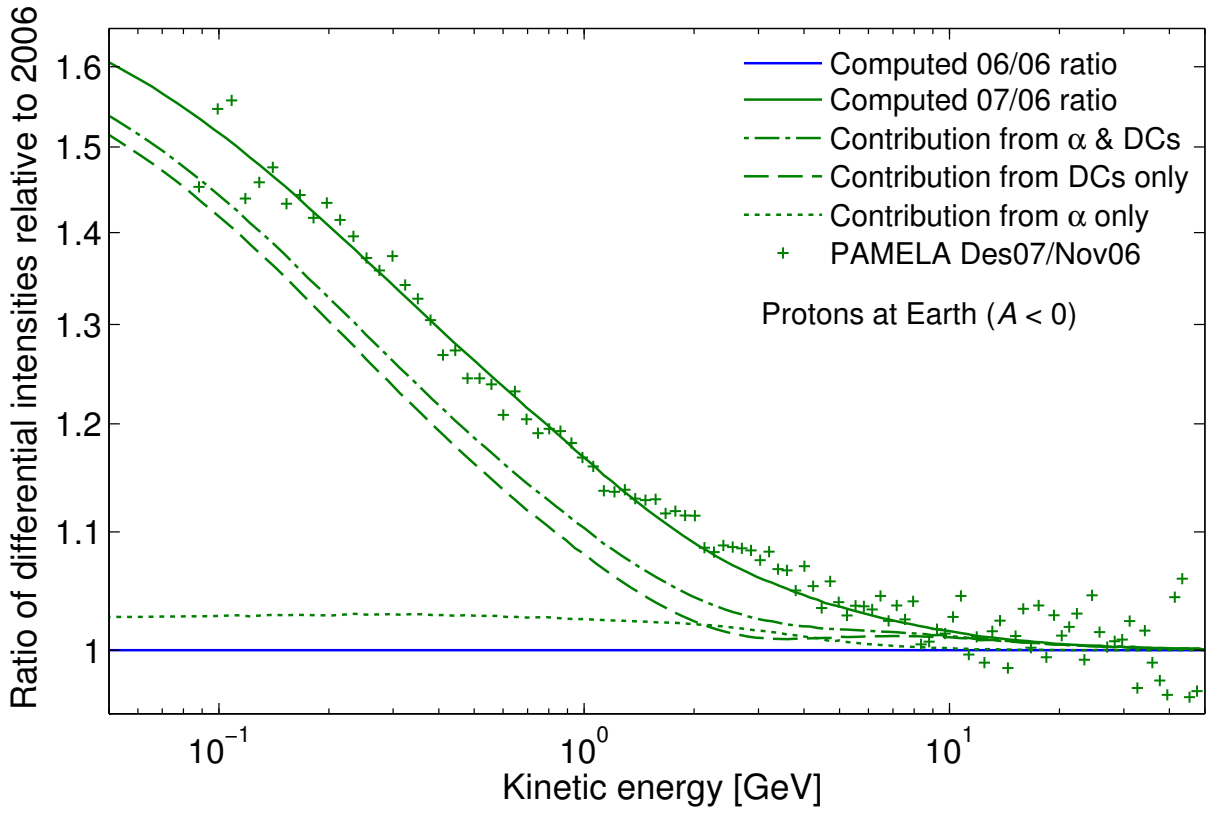

Figure 4.13: The proton energy spectra ratios of 2007 relative to 2006 (for an $A < 0$ cycle). Illustrated in this figure, by the solid green line, is the increase in intensity for 2007 across all energies (with respect to 2006) and where all modulation processes are taken into account. The PAMELA proton measurements are given by the symbols. Also shown by the dotted and dashed lines, respectively, are the relative contributing spectra levels as a result of changes in the tilt angle (α) and diffusion (DCs) only, where changes in global particle drifts due to a variation in the HMF magnitude (via Equation 3.47) are kept fixed. The dashed-dotted line represents the energy spectrum as a result of changing both the tilt angle and diffusion coefficients. The region between the solid and dashed-dotted green lines correspond to the contribution delivered by global particle drifts via Equation 3.47 between 2006 and 2007.

modulation process from the solutions obtained in Figures 4.7 to 4.10 is isolated and its contributing effects on particle intensities are studied. This is done by taking the 2006 computed spectrum as a reference spectrum at the onset of solar minimum conditions, against which the subsequent computed spectra are compared. By separately varying only the current-sheet tilt angle and diffusion coefficients, as well as a combination of these, while keeping B in Equation 3.47 unchanged, the effects from each of these modulation processes can clearly be distinguished.

Figure 4.13 gives the ratio of differential intensities for the 2007 spectrum relative to that of 2006. The solid green line represents the intensity increase, from 2006 to 2007, due to the combined contribution from changes in the current-sheet tilt angle, diffusion coefficients, and global drifts. Indicated by the dotted and dashed lines, respectively, are the individual contributing changes as a result of changes in only the current-sheet

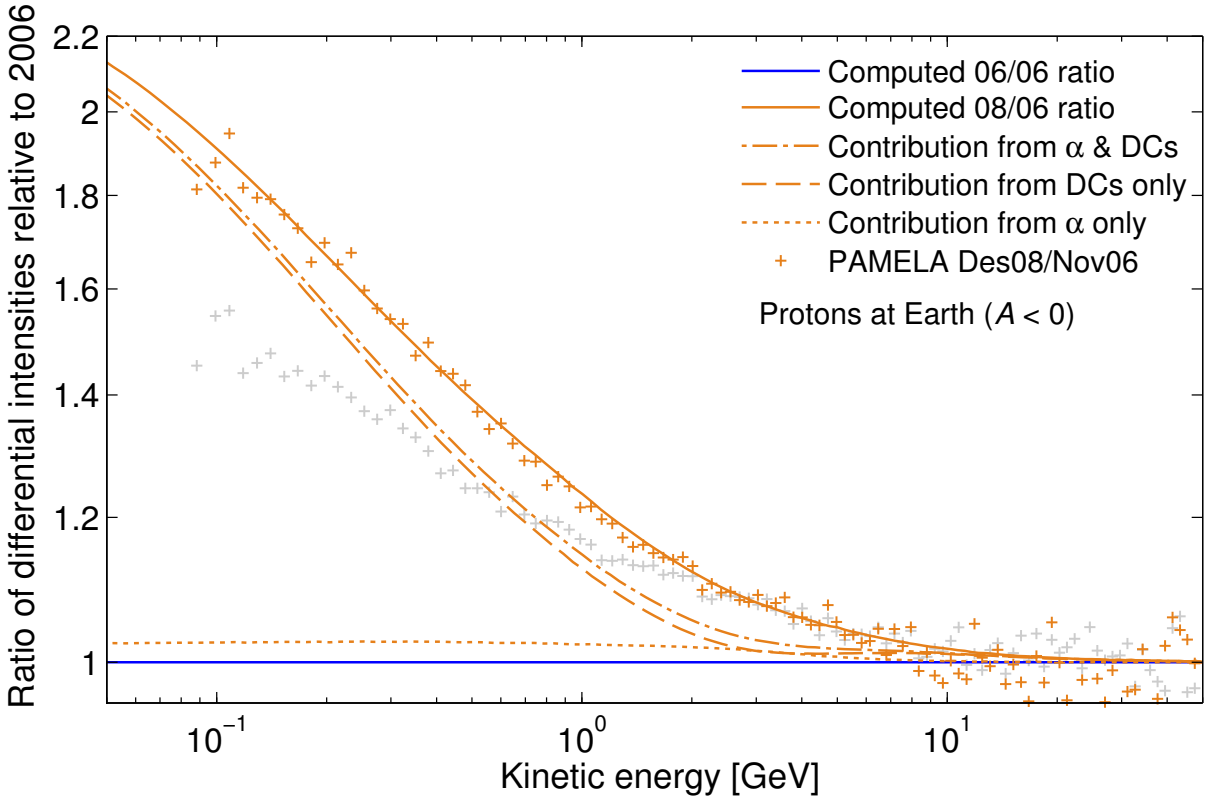

Figure 4.14: Similar to Figure 4.13, but for the proton ratios of 2008 relative to 2006. Indicated by the grey symbols are the PAMELA 2007 proton ratios relative to 2006.

tilt angle (from $\alpha = 15.7°$ to $\alpha = 14.0°$) and only the diffusion coefficients, the latter of which correspond only to a change in rigidity dependence (from $P^{0.56}$ to $P^{0.48}$) in both $\lambda_{\parallel}$ and $\lambda_{\perp}$. From these ratios it can be seen that a 10% decrease in α results in an intensity increase of $\sim 3\%$ below ~ 2 GeV, relative to the 2006 level. Considering what was found by changing the diffusion coefficients, it is evident that particle diffusion had a greater visible influence on the apparent increase in intensity from 2006 to 2007 compared to that from the tilt angle. At 1 GeV, diffusion contributed $\sim 50\%$ to the total amount of increase, while at 100 MeV the contribution was $\sim 85\%$. The dashed-dotted line gives the combined effect from the latter two processes. Finally, by adding to this the effect of global drifts via Equation 3.47, it is seen that intensities increase by $\sim 55\%$ at 1 GeV, and by $\sim 15\%$ at 100 MeV, from the level of the dashed-dotted line. The region between the solid and dashed-dotted lines consequently represents the total relative contribution delivered by global drifts due to a change in the HMF magnitude.

Figure 4.14, similar to Figure 4.13, gives the ratio of the 2008 PAMELA observations and computed spectra relative to 2006. Since the tilt angle didn't change significantly during 2008, the contribution thereof remains below $\sim 15\%$ for the time between 2006

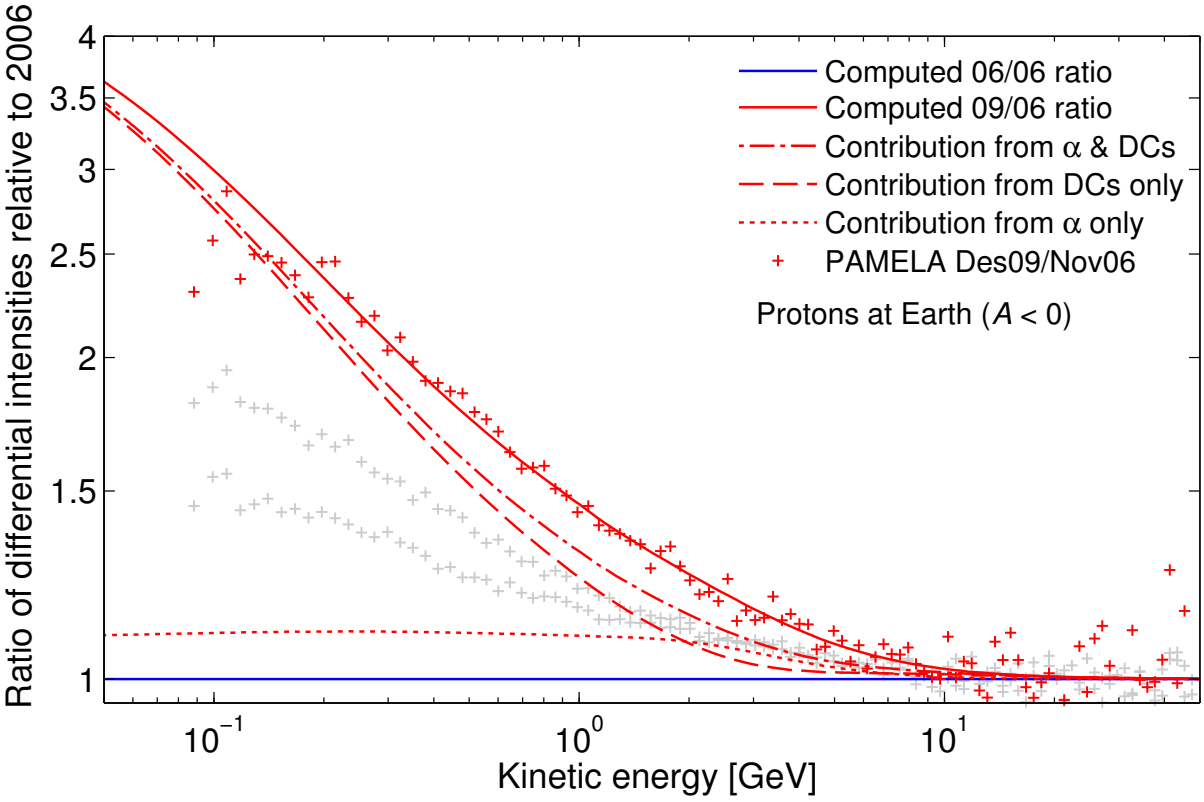

Figure 4.15: Similar to Figures 4.13 and 4.14, but for the proton ratios of 2009 relative to 2006. The grey symbols indicate the PAMELA ratios of 2007 and 2008 relative to 2006.

and 2008. Particle diffusion, with a change in rigidity dependence from $P^{0.56}$ to $P^{0.39}$ during this time (see Table 4.1), is once again primarily responsible for the majority of the intensity increase for energies below $\sim$ 1 GeV. At 1 GeV and 100 MeV, global particle drifts via κ_A (see Equation 3.47), respectively contributed $\sim$ 35% and $\sim$ 7% to the total increase in intensities. The grey symbols in Figure 4.14 represent the 2007 PAMELA ratio from Figure 4.13.

The total contributions from the various processes for 2006 to 2009 are shown in Figure 4.15, which gives the ratios of the 2009 PAMELA observations and computed spectrum relative to that of 2006. The dotted line represents the relative contribution of a $\sim 6^\circ$ decrease in the tilt angle toward the total intensity increase. Similarly, the dashed line corresponds to the relative intensity increase from particle diffusion as a result of a change in the particle MFP rigidity dependence from $P^{0.56}$ to $P^{0.28}$ (illustrated in Figure 4.12). At 1 GeV changes in the tilt angle, diffusion, and global particle drifts (via κ_A) respectively accounted for $\sim$ 25%, $\sim$ 50%, and $\sim$ 25% of the total increase in intensity. Even though, at 100 MeV, the total change in tilt angle resulted in a $\sim$ 15% intensity increase from 2006, its contribution relative to the total change is small compared to that of particle diffusion, the latter of which is responsible for more

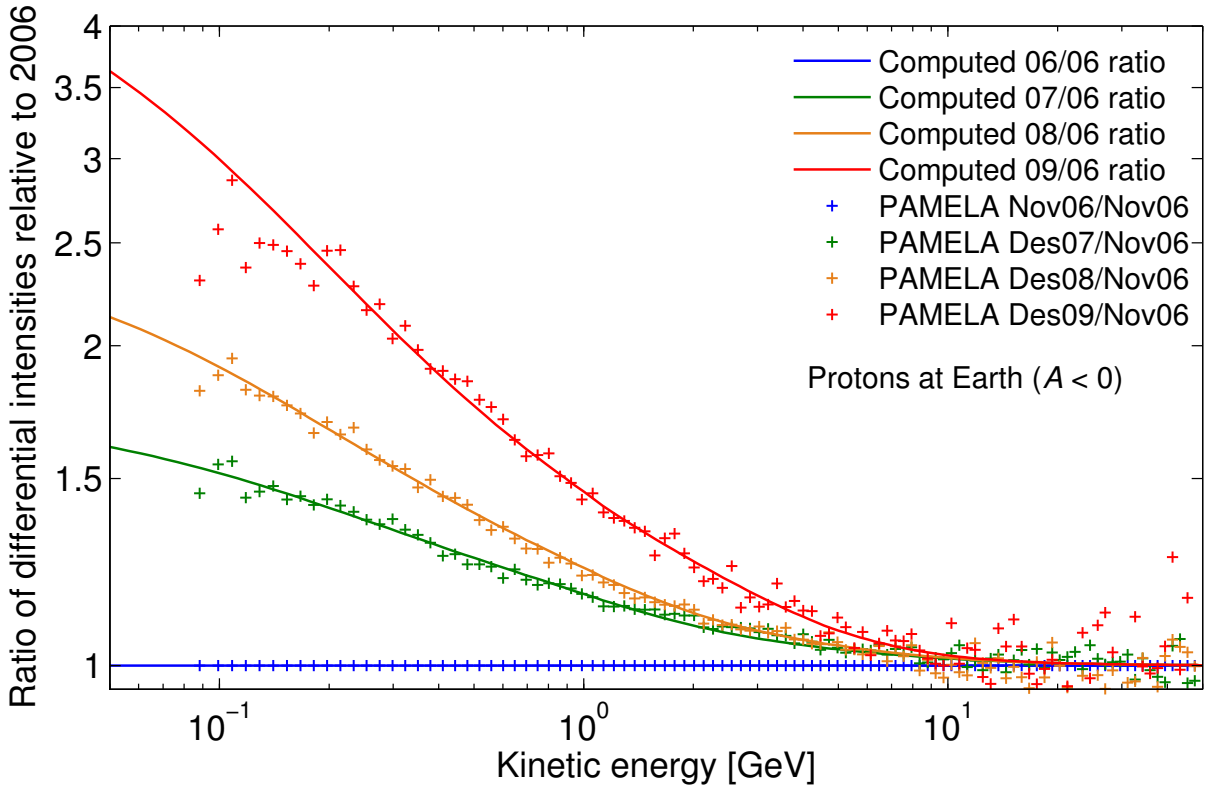

Figure 4.16: Proton ratios from the computed energy spectra of Figures 4.8 to 4.10, relative to the 2006 energy spectrum in Figure 4.7. Also shown are the corresponding PAMELA proton ratios.

than 90% of the total increase. The increase in global drifts, due to a decrease in HMF magnitude via κ_A, accounted for most of the remaining intensity increase. From these results it is clear that particle diffusion played a significant role during the recent solar minimum. However, even though this set of diffusion coefficients provide sufficient MFPs to obtain reasonable approximations to PAMELA observations, global drifts are still required in order to obtain accurate numerical solutions to observations, in contrast to what *Cliver et al.* (2011) reported. Figure 4.16 shows a graph which contains the above computed energy spectra ratios along with PAMELA observations, which serves as an additional measure of the quality and accuracy of these solutions with regard to actual particle intensities.

These relative contributions are also investigated as a function of time, from November, 2006 to December, 2009. This is shown in Figure 4.17, which give the computed differential intensities for protons at energies of 300 MeV (top panel), 600 MeV (middle panel), and 1 GeV (bottom panel) respectively. The transient effect of an increase in the tilt angle during the first half of 2008 on particle intensities is evident from these figures, which show a sudden decrease in intensity during 2008. By neglecting changes

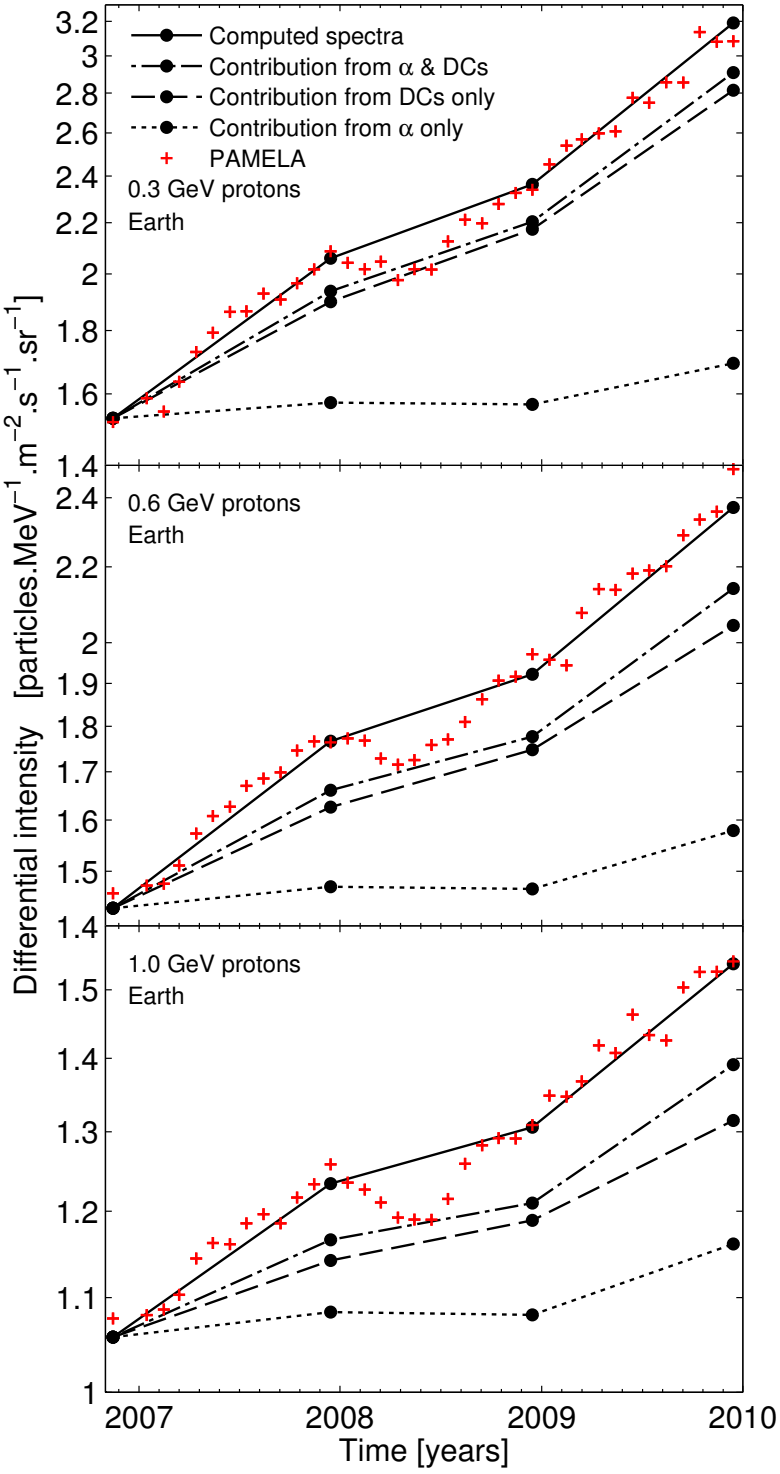

Figure 4.17: The computed proton differential intensities at 0.3 GeV (top panel), 0.6 GeV (middle panel), and 1.0 GeV (bottom panel), as function of time, from November, 2006 to December, 2009. In each of these panels only four values from the computed spectra are plotted (black dots), along with the monthly-averaged PAMELA observations. As with Figures 4.13 to 4.15, the dotted and dashed lines respectively correspond to intensity levels due to changes in only the current-sheet tilt angle and only the diffusion coefficients. The dotted-dashed line represents the combined effect from these processes, where global particle drifts, due to changes in the HMF magnitude (see Equation 3.47), are excluded. The solid line represents the total computed intensity increase from all the modulation processes combined.

in global drifts via the drift coefficient, for example, proton intensities are found to be $\sim 10\%$ lower than what was measured by PAMELA at the end of 2009. These results illustrate the importance of all the modulation processes during the period between 2006 and 2009.

4.6 Summary

The LIS for protons, as used in this study, was discussed and compared to various other LIS estimates from *Ptuskin et al.* (2006) and *Webber and Higbie* (2009), as well as to Voyager and PAMELA observations. It was found that by using a modified *Moskalenko et al.* (2002) LIS, which compared well to other LIS models, a number of conditions can be met with regard to CR observations.

This was followed by a discussion and analysis of the PAMELA proton observations from July, 2006 to December, 2009. It was found from Figure 4.4 that proton intensities reached considerable high intensities in December, 2009, especially at low energies. These high intensities can most likely be ascribed to the recent solar minimum, which displayed unusually low sunspot numbers and a noticeable drop in the average HMF, to values below 4.0 nT. A detailed discussion about the recent solar minimum was given in Section 4.4, where the sunspot numbers, the current-sheet tilt angle, the average HMF magnitude, as well as neutron monitor data from 2000 were compared to one another.

Section 4.5 started with an overview on the four sampled PAMELA spectra, from 2006 to 2009, as chosen for this study, and how the average tilt angle and HMF values are calculated for the four sampled PAMELA spectra. This was followed by detailed discussions and graphs of the computed energy spectra produced by the numerical model that accurately approximated the actual modulation conditions in the heliosphere. These yearly computed energy spectra, along with the PAMELA observations, are given in Figures 4.7 to 4.10, and are also compared to results found from other authors in Figure 4.11.

The development of the rigidity dependence of $\lambda_{\parallel}$ and $\lambda_{\perp}$ is discussed in Section 4.5.3, where it was found that, for energies below ~ 2 GeV, a dependence of $P^{0.56}$ was required to fit the 2006 PAMELA spectrum, whereas a $P^{0.28}$ dependence was required to fit the 2009 spectrum. Furthermore, the various contributions from changes in the HCS tilt angle, particle diffusion, and global particle drifts via κ_A (Equation 3.47) were investigated by considering the effect of varying each process individually. These results are given as energy spectra ratios relative to the 2006 fitted spectrum (Figures 4.13 to 4.15), and as funciton of time for different energies (Figure 4.17).

Chapter 5

Electron Modulation

5.1 Introduction

In addition to protons, the PAMELA mission also detects electrons with high precision in the energy range of interest for heliospheric modulation. Since the HMF polarity determines the drift directions of CR particles, a process in which particle charge plays an eminent role, the availability of both proton and electron observations allow for the opportunity to study charge-sign dependent modulation of CRs during the recent unusual solar minimum. By following the same approach as for protons in the previous chapter, a selection of preliminary PAMELA electron spectra is used to adjust modulation parameters in the numerical model so as to obtain accurate solutions that correspond to observed electron intensities. Such results will provide valuable insight with regard to the underlying modulation processes responsible for the observed electron intensities before and during the 2009 solar minimum.

5.2 The Local Interstellar Electron Spectrum

As with protons, knowledge of the exact shape of the electron LIS is essential for a proper study of the heliospheric modulation of Galactic CR electrons. These electrons are, however, distinctively different from protons on a number of levels. Electrons radiate synchrotron radiation, which is observed at energies between 0.1 GeV and 6.0 GeV, in the radio frequency range of ~ 0.5 MHz to 2.0 GHz (e.g. *Peterson*, 1999). Electrons are therefore the only component for which the LIS can be derived directly from the shape of the galactic polar radio spectrum (e.g. *Langner*, 2004, and *Webber and Higbie*, 2008). Even though other physical processes in the ISM also produce γ-rays and radio wavelength photons with similar energies and wavelengths than that produced by CR electrons, the diffuse continuum γ-ray emission from the galactic plane at MeV energies is, with some uncertainty, believed to originate primarily from bremsstrahlung interac-

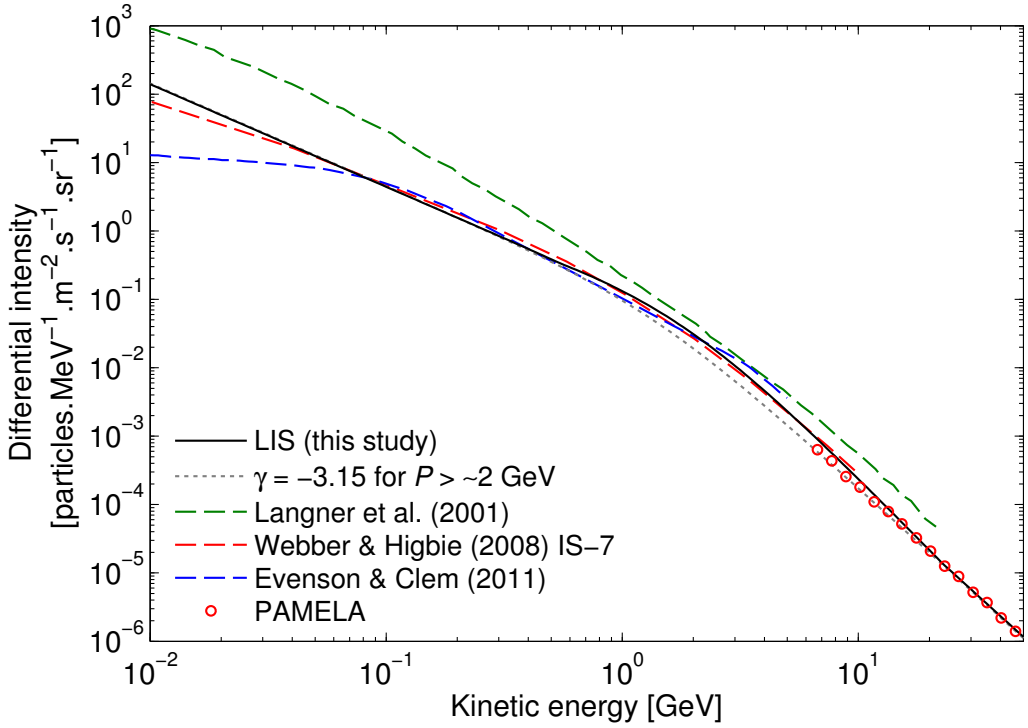

Figure 5.1: A comparison between the electron LIS used in this study (solid black) and those used/proposed by other authors, the former of which is a modified version of the IS-7 electron spectrum from *Webber and Higbie* (2008), given by the dashed red line. The proposed electron LIS models from *Langner et al.* (2001) and *Evenson and Clem* (2011) are shown by the green and blue dashed lines, respectively. At high energies the PAMELA electron intensities from November, 2006 (*PAMELA-group, private communication*), are presented by the symbols. Furthermore, the dotted grey line represents an unlikely LIS scenario where the spectral index of the electron LIS is kept fixed above $\sim$ 2 GeV at a value of $\gamma = -3.15$, while still being normalized to PAMELA data above $\sim$ 30 GeV.

tions of CR electrons with interstellar gas. The main γ-ray production mechanisms are known to be inverse Compton scattering, π^0 production, and bremsstrahlung, where the contribution from each mechanism depends on various parameters, such as interstellar electron and proton spectra, interstellar radiation and magnetic fields, gas distribution, etc. (*Strong et al.*, 2000). The dominant physical process behind γ-ray production at energies above $\sim$ 1 GeV and below $\sim$ 30 MeV remains uncertain.

At energies $\leq\sim$ 1 GeV, however, synchrotron, Compton and bremsstrahlung energy losses are relatively small, so that the galactic propagation of electrons are primarily determined by diffusion, in contrast to the nuclear components for which ionization energy loss is important at these lower energies. Apart from γ-rays and radio synchrotron photons, electron interactions in the ISM do not produce secondary particles that can be used to infer the characteristics of their propagation. Consequently, measurements of the γ-ray spectrum at low energies provide imperative constraints on electron propagation and their subsequent spectrum (see e.g. *Langner et al.*, 2001, and

Webber and Higbie, 2008).

By re-examining galactic polar radio spectrum data, *Webber and Higbie* (2008) derived a more accurate radio spectrum which was compared to that produced by electrons. They then convolved the electron spectrum directly from the single electron synchrotron emission formula for electron motion in the galactic magnetic fields in order to obtain the radio emission spectra. Finally, by using a Monte Carlo diffusion model for the propagation of electrons in a diffusive Galaxy, they calculated new electron spectra below ~ 2 GeV, which also reproduced the observed polar galactic non-thermal radio synchrotron spectrum above ~ 4 MHz (where absorption effects in the galactic disk are small). This approach allowed *Webber and Higbie* (2008) to impose new limits on the low-energy electron LIS, as well as the diffusion coefficient used in CR propagation models for electrons and protons. Figure 5.1 shows a graph in which a number of electron LIS estimates are compared to the LIS used in this study (solid black), the latter of which is a modified version of the IS-7 spectrum from *Webber and Higbie* (2008), given by the dashed red line.

The electron spectrum used in this study is essentially two power laws, which goes as $E^{-1.5}$ for $E <\sim 1$ GeV and as $E^{-3.13}$ for $E >\sim 2$ GeV. The assumed $E^{-1.5}$ dependence at lower energies is based on a study by *Nndanganeni* (2011), who used Voyager 1 electron data observed beyond the termination shock. A similar result was reported by *Caballero-Lopez et al.* (2010). The $E^{-3.13}$ dependence at higher energies is, however, obscured by an unusual region of enhanced intensities observed between ~ 0.5 GeV and ~ 20.0 GeV. The $E^{-3.13}$ dependence is therefore only visible above ~ 20 GeV. When considering the dotted grey LIS in Figure 5.1, along with PAMELA electron observations above 6 GeV (given by the symbols), the above mentioned regional intensity enhancement is quite apparent. This LIS, being normalized to PAMELA observations above ~ 30 GeV (where heliospheric modulation effects are negligible), has a spectral index of $\gamma = -3.15$. According to *Adriani et al.* (2011c), who conducted a study of electron measurements made by PAMELA during July, 2006 to January, 2010, between 1 GeV and 625 GeV, a spectral index of $\gamma = -3.18 \pm 0.05$ is required for electrons above 30 GeV. For energies below ~ 30 GeV, where modulation effects become increasingly important and should account for a noticeable decrease in CR intensity, the observed electron intensities from PAMELA are slightly above the dotted grey LIS. Since no process in the heliosphere is able to accelerate CR particles up to such high energies, it is assumed that the emergence of such a "bump" in the observations could most likely be ascribed to a process or source effect in the interstellar medium. This enhancement

has therefore been incorporated into the LIS used in this study, which is given by

$$j_{LIS,e^-} = \begin{cases} \dfrac{0.132}{\beta^2}\left[\dfrac{\left(\frac{E}{E_L}\right)^{1.6}+\left(\frac{E_{k_1}}{E_L}\right)^{1.6}}{1+\left(\frac{E_{k_1}}{E_L}\right)^{1.6}}\right]^{\frac{b_1-a_1}{1.6}}\left(\dfrac{E}{E_L}\right)^{a_1} & \text{for } 0.55\,\text{GeV} \leq E \leq 22.70\,\text{GeV} \\ \dfrac{0.118}{\beta^2}\left[\dfrac{\left(\frac{E}{E_L}\right)^{3.0}+\left(\frac{E_{k_2}}{E_L}\right)^{3.0}}{1+\left(\frac{E_{k_2}}{E_L}\right)^{3.0}}\right]^{\frac{b_2-a_2}{3.0}}\left(\dfrac{E}{E_L}\right)^{a_2} & \text{elsewhere,} \end{cases} \tag{5.1}$$

with $E_L = 1\,\text{GeV}$ taking care of the units, and where $E_{k_1} = 1.7\,\text{GeV}$, $E_{k_2} = 1.4\,\text{GeV}$, $a_1 = -1.00$, $b_1 = -3.54$, $a_2 = -1.50$, and $b_2 = -3.13$ are parameters that determine the shape of the LIS.

The LIS in Equation 5.1 is quite similar to its original counterpart across all energies, with regard to absolute intensity and shape, evident from Figure 5.1. Even though the LIS derived by *Langner et al.* (2001; dashed green), using polar synchrotron data as well as electron observations from Pioneer 10 as constraints, is consistent with the LIS calculated by *Peterson* (1999) and has been considered a reasonable LIS for CR electrons, it is significantly higher (by a factor of ~ 8 below 100 MeV) than the LIS used in this study, as well as the other LIS models. Clearly it should also be re-normalized to the PAMELA observations at high energies. The dashed blue line represents the recently proposed 2009 electron LIS from *Evenson and Clem* (2011), who claim to have measured a complete electron spectrum between 20 MeV and 5 GeV for the first time during the 2009 flight of the balloon borne instrument LEE, as a result of the low level of solar modulation in this time. At energies above ~ 100 MeV the *Evenson and Clem* (2011) electron LIS corresponds to both the original and modified *Webber and Higbie* (2008) LIS. By taking into account the above discussed LIS models, as well as PAMELA electron data, it evidently follows from Figure 5.1 that the electron LIS used in this study is most reasonable. However, this LIS will have to be tested against Voyager 1 observations once the spacecraft is beyond the heliopause.

5.3 The PAMELA Electron Spectra

As previously mentioned, the combination of devices that comprises the PAMELA detector (discussed in Section 2.9) makes it possible to conduct high precision studies of charged CRs over a wide range of energies (100 MeV to 100's GeV), with satisfactory statistics (*Mocchiutti et al.*, 2011). Even though measurements of the electron energy spectrum, among other, forms part of one of PAMELA's primary scientific goals, which

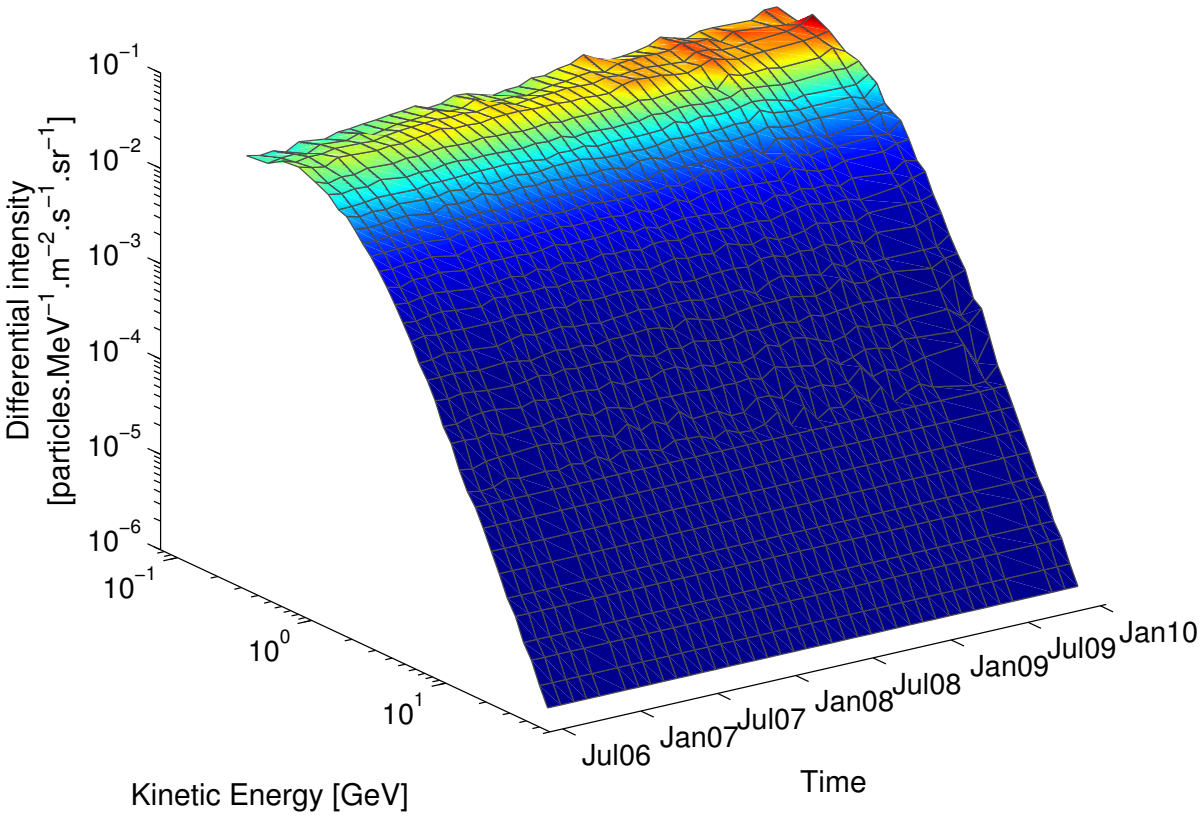

Figure 5.2: An overview of how the electron intensities developed from July, 2006, to December, 2009, according to PAMELA observations. This surface is constructed by interpolating between monthly energy spectra averages. Data obtained from the *PAMELA-group* (*private communication*).

is to search for exotic phenomena, such as dark matter particle annihilations, these observations at low energies can significantly contribute to studies of CR modulation in the heliosphere, especially charge-sign dependent modulation.

In a study of the high-energy electron component (1 GeV to 625 GeV), *Adriani et al.* (2011c) presented the results of a selection of more than 3.7×10^5 electron measurements made by PAMELA between July, 2006 and January, 2010. Figure 5.2 gives a graphical overview of the low-energy CR electron measurements from PAMELA, interpolated from monthly averages. This plot illustrates how electron intensities have developed from July, 2006 to December, 2009, where the most apparent intensity increase during this time is highlighted by the varying color-coded region below ~ 2 GeV.

Figure 5.3 gives a similar plot of the observed electron energy spectra, where the color-bar indicates the progress in time. Evident from this figure is that the electron spectrum above ~ 12 GeV is assumed as a ~ 4-year average spectrum at these energies, computed from the monthly-averaged electron spectra from 2006 to 2009.

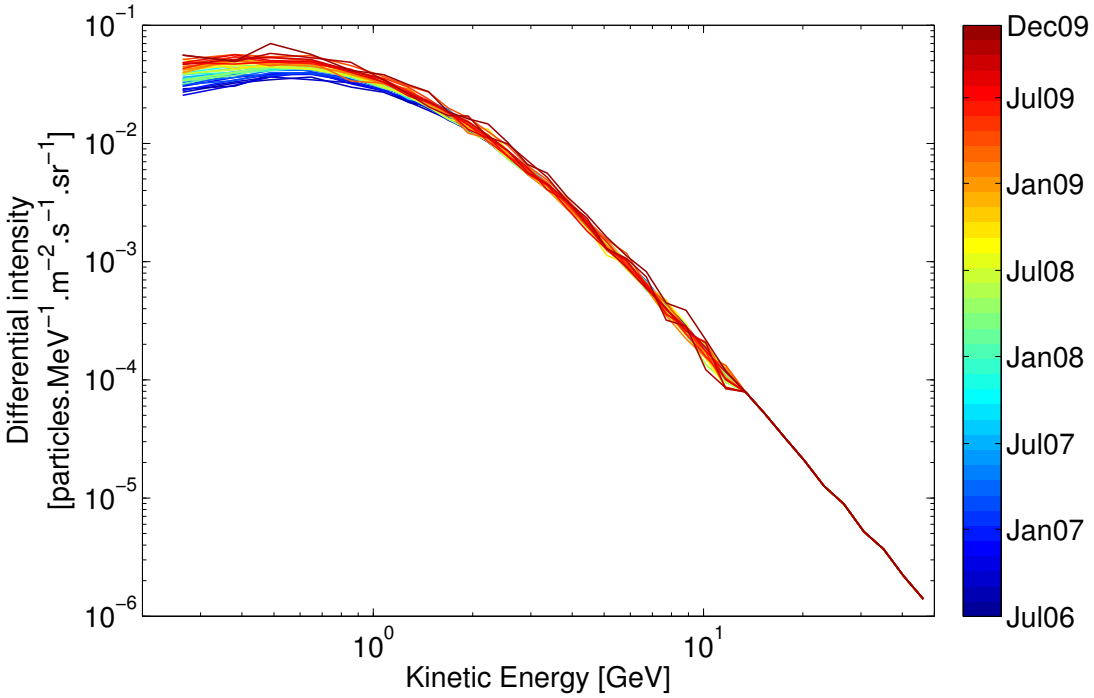

Figure 5.3: The colored curves indicate how the electron spectra developed as particle intensities approached the period of minimum CR modulation, from July, 2006 (blue), to December, 2009 (red). The region between the blue and red curves indicates the spread in electron intensities during this time. A single averaged spectrum has been assumed for particle intensities above $\sim$ 12 GeV for each month. Data obtained from the *PAMELA-group* (*private communication*).

The data available for this study shows that electron intensities also reached a maximum at the end of 2009. Compared to protons (Figure 4.3), the total increase in electron intensities during this time is noticeably smaller. It is seen from Figure 5.3 that the differential intensities increased by a factor of $\sim$ 2, from $\sim$ 3.3×10^{-2} particles.m^{-2}.s^{-1}.sr^{-1}.MeV^{-1} in July, 2006, in the region of the peak ($\sim$ 600 MeV), up to a maximum intensity of $\sim$ 7.0×10^{-2} particles.m^{-2}.s^{-1}.sr^{-1}.MeV^{-1} at a lower energy, around 500 MeV. As for protons, the energy at which the maximum intensity occurs (peaks) has shifted to lower energies from 2006 to 2009. In the energy range between $\sim$ 1 GeV and $\sim$ 10 GeV, the intensities increased by an average factor of 1.4 from July, 2006 to the end of 2009. These features are further illustrated in Figure 5.4, which gives the monthly-averaged spectra ratios for consecutive months from July, 2006 to December, 2009, relative to the July, 2006 spectrum. The same as with protons, electron intensities also experienced the largest increase at lower energies.

As a result of the energy distribution and the apparent large intensity fluctuations, the electron spectra ratios in Figure 5.4 don't display a clear and steady incremental development as the proton ratios do in Figure 4.4. It follows that in the energy range

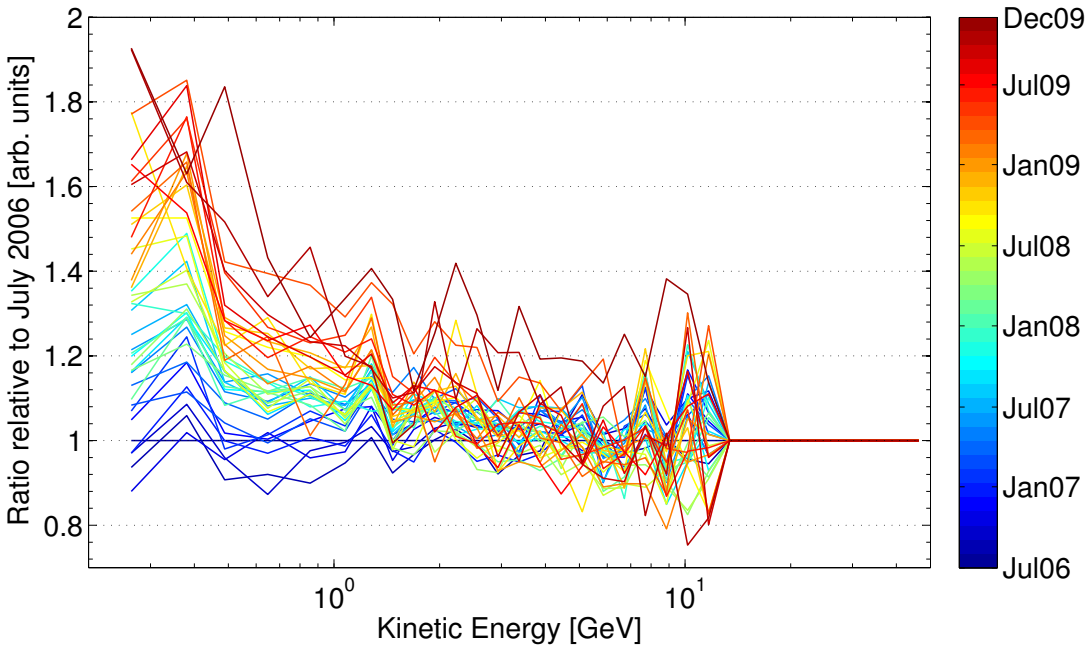

Figure 5.4: Ratios of consecutive PAMELA monthly-averaged electron spectra with respect to July, 2006. The color-bar indicates the time that corresponds to the electron ratios. Data obtained from the *PAMELA-group* (*private communication*).

between ~ 5 GeV and ~ 12 GeV, electron observations are distributed within a range of $\sim 20\%$ above and below the July, 2006 level. Even though significant fluctuations are still present, the electron intensities for consecutive months display a notable increase below ~ 5 GeV. The distribution in the measurements can be ascribed to systematic uncertainties as a result of instrumental effects such as selection efficiencies and energy determination (*Adriani et al.*, 2011c). This illustrates the difficulty involved in obtaining accurate electron observations.

5.4 Modelling the PAMELA Electron Spectra

5.4.1 A Sample Selection of PAMELA Spectra

Following the same procedure as for protons, the aim is to simulate the propagation and modulation of CR electrons in a heliosphere for which the modulation conditions are, on average, representative of the actual modulation conditions that prevailed during the recent solar minimum. Even though a vast range of monthly-averaged spectra is available, only an intermittent sample selection of electron spectra between July, 2006 and December, 2009, is considered. By once again taking yearly averages for the current-sheet tilt angle, as well as for the HMF (whereas for the axis-symmetrical so-

lar wind a single radial and polar angle profile is assumed), the required modulation conditions can be successfully reproduced.

A similar sample selection of electron spectra has been made as for protons (see Section 4.5.1). However, due to large electron intensity fluctuations that appear in certain months, minor changes were made to the selection of the 2008 and 2009 electron spectra. The November and December monthly-averaged spectra were chosen for the years 2006 and 2007, respectively. For 2008, the November spectrum was chosen, whereas for 2009, due to significant fluctuations in the data, an average spectrum was calculated from the monthly spectra of October, November, and December. These selected spectra are from hereon referred to as the 2006, 2007, 2008, and 2009 spectra.

Apart from minor differences for the 2008 and 2009 spectra, the sampled electron spectra are taken around the same time than the proton sampled spectra. Since, over the timespan of a year, the differences in the 2008 and 2009 spectra contribute to insignificant tilt angle and HMF variations, the effect on the modulated spectra from such changes are considered negligible. Consequently, the average current-sheet tilt angle and B_e values for the electron spectra are similar to that used for protons, i.e. for the consecutive years, from 2006 to 2009, the average tilt angle values are $15.7°$, $14.0°$, $14.3°$, and $10.0°$ respectively, with corresponding average B_e values of 5.05 nT, 4.50 nT, 4.25 nT, and 3.95 nT (see Section 4.5.1 for a detailed discussion on how these averages are calculated).

With these parameters incorporated into the numerical model, along with the variation in the TS, the diffusion coefficients were systematically adjusted while still adequately adhering to conditions imposed on particle MFPs according to the theory, in order to obtain results that give appropriate fits to the selection of electron spectra from PAMELA. These results are discussed in the following sections.

5.4.2 The Numerically Reproduced PAMELA Spectra

Figure 5.5 gives the electron differential intensity spectrum measured by PAMELA (symbols) during November, 2006, overlaid by the computed 2006 spectra at heliocentric distances of 1 AU, 30 AU, 60 AU, and 90 AU, in the equatorial plane for an $A < 0$ polarity cycle. Since the PAMELA electron data available for this study is limited to energies down to 250 MeV, the modulation modelling was limited to an energy range of 100 MeV to 50 GeV. During the preceding year, the HCS had an average tilt angle of $\alpha = 15.7°$ and the HMF at Earth had an average field magnitude of $B_e = 5.05$ nT. It is evident from Figure 5.5 that the computed 2006 spectrum at Earth accurately reproduces the observed electron intensities from PAMELA. The electron modulation features shown here, for example the increases in intensity below 200 MeV to 300 MeV

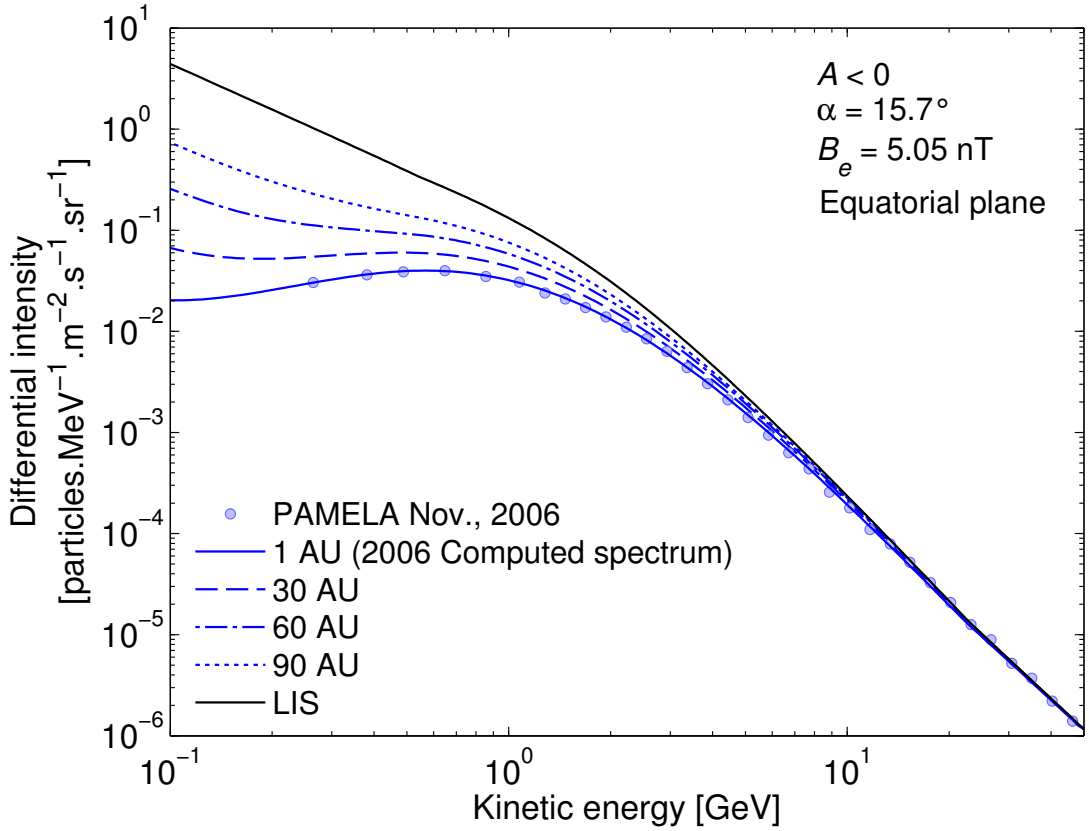

Figure 5.5: The PAMELA monthly-averaged electron observations for November, 2006, with the computed spectra overlaid. The dotted, dashed-dotted, and dashed lines correspond to the modulated intensities in the equatorial plane at 90 AU, 60 AU, and 30 AU respectively, together with the LIS (solid black) at 120 AU. The modelled spectra are for an $A < 0$ cycle, where $\alpha = 15.7°$ and $B_e = 5.05$ nT.

at Earth and with radial distance, are consistent with what is known for electron modulation (see e.g. *Potgieter*, 1996).

At energies above $\sim$ 30 GeV, where the effects of heliospheric modulation can be neglected, the electron LIS is normalized to the PAMELA observations with a spectral index of $\gamma = -3.13$. At $\sim$ 20 GeV the electron LIS starts to deviate slightly from this spectral index in order to account for the electron intensity levels measured by PAMELA between $\sim$ 4 GeV and $\sim$ 20 GeV. With this LIS, the modulated spectrum at Earth for 1 GeV electrons, although just a mere factor $\sim$ 1.2 below the LIS, corresponds well to PAMELA observations. Furthermore, for 1 GeV electrons at Earth, heliospheric modulation accounts for an intensity decrease of a factor of $\sim$ 4 relative to the LIS. The corresponding intensities for this energy at 30 AU, 60 AU, and 90 AU, are factors of $\sim$ 3.0, $\sim$ 2.2, and 1.7, respectively, lower than the LIS. The observed and computed spectra reach a local maximum around 600 MeV before intensities start decreasing toward the characteristic turning point situated around 100 MeV

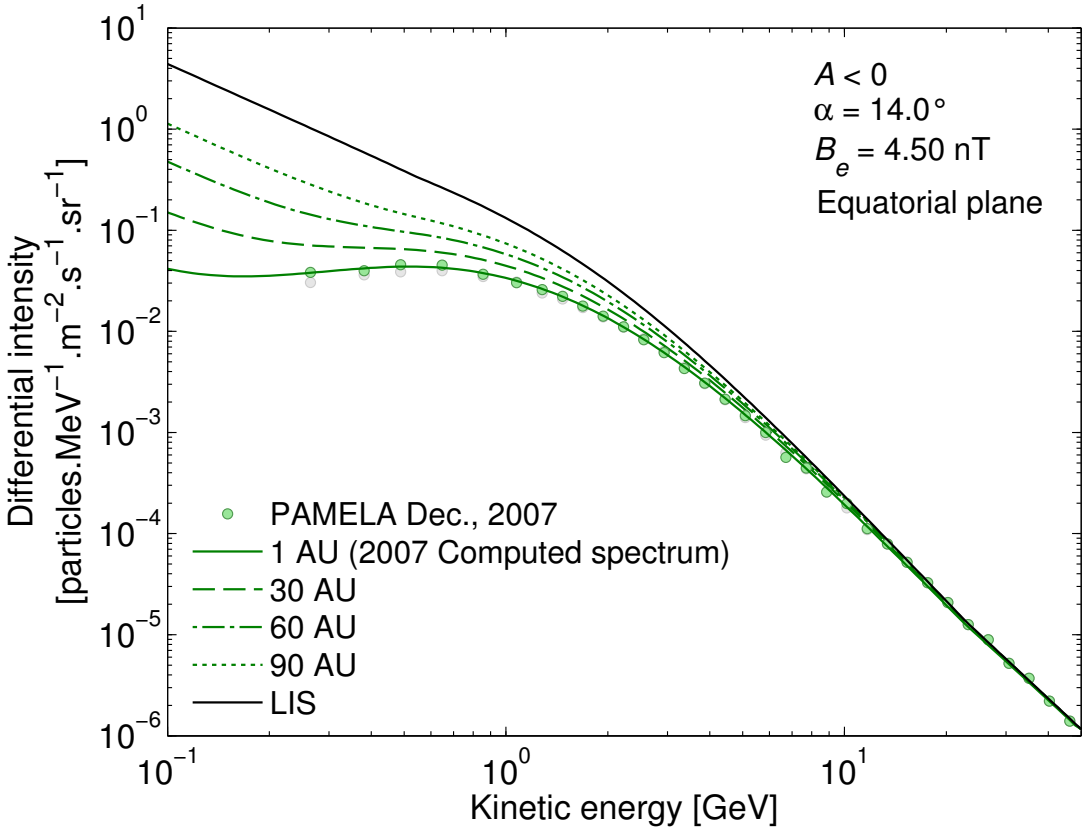

Figure 5.6: Similar to Figure 5.5, but for the December, 2007, PAMELA electron spectrum with the corresponding computed spectra overlaid, with $\alpha = 14.0°$ and $B_e = 4.50$ nT. For comparison, the light-grey data points correspond to the 2006 PAMELA spectrum shown in Figure 5.5.

at Earth, but at higher energies for larger radial distances. At this local maximum, which, in terms of the available PAMELA electron data, is also the global maximum for electron observations during this period, the differential intensity for electrons is $\sim 4 \times 10^{-2}$ particles.m^{-2}.s^{-1}.sr^{-1}.MeV^{-1}.

The December, 2007, PAMELA electron spectrum is presented in Figure 5.6, for which the tilt angle and the average HMF at Earth had average values of $\alpha = 14.0°$ and $B_e = 4.50$ nT, respectively, during the preceding year. Apart from minor deviations above ~ 7 GeV and below ~ 700 MeV, the overlaid 2007 computed spectrum at Earth gives a proper representation of the PAMELA observations. Also given by the grey data points are the November, 2006 electron measurements from Figure 5.5. For energies above ~ 2 GeV the 2007 spectrum remain unchanged, while at lower energies intensity increases not more than a factor of ~ 1.35 were observed. From PAMELA's observations, electron intensities at Earth increased by $\sim 30\%$ during 2007, reaching a local maximum intensity of $\sim 5 \times 10^{-2}$ particles.m^{-2}.s^{-1}.sr^{-1}.MeV^{-1} around 550 MeV. The changes in the electron spectrum were accurately reproduced by carefully adjust-

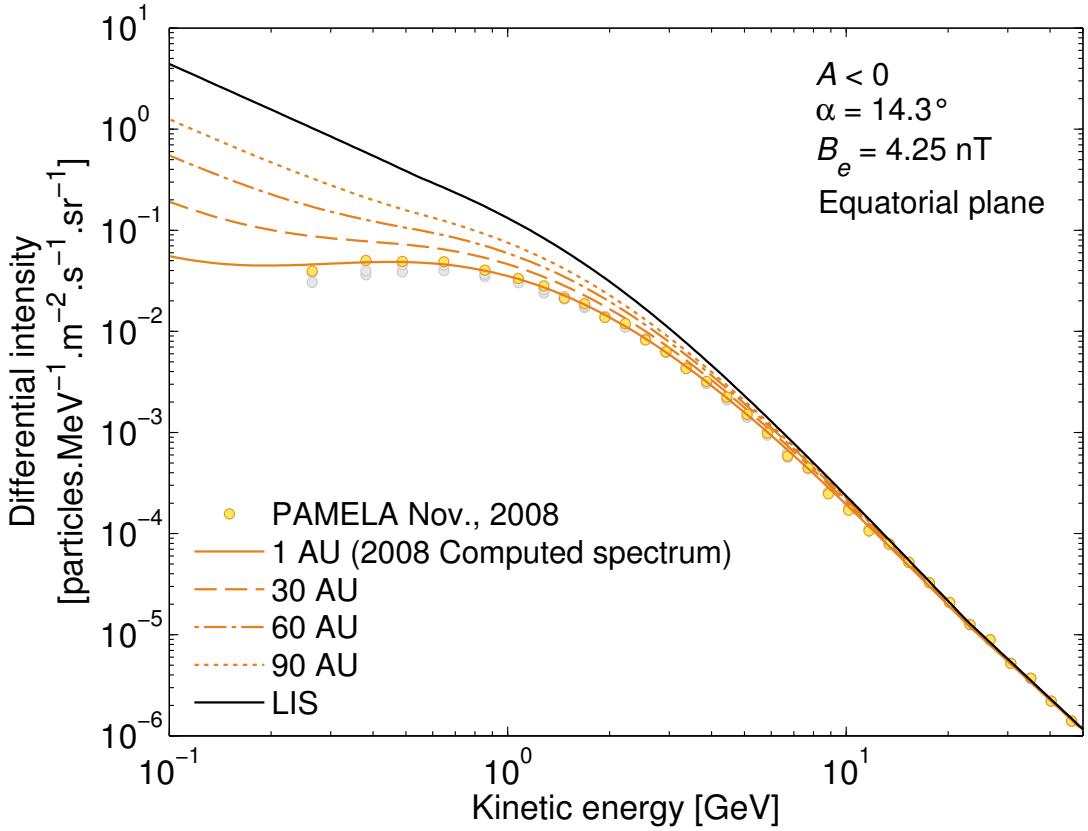

Figure 5.7: Similar to Figure 5.5 and Figure 5.6, but for the November, 2008, PAMELA spectrum, where the light-grey data points represent the 2006 and 2007 PAMELA spectra, as shown in the previous figures. Here $\alpha = 14.3°$ and $B_e = 4.25$ nT.

ing the rigidity dependence of the particle MFPs (shown in the next section), along with the assumed changes in α and B_e.

Figure 5.7 shows the observations for the observed November, 2008 spectrum. Similar to the 2006 and 2007 spectra, the 2008 computed spectrum accurately represents observations, with small deviations at high ($>\sim 7$ GeV) and low ($<\sim 700$ MeV) energies. As was the case for the 2007 spectrum, electron intensities increased noticeably only below ~ 2 GeV during 2008, where the largest increase of $\sim 15\%$ appeared around 500 MeV.

The highest observed electron spectrum during the recent solar minimum (from available data) was measured at the end of 2009, where intensities reached levels of $\sim 6 \times 10^{-2}$ particles.m^{-2}.s^{-1}.sr^{-1}.MeV^{-1} also at ~ 500 MeV. Due to significant fluctuations in the December, 2009, electron spectrum, an average spectrum was calculated from the October, November, and December monthly spectra of the same year.

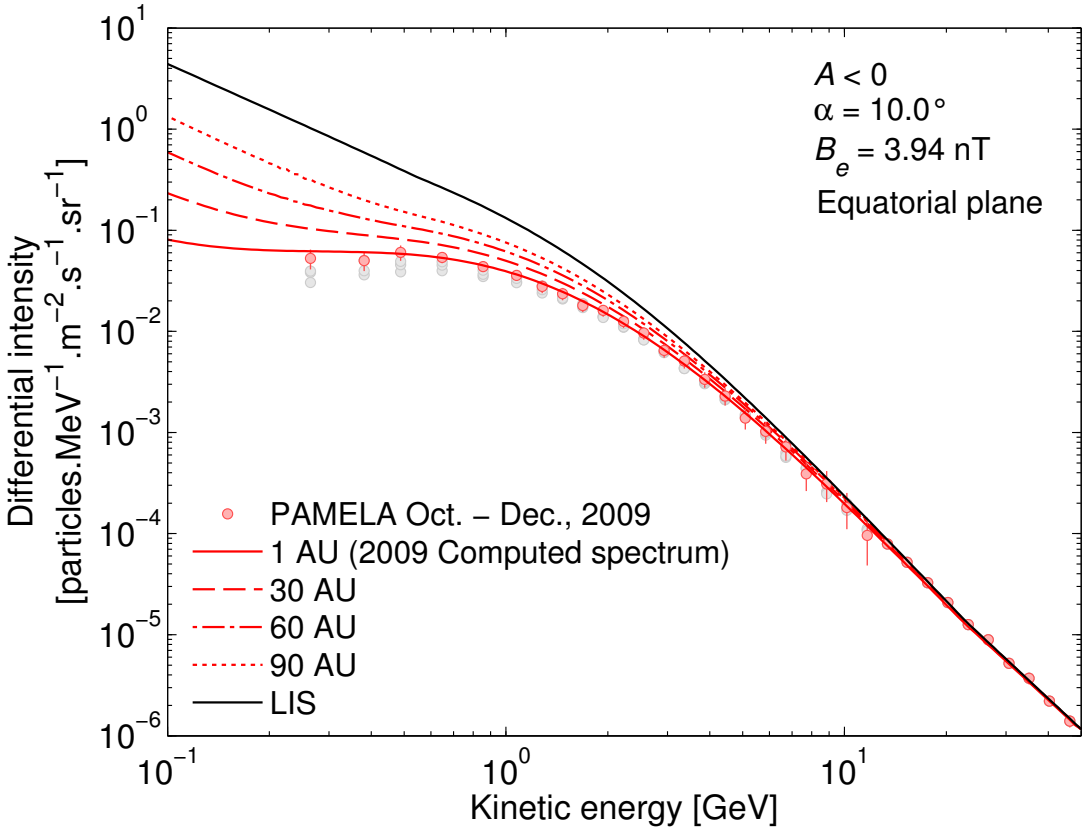

Figure 5.8: Similar to Figure 5.5 and Figure 5.6, but for the average of the October, November, and December, 2009, PAMELA electron spectra. The average from these spectra was taken due to a considerable amount of fluctuations present in the December, 2009, observed spectrum. The light-grey data points correspond to the 2006, 2007, and 2008 spectra. For these computations, $\alpha = 10.0°$ and $B_e = 3.94$ nT.

This three-month averaged spectrum, shown in Figure 5.8 (along with the computed spectra), considerably reduced the fluctuations in intensities observed in these spectra. The uncertainty in intensities during this time is evident from the comparatively larger error-bars at energies below ~ 12 GeV, of the order of $\sim 50\%$ around 10 GeV, and $\sim 20\%$ around 300 MeV. For the observed spectra in Figures 5.5 to 5.7, the corresponding error bars are small enough to be neglected.

It is readily observed from the measurements in Figure 5.8 that electron intensities experienced increases across the lower energy range up to 5 GeV during 2009. With the necessary change in rigidity dependence of the particle MFPs, and by using an average tilt angle and HMF magnitude at Earth of $10°$ and 3.94 nT, respectively, the 2009 PAMELA electron spectrum was once again reproduced with the numerical model. Overall, between November, 2006, and December, 2009, electron intensities increased by a factor of ~ 1.7 in the region of the characteristic local maximum, at energies around 500 MeV.

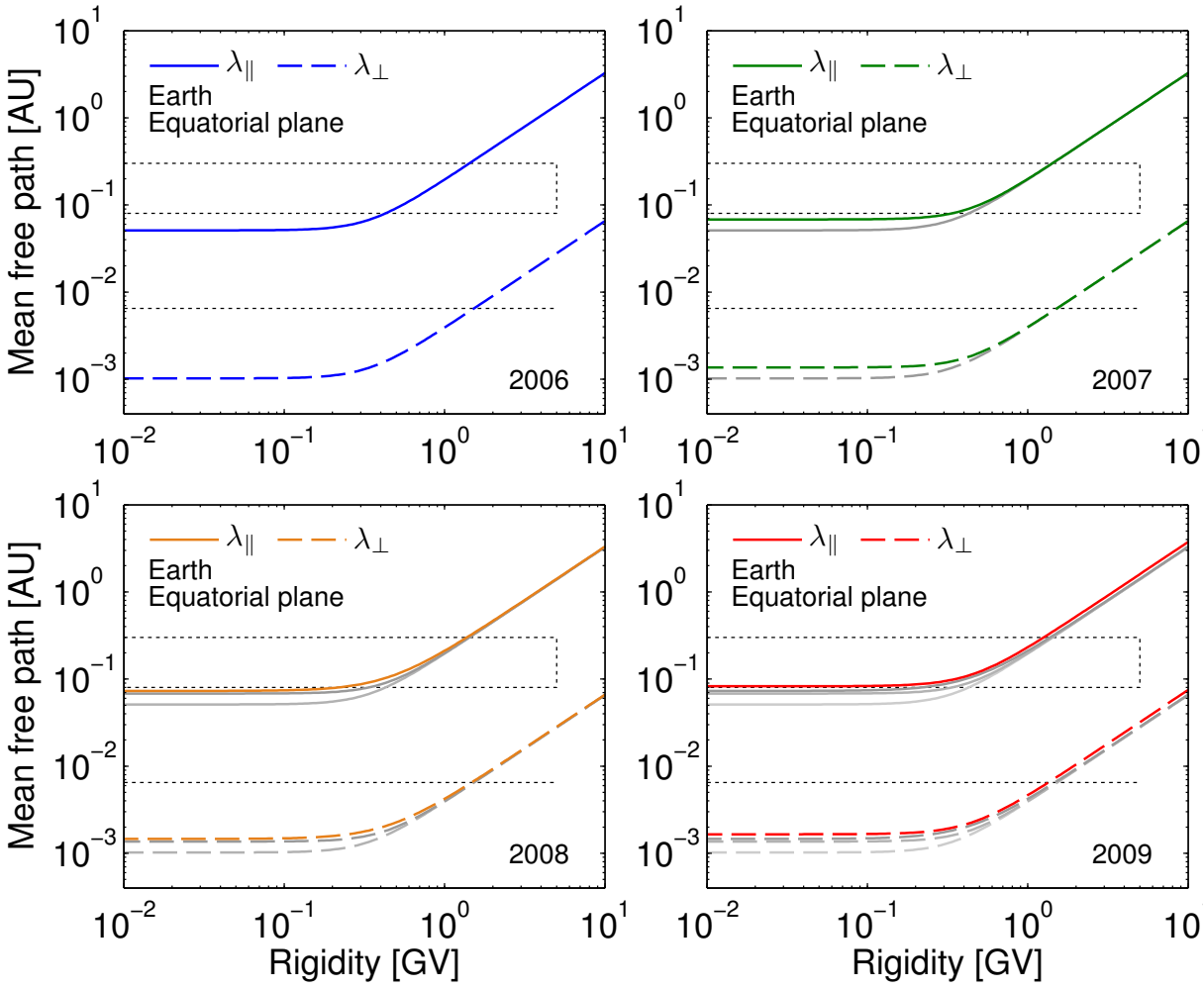

Figure 5.9: Rigidity dependencies for the parallel and perpendicular ($\lambda_{\perp,r}$ and $\lambda_{\perp,\theta}$) MFPs of electrons at Earth in the equatorial plane. These panels illustrate how the rigidity dependence for the MFPs was required to change from 2006 to 2009 in order to obtain the computed spectra of Figures 5.5 to 5.8. The grey lines correspond to the MFPs of the prior years. The perpendicular MFP is scaled by 2% of the parallel MFP. See Section 3.3 for a detailed discussion on particle MFPs.

5.4.3 Development of the Electron Rigidity Dependence

By using the same line of reasoning that has been assumed for protons (see Section 4.5.3), it can be concluded from discussions in the above sections that electron MFPs, in particular at low rigidities, also increased during the recent solar minimum. Such an increase in the MFPs can be confirmed from the computed spectra in Figures 5.5 to 5.8, for which the rigidity dependence of the MFPs (parallel and perpendicular to the average magnetic field) is changed so as to obtain larger particle MFPs for consecutive years below ~ 500 MV. Through the implementation of such changes the developing increase in electron intensities, from 2006 to 2009, were accurately reproduced.

Table 5.1: Summary of best-fit parameters used to produce the 2006 to 2009 computed electron spectra (see Equations 3.30 to 3.35 and Equation 3.47).

Parameter	**2006**	**2007**	**2008**	**2009**
α [deg]	15.7	14.0	14.3	10.0
B_e [nT]	5.05	4.50	4.25	3.94
$\kappa_{\parallel,0}$ [10^{20} cm^2.s^{-1}]	1482	1342	1345	1370
$\kappa^0_{\perp,r}$, $\kappa^0_{\perp,\theta}$	0.02	0.02	0.02	0.02
$\kappa_{A,0}$	1.0	1.0	1.0	1.0
a	0.00	0.00	0.00	0.00
b	1.23	1.23	1.23	1.23
c	3.0	3.0	2.3	2.7
d	3.0	3.0	3.0	3.0
$P_{A,0}$	$\frac{1}{\sqrt{10}}$	$\frac{1}{\sqrt{10}}$	$\frac{1}{\sqrt{10}}$	$\frac{1}{2\sqrt{10}}$
P_k [GV]	0.34	0.43	0.45	0.45

Figure 5.9 depicts graphs of how the rigidity dependence for $\lambda_\parallel$ (solid) and $\lambda_\perp$ (in the radial and polar directions; dashed) at Earth were required to change in order to reproduce PAMELA observations. Apart from a small increase in absolute value for 2009, in order to account for increased fluctuations and the slightly higher intensities during this time, the rigidity dependence slope of $P^{1.23}$ is kept unchanged above ~ 1 GV. For rigidities below ~ 200 MV the parallel and perpendicular electron MFPs are assumed to be rigidity independent.

The rigidity dependence for the parallel and perpendicular electron MFPs during 2006 are given in the top left panel of Figure 5.9. Here both MFPs are constant at 5×10^{-2} AU and 1×10^{-3} AU, respectively, for low rigidities, up to the bend at around 300 MV, where the MFPs transition occurs into the $P^{1.23}$ dependence. At low rigidities (< 300 MV), $\lambda_\parallel$ and $\lambda_\perp$ are below the Palmer consensus region (*Palmer*, 1982), but intersect it around around ~ 1 GV and 1.3 GV, respectively. For the 2007 computed spectrum (top right) the MFPs have increased by a factor of ~ 1.4 below ~ 200 MV along with a corresponding shift in the bend, which now occurs at a slightly higher rigidity of ~ 400 MV. This was followed by a comparatively smaller increase during 2008 (bottom left). The bottom right panel of Figure 5.9 gives the $\lambda_\parallel$ and $\lambda_\perp$ MFPs required to obtain an accurate representation to the PAMELA electron spectrum at the end of 2009, together with the MFPs used for the prior years (grey curves). During 2009, $\lambda_\parallel$ and $\lambda_\perp$ reached maximum values of $\sim 8 \times 10^{-2}$ AU and $\sim 1.7 \times 10^{-3}$ AU, respectively, below ~ 200 MV. Evidently, the electron MFPs at low rigidities increased by a notable 60% between 2006 and 2009, while still in reasonable accord with the Palmer

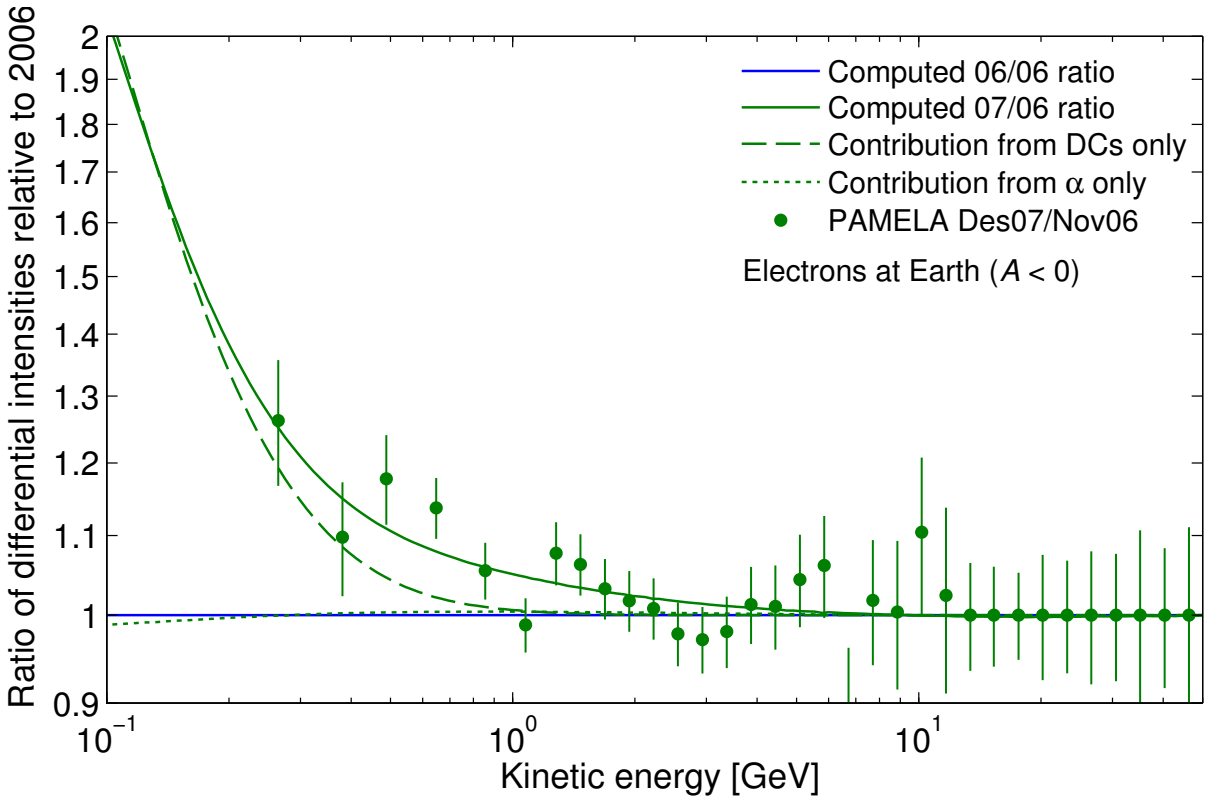

Figure 5.10: The electron energy spectra ratios of 2007 relative to 2006 (for an $A < 0$ cycle). The solid green line represents is the increase in intensity for 2007 across all energies, with respect to 2006, where all modulation processes are taken into account. The PAMELA electron measurements are given by the symbols (along with the appropriate error bars). Also shown by the dotted and dashed lines, respectively, are the relative contributing levels as a result of changes in the tilt angle (α) and diffusion (DCs) only, where changes in global particle drifts due to variations in the HMF magnitude (via Equation 3.47) are kept fixed. The region between the solid and dashed green lines correspond to the contribution yielded by global particle drifts via Equation 3.47 between 2006 and 2007.

consensus values.

Table 5.1 gives an overview of all the modulation parameters related to the yearly computed electron spectra from 2006 to 2009 (as they appear in Equations 3.30 to 3.35 and Equation 3.47). See also Sections 3.3 and 3.4 for discussions with regard to these parameters. A similar overview was given for protons in Table 4.1.

5.4.4 Contribution from Various Modulation Processes

In order to determine the effect that each major modulation process had on the development of electron intensities during the recent solar minimum (according to the adopted theoretical models discussed in Chapter 3), as well as to ascertain how well the computed spectra agree with PAMELA observations, the energy spectra ratios for consecutive years are investigated relative to 2006. By eliminating the progressive changes

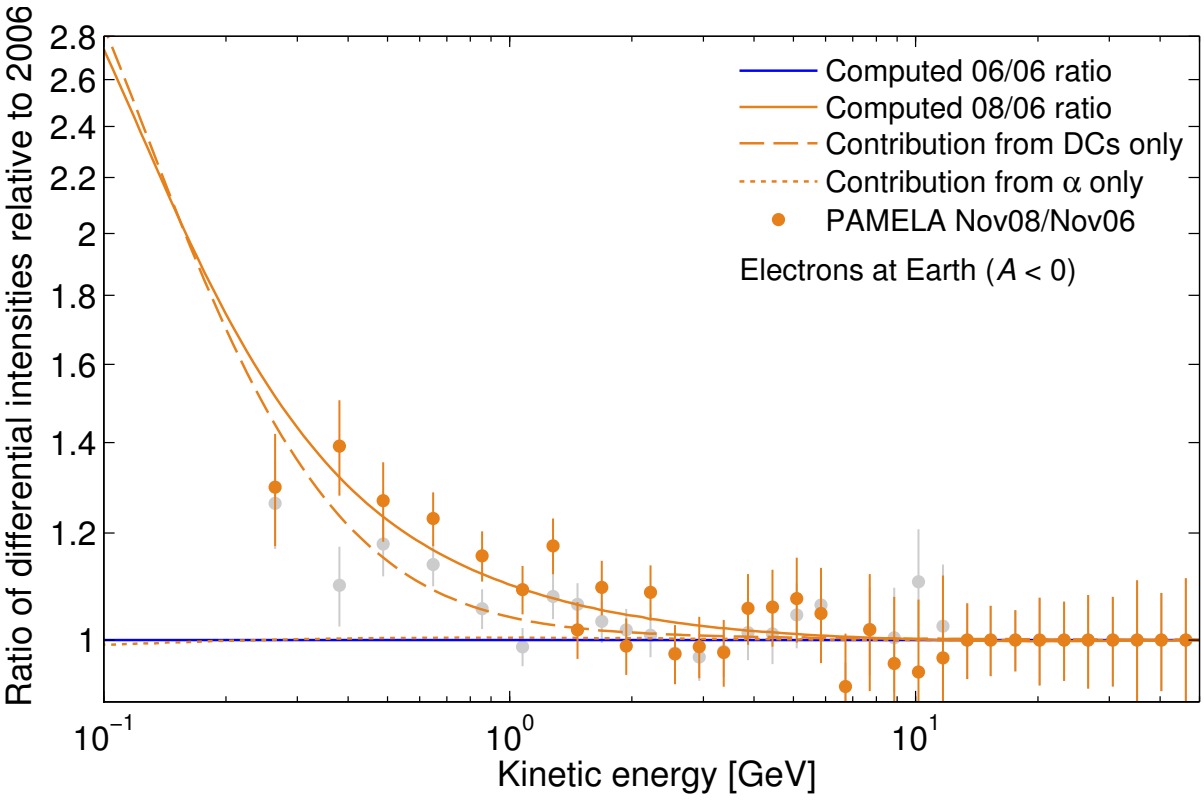

Figure 5.11: Similar to Figure 5.10, but for the electron ratios of 2008 relative to 2006. Indicated by the grey symbols are the PAMELA 2007 electron ratios relative to 2006.

in particle drifts, caused by the decreasing HMF, as well as changes in the diffusion coefficients during 2006 to 2009, the influence from these processes are highlighted. A similar method was followed for protons (see Section 4.5.4).

Figure 5.10 gives the electron energy spectra ratios of 2007 relative to 2006. The solid green line represents the ratio of the computed solutions in Figures 5.5 and 5.6, where all modulation processes have been taken into account. The dotted line, which almost follows the reference line (blue) at unity, represents the relative intensity contribution of a $1.7°$ tilt angle change from 2006 to 2007. Here the effects of changes in the diffusion coefficients as well as in particle drifts via the magnetic field (Equation 3.47) were excluded. Since electrons drift into the heliosphere from the polar regions downward and outward along the HCS during an $A < 0$ polarity cycle, these particles are minimally dependent on changes in the tilt angle, as opposed to protons which drift inward along the current-sheet (see also *Potgieter*, 1996). The minuscule effect of such a tilt angle change on electron intensities during the recent solar minimum is illustrated, both qualitatively and quantitatively, in the ratio of these solutions. It follows from the larger error bars shown in this figure that the electrons cannot be observed with the same accuracy as protons (compare e.g. Figure 5.10 with Figure 4.13).

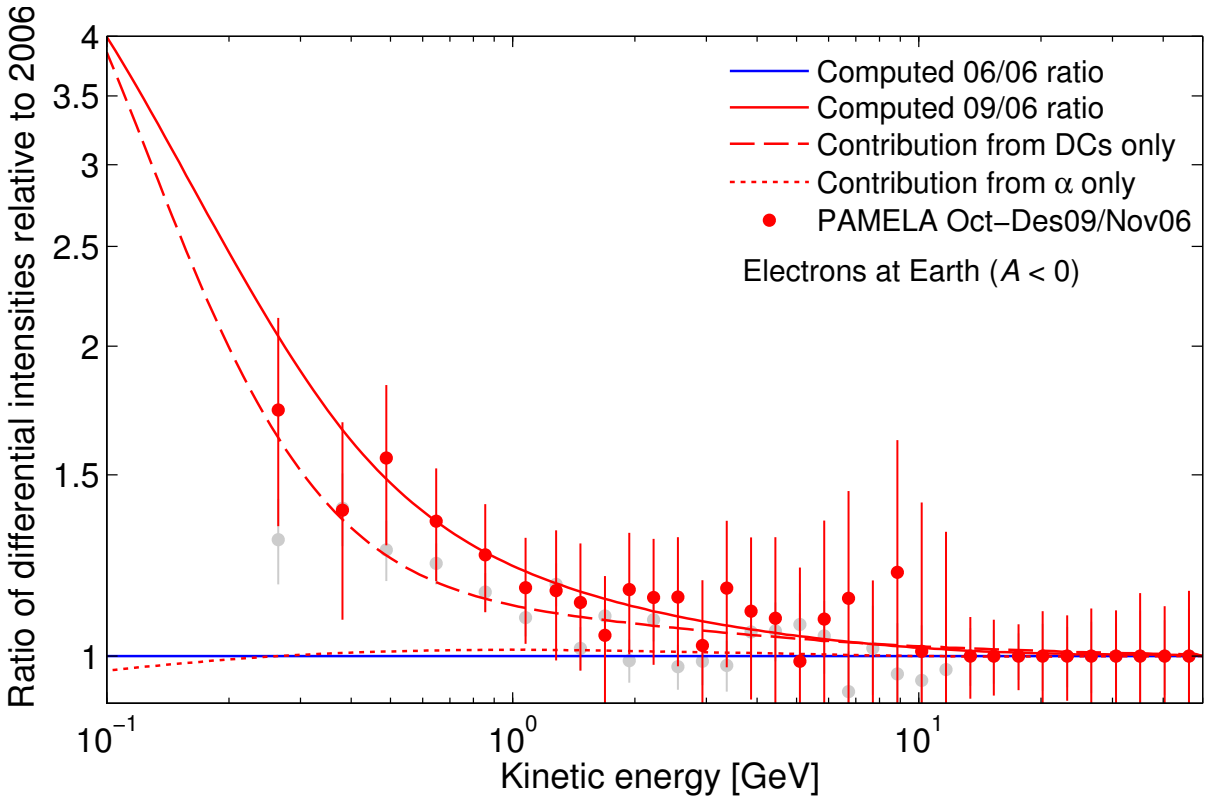

Figure 5.12: Similar to Figures 5.10 and 5.11, but for the electron ratios of 2009 relative to 2006. The grey symbols now correspond to PAMELA's 2008 electron ratios.

The dashed line in Figure 5.10 indicates the relative contribution as yielded by changes in only the diffusion coefficients toward the intensity increase, from 2006 to 2007. The region between the dashed and solid lines represents the intensity contribution delivered by global particle drifts through the drift coefficient in Equation 3.47. Compared to the effect of a tilt angle change, it is apparent that particle diffusion (parallel and perpendicular to the mean HMF) is responsible for a notable fraction of the increase in electron intensities for energies below ~ 1 GeV. For energies above ~ 1 GeV the assumed diffusion coeffcients of 2007, as a result of identical MFPs above ~ 1 GV, produced no changes in electron intensities between 2006 and 2007. Even though the inclusion of changes in diffusion leads to substantially higher intensities, the dashed line falls below a number of observed PAMELA electron ratios of the November, 2006, and December, 2007, spectra (symbols). It follows from the difference between the solid and dashed line that changes in particle drifts via the drift coefficient already begin to contribute notably to intensity increases at ~ 5 GeV. At ~ 1 GeV, the change in global drifts is responsible for about 90% of the increase in electron intensities between 2006 and 2007. Furthermore, at 400 MeV, changes in particle diffusion and global drifts (via the drift coefficient) contributed to $\sim 55\%$ and $\sim 45\%$ of the total increase in in-

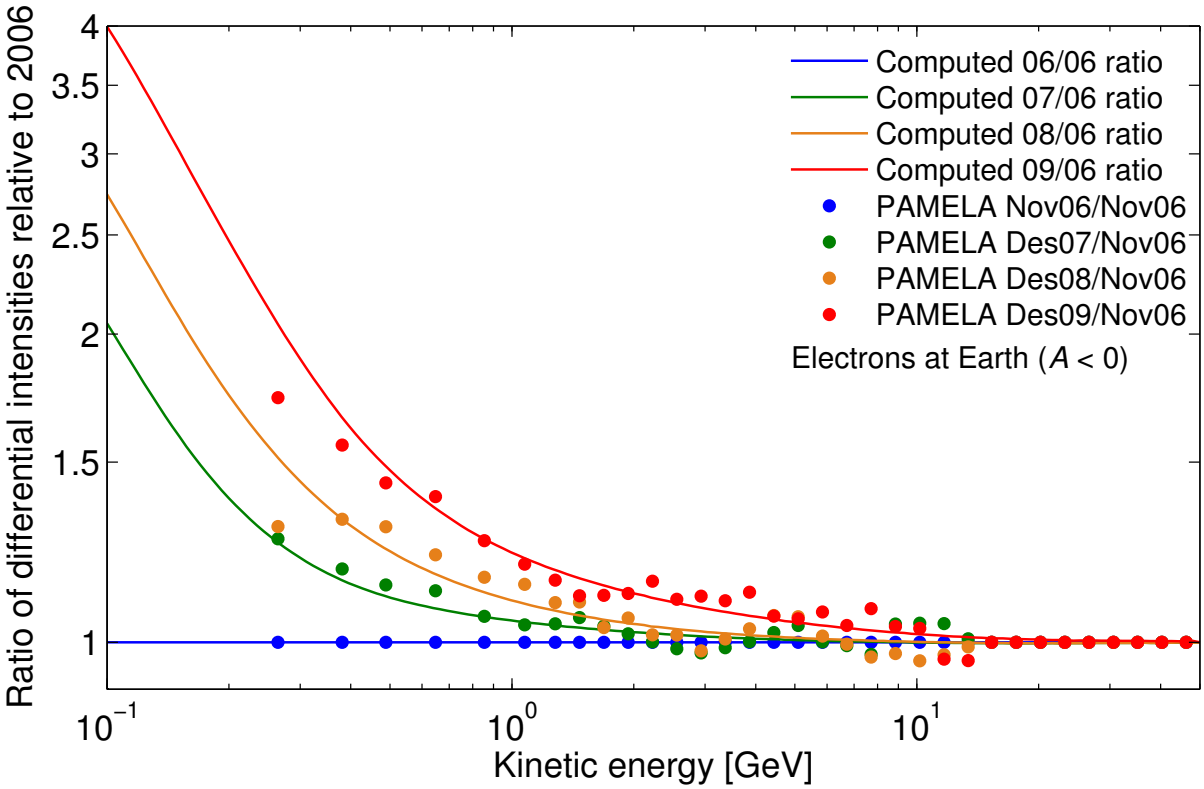

Figure 5.13: Electron ratios from the computed energy spectra of Figures 5.6 to 5.8, relative to the 2006 energy spectrum in Figure 5.5. Also shown are running three-bin averaged PAMELA electron ratios for the corresponding years.

tensity during this time, respectively. From the dashed and solid lines, for energies below $\sim$ 130 MeV, it can also be seen that the inclusion of changes in global particle drifts through the drift coefficient causes intensities to be slightly decreased. This phenomenon comes as a result of the "playoff" between particle diffusion in the upward polar direction ($\kappa_{\perp,\theta}$), and the opposing downward drift motions (see also *Potgieter*,1996).

As a result of the intensity fluctuations in electron observations, a larger amount of variations subsequently exist in the corresponding ratios in Figure 5.10. However, by taking the error-bars into account, which effectively designates a region of credible solutions, the ratio of the 2007 computed spectrum (which includes all modulation processes) gives a fairly accurate overall description of the PAMELA 2007 ratios.

A similar plot for the ratios of the 2008 electron spectra relative to 2006 is shown in Figure 5.11. The dotted, dashed, and solid lines again represent the ratios of energy spectra as discussed for Figure 5.10. The PAMELA 2008 to 2006 electron ratios are given by the orange symbols, whereas the grey symbols, for comparison, represent the 2007 to 2006 ratios. Although the 2008 ratios are quite similar in magnitude to those

of 2007 above ~ 3 GeV, a reasonably clear modulation progress in the 2008 PAMELA ratios is identified. Compared to Figure 5.10, similar qualitative effects are seen in the computed energy spectra ratios of 2008. It follows from Figure 5.11 that changes in the diffusion coefficients and global drifts (via Equation 3.47) at 1 GeV each contributed $\sim 40\%$ and $\sim 60\%$, respectively, toward the total intensity increase between 2006 and 2008. The effect of the inward drift motions of electrons acting against outward diffusion in the polar direction is also visible below ~ 600 MeV. Apart from an unpersuasive data-point at ~ 260 MeV, the solid line gives a satisfactory representation of the PAMELA 2008 ratios.

The ratios of 2009 relative to 2006 are shown in Figure 5.12. The red and grey symbols respectively represent the observed ratios of October to December, 2009, and November, 2008. The significant variation in the 2009 ratios is evident from the error-bars, which essentially forms a broad band of possible intensities. Even though such a band also facilitates a number of possible numerical solutions, the 2009 computed spectrum gives a highly probable estimate which takes all observations into account, in particular those above ~ 500 MeV. While intensities remain marginally affected by the change in tilt angle between 2006 and 2009, the effect of the overall increase in particle MFPs during this time is seen to already contribute noticeably to intensity increases below energies as high as ~ 10 GeV. The effect of global particle drifts, resulting from changes in the HMF magnitude, account for $\sim 45\%$ of the observed increase in electron intensities at 1 GeV, with the set of modulation paramters assumed for these ratios.

As an overview of the above discussed ratios, Figure 5.13 gives a combined plot of the ratios of computed spectra at Earth, from 2006 to 2009 (Figures 5.5 to 5.8), relative to 2006. Here running averages are calculated for the corresponding PAMELA ratios in Figures 5.10 to 5.12, which are shown by the color-coded sets of symbols. Since the variation of observed electron intensities resulted in ratios that overlap significantly, these running averages were calculated in order to obtain unambiguous ratios with resolved shapes. Compared to the ratios from Figures 5.10 to 5.12, those in Figure 5.13 shows a clearer recognizable progress in electron intensities. From these ratios it follows that the 2007 and 2008 PAMELA spectra are remarkably similar above ~ 2 GeV, whereas the 2009 PAMELA spectrum shows, on average, higher intensities for energies below ~ 10 GeV.

Figure 5.14 gives an overview of how electron differential intensities developed during the recent solar minimum, according to the computed spectra of 2006 to 2009. Shown in the top, middle, and bottom panels are the intensities at energies of 500 MeV, 1 GeV, and 2 GeV, respectively. The dotted, dashed and solid curves correspond to the scenarios discussed in Figures 5.10 to 5.12. It is evident from Figure 5.14 that for the small tilt angle changes during 2007 and 2008, particle intensities, across the energy

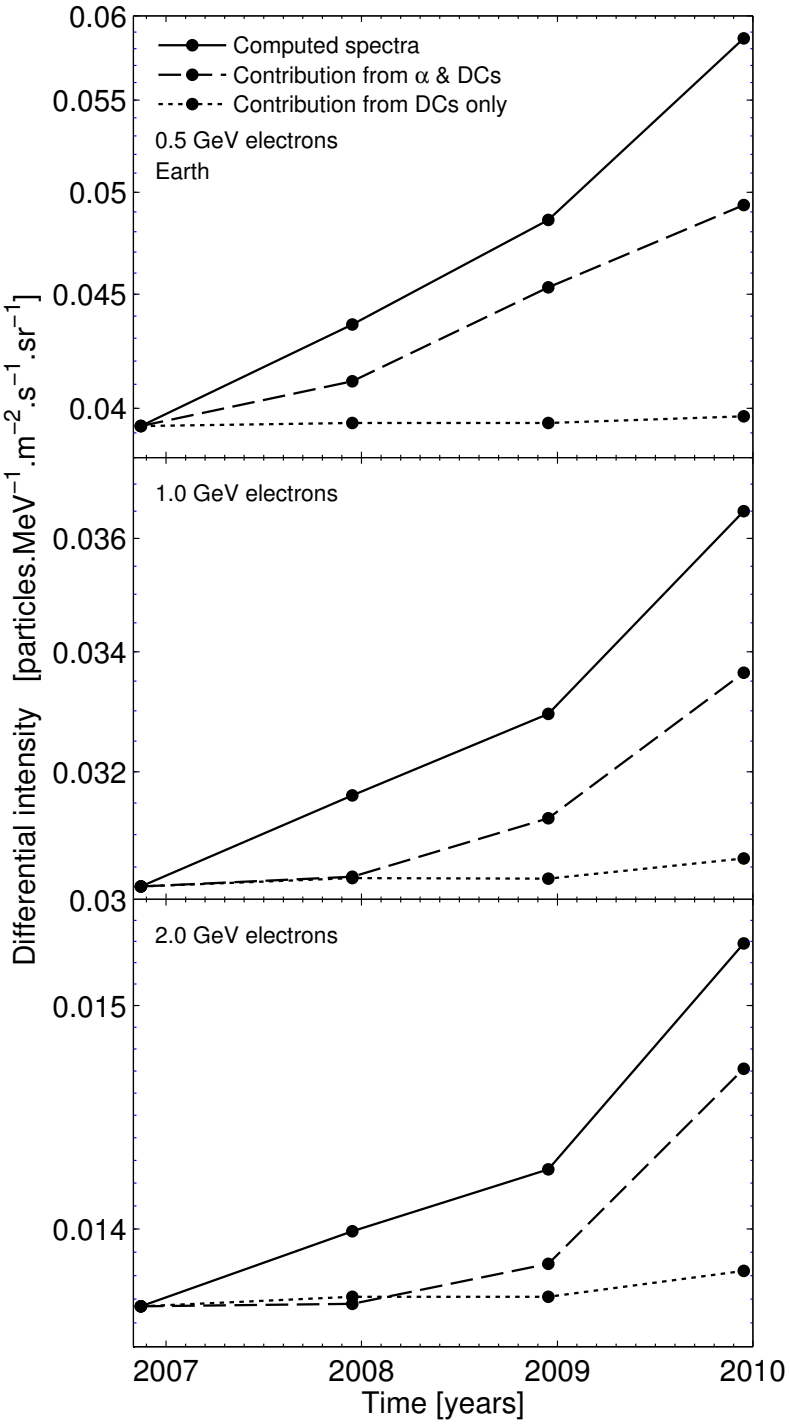

Figure 5.14: The computed differential intensities for electrons at 0.5 GeV (top panel), 1.0 GeV (middle panel), and 2.0 GeV (bottom panel), as a function of time, from November, 2006, to December, 2009. In each of these panels only four values from the computed spectra are plotted (black dots). As with Figures 5.10 to 5.12, the dotted and dashed lines respectively correspond to intensity levels due to changes in only the current-sheet tilt angle and only the diffusion coefficients, where global particle drifts due to changes in the HMF magnitude (via Equation 3.47) were excluded. The solid line represents the total computed intensity increase from all the modulation processes combined.

range of interest, were relatively unaffected. For 2009, however, during which time the tilt angle decreased by $4°$, a small but noticeable effect can be seen for energies above ~ 1 GeV. Due to the increase in electron MFPs, as discussed in Section 5.4.3, it is clear from the dashed line in all three panels that particle diffusion is the primary (but not exclusive) process responsible for the overall progressive increase in electron intensities. It can furthermore be seen from the region between the solid and dashed lines that the effect of global particle drifts, resulting from changes in the HMF magnitude (via Equation 3.47), yield a nearly constant contributing factor toward the total intensity increase over time for energies above ~ 1 GeV, whereas at ~ 500 MeV this factor shows a slight increase for 2009.

5.5 Summary

In this chapter a new LIS, based on the *Webber and Higbie* (2008) electron LIS, was discussed. It was shown that this LIS, approximated by two power laws, compares well to the recently proposed *Evenson and Clem* (2011) LIS only for energies above ~ 100 MeV. The *Langner et al.* (2001) electron LIS, however, gives somewhat higher intensity levels. By assuming a $\gamma = -3.13$ spectral index above ~ 20 GeV the LIS used for this study can easily be normalized to PAMELA data. For energies below 20 GeV, a region of notably higher intensities is observed in the PAMELA electron data, which was compensated for by a similar region in the assumed LIS where intensities deviate from a power law. This assumption for the LIS led to accurate computed spectra at Earth.

An overview of the PAMELA electron observations was given in Section 5.3 in light of the recent solar minimum. It followed from Figures 5.3 and 5.4 that, due to a combination of statistical and systematic errors, the PAMELA electron observations display notable fluctuations. Consequently, for the purpose of modelling the heliospheric propagation and modulation of electrons between 2006 and 2009, certain monthly-averaged spectra that exhibit large fluctuations were avoided and averaged spectra were calculated over time and energy when required. For energies above ~ 12 GeV, a single averaged observed spectrum was used.

By following the same procedure as for protons, the numerical model was used to compute solutions that accurately imitates the sample selection of PAMELA electron spectra (taken at the end of each consecutive year). These computed spectra, together with the corresponding PAMELA observations, were presented in Figures 5.5 to 5.8. Apart from minor differences in intensities at low and high energies, the energy spectrum progress (modulation) between 2006 and 2009 was reproduced. It was found that intensities in the region of the characteristic peak in the spectra (around ~ 500 MeV) increased by a factor of ~ 1.7 during this time, while for energies above ~ 5 GeV electron

intensities, apart from the apparent fluctuations, remained essentially unchanged.

In Section 5.4.3 the consecutive ratios of the computed and measured spectra from 2006 to 2009, relative to 2006, were studied. By eliminating the contributing effects of changes in global particle drifts, produced by a decrease in B_e (via the drift coefficient), and by considering scenarios where changes in only the tilt angle and only the diffusion coefficients were taken into account, the relative contribution from each major modulation process during the recent solar minimum were identified. These results were presented as energy spectra ratios in Figures 5.10 to 5.13, and as differential intensities as a function of time in Figure 5.14. It was found from the energy spectra ratios, which serve as an additional measure of accuracy, that the computed solutions in Figures 5.5 to 5.8 agree well with PAMELA observations. It was also identified that changes in the HCS tilt angle contributed a minimal amount to the total modulation between 2006 and 2009, while particle diffusion and global drifts (via the drift coefficient) were the key contributing processes.

Chapter 6

Electron to Proton Ratios

6.1 Introduction

Since oppositely charged particles in the heliosphere experience different drift motions, a clear charge-sign dependence exists for the modulation of these particles – a phenomenon which is predicted by numerical drift models. With access to accurate (preliminary) proton and electron observations during the recent solar minimum (2006 to 2009), via PAMELA, a comprehensive study of the electron to proton ratio at Earth is possible. Such a study will yield essential insight with regard to the charge-sign dependence of CR modulation during this time. Furthermore, by comparing the subsequent ratios from the observed and computed spectra, as is done in this chapter, the progress in the electron to proton ratio can be identified for the period between 2006 and 2009. This will illustrate the difference in electron and proton modulation caused by gradient and curvature drifts.

6.2 Previous Observations and Modelling Studies

As previously discussed, it is well known that electrons, for example, as a result of the large-scale configuration of HMF gradients, curvatures, and the HCS, will drift inward into the heliosphere, primarily over the polar regions and outward along the HCS in the equatorial region, during an $A < 0$ magnetic cycle. For such a cycle the HMF is directed toward the Sun in the Northern hemisphere, and away from the Sun in the Southern hemisphere (as was the case for the recent solar minimum). Protons, however, will drift inward along the HCS and outward over the polar regions. During an $A > 0$ cycle, the drift directions of these particles reverse.

The effect of particle drifts, specifically along the HCS, has been widely recognized to be responsible for the characteristic shape of the CR intensity profile near Earth during solar minimum conditions (e.g. *Jokipii and Thomas*, 1981, and *Potgieter and Moraal*,

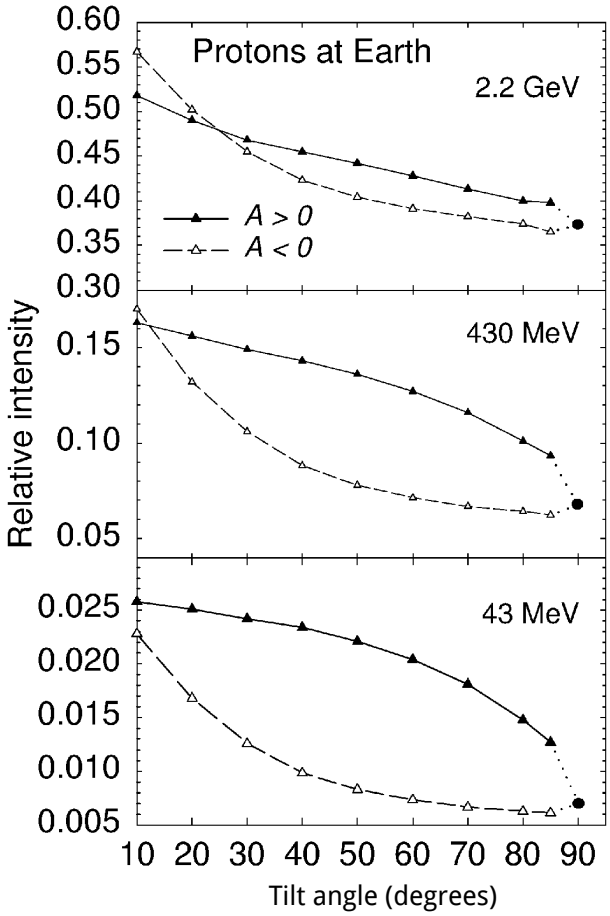

Figure 6.1: Intensity-tilt profiles at Earth for 2.2 GeV, 430 MeV, and 43 MeV protons. The filled circles at $90°$ denote the no-drift solutions. Figure taken from *Burger and Potgieter* (1999). See also *Potgieter et al.* (2001a).

1985). Using a 2D steady-state numerical modulation model, *Burger and Potgieter* (1999) performed a theoretical assessment of the effects that a changing current-sheet tilt angle has on the intensity-time profiles of positively and negatively charged particles at Earth. Their results for protons, at energies of 2.2 GeV, 430 MeV and 43 MeV, are summarized by the plots in Figure 6.1, which show how the intensity of CR protons vary relative to the corresponding interstellar value as function of tilt angle. Evidently, a classic drift behaviour can be identified at all three energies from this figure. For positively charged particles during an $A < 0$ cycle, the intensity profile shows a peak-shaped response to a changing tilt angle around solar minimum. This behaviour is a direct consequence of the drift direction experienced by positively charged particles inward along the HCS. A larger tilt angle leads to a more wavy current-sheet, more modulation, and lower intensities, whereas a small tilt angle leads to a less wavy current-sheet, less modulation, and higher intensities. Conversely, for an $A > 0$ cycle, the intensity profile is flatter compared to an $A < 0$ cycle, since positively charged

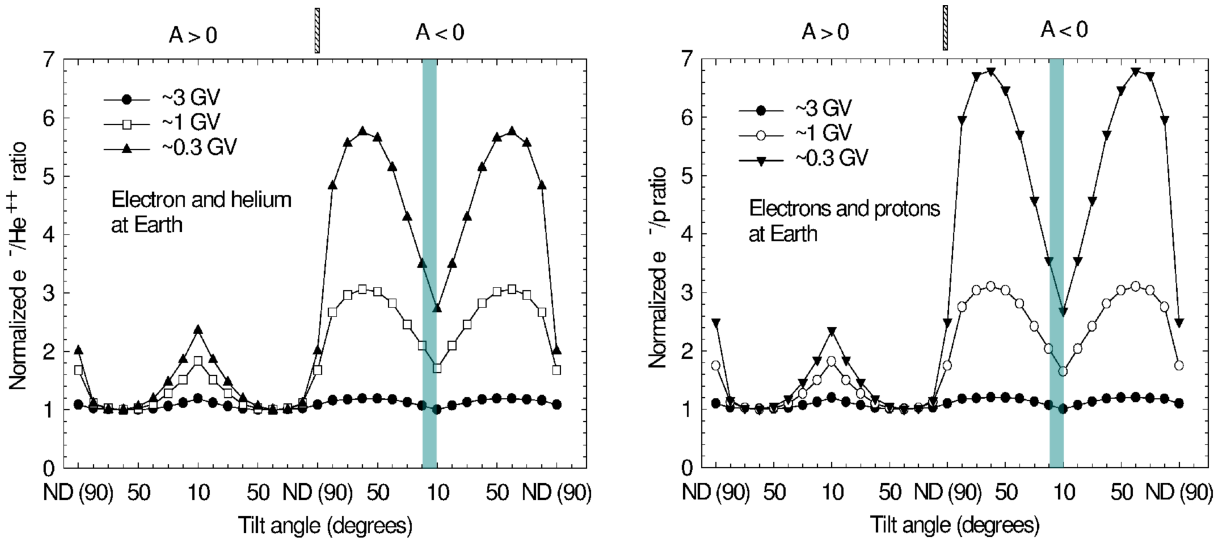

Figure 6.2: Tilt angle and solar polarity-sign dependence of the e^-/He^{++} (left) and e^-/p (right) ratios. These ratios are normalized with respect to the minimum value for each ratio. Figure adapted from *Burger and Potgieter* (1999).

particles drift freely inward over the polar regions. From a comparison between the 2D model used by *Burger and Potgieter* (1999), and a 3D model (similar to the one used in this study), *Hattingh* (1998) showed that these models have the same qualitative behaviour with tilt angle, as well as, to a large extent, the same quantitative behaviour. See also *Ferreira et al.* (1999).

Burger and Potgieter (1999) also investigated the tilt angle dependence of CR intensity ratios at Earth, the results of which are given in Figure 6.2. Shown in the left and right panels are the e^-/He^{++} and e^-/p ratios at energies of ~ 3 GV, ~ 1 GV and ~ 0.3 GV, normalized with respect to the minimum value for each ratio. Even though these ratios differ somewhat quantitatively, they possess the same qualitative behaviour. During an $A < 0$ cycle, the ratios have an "m" shape, changing rapidly with tilt angle, while during an $A > 0$ cycle, the ratios have a "w" shape and are less responsive to tilt angle changes. It is also observed that changes in the ratios become larger with decreasing rigidity. The shaded regions give an approximate indication of where the solar minimum period between 2006 and 2009 would fit. The results of this hypothetical solar activity cycle of *Burger and Potgieter* (1999) agree qualitatively with observations (e.g. *Bieber et al.*, 1999). See also *Potgieter et al.* (2001a).

The results of *Langner* (2004), who also examined the charge-sign dependent modulation of electrons, protons and positrons, using a 2D drift model with shock acceleration, is given in Figure 6.3. Shown in this figure are the intensity ratios of electrons to positrons (top panels) and electrons to protons (bottom panels), for typical solar minimum (left) and maximum (right) conditions, when $\alpha = 10°$ and $\alpha = 75°$ re-

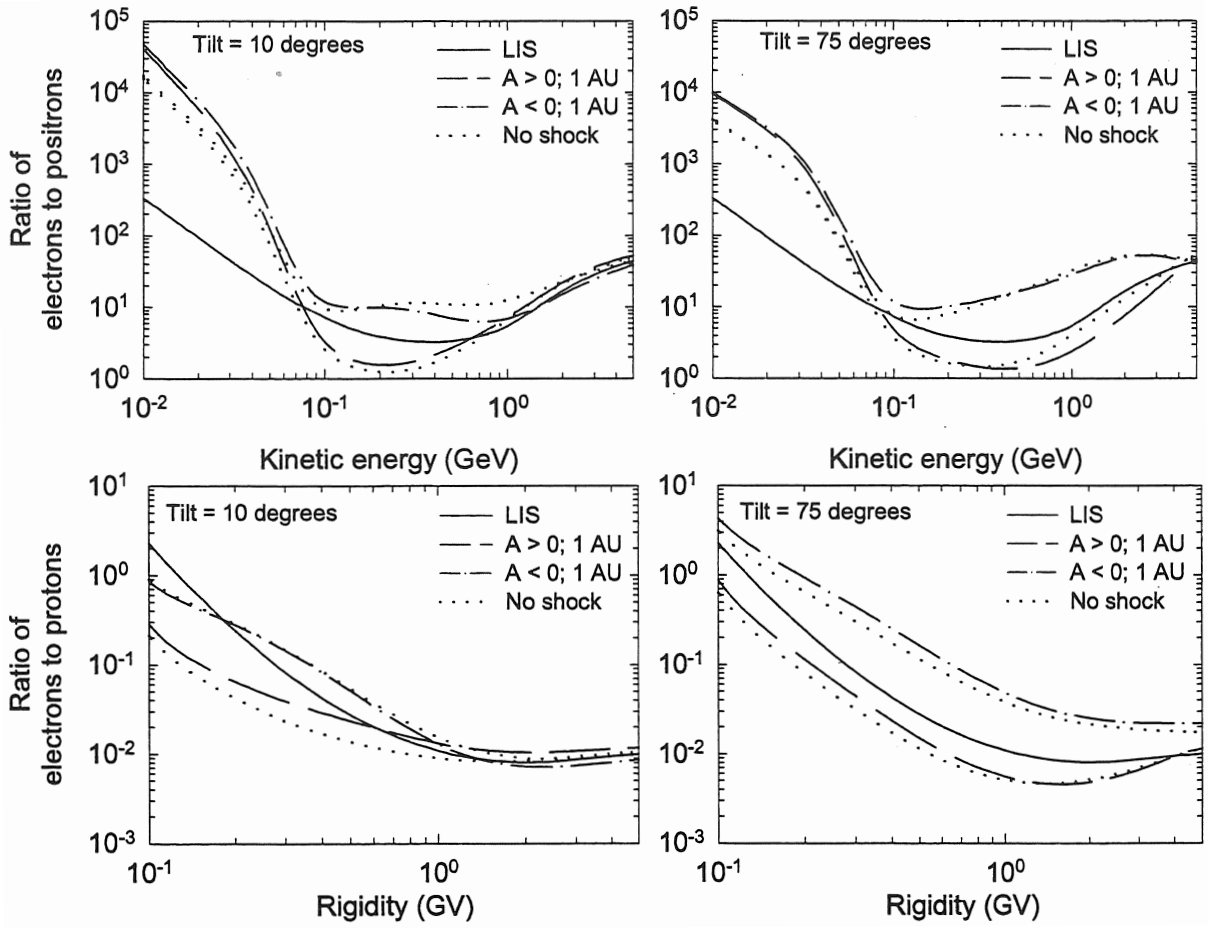

Figure 6.3: The differential intensity ratios of electrons to positrons and electrons to protons for $A > 0$ and $A < 0$ polarity cycles at Earth, as function of rigidity. The panels on the left are for typical solar minimum conditions (when $\alpha = 10°$), while the panels on the right are for solar maximum conditions (when $\alpha = 75°$). Figure taken from *Langner* (2004). See also *Langner and Potgieter* (2004) and *Potgieter and Langner* (2004).

spectively. For the electron simulations a, Jovian source was included. *Langner* (2004) found that drift effects become negligible for electrons and positrons below energies of $\sim$ 100 MeV, which is evident from Figure 6.3, where the e^-/e^+ ratios of the two polarity cycles converge at low energies. The differences between these polarity cycles are even less for the non-shock solutions, given by the dotted lines. For $\alpha = 10°$, the difference between the two polarity cycles for the e^-/e^+ ratio at Earth are apparent for energies from $\sim$ 80 MeV to $\sim$ 1 GeV and even more so for a tilt angle of 75°. The e^-/p ratio, only shown for rigidities above 100 MeV, has a similar qualitative tendency. See also *Potgieter et al.* (2001b), *Langner and Potgieter* (2004), and *Potgieter and Langner* (2004) for similar charge-sign dependent studies. See also the reviews by *Potgieter* (2008, 2010, 2011) and *Heber and Potgieter* (2006).

The Ulysses mission provided a unique opportunity to study the long-term prop-

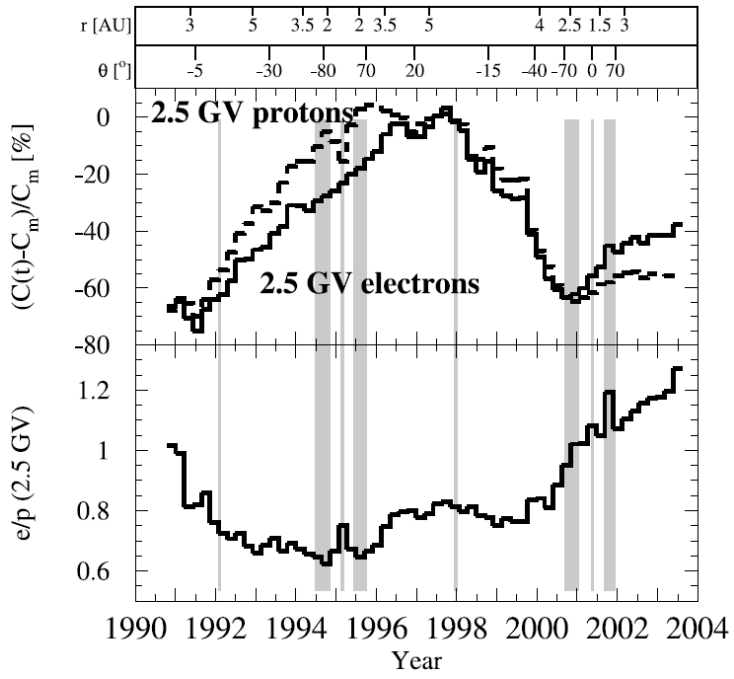

Figure 6.4: 78-day averaged quiet time variation ($C(t) - C_m/C_m$) of ~ 2.5 GV protons and electrons (top panel) and the corresponding e^-/p ratio (bottom panel), from November, 1990 to February, 2003. The shaded regions indicate the time periods of Ulysses' fast latitude scans, as well as its encounter with Jupiter in 1992. Figure taken from *Heber et al.* (2003).

agation and modulation of galactic CRs through *in situ* measurements in the heliosphere. Using ~ 2.5 GV electron and proton measurements from Ulysses, *Heber et al.* (2002) investigated charge-sign dependent modulation over the period from 1991 to 2000. This was done by constructing an equatorial equivalent of the e^-/p ratio in order to account for the latitudinal variation of particle intensities. They found that the equatorial e^-/p ratio increased with the approach of solar maximum, which is indicative of diminishing drift effects and the transition to diffusion-dominated modulation. *Heber et al.* (2002) concluded that the variation of the e^-/p ratio, over the period from 1991 to 2000, indicates that drift effects are indeed important over a large part of the 11-year $A > 0$ solar cycle. Their results are also qualitatively consistent with predictions from the steady state model of *Burger and Potgieter* (1999). Figure 6.4 shows a compilation of the 78-day averaged quiet time counting rates from Ulysses for ~ 2.5 GV electrons and protons, from November, 1990 to February, 2003 (*Heber et al.*, 2003). Both counting rates (top panel) are presented as percentage changes with respect to the rates measured in mid 1997 (C_m) at solar minimum. The observed variations in the intensities are caused by temporal variations as well as by spatial variations as a result of the Ulysses trajectory. Shown in the bottom panel, is the corresponding e^-/p ratio. See also *Heber et al.* (2009) for a study of the modulation of galactic CR protons and electrons during the

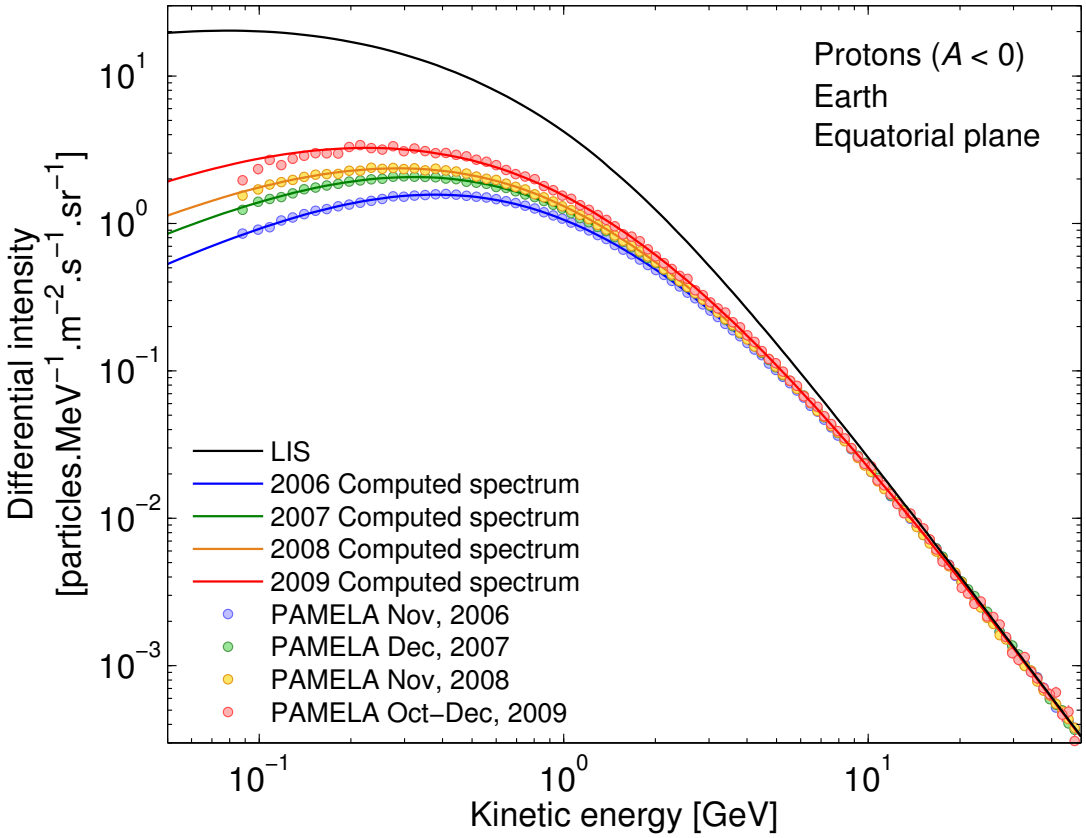

Figure 6.5: PAMELA proton spectra of 2006 (blue symbols) to 2009 (red symbols), overlaid by the corresponding computed spectra (solid lines) for an $A < 0$ cycle (see Figures 4.7 to 4.10). During this time the tilt angle changed from $\sim 15.7°$ to $\sim 10.0°$, with an accompanying change in B_e from ~ 5.05 nT to ~ 3.94 nT. See also Section 4.5.3 and Figure 4.12 for a discussion of how the rigidity dependence of $\lambda_{\parallel}$ and $\lambda_{\perp}$ for protons were changed in order to reproduce the PAMELA observations.

recent unusual solar minimum.

For a perspective of the time-dependence of charge-sign dependent modulation of CRs in the heliosphere, see *Ferreira et al.* (2003) and *Ndiitwani et al.* (2005).

6.3 Comparison of Proton and Electron Spectra

Figures 6.5 and 6.6 give an overview of the proton and electron spectra, respectively, from 2006 to 2009, showing the PAMELA observations overlaid by the corresponding computed spectra (see proton results in Figures 4.7 to 4.10, and electron results in Figures 5.5 to 5.8). These figures illustrate how the proton and electron intensities increased during the recent solar minimum. As discussed in detail in Section 4.5.1, the current-sheet tilt angle decreased by more than $5°$, from $\sim 15.7°$ in 2006, to $\sim 10.0°$ in 2009, along with a ~ 1.00 nT decrease in the average HMF at Earth, from ~ 5.05 nT to

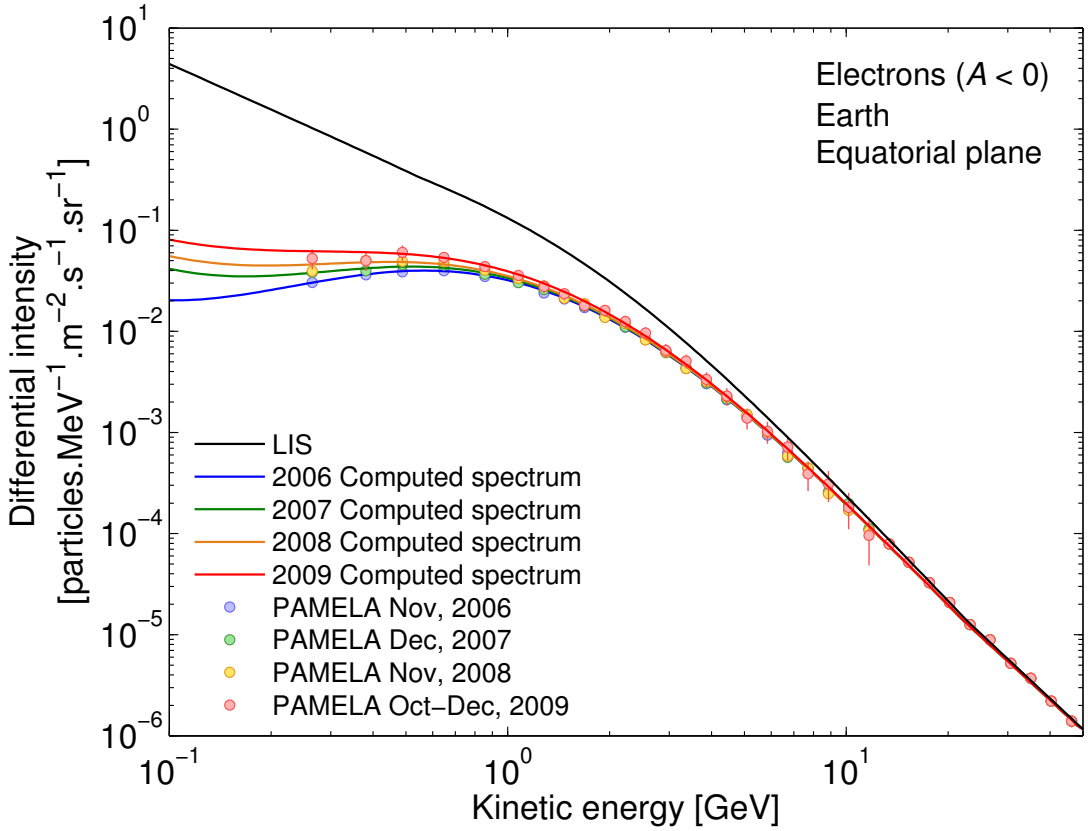

Figure 6.6: Similar to Figure 6.5, but for electrons (see Figures 5.5 to 5.8). See also Section 5.4.3 for a discussion of how the rigidity dependence of $\lambda_{\parallel}$ and $\lambda_{\perp}$ for electrons were changed to reproduce the PAMELA observations.

~ 3.94 nT. It was also found that $\lambda_{\parallel}$ and $\lambda_{\perp}$ (radial and polar) had to be increased in order to reproduce the PAMELA observations (see Sections 4.5.3 and 5.4.3).

It is known that protons experience large adiabatic energy losses at low energies, which result in the characteristic adiabatic slope observed in their modulated spectra. For electrons at the same energy, however, adiabatic energy losses are much smaller, leading to modulated spectral slopes that are similar to that of the electron LIS, for energies below ~ 50 GeV. These characteristics account for another prominent feature observed in the e^-/p ratios, namely the rapid increase in the ratio below ~ 100 MV.

Figures 6.7 and 6.8 give an overview of the normalized proton and electron intensities, respectively, as function of time, for rigidities below ~ 10 GV (shown on the same scale). The time profile of each rigidity is normalized with respect to the intensity measured in July, 2006. The difference between the development of electron and proton intensities with time is quite apparent from the shape of these profiles. This effect is further illustrated in Figure 6.9, which shows the proton (light-red lines) and electron (light-blue lines) intensities between rigidities of ~ 0.5 GV and ~ 1.0 GV, as

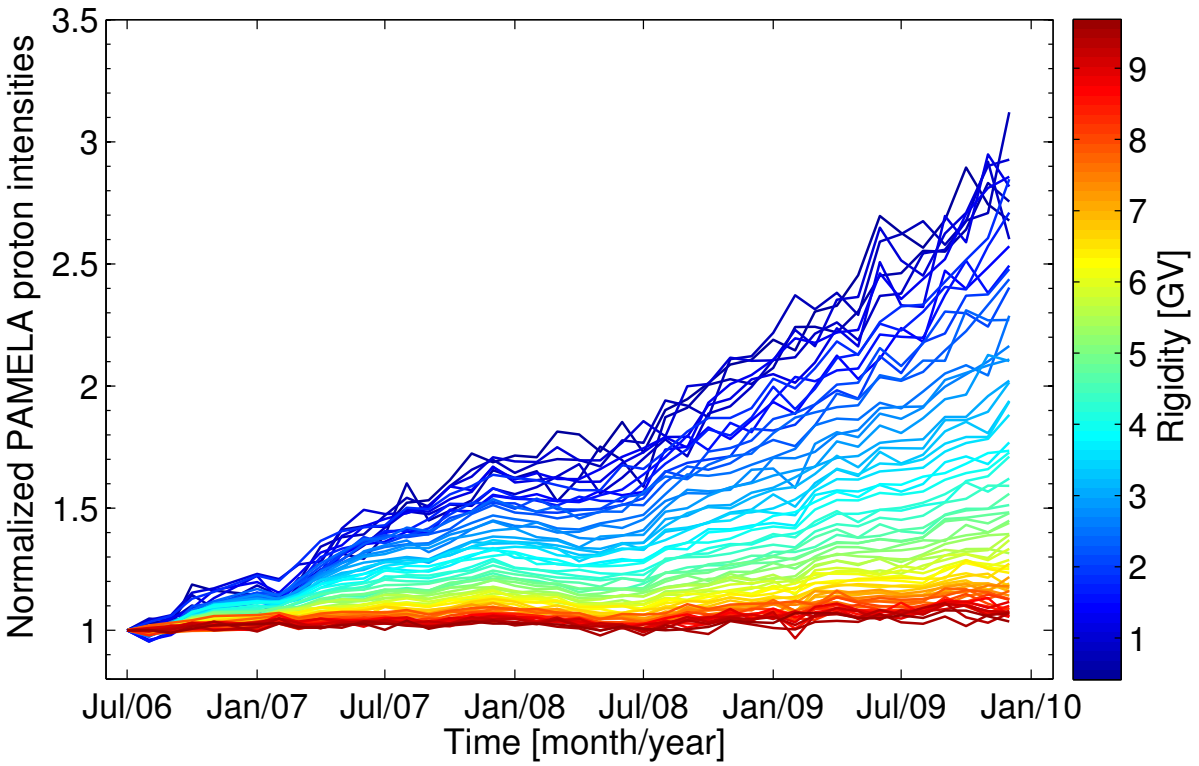

Figure 6.7: Normalized PAMELA proton observations for rigidities below $\sim$ 10 GV, as function of time, from July, 2006 to December, 2009. The rigidity values of these time profiles are indicated by the colorbar, where rigidities above $\sim$ 9 GV correspond to dark-red, and rigidities below $\sim$ 2 GV correspond to dark-blue. The time profile for each rigidity is normalized with respect to the value in July, 2006. Data obtained from the *PAMELA-group* (*private communication*).

function of time, along with the corresponding average intensities (symbols). While proton intensities increased rapidly as modulation conditions declined toward the end of 2009, the increase in electron intensities were significantly less. From July, 2006 to December, 2009, proton intensities, on average, increased by a factor of ~ 2.5 for rigidities between ~ 0.5 GV and ~ 1.0 GV, whereas the corresponding electron intensities increased only by a factor of ~ 1.4. For protons and electrons, these correspond to average increases in the differential intensity from ~ 1.25 to ~ 3.10, and from $\sim 3.65 \times 10^{-2}$ to $\sim 4.91 \times 10^{-2}$, respectively (in units of particles.m^{-2}.s^{-1}.sr^{-1}.MeV^{-1}). As a result, the proton intensity-time profile has a distinct peaked shape, compared to the rather flatter electron time profile. Since $\lambda_{\parallel}$ and $\lambda_{\perp}$ (in the radial and polar directions) for both particles are fairly similar in this rigidity range (see Figures 4.12 and 5.9), this difference in the time profiles is a direct result of the effect of gradient, curvature, and HCS drift motions, and is qualitatively consistent with what *Heber et al.* (2009) predicted. The intensity of electrons, which gain easy access via the polar regions, already reached

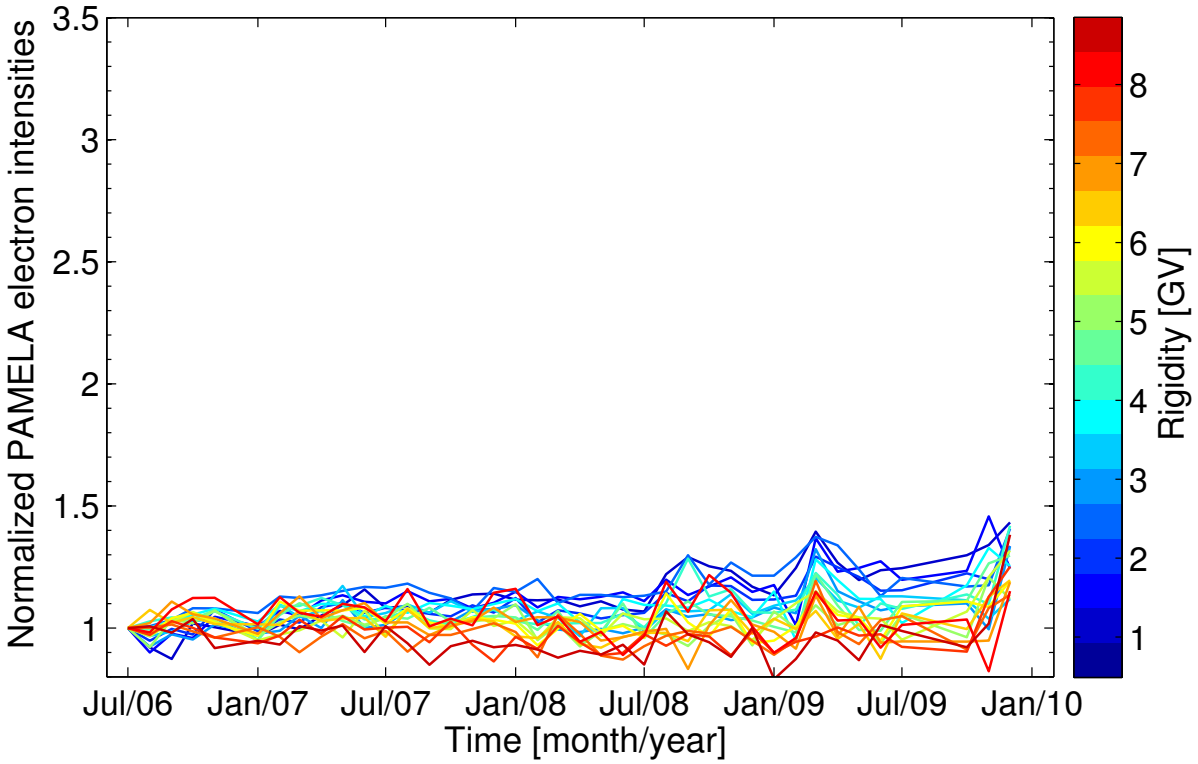

Figure 6.8: Similar to Figure 6.7, but for electrons. Data obtained from the *PAMELA-group* (*private communication*).

solar minimum levels, while the intensity of protons, drifting along the HCS in the equatorial region, still increased considerably.

From Figure 6.8 it is also evident that, apart from significant fluctuations in electron observations, electrons above ~ 6 GV remained, on average, at the same intensity level measured in July, 2006. A similar effect is seen for protons, but at a higher rigidity (around ~ 10 GV). See also Figures 4.3 and 4.4 in Chapter 4, and Figures 5.3 and 5.4 in Chapter 5.

6.4 Electron to Proton Ratios

For an improved understanding of the charge-sign dependent modulation of CR particles during the recent solar minimum, the subsequent electron to proton ratios are investigated. Figures 6.10 to 6.13 give the e^-/p ratios of the PAMELA observations (symbols) and computed spectra (solid lines), calculated from the 2006 to 2009 spectra in Figures 6.5 and 6.6. The dotted lines represent the e^-/p LIS ratio. It is evident from these figures that for rigidities above ~ 20 GV, where heliospheric modulation is at a minimum (or negligible to a certain extent), the e^-/p ratio has a steady slope which is

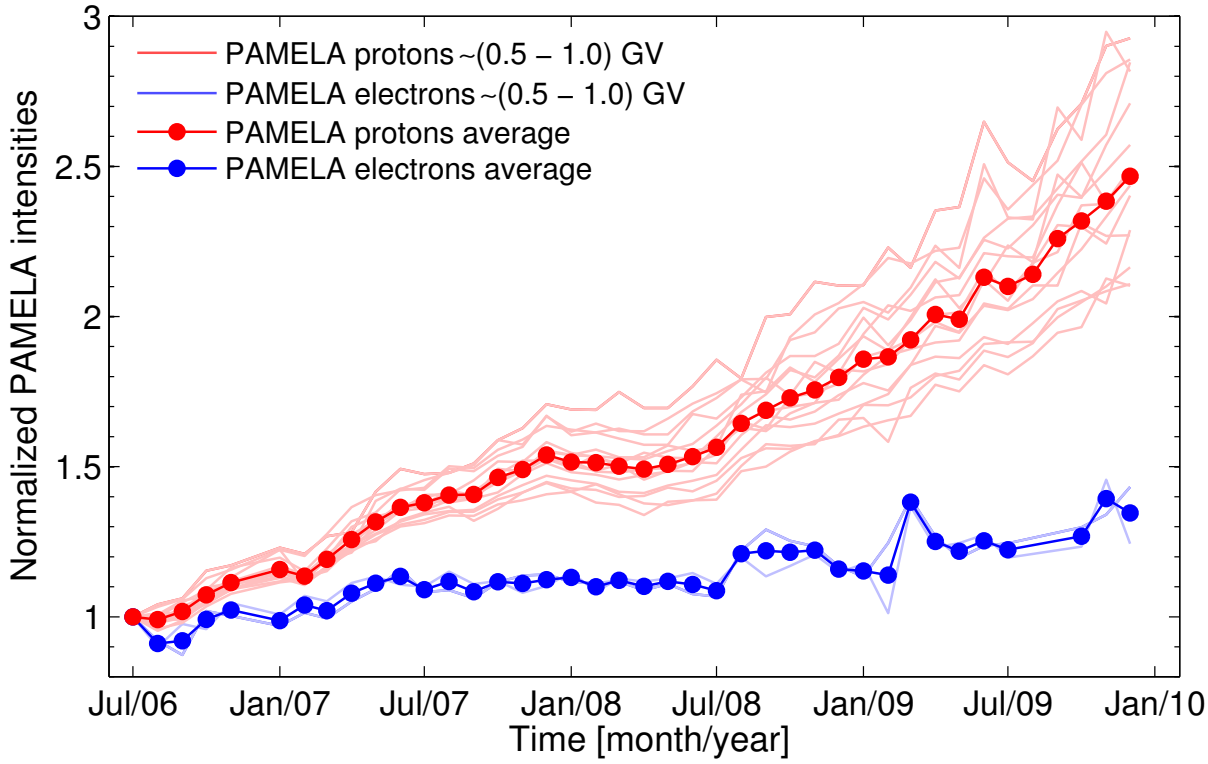

Figure 6.9: Normalized proton (light-red lines) and electron (light-blue lines) intensities between ~ 0.5 GV and ~ 1.0 GV, as function of time, from July, 2006 to December, 2009. The red and blue symbols represent the average intensities of protons and electrons, respectively. These intensity-time profiles are normalized with respect to the intensity measured in July, 2006.

almost identical to that of the LIS ratio. The effect of the region of enhanced intensities in the electron LIS, which was added to account for slightly higher than usual electron intensities below $\sim$ 20 GeV (see Section 5.2), is seen in all the ratios at $\sim$ 20 GV. Here the slope of the e^-/p ratios, together with the LIS, become noticeably steeper below $\sim$ 20 GV, consistent with the shape of the electron LIS. Apart from slight deviations between $\sim$ 3 GV and $\sim$ 10 GV, the ratios of computed spectra in Figures 6.10 to 6.13 give a reasonably good representation of the PAMELA e^-/p ratios, with regard to shape and absolute value. It is also evident from PAMELA observations and model results that protons dominated electrons at rigidities above $\sim$ 70 MV.

As conditions in the heliosphere approached solar minimum, proton intensities, which hadn't yet reached their actual solar minimum levels by ~2008, continued to increase substantially due to curvature and gradient drift effects (as predicted by *Ferreira and Potgieter*, 2004), because protons drift into the heliosphere along the HCS. *Heber et al.* (2009) consequently predicted that, if the tilt angle would decrease below 10° during the recent minimum, proton intensities could increase by 30% from ~2008, to reach

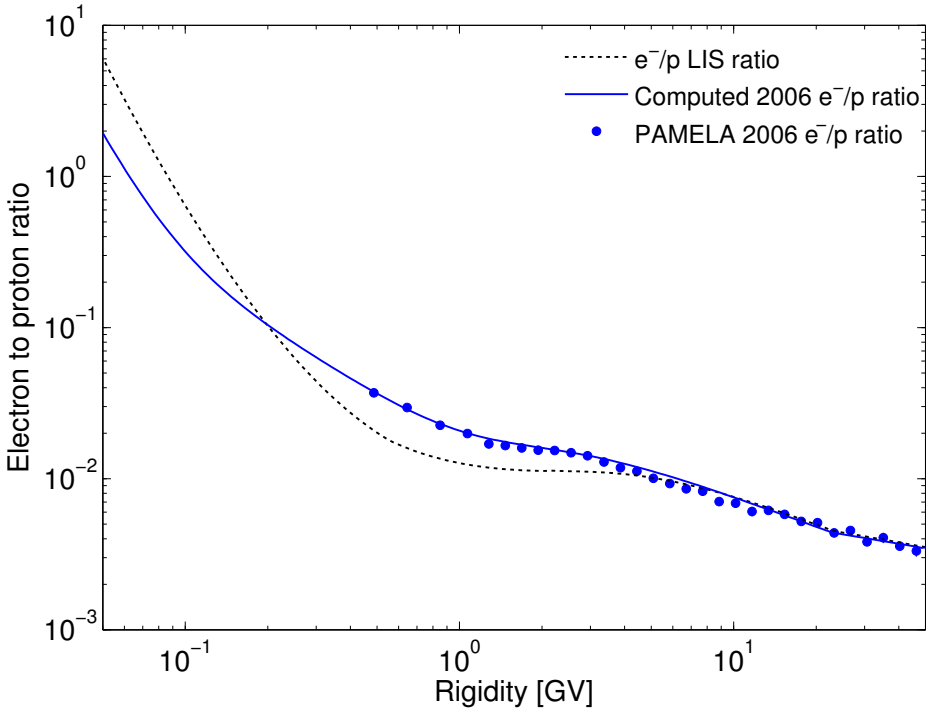

Figure 6.10: PAMELA electron to proton ratio for 2006 (symbols), overlaid by the corresponding computed ratio (solid blue). The electron to proton LIS ratio is represented by the dotted line.

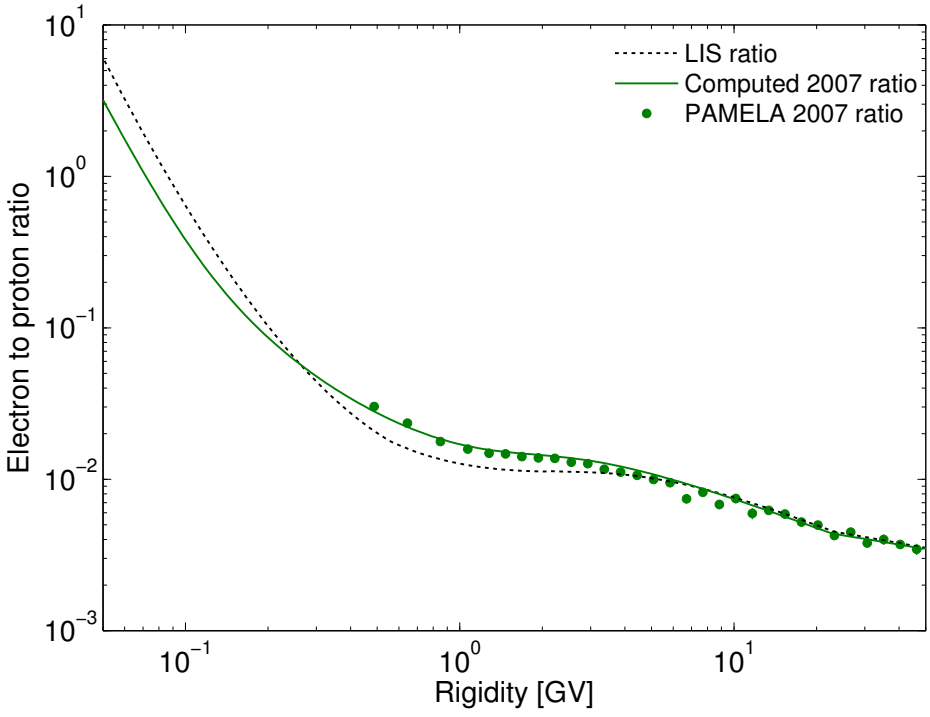

Figure 6.11: Similar to Figure 6.10, but for the 2007 PAMELA observations and computed spectra.

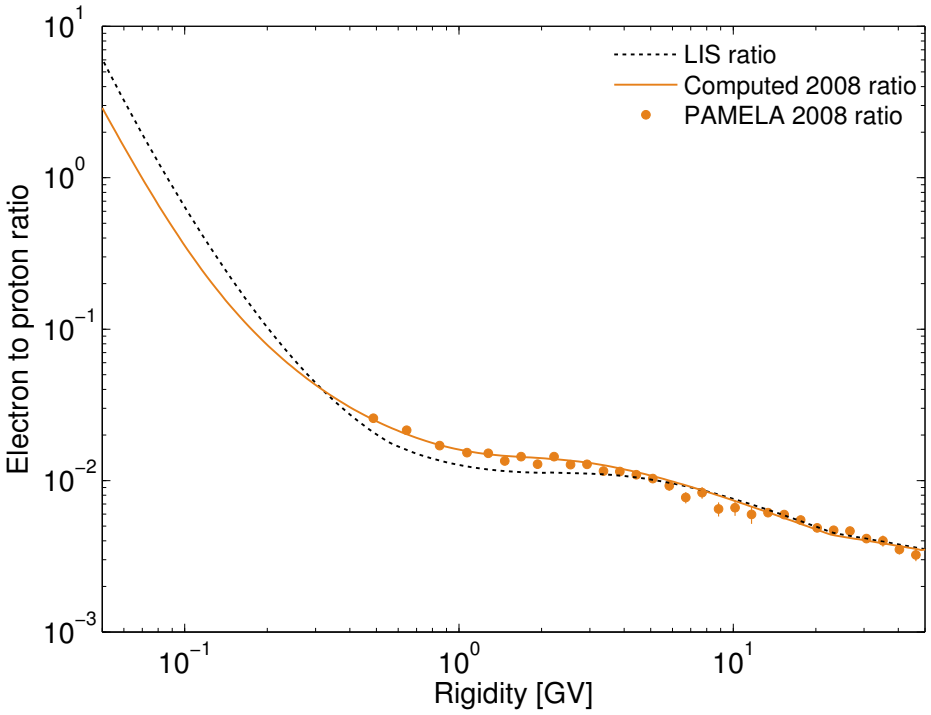

Figure 6.12: Similar to Figure 6.10, but for the 2008 PAMELA observations and computed spectra.

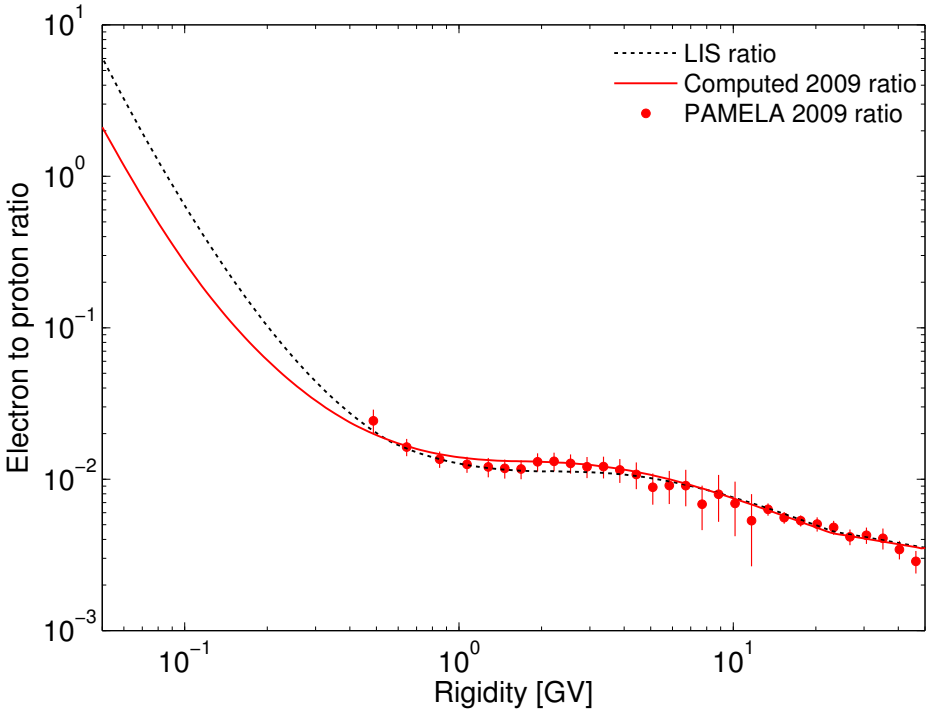

Figure 6.13: Similar to Figure 6.10, but for the 2009 PAMELA observations and computed spectra.

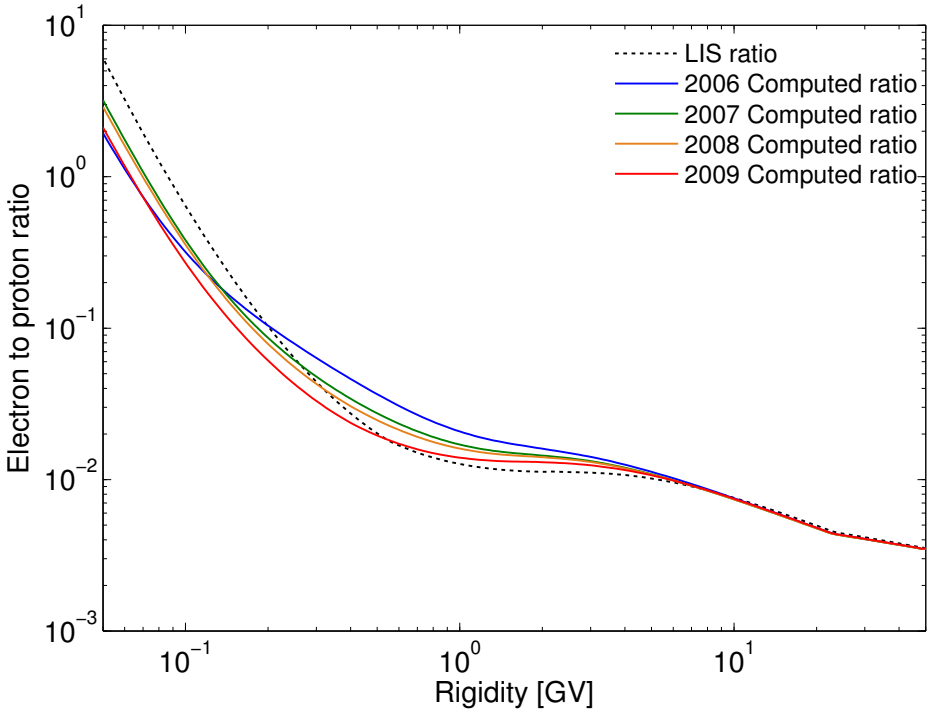

Figure 6.14: Computed electron to proton ratios, from 2006 to 2009, as function of rigidity (solid lines), compiled from the previous four figures. The electron to proton LIS ratio is represented by the dotted line.

the highest intensities ever measured in heliospheric space. This can be verified from Figure 6.5, from which it is evident that proton intensities increased by $\sim 45\%$ from 2008 to 2009, due to the combined effect of a decreasing tilt angle and average HMF strength, as well as rigidity dependent changes in $\lambda_{\parallel}$ and $\lambda_{\perp}$ (in the radial and polar directions). Similar intensity increases occurred for protons between 2006 and 2007, and between 2007 and 2008. Electrons, on the other hand, easily drift into the heliosphere over the poles, so that, apart from small increases at lower energies, their intensities already reached solar minimum level around 2008. As a result of the comparatively larger increase in proton intensities, the apparent decrease in the e^-/p ratio from 2006 to 2009 can be ascribed to both diffusion and drift motions experienced primarily by protons during an $A < 0$ cycle.

In 2006, proton intensities exceeded that of electrons by a factor of ~ 50 around 1 GV, and by ~ 140 around 10 GV. Since proton intensities increased noticeably more than electrons from 2006 to 2007, the e^-/p ratio decreased by about 15% at 1 GV. At higher rigidities (above ~ 10 GV), the e^-/p ratio remained unchanged to a certain extent during this time. A similar qualitative behaviour is observed for 2008 and 2009, except that the e^-/p ratios for these periods only increased notably below ~ 3 GV. Even though the 2009 PAMELA ratio shows significant variation in observations, the

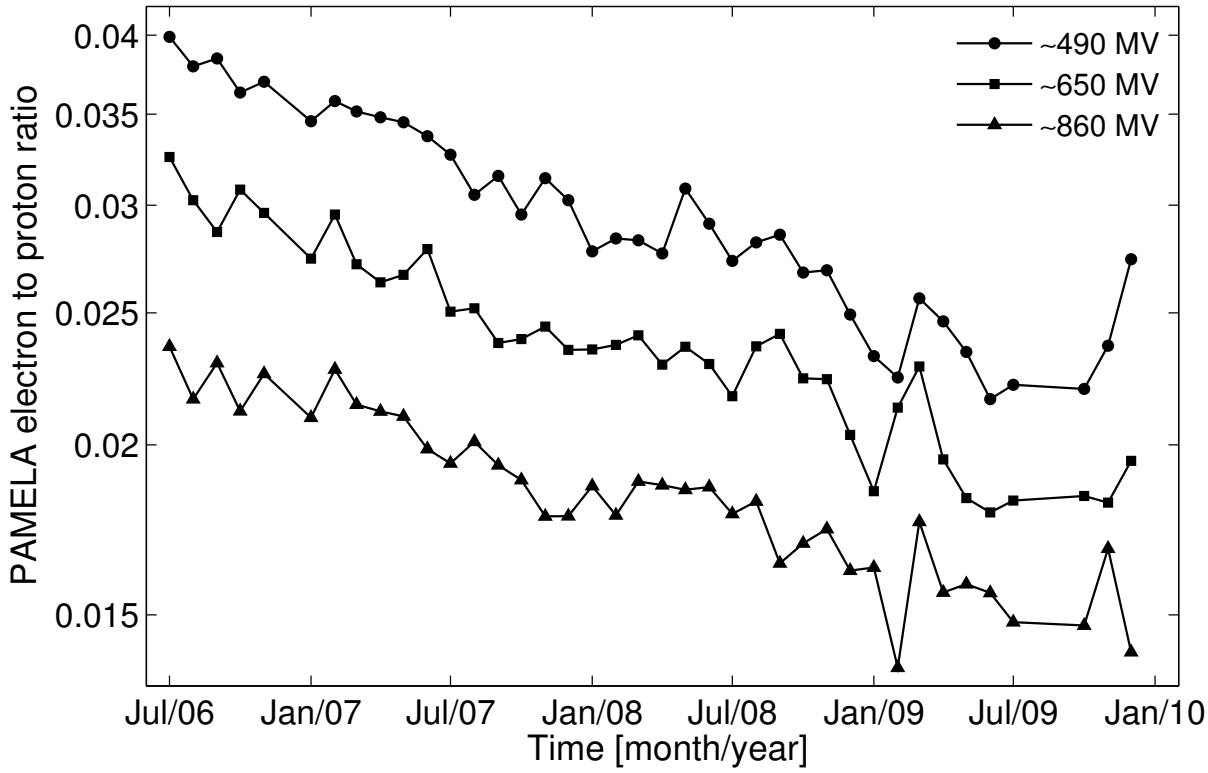

Figure 6.15: PAMELA electron to proton ratios at rigidities of ~ 490 MV (circles), ~ 650 MV (squares) and ~ 860 MV (triangles), as function of time, from July, 2006 to December, 2009.

computed ratio still gives an accurate representation of the PAMELA e^-/p ratio. From 2006 to 2009, the e^-/p ratio at 1 GV decreased by $\sim 35\%$, from a factor of $\sim 2 \times 10^{-2}$ to $\sim 1.35 \times 10^{-2}$. Qualitatively, the e^-/p results of *Langner* (2004) (bottom left panel in Figure 6.3) and *Burger and Potgieter* (1999) (right panel in Figure 6.2) are in good agreement with the computed and observed ratios in Figures 6.10 to 6.13.

In Figure 6.14 a combined plot of the e^-/p ratios is shown, calculated from the computed spectra in Figures 6.5 and 6.6, along with the LIS ratio. An interesting feature observed in this figure, is the crossing of the computed e^-/p ratios and the LIS ratio below ~ 1 GV. In 2006 the modulated e^-/p ratio crossed the LIS ratio at around 200 MV, while still being considerably higher than the LIS ratio for rigidities above ~ 200 MV and below ~ 5 GV. In 2007 this crossing shifted to ~ 250 MV, accompanied by a decrease in the e^-/p ratio which tends toward the LIS ratio. A similar development is observed in the subsequent years. In 2009, where the crossing occurred at ~ 600 MV, the e^-/p ratio is significantly close to the LIS ratio. This progress indicates that, as modulation conditions declined from 2006 to 2009, the modulated e^-/p ratio approached the LIS ratio for rigidities above ~ 600 MV. Considering the PAMELA 2009 ratio in Figure 6.13, it might have been possible for PAMELA to measure the LIS ratio indi-

rectly via the modulated e^-/p ratio if solar minimum conditions had persisted after 2009.

Figure 6.15 gives the time dependence of the e^-/p PAMELA ratios for rigidities of ~ 490 MV (circles), ~ 650 MV (squares), and ~ 860 MV (triangles). It is evident that the e^-/p ratios at these rigidities decreased in a similar manner (by a factor of ~ 1.7) from July, 2006 to December, 2009. Since, according to the modelled spectra, the diffusion coefficients of electrons and protons are expected to be fairly similar in this rigidity range, it follows that the decrease observed in the e^-/p ratios in Figure 6.15 is primarily due to particle drifs. The decreases in the e^-/p ratios are supportive of the predictions of *Burger and Potgieter* (1999; see shaded region in the right panel of Figure 6.2). A similar argument was given above for the e^-/p observations in Figures 6.7 to 6.9.

The importance of simultaneous measurements of protons and electrons, in order to better understand the modulation of galactic CRs in the heliosphere, is emphasized by the work of *Heber et al.* (2009), who conducted a detailed study of the modulation of these particles during the recent solar minimum using Ulysses observations. Moreover, the work done by *Ferreira and Potgieter* (2004) essentially implies that such measurements (Figures 6.5 to 6.13) can only be understood correctly if all physical transport processes in the heliosphere are taken into account.

Ultimately, by using simultaneously observed electron and positron measurements from PAMELA – when the latter becomes available – an even more accurate study of charge-sign dependent modulation will be possible. Such a study will yield definitive results with regard to the amount of gradient, curvature, and HCS drifts that CR particles experienced during the recent solar minimum.

6.5 Summary

In this chapter an overview of previous charge-sign dependent modulation studies was given. From an investigation of the tilt angle dependence of CR protons at Earth, *Burger and Potgieter* (1999) showed that the intensity-tilt profile of protons has a peaked shape during an $A < 0$ magnetic polarity cycle around solar minimum, whereas for an $A > 0$ cycle the response is much flatter (Figure 6.1). The shapes of these profiles are a direct consequence of drifts, in particular drift along the HCS. They also investigated the tilt angle and solar polarity-sign dependence of e^-/He^{++} and e^-/p ratios at Earth (Figure 6.2). The distinct "w" and "m" shapes, predicted in the ratios during $A > 0$ and $A < 0$ cycles, respectively, are another consequence of the effect of particle drifts.

The e^-/e^+ and e^-/p ratios of *Langner* (2004) and *Langner and Potgieter* (2004) were shown in Figure 6.3, which give an indication of the energy dependence of these ratios. Furthermore, by using corrected electron and proton observations from Ulysses, *Heber*

et al. (2002) studied charge-sign dependent modulation of CRs during the period of 1991 to 2000. They found that the e^-/p ratio increased with the approach of solar maximum, which indicated that particle drifts were diminishing. From the variation in the e^-/p ratio, *Heber et al.* (2002) concluded that drifts were important over a large part of the 11-year $A > 0$ cycle, from 1991 to 2000.

In Section 6.3 an overview was given of the proton and electron results presented in Chapters 4 and 5, respectively (see Figures 6.5 and 6.6). The PAMELA proton and electron observations were investigated as function of time, in light of charge-sign dependent modulation. The distinct peak-shaped intensity-time profile expected from protons, which drift inward along the HCS in the equatorial region, is clearly identifiable from the PAMELA observations in Figure 6.7, whereas Figure 6.8 shows the comparatively flatter profiles of electrons, which drift inward over the poles. The difference in these characteristic time profiles can be ascribed to particle drifts.

In order to study charge-sign dependent modulation of CRs in the heliosphere, the subsequent electron and proton spectra from 2006 to 2009 were used to calculate the corresponding e^-/p ratios from PAMELA observations and the computed spectra. These ratios were shown in Figures 6.10 to 6.13. Apart from slight deviations, the computed ratios give reasonably accurate representations of the PAMELA ratios. From the shape of these ratios, certain characteristic features of the modulation of protons and electrons are readily observed. For example, the rapid increase in the e^-/p ratio at low rigidities is indicative of the large adiabatic energy losses experienced by protons at low energies (and the lack thereof for eletrons). Proton intensities, as a result of the combined effects from diffusion and particle drifts, increased notably more than electrons from 2006 to 2009. Consequently, the e^-/p ratio at 1 GV decreased by $\sim 35\%$ during this time, from a factor of $\sim 2 \times 10^{-2}$ to $\sim 1.35 \times 10^{-2}$. It was also found from Figure 6.14 that the decrease in the modulated e^-/p ratio from 2006 to 2009 tends toward the LIS ratio. As a result, the observed (and computed) modulated e^-/p ratio of 2009 is almost similar to that of the LIS above ~ 600 MV. In Figure 6.15, the time dependence of the e^-/p ratios were also investigated. These results were found to be in agreement with the work of *Burger and Potgieter* (1999), *Langner* (2004), and *Langner and Potgieter* (2004).

When positron observations from PAMELA become available, a more accurate study of the effect that particle drifts had on CR modulation during the recent solar minimum will be possible from the e^-/e^+ ratio (see e.g. *Potgieter and Langner*, 2004).

Chapter 7

Summary and Conclusions

A preparatory introduction of the physics related to the heliospheric modulation of CRs was given in Chapter 2. The analytical description of the SW, as assumed in this study, was discussed and expressions were given for radial and polar angle dependencies of the SW speed profile that best corresponds to observations. This was followed by a detailed discussion of the structure of the Parker magnetic field and modifications thereof. For this study, as was done by *Langner* (2004), the *Jokipii and Kóta* (1989) modification for the heliospheric Parker spiral field has been adopted. A mathematical description of the HCS was given here, as well as a discussion of the variations observed in CRs due to the solar cycle. This chapter concluded with an extensive overview of the PAMELA space mission and the exceptional capabilities of this CR detector.

In Chapter 3 an overview was given of the numerical transport and modulation model for CRs, along with the various underlying physical processes that contribute toward the modulation of these particles. This consisted of discussions of the TPE, the diffusion tensor, particle diffusion and particle drifts. In this study a simplified approach was assumed for the diffusion coefficients of both protons and electrons, where the spatial dependence of $\kappa_{\parallel}$ and $\kappa_{\perp}$ (in the radial and polar directions) goes as B^{-1}, and where the rigidity dependence of these coefficients is taken to be a combination of two power-laws. Furthermore, $\kappa_{\perp,r}$ and $\kappa_{\perp,\theta}$ are scaled by 2% of $\kappa_{\parallel}$. Attention was given to the rigidity dependence of the parallel and perpendicular MFPs for protons and electrons in particular. Particle drifts were also discussed in detail, as well as the numerical scheme and some of the features of the 3D numerical model. As a result of the unique modulation conditions of the recent solar minimum, particle drifts, apart from being modified at low energies, are assumed to be at a maximum in this study, i.e. $\kappa_A = 1.0$.

The numerical model discussed in Chapter 3 was applied to protons in Chapter 4 in order to simulate their transport and modulation in the heliosphere. From a discussion of the proton LIS, it was found that the *Moskalenko et al.* (2002) LIS had to be adjusted

(decreased) in order to normalize it to PAMELA proton observations at energies above ~ 30 GV to a spectral index of $\gamma = -2.74$. By doing this, a reasonable proton LIS is obtained which is consistent with observations and other LIS models. Furthermore, following an extensive overview of the PAMELA monthly-averaged proton spectra, it was found that proton intensities around ~ 100 MeV increased by a factor of ~ 3, from July, 2006 to December, 2009, while remaining nearly unchanged at energies above ~ 15 GeV. The exceptional quiet modulation conditions that prevailed during the recent solar minimum was investigated in light of the average HMF, the HCS tilt angle, NM counts and SSNs. From an overview of these parameters in Figure 4.5, it was also found that the average HMF at Earth reached values as low as ~ 3.5 nT in 2009, accompanied by HCS tilt angle values below 10°. Neutron monitor counts reached intensities in excess of that measured during the previous $A < 0$ solar minimum in March, 1987, while SSNs remained low longer than usual.

The aim of the study in Chapter 4 was to reproduce a selection of four consecutive PAMELA monthly-averaged proton reference spectra, from November, 2006 to December, 2009, each of which is separated by approximately 1 year. This was done in Chapter 4 by using ~ 1 year antecedent averaged values for α and B_e in the numerical model, which correspond to the reference spectra. From the first to the last reference spectrum, these values for α are 15.7°, 14.0°, 14.3° and 10.0°; and for B_e they are 5.05 nT, 4.50 nT, 4.25 nT and 3.94 nT. Moreover, by changing the rigidity dependence of $\lambda_{\parallel}$ and $\lambda_{\perp}$ (both radial and perpendicular), the amount of diffusion could be carefully adjusted in order to produce spectra that accurately represent the PAMELA reference spectra. These computed spectra, along with the PAMELA reference spectra, are presented in Figures 4.7 to 4.10. Figure 4.12 illustrates how the rigidity dependence of the proton MFPs had to change in order to reproduce the PAMELA reference spectra. At rigidities below ~ 2 GV, the MFPs for protons changed from a $P^{0.56}$ dependence in 2006 to a $P^{0.48}$ dependence in 2007, and from a $P^{0.39}$ dependence in 2008 to a $P^{0.28}$ dependence in 2009. At 1 GV, for example, $\lambda_{\parallel}$ increased by a factor of more than 20, from ~ 0.13 AU in 2006, to ~ 3 AU in 2009. Above ~ 5 GV the proton MFPs had a steady $P^{1.95}$ dependence during this time. See Table 4.1 for a summary of these parameters. The extent to which certain individual modulation processes contributed to the total observed modulation from 2006 to 2009 was also investigated, the results of which are given in Figures 4.13 to 4.15 as energy spectra ratios relative to November, 2006, and as differential intensities as function of time in Figure 4.17.

It follows from the above-mentioned results that proton intensities experienced a substantial increase at lower energies (below ~ 1 GeV), which, in order to reproduce the PAMELA reference spectra, required a similar increase in $\lambda_{\parallel}$ and $\lambda_{\perp}$ (radial and polar). Furthermore, it was found from the ratios in Figures 4.13 to 4.15 that changes

in the HCS tilt angle, the diffusion coefficients and global drifts (via the HMF in Equation 3.47) *all* contribute to noticeable increases in proton intensities for consecutive years. At 1 GeV, the changes in the tilt angle, diffusion coefficients, and global drifts (via the drift coefficient) respectively accounted for $\sim 20\%$, $\sim 60\%$ and $\sim 30\%$ of the total intensity increase from 2006 to 2009. Using the numerical model, it is shown in Figure 4.17 that by excluding, for example, the effect of global particle drifts, which result from the decrease in the HMF (via the drift coefficient), proton intensities could have been $\sim 10\%$ below the intensity level observed by PAMELA at the end of 2009. It is apparent, however, that the prominent effects of diffusion may have overshadowed the effects that result from changes in the tilt angle and global drifts, as modulation had come to a minimum by the end of 2009. Nonetheless, this study serves to illustrate the importance of each of these processes, especially for the recent solar minimum, during which drifts were expected to be a maximum. It is therefore concluded that *all* modulation processes contributed, to some extent, to the observed changes in the proton energy spectra.

In Chapter 5 a similar study was done for electrons. The electron LIS which is used here, assumed to consist of two power laws, is based on the *Webber and Higbie* (2008) IS-7 LIS, and was normalized to PAMELA electron observations at energies above ~ 30 GeV, to a spectral index of $\gamma = -3.15$. Below ~ 20 GeV, the electron LIS was modified with slightly enhanced intensities in order to account for a region of unusually higher intensities observed in PAMELA electron spectra at Earth. This was followed by an overview of PAMELA's monthly-averaged electron spectra from July, 2006 to December, 2009. It is evident from this overview that electrons experienced the largest increase in intensities below ~ 1 GeV, similar to what was found for protons. However, the increase in electron intensities from 2006 to 2009 is significantly less than for protons. At ~ 300 MeV, for example, electron intensities increased by a factor of only ~ 1.8. It should also be noted that above ~ 23 GeV a single averaged electron spectrum was used.

Figures 5.5 to 5.8 show a selection of four PAMELA electron spectra which serve as reference spectra, overlaid by the corresponding computed spectra. These reference spectra correspond to the proton reference spectra, so that the same values of α and B_e used for protons were used in reproducing the electron reference spectra. Figure 5.9 shows how the rigidity dependence of $\lambda_{\parallel}$ and $\lambda_{\perp}$ (radial and polar) for electrons was changed in order to obtain solutions that best represent the reference spectra. The electron MFPs have a $P^{1.23}$ dependence above ~ 1 GV, but are assumed to be independent of rigidity below ~ 200MV. The PAMELA reference spectra was reproduced by using $\lambda_{\parallel} \approx 5 \times 10^{-2}$ AU for 2006, $\lambda_{\parallel} \approx 6.8 \times 10^{-2}$ AU for 2007, $\lambda_{\parallel} \approx 7.2 \times 10^{-2}$ AU for 2008 and $\lambda_{\parallel} \approx 8.2 \times 10^{-2}$ AU for 2009. The bend between the rigidity independent range

and the $P^{1.23}$ dependence occured around 340 MV in 2006, at ~ 430 MV in 2007 and at ~ 450 MV thereafter (see Table 5.1 for a summary of the modulation parameters). A study was also conducted of how changes in the tilt angle, the diffusion coefficients and global drifts (via κ_A) contribute to the observed intensity increases from 2006 to 2009. These results are presented in Figures 5.10 to 5.12 as ratios of energy spectra relative to the first reference spectrum of July, 2006.

From the results discussed above, it follows that $\lambda_{\parallel}$ for electrons increased by a factor of ~ 1.65 below ~ 200 MV, from 2006 to 2009, which is significantly less than for protons. Furthermore, from the ratios in Figures 5.10 to 5.12, it was found that electrons are almost unaffected by the changes that occurred in the tilt angle during the recent solar minimum, while changes in the diffusion coefficients and global drifts (via the drift coefficient) played major roles. According to simulation results in Figure 5.14, the total changes in the tilt angle, diffusion coefficients and global drift (via κ_A) contributed $\sim 5\%$, $\sim 50\%$ and $\sim 45\%$ respectively at 1 GeV. Similar to what was concluded for protons, an accurate study of electron modulation during the recent solar minimum is only possible when all modulation processes are taken into account, especially global drifts and diffusion, since each of these processes contributed to some extent to the changes observed in the electron energy spectra.

An overview of previous observations and modelling studies from *Burger and Potgieter* (1999), *Langner* (2004), and *Heber et al.* (2003) was given in Chapter 6. The proton and electron results from Chapters 4 and 5 were summarized in Figures 6.5 to 6.6, which show combined plots of the PAMELA reference spectra, along with the corresponding computed spectra. This was followed by discussions of PAMELA proton and electron observations as a function of time. By plotting these normalized intensities on the same scale, the distinct shapes expected for oppositely charged partices were identifiable from their time profiles. The proton time profiles were peak-shaped, while the electron time profiles were noticeably flatter. This effect was quantitatively illustrated in Figure 6.9, where the intensities of protons and electrons between ~ 0.5 GV and ~ 1.0 GV were plotted as a function of time and normalized with respect to November, 2006. Over the time period from November, 2006 to December, 2009, proton intensities in this rigidity range increased on average by a factor of ~ 2.5, while electron intensities only increased by ~ 1.4. This difference between the modulation of protons and electrons is primarily ascribed to drifts, since the diffusion coefficients of protons and electrons are quite similar at these rigidities. During an $A < 0$ magnetic cycle, protons drift into the heliosphere along the HCS in the equatorial plain, their intensities haven't yet reached solar minimum levels, which is why proton intensities still increased substantially until the end of 2009. Electrons, however, drift easily into the heliosphere over the polar regions, so that their intensities already reached minimum

levels around 2007.

The PAMELA e^-/p ratios were also investigated in Figures 6.10 to 6.13, where it was found that, apart from small fluctuations, the computed ratios agreed well to observations. At 1 GV the e^-/p ratio was $\sim 2.0 \times 10^{-2}$ in 2006, after which it decreased by $\sim 35\%$, to a value of $\sim 1.3 \times 10^{-2}$ in 2009, which is almost exactly the value observed for the LIS ratio. Another evident feature illustrated in Figure 6.14, was the development of the computed e^-/p ratios that approached the LIS ratio. Below 10 GV, the modulated e^-/p ratio crossed the LIS ratio at ~ 200 MV. This crossing shifted to ~ 600 MV, while the modulated ratio became progressively similar to the LIS ratio at rigidities above ~ 600 MV. It was concluded that if solar minimum conditions persisted after 2009, the LIS ratio might have been measured indirectly through the modulated e^-/p ratio. The time dependence of the e^-/p ratio at rigidities of ~ 490 MV, ~ 650 MV and ~ 860 MV was also discussed (Figure 6.15). It was found that the e^-/p ratio at all these rigidities decreased by a factor of ~ 1.7 from July, 2006 to December, 2009.

It can be concluded from the above results that drifts did indeed have a mentionable effect on the modulation of oppositely charged particles for the period studied. This is in contrast to the work of *Cliver et al.* (2011), who concluded that drifts were not playing a significant role during this unusual solar minimum. For an overview of how unprecedented the recent solar minimum period was, see the review of *Russell et al.* (2010). This study illustrated the importance of simultaneous measurements of protons and electrons which can be used to better understand charge-sign dependent modulation of CRs in the heliosphere.

With the exceptional quality of PAMELA data, the recent solar minimum has been thoroughly observed with regard to CR intensities at Earth. Never before has such an extensive collection of energy spectra been available to investigate the modulation of CRs during solar minimum, much less one for which modulation conditions were remarkably quiet, as was the case for the recent solar minimum. Moreover, the benchmarked 3D modulation model used in this study provides the opportunity to simulate the transport and modulation of CRs in a realistic heliosphere, yielding compelling results that can be validated using PAMELA data. With a combination of computed results and accurate PAMELA data, an in-depth study of CR modulation, especially charge-sign dependent modulation, was possible.

Even though PAMELA positron observations have not yet been made available by the end of 2011, a future study of both electrons and positrons will allow for an even more detailed investigation of CR modulation. Such a study will produce credible results concerning the amount of gradient, curvature and HCS drifts that oppositely charged CR particles experience in the heliosphere during solar minimum periods, especially if so unusual as the recent one. Predictions can then be made for the next

solar minimum, when $A > 0$.

References

Adriani, O., et al., New measurement of the antiproton-to-proton flux ratio up to 100 GeV in the cosmic radiation, *Physical Review Letters*, *102*, 05101, 1–5, 2009a.

Adriani, O., et al., The PAMELA space mission, *Nuclear Physics B Proceedings Supplements*, *188*, 296–298, 2009b.

Adriani, O., et al., PAMELA measurements of cosmic-ray proton and helium spectra, *Science*, *332*, 69–72, 2011a.

Adriani, O., et al., Observations of the December 13 and 14, 2006, solar particle events in the 80 MeV/n - 3 GeV/n range from space with PAMELA detector, *Astrophysical Journal*, *742*, 102, 1–11, 2011b.

Adriani, O., et al., Cosmic-ray electron flux measured by the PAMELA experiment between 1 and 625 GeV, *Physical Review Letters*, *106*, 201101, 1–5, 2011c.

Alfven, H., Electric currents in cosmic plasmas, *Reviews of Geophysics and Space Physics*, *15*, 271–284, 1977.

Atoyan, A. M., F. A. Aharonian, and H. J. Völk, Electrons and positrons in the galactic cosmic rays, *Physical Review D (Particles, Fields, Gravitation, and Cosmology)*, *52*, 3265–3275, 1995.

Balogh, A., E. J. Smith, B. T. Tsurutani, D. J. Southwood, R. J. Forsyth, and T. S. Horbury, The heliospheric magnetic field over the south polar region of the Sun, *Science*, *268*, 1007–1010, 1995.

Bieber, J. W., R. A. Burger, R. Engel, T. K. Gaisser, S. Roesler, and T. Stanev, Antiprotons at solar maximum, *Physical Review Letters*, *83*, 674–677, 1999.

Bieber, J. W., and W. H. Matthaeus, Cosmic ray pitch angle scattering in dynamical magnetic turbulence, in *Proceedings of the International Cosmic Ray Conference, 3*, 248-251, 1991.

Bieber, J. W., W. H. Matthaeus, A. Shalchi, and G. Qin, Nonlinear guiding center theory of perpendicular diffusion: General properties and comparison with observation, *Geophysical Research Letters*, *31*, L10805, 1–4, 2004.

Bieber, J. W., W. H. Matthaeus, C. W. Smith, W. Wanner, M.-B. Kallenrode, and G. Wibberenz, Proton and electron mean free paths: The Palmer consensus revisited, *Astrophysical Journal*, *420*, 294–306, 1994.

Biermann, L., The solar wind and the interplanetary media, in *Space Astrophysics*, edited by Liller, W., pp. 150–156, New York: McGraw-Hill, 1961.

Boezio, M., et al., PAMELA and indirect dark matter searches, *New Journal of Physics*, *11*, 105023, 1–25, 2009.

Burger, R. A., On the theory and application of drift motion of charged particles in inhomogeneous magnetic fields, Ph.D. thesis, Potchefstroom University, South Africa, 1987.

Burger, R. A., Cosmic-ray modulation and the heliospheric magnetic field, *Advances in Space Research*, *35*, 636–642, 2005.

Burger, R. A., and M. Hattingh, Effect of Fisk-type heliospheric magnetic fields on the latitudinal transport of cosmic rays, in *Proceedings of the International Cosmic Ray Conference, 9,* 3698-3701, 2001.

Burger, R. A., and M. Hitge, The effect of a Fisk-type heliospheric magnetic field on cosmic-ray modulation, *Astrophysical Journal Letters*, *617*, L73–L76, 2004.

Burger, R. A., T. P. J. Krüger, M. Hitge, and N. E. Engelbrecht, A Fisk-Parker hybrid heliospheric magnetic field with a solar-cycle dependence, *Astrophysical Journal*, *674*, 511–519, 2008.

Burger, R. A., H. Moraal, and G. M. Webb, Drift theory of charged particles in electric and magnetic fields, *Astrophysics and Space Science*, *116*, 107–129, 1985.

Burger, R. A., and M. S. Potgieter, The calculation of neutral sheet drift in two-dimensional cosmic-ray modulation models, *Astrophysical Journal*, *339*, 501–511, 1989.

Burger, R. A., and M. S. Potgieter, The effect of large heliospheric current sheet tilt angles in numerical modulation models: A theoretical assessment, in *Proceedings of the International Cosmic Ray Conference, 7,* 13-16, 1999.

Burger, R. A., M. S. Potgieter, and B. Heber, Rigidity dependence of cosmic ray proton latitudinal gradients measured by the Ulysses spacecraft: Implications for the diffusion tensor, *Journal of Geophysical Research*, *105*, 27447–27456, 2000.

Caballero-Lopez, R. A., H. Moraal, and F. B. McDonald, The modulation of galactic cosmic-ray electrons in the heliosheath, *Astrophysical Journal*, *725*, 121–127, 2010.

Casolino, M., et al., The PAMELA experiment: A space-borne observatory for heliospheric phenomena, *Advances in Space Research*, *41*, 2043–2049, 2008.

Casolino, M., et al., Cosmic ray measurements with PAMELA experiment, *Nuclear Physics B Proceedings Supplements*, *190*, 293–299, 2009.

Chenette, D. L., T. F. Conlon, and J. A. Simpson, Burst of relativistic electrons from Jupiter observed in interplanetary space with the time variation of the planetary rotation period, *Journal of Geophysical Research*, *79*, 3551–3558, 1974.

Cliver, E. W., Solar energetic particles: Acceleration and transport, in *Proceedings of the International Cosmic Ray Conference, 516,* 103-119, 2000.

Cliver, E. W., I. G. Richardson, and A. G. Ling, Solar drivers of 11-yr and long-term cosmic ray modulation, *Space Science Reviews,* available online, 2011.

De Simone, N., Galactic and solar proton flux measurements in the energy range 80 MeV - 1.2 TeV with the PAMELA space experiment, Ph.D. thesis, University of Rome Tor Vergata, Italy, 2011.

Di Felice, V., Low energy electron and positron measurements in space with the PAMELA experiment, Ph.D. thesis, University of Rome Tor Vergata, Italy, 2010.

Douglas, J., On the numerical integration $\frac{\partial^2 u}{\partial x^2} + \frac{\partial^2 u}{\partial y^2} = \frac{\partial u}{\partial t}$ by implicit methods, *Journal of the Society for Industrial and Applied Mathematics*, *3*, 42–65, 1955.

Douglas, J., Alternating direction methods for three space variables, *Numerische Mathematik*, *4*, 41–63, 1962.

Earl, J. A., The diffusive idealization of charged-particle transport in random magnetic fields, *Astrophysical Journal*, *193*, 231–242, 1974.

Engelbrecht, N. E., On the heliospheric diffusion tensor and its effect on 26-day recurrent cosmic ray variations, Master's dissertation, North-West University, South Africa, 2008.

Evenson, P., and J. Clem, Cosmic ray electron spectrum in 2009, in *Proceedings of the International Cosmic Ray Conference, 11,* 54-58, 2011.

Ferreira, S. E. S., A study of the modulation of cosmic ray electrons in the heliosphere, Master's dissertation, Potchefstroom University, South Africa, 1998.

Ferreira, S. E. S., The heliospheric transport of galactic cosmic rays and jovian electrons, Ph.D. thesis, Potchefstroom University, South Africa, 2002.

Ferreira, S. E. S., and M. S. Potgieter, Long-term cosmic-ray modulation in the heliosphere, *Astrophysical Journal*, *603*, 744–752, 2004.

Ferreira, S. E. S., M. S. Potgieter, and R. A. Burger, Comparison of a two- and three-dimensional drift model, in *Proceedings of the International Cosmic Ray Conference, 7,* 77-80, 1999.

Ferreira, S. E. S., M. S. Potgieter, R. A. Burger, and B. Heber, Modulation effects of anisotropic perpendicular diffusion on cosmic ray electron intensities in the heliosphere, *Journal of Geophysical Research*, *105*, 18305–18314, 2000.

Ferreira, S. E. S., M. S. Potgieter, R. A. Burger, B. Heber, and H. Fichtner, Modulation of Jovian and galactic electrons in the heliosphere: 1. Latitudinal transport of a few MeV electrons, *Journal of Geophysical Research*, *106*, 24979–24988, 2001a.

Ferreira, S. E. S., M. S. Potgieter, B. Heber, and H. Fichtner, Charge-sign dependent modulation in the heliosphere over a 22-year cycle, *Annales Geophysicae*, *21*, 1359–1366, 2003.

Ferreira, S. E. S., M. S. Potgieter, B. Heber, H. Fichtner, R. A. Burger, and P. Ferrando, A study of the compatibility between observations and model simulations for Jovian and galactic electrons, *Advances in Space Research*, *27*, 553–558, 2001b.

Fichtner, H., Anomalous cosmic rays: Messengers from the outer heliosphere, *Space Science Reviews*, *95*, 639–754, 2001.

Fichtner, H., M. Potgieter, S. Ferreira, and A. Burger, On the propagation of Jovian electrons in the heliosphere: Transport modelling in 4-D phase space, *Geophysical Research Letters*, *27*, 1611–1614, 2000.

Fichtner, H., M. S. Potgieter, S. E. S. Ferreira, B. Heber, and R. A. Burger, Time-dependent 3-D modelling of the heliospheric propagation of few-MeV electrons, in *Proceedings of the International Cosmic Ray Conference, 9,* 3666-3669, 2001.

Fichtner, H., and K. Scherer, The heliosphere: A brief overview, in *The Outer Heliosphere: Beyond the Planets*, edited by K. Scherer, H. Fichtner, and E. Marsch, pp. 1–12, Katlenburg-Lindau: Copernicus Publications, 2000.

Fisk, L. A., Solar modulation of galactic cosmic rays, 2., *Journal of Geophysical Research*, *76*, 221–226, 1971.

Fisk, L. A., Modulation of solar cosmic rays, *NASA Special Publication*, *342*, 418, 1973.

Fisk, L. A., Motion of the footpoints of heliospheric magnetic field lines at the Sun: Implications for recurrent energetic particle events at high heliographic latitudes, *Journal of Geophysical Research*, *101*, 15547–15554, 1996.

Fisk, L. A., An overview of the transport of galactic and anomalous cosmic rays in the heliosphere: Theory, *Advances in Space Research*, *23*, 415–423, 1999.

Florinski, V., G. P. Zank, and N. V. Pogorelov, Galactic cosmic ray transport in the global heliosphere, *Journal of Geophysical Research*, *108*, 1228, SSH1: 1–16, 2003.

Forbush, S. E., Three unusual cosmic-ray increases possibly due to charged particles from the Sun, *Physical Review*, *70*, 771–772, 1946.

Forsyth, R. J., A. Balogh, E. J. Smith, G. Erdös, and D. J. McComas, The underlying Parker spiral structure in the Ulysses magnetic field observations, 1990-1994, *Journal of Geophysical Research*, *101*, 395–404, 1996.

Gaisser, T. K., and R. K. Schaefer, Cosmic-ray secondary antiprotons - A closer look, *Astrophysical Journal*, *394*, 174–183, 1992.

Giacalone, J., and J. R. Jokipii, The transport of cosmic rays across a turbulent magnetic field, *Astrophysical Journal*, *520*, 204–214, 1999.

Ginzburg, V. L., and S. I. Syrovatskii, *The origin of cosmic rays,* 62 pp., New York: Gordon and Breach, 1969.

Gleeson, L. J., and W. I. Axford, Cosmic rays in the interplanetary medium, *Astrophysical Journal Letters*, *149*, L115–L118, 1967.

Gleeson, L. J., and W. I. Axford, The Compton-getting effect, *Astrophysics and Space Science*, *2*, 431–437, 1968.

Haasbroek, L. J., Modulation of cosmic rays in the heliosphere: A model study of the Ulysses mission (in Afrikaans), Ph.D. thesis, Potchefstroom University, South Africa, 1993.

Haasbroek, L. J., and M. S. Potgieter, The modulation of cosmic rays in the high latitude heliosphere: A computer simulation, *Space Science Reviews*, *72*, 385–390, 1995.

Haasbroek, L. J., M. S. Potgieter, and J. A. le Roux, The time-dependent recovery after the large cosmic-ray decrease in 1991, in *Proceedings of the International Cosmic Ray Conference, 4,* 710-713, 1995.

Hattingh, M., Drift of cosmic rays at a wavy neutral sheet in the heliosphere (in Afrikaans), Master's dissertation, Potchefstroom University, South Africa, 1993.

Hattingh, M., The modulation of galactic cosmic rays in a three-dimensional heliosphere, Ph.D. thesis, Potchefstroom University, South Africa, 1998.

Heber, B., Modulation of galactic and anomalous cosmic rays in the inner heliosphere, *Advances in Space Research*, *27*, 451–460, 2001.

Heber, B., J. M. Clem, R. Müller-Mellin, H. Kunow, S. E. S. Ferreira, and M. S. Potgieter, Evolution of the galactic cosmic ray electron to proton ratio: Ulysses COSPIN/KET observations, *Geophysical Research Letters*, *30*, 8032, ULY 6: 1–4, 2003.

Heber, B., et al., Ulysses cosmic ray and solar particle investigation/Kiel Electron Telescope observations: Charge sign dependence and spatial gradients during the 1990-2000 $A > 0$ solar magnetic cycle, *Journal of Geophysical Research*, *107*, 1274, SSH 2: 1–10, 2002.

Heber, B., A. Kopp, J. Gieseler, R. Müller-Mellin, H. Fichtner, K. Scherer, M. S. Potgieter, and S. E. S. Ferreira, Modulation of galactic cosmic ray protons and electrons during an unusual solar minimum, *Astrophysical Journal*, *699*, 1956–1963, 2009.

Heber, B., and M. S. Potgieter, Cosmic rays at high heliolatitudes, *Space Science Reviews*, *127*, 117–194, 2006.

Heber, B., T. R. Sanderson, and M. Zhang, Corotating interaction regions, *Advances in Space Research*, *23*, 567–579, 1999.

Hoeksema, J. T., Large-scale structure of the heliospheric magnetic field - 1976-1991, in *Solar Wind Seven Colloquium*, edited by E. Marsch and R. Schwenn, pp. 191–196, 1992.

Jokipii, J. R., Cosmic-ray propagation. I. Charged particles in a random magnetic field, *Astrophysical Journal*, *146*, 480–487, 1966.

Jokipii, J. R., Particle acceleration at a termination shock. I - Application to the solar wind and the anomalous component, *Journal of Geophysical Research*, *91*, 2929–2932, 1986.

Jokipii, J. R., Latitudinal heliospheric magnetic field: Stochastic and causal components, *Journal of Geophysical Research*, *106*, 15841–15848, 2001.

Jokipii, J. R., and D. A. Kopriva, Effects of particle drift on the transport of cosmic rays. III - Numerical models of galactic cosmic-ray modulation, *Astrophysical Journal*, *234*, 384–392, 1979.

Jokipii, J. R., and J. Kóta, The polar heliospheric magnetic field, *Geophysical Research Letters*, *16*, 1–4, 1989.

Jokipii, J. R., J. Kóta, J. Giacalone, T. S. Horbury, and E. J. Smith, Interpretation and consequences of large-scale magnetic variances observed at high heliographic latitude, *Geophysical Research Letters*, *22*, 3385–3388, 1995.

Jokipii, J. R., and E. H. Levy, Effects of particle drifts on the solar modulation of galactic cosmic rays, *Astrophysical Journal Letters*, *213*, L85–L88, 1977.

Jokipii, J. R., E. H. Levy, and W. B. Hubbard, Effects of particle drift on cosmic-ray transport. I - General properties, application to solar modulation, *Astrophysical Journal*, *213*, 861–868, 1977.

Jokipii, J. R., and E. N. Parker, On the convection, diffusion, and adiabatic deceleration of cosmic rays in the solar wind, *Astrophysical Journal*, *160*, 735–744, 1970.

Jokipii, J. R., and B. Thomas, Effects of drift on the transport of cosmic rays. IV - Modulation by a wavy interplanetary current sheet, *Astrophysical Journal*, *243*, 1115–1122, 1981.

Kóta, J., 3-D simulations of heliospheric transport: A comparison of models, in *Proceedings of the International Cosmic Ray Conference, 2,* 25-28, 1997.

Kóta, J., Cosmic-ray modulation and the structure of the heliospheric magnetic field, in *Proceedings of the International Cosmic Ray Conference, 7,* 9-12, 1999.

Kóta, J., and J. R. Jokipii, Effects of drift on the transport of cosmic rays. VI - A three-dimensional model including diffusion, *Astrophysical Journal*, *265*, 573–581, 1983.

Kóta, J., and J. R. Jokipii, 3-D distribution of cosmic rays in the outer heliosphere, in *Proceedings of the International Cosmic Ray Conference, 4,* 680-683, 1995.

Koyama, K., R. Petre, E. V. Gotthelf, U. Hwang, M. Matsuura, M. Ozaki, and S. S. Holt, Evidence for shock acceleration of high-energy electrons in the supernova remnant SN1006, *Nature*, *378*, 255–258, 1995.

Krieger, A. S., A. F. Timothy, and E. C. Roelof, A coronal hole and its identification as the source of a high velocity solar wind stream, *Solar Physics*, *29*, 505–525, 1973.

Krüger, H. A., A calibration neutron monitor for long-term cosmic ray modulation studies, Ph.D. thesis, North-West University, South Africa, 2006.

Langner, U. W., Effects of different local interstellar spectra on the heliospheric modulation of cosmic rays, Master's dissertation, Potchefstroom University, South Africa, 2000.

Langner, U. W., Effects of termination shock acceleration on cosmic rays in the heliosphere, Ph.D. thesis, Potchefstroom University, South Africa, 2004.

Langner, U. W., O. C. de Jager, and M. S. Potgieter, On the local interstellar spectrum for cosmic ray electrons, *Advances in Space Research*, *27*, 517–522, 2001.

Langner, U. W., and M. S. Potgieter, Effects of the solar wind termination shock on charge-sign dependent cosmic ray modulation, *Advances in Space Research*, *34*, 144–149, 2004.

Langner, U. W., M. S. Potgieter, and W. R. Webber, Modulation of cosmic ray protons in the heliosheath, *Journal of Geophysical Research*, *108*, 8039, LIS 14: 1–9, 2003.

Lapidus, L., and G. Pinder, *Numerical solution of partial differential equations in science and engineering,* 677 pp., New York: Wiley-Interscience, 1982.

le Roux, J. A., The solar modulation of galactic cosmic rays as described by a time-dependent drift model, Ph.D. thesis, Potchefstroom University, South Africa, 1990.

le Roux, J. A., and M. S. Potgieter, The simulation of complete 11 and 12 year modulation cycles for cosmic rays in the heliosphere using a drift model with global merged interaction regions, *Astrophysical Journal*, *442*, 847–851, 1995.

le Roux, J. A., M. S. Potgieter, and V. S. Ptuskin, A transport model for the diffusive shock acceleration and modulation of anomalous cosmic rays in the heliosphere, *Journal of Geophysical Research*, *101*, 4791–4804, 1996.

Levy, E. H., The interplanetary magnetic field structure, *Nature*, *261*, 394–395, 1976.

Li, H., C. Wang, and J. D. Richardson, Properties of the termination shock observed by Voyager 2, *Geophysical Research Letters*, *351*, L19107: 1–4, 2008.

Marsch, E., Kinetic physics of the solar wind plasma, in *Physics of the Inner Heliosphere II*, edited by Schwenn, R. and Marsch, E., pp. 45–133, Berlin: Springer-Verlag, 1991.

Marsch, E., W. I. Axford, and J. F. McKenzie, Solar wind, in *Dynamic Sun*, edited by Dwivedi, B. N., pp. 374–402, Cambridge University Press, 2003.

Matthaeus, W. H., G. Qin, J. W. Bieber, and G. P. Zank, Nonlinear collisionless perpendicular diffusion of charged particles, *Astrophysical Journal Letters*, *590*, L53–L56, 2003.

McComas, D. J., R. W. Ebert, H. A. Elliott, B. E. Goldstein, J. T. Gosling, N. A. Schwadron, and R. M. Skoug, Weaker solar wind from the polar coronal holes and the whole Sun, *Geophysical Research Letters*, *35*, L18103: 1–5, 2008.

McDonald, F. B., N. Lal, and R. E. McGuire, Cosmic ray recovery and solar minimum phase of solar cycle 22 - An interim report, *Journal of Geophysical Research*, *103*, 373–379, 1998.

McDonald, F. B., W. R. Webber, and D. V. Reames, Unusual time histories of galactic and anomalous cosmic rays at 1 AU over the deep solar minimum of cycle 23/24, *Geophysical Research Letters*, *37*, L18101: 1–5, 2010.

McKibben, R. B., Cosmic-ray diffusion in the inner heliosphere, *Advances in Space Research*, *35*, 518–531, 2005.

Menn, W., et al., The absolute flux of protons and helium at the top of the atmosphere using IMAX, *Astrophysical Journal*, *533*, 281–297, 2000.

Mewaldt, R. A., et al., Record-setting cosmic-ray intensities in 2009 and 2010, *Astrophysical Journal Letters*, *723*, L1–L6, 2010.

Minnie, J., Observational constraints on the heliospheric diffusion tensor for galactic cosmic rays, Master's dissertation, Potchefstroom University, South Africa, 2002.

Minnie, J., An ab initio approach to the heliospheric modulation of galactic cosmic rays, Ph.D. thesis, North-West University, Potchefstroom, South Africa, 2006.

Minnie, J., J. W. Bieber, W. H. Matthaeus, and R. A. Burger, Suppression of particle drifts by turbulence, *Astrophysical Journal*, *670*, 1149–1158, 2007.

Mocchiutti, E., et al., PAMELA and electrons, *Nuclear Instruments and Methods in Physics Research A*, *630*, 28–35, 2011.

Moraal, H., Proton modulation near solar minimum periods in consecutive solar cycles, in *Proceedings of the International Cosmic Ray Conference, 6,* 140-143, 1990.

Moraal, H., and L. J. Gleeson, Three-dimensional models of the galactic cosmic-ray modulation, in *Proceedings of the International Cosmic Ray Conference, 12,* 4189-4194, 1975.

Moraal, H., L. J. Gleeson, and G. M. Webb, Effects of charged particle drifts on the modulation of the intensity of galactic cosmic rays, in *Proceedings of the International Cosmic Ray Conference, 3,* 1-6, 1979.

Moskalenko, I. V., A. W. Strong, J. F. Ormes, and M. S. Potgieter, Secondary antiprotons and propagation of cosmic rays in the Galaxy and heliosphere, *Astrophysical Journal*, *565*, 280–296, 2002.

Ndiitwani, D. C., S. E. S. Ferreira, M. S. Potgieter, and B. Heber, Modelling cosmic ray intensities along the Ulysses trajectory, *Annales Geophysicae*, *23*, 1061–1070, 2005.

Nndanganeni, R. R., Modelling of galactic cosmic ray electrons in the heliosphere, Master's dissertation, North-West University, South Africa, 2011.

Palmer, I. D., Transport coefficients of low-energy cosmic rays in interplanetary space, *Reviews of Geophysics and Space Physics*, *20*, 335–351, 1982.

Parker, E. N., Cosmic-ray modulation by solar wind, *Physical Review*, *110*, 1445–1449, 1958.

Parker, E. N., *Interplanetary Dynamical Processes,* 284 pp., New York: Interscience Publishers, 1963.

Parker, E. N., The passage of energetic charged particles through interplanetary space, *Planetary and Space Science*, *13*, 9–49, 1965.

Parker, E. N., A history of early work on the heliospheric magnetic field, *Journal of Geophysical Research*, *106*, 15797–15802, 2001.

Peaceman, D. W., and H. H. Rachford, The numerical solution of parabolic and elliptic differential equations, *Journal of the Society for Industrial and Applied Mathematics*, *3*, 28–41, 1955.

Perko, J. S., and L. A. Fisk, Solar modulation of galactic cosmic rays. V - Time-dependent modulation, *Journal of Geophysical Research*, *88*, 9033–9036, 1983.

Pesses, M. E., D. Eichler, and J. R. Jokipii, Cosmic ray drift, shock wave acceleration, and the anomalous component of cosmic rays, *Astrophysical Journal Letters*, *246*, L85–L88, 1981.

Peterson, J. D., A new look at galactic polar radio emission and the local interstellar electron spectrum, in *Proceedings of the International Cosmic Ray Conference, 4,* 251-254, 1999.

Phillips, J. L., et al., Ulysses solar wind plasma observations from pole to pole, *Geophysical Research Letters*, *22*, 3301–3304, 1995.

Picozza, P., et al., PAMELA: A payload for antimatter matter exploration and light-nuclei astrophysics, *Astroparticle Physics*, *27*, 296–315, 2007.

Picozza, P., et al., Dark matter research and the PAMELA space mission, in *Proceedings of the American Institute of Physics Conference, 1166,* 141-150, 2009.

Potgieter, M. S., The modulation of galactic cosmic rays as described by a three-dimensional drift model, Ph.D. thesis, Potchefstroom University, South Africa, 1984.

Potgieter, M. S., Heliospheric terminal shock acceleration and modulation of the anomalous cosmic-ray component, *Advances in Space Research*, *9*, 21–24, 1989.

Potgieter, M. S., Heliospheric modulation of galactic electrons: Consequences of new calculations for the mean free path of electrons between 1 MeV and $\sim$10 GeV, *Journal of Geophysical Research*, *101*, 24411–24422, 1996.

Potgieter, M. S., The modulation of galactic cosmic rays in the heliosphere: Theory and models, *Space Science Reviews*, *83*, 147–158, 1998.

Potgieter, M. S., Heliospheric modulation of cosmic ray protons: Role of enhanced perpendicular diffusion during periods of minimum solar modulation, *Journal of Geophysical Research*, *105*, 18295–18304, 2000.

Potgieter, M. S., Solar cycle variations and cosmic rays, *Journal of Atmospheric and Solar-Terrestrial Physics*, *70*, 207–218, 2008.

Potgieter, M. S., The dynamic heliosphere, solar activity, and cosmic rays, *Advances in Space Research*, *46*, 402–412, 2010.

Potgieter, M. S., Cosmic rays in the inner heliosphere: Insights from observations, theory and models, *Space Science Reviews,* available online, 2011.

Potgieter, M. S., R. A. Burger, and S. E. S. Ferreira, Modulation of cosmic rays in the heliosphere from solar minimum to maximum: A theoretical perspective, *Space Science Reviews*, *97*, 295–307, 2001a.

Potgieter, M. S., and S. E. S. Ferreira, The importance of perpendicular diffusion in the heliospheric modulation of cosmic ray electrons, *Advances in Space Research*, *23*, 463–466, 1999.

Potgieter, M. S., and S. E. S. Ferreira, Effects of the solar wind termination shock on the modulation of Jovian and galactic electrons in the heliosphere, *Journal of Geophysical Research*, *107*, 1089, SSH 1: 1–9, 2002.

Potgieter, M. S., and L. J. Haasbroek, The simulation of base-line cosmic-ray modulation for the Ulysses trajectory, in *Proceedings of the International Cosmic Ray Conference, 3,* 457-460, 1993.

Potgieter, M. S., and U. W. Langner, Heliospheric modulation of cosmic-ray positrons and electrons: Effects of the heliosheath and the solar wind termination shock, *Astrophysical Journal*, *602*, 993–1001, 2004.

Potgieter, M. S., U. W. Langner, and S. E. S. Ferreira, Cosmic ray electron to positron ratios in the heliosphere, *Advances in Space Research*, *27*, 523–528, 2001b.

Potgieter, M. S., J. A. le Roux, and R. A. Burger, Interplanetary cosmic ray radial gradients with steady state modulation models, *Journal of Geophysical Research*, *94*, 2323–2332, 1989.

Potgieter, M. S., J. A. le Roux, L. F. Burlaga, and F. B. McDonald, The role of merged interaction regions and drifts in the heliospheric modulation of cosmic rays beyond 20 AU - A computer simulation, *Astrophysical Journal*, *403*, 760–768, 1993.

Potgieter, M. S., and H. Moraal, A drift model for the modulation of galactic cosmic rays, *Astrophysical Journal*, *294*, 425–440, 1985.

Ptuskin, V. S., Origin of galactic cosmic rays: sources, acceleration and propagation (OG-2), in *Proceedings of the International Cosmic Ray Conference, 10,* 317-328, 2005.

Ptuskin, V. S., I. V. Moskalenko, F. C. Jones, A. W. Strong, and V. N. Zirakashvili, Dissipation of magnetohydrodynamic waves on energetic particles: Impact on interstellar turbulence and cosmic-ray transport, *Astrophysical Journal*, *642*, 902–916, 2006.

Richardson, J. D., C. Wang, and K. I. Paularena, The solar wind: From solar minimum to solar maximum, *Advances in Space Research*, *27*, 471–479, 2001.

Roberts, D. A., J. Giacalone, J. R. Jokipii, M. L. Goldstein, and T. D. Zepp, Spectra of polar heliospheric fields and implications for field structure, *Journal of Geophysical Research*, *112*, A08103, 1–6, 2007.

Rossi, B., and S. Olbert, *Introduction to the physics of space,* 454 pp., New York: McGraw-Hill, 1970.

Russell, C. T., J. G. Luhmann, and L. K. Jian, How unprecedented a solar minimum?, *Reviews of Geophysics*, *48*, RG2004: 1–16, 2010.

Scherer, K., H. Fichtner, R. D. Strauss, S. E. S. Ferreira, M. S. Potgieter, and H.-J. Fahr, On cosmic ray modulation beyond the heliopause: Where is the modulation boundary?, *Astrophysical Journal*, *735*, 128, 1–5, 2011.

Schlickeiser, R., On the interplanetary transport of solar cosmic rays, *Journal of Geophysical Research*, *93*, 2725–2729, 1988.

Schlickeiser, R., *Cosmic ray astrophysics,* 519 pp., Berlin: Springer, 2002.

Schwenn, R., The average solar wind in the inner heliosphere: Structures and slow variations, in *Proceedings of the NASA Conference Publication, 2280,* 489-507, 1983.

Sheeley, N. R., Jr., et al., Measurements of flow speeds in the corona between 2 and 30 R_{sun}, *Astrophysical Journal*, *484*, 472–478, 1997.

Simon, P., The solar activity cycle, *L'Astronomie*, *94*, 417–430, 1980.

Simpson, J. A., D. Hamilton, G. Lentz, R. B. McKibben, A. Mogro-Campero, M. Perkins, K. R. Pyle, A. J. Tuzzolino, and J. J. O'Gallagher, Protons and electrons in Jupiter's magnetic field: Results from the University of Chicago Experiment on Pioneer 10, *Science*, *183*, 306–309, 1974.

Smith, E. J., Interplanetary magnetic field over two solar cycles and out to 20 AU, *Advances in Space Research*, *9*, 159–169, 1989.

Smith, E. J., The heliospheric current sheet, *Journal of Geophysical Research*, *106*, 15819–15832, 2001.

Smith, E. J., The global heliospheric magnetic field, in *The Heliosphere through the Solar Activity Cycle*, edited by A. Balogh, L. J. Lanzerotti, and S. T. Suess, pp. 79–150, Berlin: Springer, 2008.

Smith, E. J., and A. Balogh, Decrease in heliospheric magnetic flux in this solar minimum: Recent Ulysses magnetic field observations, *Geophysical Research Letters*, *35*, L22103, 1–4, 2008.

Smith, C. W., and J. W. Bieber, Solar cycle variation of the interplanetary magnetic field spiral, *Astrophysical Journal*, *370*, 435–441, 1991.

Smith, E. J., and R. G. Marsden, Ulysses observations at solar maximum: Introduction, *Geophysical Research Letters*, *30*, 8027, ULY 1: 1–4, 2003.

Snodgrass, H. B., Magnetic rotation of the solar photosphere, *Astrophysical Journal*, *270*, 288–299, 1983.

Steenkamp, R., Shock acceleration as source of the anomalous component of cosmic rays in the heliosphere, Ph.D. thesis, Potchefstroom University, South Africa, 1995.

Sternal, O., N. E. Engelbrecht, R. A. Burger, S. E. S. Ferreira, H. Fichtner, B. Heber, A. Kopp, M. S. Potgieter, and K. Scherer, Possible evidence for a Fisk-type heliospheric magnetic field. I. Analyzing Ulysses/KET electron observations, *Astrophysical Journal*, *741*, 23, 1–12, 2011.

Stix, M., *The Sun: An introduction*, 490 pp., Berlin: Springer, 2004.

Stone, E. C., A. C. Cummings, F. B. McDonald, B. C. Heikkila, N. Lal, and W. R. Webber, Voyager 1 explores the termination shock region and the heliosheath beyond, *Science*, *309*, 2017–2020, 2005.

Stone, E. C., A. C. Cummings, F. B. McDonald, B. C. Heikkila, N. Lal, and W. R. Webber, An asymmetric solar wind termination shock, *Nature*, *454*, 71–74, 2008.

Strauss, R. D., Modelling of anomalous cosmic rays, Master's dissertation, North-West University, South Africa, 2010.

Strauss, R. D., M. S. Potgieter, and S. E. S. Ferreira, The heliospheric transport and modulation of multiple charged anomalous oxygen revisited, *Astronomy and Astrophysics*, *513*, A24, 1–6, 2010a.

Strauss, R. D., M. S. Potgieter, S. E. S. Ferreira, and M. E. Hill, Modelling anomalous cosmic ray oxygen in the heliosheath, *Astronomy and Astrophysics*, *522*, A35, 1–8, 2010b.

Strong, A. W., I. V. Moskalenko, and O. Reimer, Diffuse continuum gamma rays from the galaxy, *Astrophysical Journal*, *537*, 763–784, 2000.

Suess, S. T., The heliopause, *Reviews of Geophysics*, *28*, 97–115, 1990.

Svalgaard, L., and E. W. Cliver, A floor in the solar wind magnetic field, *Astrophysical Journal*, *661*, L203–L206, 2007.

Tanimori, T., et al., Discovery of TeV gamma rays from SN 1006: Further evidence for the supernova remnant origin of cosmic rays, *Astrophysical Journal Letters*, *497*, L25–L28, 1998.

Teufel, A., and R. Schlickeiser, Analytic calculation of the parallel mean free path of heliospheric cosmic rays. II. Dynamical magnetic slab turbulence and random sweeping slab turbulence with finite wave power at small wavenumbers, *Astronomy and Astrophysics*, *397*, 15–25, 2003.

Thomas, B. T., and E. J. Smith, The structure and dynamics of the heliospheric current sheet, *Journal of Geophysical Research*, *86*, 11105–11110, 1981.

Visser, D. J., The effect of turbulence-modified drift on the modulation of cosmic rays in the heliosphere, Master's dissertation, North-West University, South Africa, 2009.

Wang, Y.-M., E. Robbrecht, and N. R. Sheeley, Jr., On the weakening of the polar magnetic fields during solar cycle 23, *Astrophysical Journal*, *707*, 1372–1386, 2009.

Wang, Y.-M., and N. R. Sheeley, Jr., Solar implications of Ulysses interplanetary field measurements, *Astrophysical Journal Letters*, *447*, L143–L146, 1995.

Webber, W. R., and P. R. Higbie, Limits on the interstellar cosmic ray electron spectrum below $\sim$1-2 GeV derived from the galactic polar radio spectrum and constrained by new Voyager 1 measurements, *Journal of Geophysical Research*, *113*, A11106, 1–10, 2008.

Webber, W. R., and P. R. Higbie, Galactic propagation of cosmic ray nuclei in a model with an increasing diffusion coefficient at low rigidities: A comparison of the new interstellar spectra with Voyager data in the outer heliosphere, *Journal of Geophysical Research*, *114*, A02103, 1–6, 2009.

Webber, W. R., and D. S. Intriligator, Voyagers 1 and 2 in a shrunken and squashed heliosphere, *Journal of Geophysical Research*, *116*, A06105, 1–8, 2011.

Whang, Y. C., and L. F. Burlaga, Anticipated Voyager crossing of the termination shock, *Geophysical Research Letters*, *27*, 1607–1610, 2000.

Wilcox, J. M., and N. F. Ness, Quasi-stationary corotating structure in the interplanetary medium, *Journal of Geophysical Research*, *70*, 5793–5805, 1965.

Williams, T., The influence of the wavy heliospheric neutral sheet on the modulation of cosmic rays (in Afrikaans), Ph.D. thesis, Potchefstroom University, South Africa, 1990.

Zank, G. P., Interaction of the solar wind with the local interstellar medium: A theoretical perspective, *Space Science Reviews*, *89*, 413–688, 1999.

Zurbuchen, T. H., N. A. Schwadron, and L. A. Fisk, Direct observational evidence for a heliospheric magnetic field with large excursions in latitude, *Journal of Geophysical Research*, *102*, 24175–24182, 1997.

Acknowledgements

First and foremost, praise and thanks goes to my Lord and Saviour, Jesus Christ, for the many blessings undeservedly bestowed upon me.

It is my pleasure to thank the following persons and institutions for their support:

- Prof. M. S. Potgieter, my supervisor, for his much needed guidance, assistance and expertise throughout this study, as well as for the care and attention to detail with which he has helped me to finish this work.
- Dr. M. Hitge, my assistant supervisor, for her assistance and helpful discussions concerning my queries about the 3D model, especially during the initial phase of this study.
- The PAMELA-group for giving me access to preliminary PAMELA data. In particular I would like to thank Drs. M. Boezio, V. Di Felice, and N. De Simone for preparing the proton and electron data and for their support and assistance with regard to data-related queries.
- Profs. R. A. Burger, S. E. S. Ferreira, and H. Moraal for useful research related discussions.
- Mr. R. D. Strauss, Mr. N. E. Engelbrecht, Mr. R. Manuel, Ms. R. R. Nndanganeni, and Mr. G. S. Nkosi for their time and assistance on numerous occasions.
- Mrs. M. P. Sieberhagen, Mrs. E. van Rooyen, and Mrs. L. van Wyk for their help in handling administrative matters.
- Mr. M. Holleran for his aid with computer-related problems and queries.
- The National Research Foundation and the Center for Space Research at the North-West University for financial support throughout my studies.

A special thanks goes to:

- Jana Coetzer, for her precious and constant love, support and encouragement.
- My parents and my brother, for their provision, love and support.

Etienne Eben Vos
Center for Space Research, North-West University
December, 2011.